Search for Atmospheric Muon-Neutrinos and Extraterrestric Neutrino Point Sources in the 1997 AMANDA-B10 Data

korrigierte Version

D I S S E R T A T I O N

zur Erlangung des akademischen Grades
doctor rerum naturalium
(dr. rer. nat.)
im Fach Physik

eingereicht an der
Mathematisch-Naturwissenschaftlichen Fakultät I
Humboldt-Universität zu Berlin

von
Dipl.-Phys. Alexander Prinz Biron von Curland
geboren am 18.09.1972 in München

Präsident der Humboldt-Universität zu Berlin:
Prof. Dr. Jürgen Mlynek

Dekan der Mathematisch-Naturwissenschaftlichen Fakultät I:
Prof. Dr. Bernhard Ronacher

Gutachter:

1. . . . . .
2. . . . . .
3. . . . . .

Tag der mündlichen Prüfung: . . . . . .

Abstract

The young field of high energy neutrino astronomy can be motivated by the search for the origin of the charged cosmic rays. Large astrophysical objects like AGNs or supernova remnants are candidates to accelerate hadrons which then can interact to eventually produce high energy neutrinos. Neutrino-induced muons can be detected via their emission of Cherenkov light in large neutrino telescopes like AMANDA. More than 10^9 atmospheric muon events and approximately 5000 atmospheric neutrino events were registered by AMANDA-B10 in 1997. Out of these, 223 atmospheric neutrino candidate events have been extracted. This data set contains approximately 15 background events. It allows to confirm the expected sensitivity of the detector towards neutrino events. A second set containing 369 events (approximately 270 atmospheric neutrino events and 100 atmospheric muon events) was used to search for extraterrestrial neutrino point sources. Neither a binned search, nor a cluster search, nor a search for preselected sources gave indications for the existence of a strong neutrino point source. Based on this result, flux limits were derived. Assuming E_ν^{-2} spectra, typical flux limits for selected sources of the order of $\Phi_\mu^{limit} \sim 10^{-14}\,\mathrm{cm}^{-2}\mathrm{s}^{-1}$ for muons and $\Phi_\nu^{limit} \sim 10^{-7}\,\mathrm{cm}^{-2}\mathrm{s}^{-1}$ for neutrinos have been obtained.

Keywords:
AMANDA , Neutrinos, Point Source, Astro-particle-physics

Deutsche Zusammenfassung

Die vorliegende Dissertation beschäftigt sich einerseits mit der Suche nach atmosphärischen Myonneutrinos und andererseits mit der Suche nach extraterrestrischen Neutrinopunktquellen in dem Datensatz, welcher im Jahre 1997 durch den AMANDA-Detektor aufgenommenen wurde.

In dieser Arbeit wird zunächst die kosmische Strahlung eingeführt. Die Suche nach den Quellen dieser Strahlung wurde bisher insbesondere mit Hilfe der geladenen kosmischen Strahlung selber, sowie mit Hilfe von Cherenkovteleskopen für γ-Strahlen durchgeführt. Die mit diesen Techniken gewonnenen Erkenntnisse lassen bisher jedoch noch keine eindeutigen Schlüsse über die Quellen der geladenen kosmischen Strahlung zu. Dies motiviert den Versuch, mit Hilfe der Neutrinoastronomie ein neues Fenster zu den Quellen zu eröffnen.

Es gibt theoretische Modelle für verschiedene potentielle Neutrinoquellen. Szenarien, in denen massive Teilchen zerfallen und die Zerfallsprodukte ihre kinetische Energie aus der freigewordenen Ruhemasse gewinnen, spielen in dieser Arbeit eine untergeordnete Rolle. Ausführlicher dargestellt werden die konventionellen Modelle, in denen geladene Teilchen mit Hilfe der sogenannten Fermibeschleunigung in astrophysikalischen Schockwellen und/oder Magnetfeldern beschleunigt werden. Hochenergetische Neutrinos entstehen nur bei Quellen, welche Hadronen beschleunigen. Insbesondere die Klasse der aktiven galaktischen Kerne (AGNs) sind hierbei interessant. Die vor einigen Jahren entwickelten vereinheitlichten AGN-Schemata sind ein wichtiger Schritt auf dem Weg, diese Objekte zu verstehen. Andere potentielle Quellen sind Supernovae und ihre Überreste, Mikroquasare, sowie die Quellen hochintensiver Gammastrahlenausbrüche (GRBs). Hoch spekulativ sind Quellen, welche im elektromagnetischen Spektrum unsichtbar sind, oder auch bisher vollkommen unerwartete Quellen. Unabhängig von der genauen Natur möglicher Neutrinoquellen müssen für die Beschreibung der von ihnen ausgesendeten Neutrinoflüsse Oszillationseffekte zwischen den verschiedenen Neutrinofamilien berücksichtigt werden.

Der Nachweis der hochenergetischen Neutrinos soll mit dem AMANDA-Detektor oder ähnlichen Teleskopen erfolgen. Das derzeitige AMANDA-Teleskop (AMANDA-II) wurde in den Jahren 1995 bis 2000 aufgebaut. Es basiert auf dem Nachweis von neutrinoinduzierten Myonen mit Hilfe des Cherenkoveffektes. Das Cherenkovlicht wird hierbei von, in einem Gitter angeordneten, großen Sekundärelektronenvervielfachern registriert. Die gewonnene Zeitinformation erlaubt eine Richtungsrekonstruktion. Das Charakteristikum für ein Neutrinoereignis ist ein aufwärts laufendes Myon, da das Neutrino das einzige bekannte Teilchen ist, welches die Erde durchqueren und ein aufwärts laufendes Myon erzeugen kann. Die vorliegende Arbeit untersucht Daten, die mit Hilfe des AMANDA-B10-Detektors im Jahre 1997 genommen wurden. Die Daten bestehen aus etwa 10^9 atmosphärischen Myon- und etwa 5000 atmosphärischen Neutrinoereignissen.

Um die experimentell gewonnenen Daten analysieren zu können, wird der Vergleich zu simulierten Daten benötigt. Im Rahmen dieser Arbeit wurden Flüsse atmosphärischer Myonen mit den Programmen *basiev* und *CORSIKA*, Flüsse neutrinoinduzierter Myonen mit *nusim* und *nu2mu* generiert. Während eine hohe Zahl von neutrinoinduzierten Myonen simuliert werden konnte, blieb die Zahl der simulierten atmosphärischen Myonen weit hinter der Zahl der experimentell gemessenen zurück. Die Propagation der simulierten Myonen sowie die Detektorsimulation erfolgte mit den Programmen *mudedx* bzw.

AMASIM. Die Zeit-, Orts- und Amplitudeninformationen der gemessenen – wie auch der simulierten – Daten wurden anschließend kalibriert.

Das erste Ziel der Analyse war die Extrahierung eines Satzes atmosphärischer Neutrinos und ein Verständnis der absoluten Sensitivität des Detektors. Die hierfür notwendige Prozessierung der Daten erfolgte in mehreren Schritten. Dabei wechselten sich immer exaktere (aber auch immer langsamere) Richtungsrekonstruktionen mit immer strengeren Qualitäts- und Winkelschnitten zur Datenreduktion ab. Die Rekonstruktionen bestanden sowohl aus schnellen analytischen Richtungsapproximationen, wie auch aus solchen, die auf langsamen Minimierung von Likelihoodfunktionen basierten. Die Schnitte wurden auf topologische Grössen, wie auch auf Parameter, welche aus der Rekonstruktion gewonnen wurden, angewandt. Die Schnitte waren notwendig, um Neutrinoereignisse aus dem weit zahlreicheren Untergrund atmosphärischer Myonenereignisse herauszufiltern. Es wurden zwei stark reduzierte Datensätze („BG-10“ mit 223 Ereignissen und „BG-100“ mit 369 Ereignissen) aus den gemessenen Daten extrahiert. Es konnte gezeigt werden, dass hiervon ca. 15 bzw. 100 Ereignisse durch atmosphärische Myonen bedingt waren. Die Ergebnisse stimmen sehr gut mit der Erwartung für atmosphärische Neutrinos überein, wobei die Erwartung eine Unsicherheit von bis zu 63 % aufweist. Mit dem BG-10 Datensatz war somit das erste Ziel der Analyse erfüllt.

Der BG-100 Datensatz sollte dem zweiten Ziel dieser Arbeit dienen: der Suche nach extraterrestrischen Neutrinoquellen. Für dieses zweite Ziel musste zunächst mit der *effektiven Fläche* ein Maß für die Sensitivität des Detektors bezüglich extraterrestrischer Neutrinos eingeführt werden. Anschließend wurde die Güte der Richtungsrekonstruktion bestimmt. Hiermit konnte die optimale Grösse der zu benutzenden Suchfenster festgelegt werden. Für diese Suchfenster wurde dann die Effizienz der Rekonstruktion bestimmt. Die Effizienz ist ein Maß für den Anteil der Neutrinoereignisse, für den die Rekonstruktion korrekt bestimmt, aus welchem Suchfenster sie stammen.

Nach diesen vorbereitenden Untersuchungen konnte die Quellsuche beginnen. Für diese Suche waren nun sowohl atmosphärische Myonereignisse, als auch Ereignisse, die durch atmosphärische Neutrinos hervorgerufen wurden, Untergrund. Für die Suche wurden drei verschiedene Strategien angewendet. Zunächst wurde ein Netz aus 374 aneinander angrenzenden Suchfenstern konstruiert. Basierend auf der erwarteten Anzahl von Untergrundereignissen für jedes Suchfenster wurden Wahrscheinlichkeiten berechnet, dass die Ereignisse ausschließlich Untergrundereignisse sind. Durch die große Zahl an Suchfenstern gab es einige Fenster, bei denen diese Wahrscheinlichkeit recht gering war. Insgesamt jedoch gab es keinen signifikanten Hinweis darauf, dass die Messung nicht auschließlich durch Untergrund erklärt werden kann. Die zweite Strategie bestand in dem Versuch, mit Hilfe einer Clusteranalyse Punktquellen zu finden. Auch hier wurden keine Hinweise auf Punktquellen gefunden. Schließlich wurde in Richtung von 62 vorselektierten potentiellen Quellen nach Ereignisüberschüssen gesucht – ebenfalls ohne ein positives Ergebnis.

Daraufhin wurden obere Flussgrenzen abgeleitet. Diese Grenzen wurden sowohl richtungsunabhängig als auch für die zuvor selektierten potentiellen Quellen berechnet. In beiden Fällen wurde dabei für das Quellspektrum ein spektraler Index $\gamma = -2$ angenommen. Für Neutrinoenergien $E_\nu > 10\,\mathrm{GeV}$ und Deklinationen $\delta > 33°$ wurden integral folgende globale, obere Flussgrenzen berechnet: $\Phi_\mu^{limit} = 1.41 \cdot 10^{-14}\,\mathrm{cm^{-2}s^{-1}}$ und $\Phi_\nu^{limit} = 1.65 \cdot 10^{-7}\,\mathrm{cm^{-2}s^{-1}}$. Nach der „Eichung“ am Fluss atmosphärischer Neutrinos

konnte die systematische Unsicherheit auf diese Grenzen zu 46 % (systematisch) plus 7 % (statistisch) abgeschätzt werden. Für die 62 ausgewählten Quellen wurden individuelle Flussgrenzen berechnet. Diese waren im Durchschnitt etwa einen Faktor drei besser als die integralen Grenzen für den entsprechenden Deklinationsbereich. Bei 48 potentiellen Quellen waren dies sowohl die ersten Grenzen auf ihren Neutrino- als auch die ersten Grenzen auf ihren neutrinoinduzierten Myonenfluss. Für eine weitere Quelle konnte erstmals eine Grenzen auf den Neutrinofluss abgeleitet werden. Bei den 14 restlichen Quellen konnten in fünf Fällen beide bisher publizierten Grenzen verbessert werden, in zwei weiteren zumindest die Grenze auf den Neutrinofluss. Im Anhang werden Daten bereitgestellt, mit denen die errechneten Grenzen auch in Grenzen für andere spektrale Indizes umgerechnet oder auch Grenzen für weitere Quellen abgeleitet werden können.

Schlagwörter:
AMANDA , Punktquelle, Neutrinos, Astroteilchenphysik

Contents

Deutsche Zusammenfassung **v**

List of Figures **xiii**

List of Tables **xiv**

1 Introduction **1**

2 High Energy Neutrino Point Sources **6**
2.1 Fermi Acceleration 6
2.2 Active Galactic Nuclei 8
2.2.1 The Unified Scheme 9
2.2.2 Leptonic and Hadronic Acceleration Models 11
2.3 Supernova (Remnants) 13
2.4 Microquasars 14
2.5 GRBs and Transient Sources 15
2.6 Hidden Sources 16
2.7 WIMPs and Top-Down Sources 17
2.8 Unexpected Sources 17
2.9 Neutrino Oscillations 19

3 The AMANDA Neutrino Telescope **20**
3.1 Detection Principle 20
3.1.1 Cherenkov Light 20
3.1.2 Basic Neutrino Telescope Design 21
3.2 History 21
3.3 AMANDA-B10 24
3.4 Background and Signal 25
3.5 Other Physics Potential 27

4 Data Sets Analyzed **28**
4.1 Experimental Data 28
4.2 Monte Carlo Simulation 28
4.2.1 Event Generation 28
4.2.2 Muon Propagation 30
4.2.3 Photon Propagation 30
4.2.4 Detector Response 31

5 Calibration **33**
5.1 Timing Calibration: T_0 and α 33
5.1.1 Necessary Accuracy 34
5.2 Geometry Calibration 36
5.3 Amplitude Resolution 37
5.4 Calibration of the Optical Properties 37

6 Reconstruction **40**
6.1 Line-fit . . . 41
6.2 Dipole Approximation . . . 42
6.3 Tensor of Inertia . . . 42
6.4 Likelihood Track Reconstruction . . . 43
6.4.1 Iterative Reconstruction . . . 44
6.4.2 Multi-PE Reconstruction . . . 45
6.4.3 $P_{hit}P_{nohit}$ Reconstruction . . . 45
6.4.4 Zenith-angle-weighted Reconstruction . . . 46
6.4.5 Combined Reconstructions . . . 47
6.4.6 Track and Energy Reconstruction . . . 47
6.5 Shower Reconstruction . . . 48
6.6 Optimization of Reconstruction Parameters . . . 48

7 Data Processing **51**
7.1 Processing of 1997 AMANDA Data . . . 51
7.1.1 Preprocessing . . . 51
7.1.2 Level 1 . . . 53
7.1.3 Level 2 . . . 54
7.1.4 Level 3 . . . 57
7.1.5 Level 4 . . . 60
7.2 Final Data Samples . . . 66
7.2.1 Sample Definitions and Properties . . . 66
7.2.2 Background Estimations . . . 70
7.2.3 Sample Motivations . . . 71
7.3 Systematic Uncertainties . . . 72
7.3.1 Neutrino Flux Predictions . . . 72
7.3.2 Neutrino Interaction Cross Section . . . 73
7.3.3 Neutrino Oscillations . . . 73
7.3.4 Muon Propagation . . . 74
7.3.5 Optical Properties . . . 74
7.3.6 OM Sensitivity . . . 75
7.3.7 Hardware Simulation . . . 76
7.3.8 Timing and Geometry Calibrations . . . 76
7.3.9 Amplitude Resolution . . . 77
7.3.10 Peaks in z_{COG} . . . 77
7.3.11 Summary of Systematic Uncertainties . . . 77

8 The Effective Detector Size **80**
8.1 General Definitions . . . 80
8.2 Flux Limits and the Energy-Averaged Effective Area . . . 83
8.3 The Energy-Averaged Effective Areas in AMANDA . . . 84
8.3.1 Uncertainties . . . 87

9 Resolution, Bin-size and Efficiency **88**
9.1 The Detector Resolution . . . 88
9.1.1 Determination of the Detector Resolution . . . 88
9.1.2 Analysis of the Space-angular Resolution . . . 90
9.1.3 Cross-Checks of the Simulation Results . . . 92
9.1.4 Systematic Uncertainties of the Resolution . . . 93
9.2 The Optimal Bin-Size . . . 94
9.2.1 Basic Assumptions . . . 94
9.2.2 Non-Gaussian Signal Distributions . . . 96
9.2.3 AMANDA-B10 Scenario: Small Statistics . . . 97
9.2.4 Analysis of the Optimal Bin-Size . . . 99
9.3 Reconstruction Efficiency . . . 102

10 Extraterrestrial Point Source Searches **105**
10.1 Motivation . . . 105
10.2 Data Sample . . . 106
10.3 Search Strategies . . . 107
10.4 Binned (Grid) Search . . . 108
10.4.1 Definition of the Search Grids . . . 108
10.4.2 H_0 Hypotheses . . . 110
10.4.3 Significance of Excess . . . 111
10.5 Cluster Search . . . 113
10.6 Selected Sources . . . 114
10.7 Search for Neutrino Bursts . . . 115

11 Flux Limits and Discussion of Results **118**
11.1 All-sky Flux Limits . . . 119
11.2 Specific Potential Sources . . . 123
11.2.1 TeV γ-ray Blazars . . . 124
11.2.2 MeV γ-ray selected Blazars . . . 125
11.2.3 Infrared & X-ray selected AGNs . . . 126
11.2.4 Radio selected AGNs . . . 127
11.2.5 Close Quasi Stellar Objects. . . . 128
11.2.6 Galactic TeV γ-ray Sources . . . 128
11.2.7 Microquasars . . . 130
11.2.8 Highest Energy Cosmic Ray Multiplets . . . 130
11.2.9 BL Lacertae close to Highest Energy Cosmic Ray Directions 131
11.2.10 Individual further Objects . . . 131
11.3 Comparison to other Analyzes . . . 132
11.4 Uncertainties of the Flux Limit Calculation . . . 134

12 Summary **136**

13 Outlook **137**

References **139**

A Astrophysical Parameters **I**
A.1 Units I
A.2 Astronomical Coordinate Systems II
A.2.1 Celestial Coordinates II
A.2.2 Detector Coordinates III
A.2.3 Co-moving Coordinate Systems IV
A.2.4 Projections IV

B Relativistic 2-body scattering **V**
B.1 Δ Resonance V
B.2 Electron Pair Production V

C Glossary of AGN Nomenclature **VI**

D Processing Details **IX**
D.1 OM selection IX
D.2 Run Information X
D.3 Reconstruction and Filter Summary XV
D.4 Level 4 Cuts XVI
D.5 Passing Rates XVII
D.6 Background Normalization XVIII
D.7 Event List XIX

E The Muon Energy **XXIII**

F Calculating Further Limits **XXV**

Acknowledgment **XXXIX**

Erklärung **XL**

Curriculum Vitae **XLI**

Publications **XLII**

List of Figures

1.1 The all particle cosmic ray energy spectrum . . . 1
1.2 The energy dependent mean free path of a photon . . . 3
2.1 First order Fermi acceleration . . . 7
2.2 Schematic representation of a radio-loud AGN . . . 10
2.3 Schematic representation of AGN acceleration processes . . . 12
2.4 Expected $\nu_\mu + \bar{\nu}_\mu$ fluxes from cosmic ray accelerators . . . 18
3.1 Cherenkov cone of a muon inside a PMT grid . . . 21
3.2 The present AMANDA detector . . . 23
3.3 Surface electronics of the AMANDA-B10 detector . . . 25
3.4 The origins of muons in an underground detector . . . 26
5.1 Optical properties: Effective scattering and absorption coefficients 38
7.1 Level 1 processing: θ_{LF} and v_{LF} . . . 53
7.2 Level 2 processing: θ_{LIKE} and N_{ch} . . . 55
7.3 Level 2 processing: θ_{ITER} and $N_{dir,\,ITER}(-15..25)$ . . . 56
7.4 Level 2 processing: L_{ITER} . . . 56
7.5 Level 3 processing: L_{ENERGY} and $\mathsf{L}_{SHOWER}/\mathsf{L}_{ITER}$ . . . 57
7.6 Level 3 processing: z_{COG} and $N_{dir,\,ITER}(-15..75) - N_{dir,\,SHOWER}$. 58
7.7 Level 3 processing: 2-dimensional Cuts . . . 59
7.8 Level 4: $\Psi(ITER, LF)$ and $|S^{van}_{MPE}|$ . . . 63
7.9 Level 4: $|S^{P_{hit}}|/(\theta - 90°)$ & $(N_{dir}(-15..75) - 2) \cdot L_{dir}(-15..75)$ . . 64
7.10 Level 4: $\log(\mathcal{L}_{down,\,ITER}) - \log(\mathcal{L}_{up,\,ITER})$ and $\Psi(MPE, LF)$ . . . 65
7.11 Level 4: $R_{S,\,dir,\,ITER}$ and passing rate versus quality Q . . . 66
7.12 Final event selection: Zenith angle distributions . . . 67
7.13 Reconstructed zenith angle and energy for various cut levels . . . 68
7.14 Final event selection: Number of events versus time . . . 69
7.15 Sky map of the BG-10 sample in detector coordinates . . . 72
7.16 Final event selection: v_{LF} and N_{ch} for various OM sensitivities . . 75
8.1 The effective area A_{eff} and the effective volume V_{eff} . . . 81
8.2 The zenith angle dependency of $\bar{A}_{eff}$ . . . 84
8.3 The energy dependency of $\bar{A}_{eff}$ . . . 85
8.4 The spectrum dependency of $\bar{A}_{eff}$ . . . 86
9.1 The dependency of the resolution on the reconstruction algorithm . 88
9.2 Parameterization of the detector resolution . . . 89
9.3 The dependency of the resolution on the cut level and on $\cos\theta_\mu$ . . 90
9.4 The dependency of the resolution on E_μ and on γ . . . 91
9.5 A 3×3 model search grid . . . 98
9.6 $< p_c >$ versus bin-size and optimal bin-size versus zenith angle . . 100
9.7 The dependency of the optimal bin-size on the number of events . 101
9.8 The angle and energy dependency of the efficiency ϵ_{bin} . . . 103
9.9 The spectrum dependency of the efficiency ϵ_{bin} . . . 104
10.1 Sky map of the BG-100 sample in galactic coordinates . . . 106
10.2 Sky map of the BG-100 sample in super-galactic coordinates . . . 107
10.3 The search grid #1 . . . 109

10.4 Sky map of the BG-100 sample in equatorial coordinates 110
10.5 Integral distribution of chance probabilities for the binned search . 112
10.6 Cluster multiplicities and chance probabilities for selected sources . 114
10.7 Search for GRB candidates in final experimental events 116
11.1 The declination dependency of the integral flux limits 120
11.2 The pseudo-differential flux limits 121
11.3 The spectrum dependency of the integral flux limits 122

List of Tables

2.1 The unified AGN scheme 9
5.1 Investigated potential errors during the timing calibration 36
7.1 Oscillation effects on level 4 passing rates 73
7.2 Summary of systematic uncertainties for atmospheric neutrinos . . 78
7.3 Summary of systematic uncertainties for astrophysical neutrinos . . 79
9.1 The parameterization of the resolution function $f(< \psi)$. 96
10.1 The advantages and disadvantages of potential search strategies . . 108
10.2 Comparison of AMANDA doublets to BATSE GRB detections . . . 117
11.1 Integral all sky limits on the μ and ν_μ fluxes 119
11.2 Pseudo-differential limits on the μ and ν_μ fluxes 121
11.3 Limits on integral μ and ν_μ fluxes from TeV γ-ray Blazars 124
11.4 Limits on integral μ and μ_ν fluxes from strong MeV γ-ray AGNs . 126
11.5 Limits on integral μ and ν_μ fluxes from strong X-ray AGNs 126
11.6 Limits on integral μ and ν_μ fluxes from strong infrared AGNs . . . 127
11.7 Limits on integral μ and ν_μ fluxes from strong radio-loud AGNs . . 127
11.8 Limits on integral μ and ν_μ fluxes from GHz-peaked radio AGNs . 128
11.9 Limits on integral μ and ν_μ fluxes from close QSOs 129
11.10 Limits on integral μ and ν_μ fluxes from galactic TeV γ-ray sources 129
11.11 Limits on integral μ and ν_μ fluxes from microquasars 130
11.12 Flux limits from the directions of UHECR multiplets 131
11.13 Flux limits from BL Lacs close to UHECR directions 132
11.14 Limits on integral μ and ν_μ fluxes from individual other objects . . 132
11.15 Average expected integral limits on the μ and ν_μ fluxes 133
A.1 The definitions of various astronomical coordinate systems II
D.1 Run-independent OM selection in experimental and simulated data IX
D.2 Run-dependent OM selection in experimental data IX
D.3 OM selection in simulated data X
D.4 Information on runs 304 – 523 X
D.5 Information on runs 524 – 685 XI
D.6 Information on runs 686 – 847 XII
D.7 Information on runs 948 – 1009 XIII
D.8 Information on runs 1012 – 1120 XIV
D.9 Summary information for all runs XV
D.10 The processing chain of this analysis up to level 3 XV

D.11	The processing chain of this analysis up to level 3 continued	XVI
D.12	CutEval parameterization results	XVI
D.13	Level 4 cuts for particular values of the CutEval parameter N . .	XVII
D.14	The cut passing rates of the various data sets	XVII
D.15	Summary of possible background normalizations	XIX
D.16	List of events selected between day 96 and day 202	XX
D.17	List of events selected between day 202 and day 293	XXI
D.18	List of events selected between day 294 and day 318	XXII
F.1	The $\mu_{90}(\delta)$ values needed for the calculation of all-sky flux limits .	XXV
F.2	The spectrum, energy and angle dependency of $\epsilon_{bin,\,grid}$	XXVII
F.3	The spectrum, energy and angle dependency of $\epsilon_{bin,\,grid}$	XXVIII
F.4	The spectrum, energy and angle dependency of $\epsilon_{bin,\,selected}$	XXIX
F.5	The spectrum, energy and angle dependency of ϵ_{bin}	XXX
F.6	The spectrum, energy and angle dependency of $\bar{A}_{\mu,\,eff}$	XXXI
F.7	The spectrum, energy and angle dependency of $\bar{A}_{\mu,\,eff}$	XXXII
F.8	The spectrum, energy and angle dependency of $\bar{A}_{\nu,\,eff}$	XXXIII
F.9	The spectrum, energy and angle dependency of $\bar{A}_{\nu,\,eff}$	XXXIV
F.10	The spectrum, energy and angle dependent uncertainty on $\bar{A}_{\mu,\,eff}$.	XXXV
F.11	The spectrum, energy and angle dependent uncertainty on $\bar{A}_{\mu,\,eff}$.	XXXVI
F.12	The spectrum, energy and angle dependent uncertainty on $\bar{A}_{\nu,\,eff}$.	XXXVII
F.13	The spectrum, energy and angle dependent uncertainty on $\bar{A}_{\nu,\,eff}$.	XXXVIII

1 Introduction

The first quarter of the previous century is commonly referred to as the golden age of physics. This attribute can certainly be justified solely by the advent of the two great new theories: quantum theory and the theory of relativity. But other fields of physics also made rapid and important progress. One example is the discovery of extraterrestrial radiation by Victor Hess during his balloon flights in 1912.

It was soon realized that these so-called *cosmic rays* dominantly consist of ionized atomic nuclei, in particular protons and helium and, to a lesser degree, of electrons. Since 1912 these rays have been studied extensively. Their exact composition (in combination with photo-spectroscopic information from distant celestial objects) yielded important information for our understanding of nucleosynthesis (at the big bang and in stars/supernovae). The near-perfect power law of the energy spectrum spans 30 orders of magnitude in flux and a dozen orders of magnitude in energy (see figure 1.1). It offered a sufficient flux of energetic particles for studies of collision processes – and consequently for the discovery of new particles like the muon in 1936. Particle physics would have been impossible without cosmic rays for a considerable period: Efficient earth bound particle accelerators became available only in the 1950s.

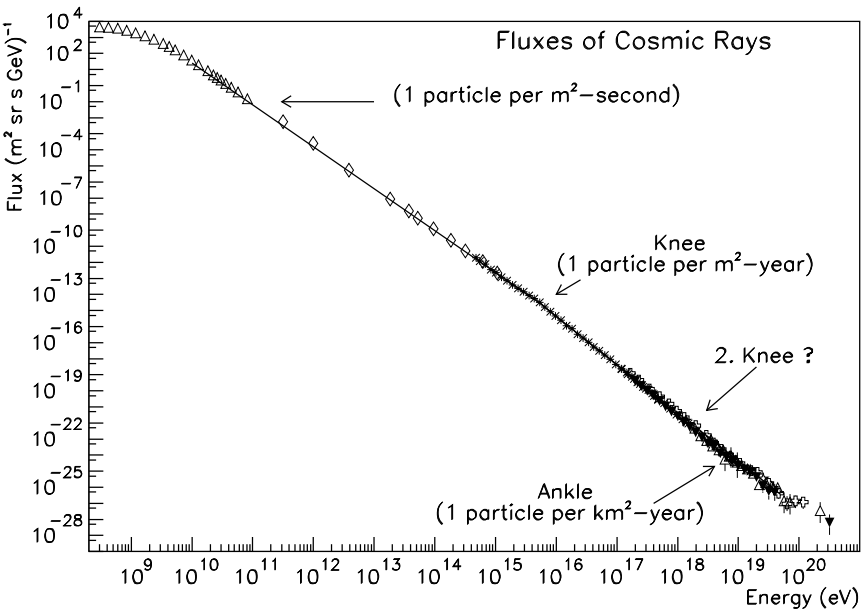

Figure 1.1: The all particle cosmic ray spectrum as measured by various groups. It has a spectrum of $\sim E^{-2.75}$ between $E \sim 10^{10}\,\text{eV}$ and $E \sim 5 \cdot 10^{15}\,\text{eV}$. At the so-called "knee", the composition seems to change to heavier elements and the spectrum steepens to $\sim E^{-3.0}$. Beyond the "ankle", at $E \sim 5 \cdot 10^{18}\,\text{eV}$, the spectrum flattens again and the composition seems to shift back to lower mass nuclei. Some data suggest the existence of a second "knee" just before the ankle. Figure taken from [231].

Despite the long history of physics with cosmic rays and cosmic ray physics, the origin of the cosmic rays is still debated today. Just like in the case of classical astronomy, one would like to determine the locations of the sources and measure their spectra (including potential time dependencies). The latter task has only been achieved for diffuse fluxes so far. The search for the actual sources which are probably outside our solar neighborhood has not succeeded yet.

The ongoing search can in principle be performed with four different messenger particles: the charged cosmic rays themselves, neutrons, photons or neutrinos. Each of these particle species has its particular advantages and disadvantages [95, 138].

Charged Cosmic Rays: The charged cosmic rays themselves are the most obvious messenger to use: If they did not interact after emission, they come from their own source. They are, however, deflected in galactic and intergalactic magnetic fields. Below an energy of approximately $\sim 10^{19}\,\mathrm{eV}$, they thus do not point back to their origin any more. Furthermore cosmic ray protons can interact with the abundant cosmic background radiation. Above a proton energy of $10^{20} - 10^{21}\,\mathrm{eV}$, the energy in the center of mass system can exceed the rest mass of the $\Delta(1232)$ resonance. Correspondingly the delta resonance is produced:

$$p + \gamma_{IR} \rightarrow \Delta + X \quad \text{for} \quad 4 \cdot E_p \cdot E_\gamma > (m_\Delta^2 - m_p^2) \;, \tag{1.1}$$

where E_p is the proton energy, E_γ that of the photon and m_p and m_Δ are the rest masses of proton and Δ-resonance respectively. The condition given in equation 1.1 is derived in appendix B.1. The limit on the proton energy for this reaction is called the Greisen-Zatsepin-Kuzmin or GZK-cutoff. In more than 99 % of the cases, the delta resonance decays to a pion and a nucleon [191], which typically has an energy just below the GZK-cutoff. The mean free path for protons of these high energies is therefore in the order of only tens of Megaparsecs[1]. So, at energies beyond the GZK-cutoff, the cosmic ray flux is expected to drop significantly. Instead, the opposite effect seems to be observed, see figure 1.1. The cause of this spectral behavior is under strong debate.

The most interesting energy range to detect charged cosmic ray sources is thus the window in between approximately $10^{19}\,\mathrm{eV}$ and $10^{20}\,\mathrm{eV}$. At these energies the fluxes are so low that only about one event per square kilometer and century is occurring. This poses an experimental challenge for the detection: Satellite- or balloon-experiments are typically limited to a size scale of $\mathcal{O}(1)\,\mathrm{m}^2$. They are thus far too small to measure such tiny fluxes (they are effectively limited to energies below $E \sim 10^{14}\,\mathrm{eV}$). Ground based experiments can cover large areas and have already measured fluxes of these enormous energies. But since they only measure decay products of the reaction between the primary particle and the earth atmosphere, they have not yet accomplished convincing primary composition measurements.

So far, no point sources of energetic charged cosmic rays have been identified. Detected anisotropies [226, 229] might be associated with so far unresolved point sources. It is hoped that the future Auger Project [14] will collect enough statistics of high energy events to resolve point sources.

[1] For the definition of astronomical units, see appendix A.1. In particular the (Mega)-parsec is defined in equation A.3

Gamma Ray Photons: Photons are the classical messenger of astronomy. In contrast to charged cosmic rays, they are not deflected by magnetic fields – photons of any energy always point back to their source. Their correlation with charged cosmic rays is not simple: Every theory describing charged cosmic ray sources also predicts processes producing high energy gamma ray photons; but not necessarily vice versa. I.e. a detected high energy gamma ray source need not be a source of charged cosmic ray nuclei. Moreover, the atmosphere is opaque to gamma rays. Just as in the case of charged cosmic rays, satellites or balloon experiments are therefore needed for direct measurements, but are restricted to "low"-energies: $E_\gamma \lesssim 10\,\mathrm{GeV}$.

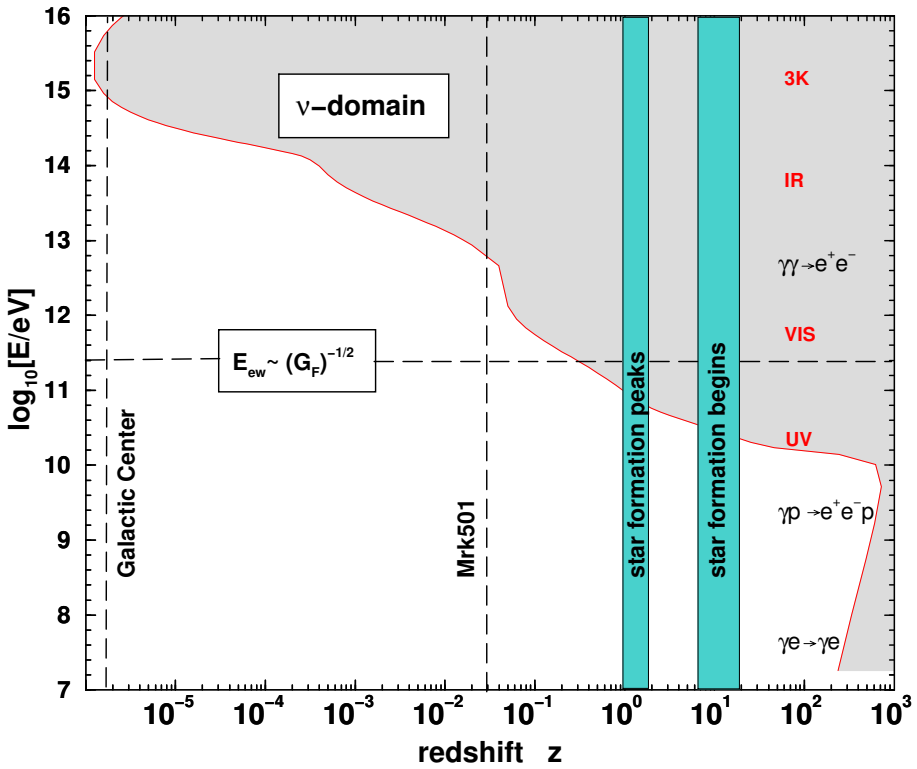

Figure 1.2: The energy dependent mean free path of a photon due to various absorption processes ($h = 0.6$, CDM cosmology). The shaded area labeled as "ν-domain" is invisible for gamma ray astronomy. For the definition of redshift, see equation A.4. Figure taken from [149].

At present, ground based experiments only measure photons with energies $E_\gamma \geq 300\,\mathrm{GeV}$. Here, the challenge lies in the separation of γ-induced air showers from the much more frequent showers induced by charged cosmic rays. And again the absorption process is relevant. Photons of TeV energy and above are absorbed by pair production of electrons on background light (visible and infrared star light, microwave background radiation and galactic radio waves). The threshold for these reactions is:

$$4 \cdot E_\gamma \cdot E_{\hat{\gamma}} > 2 \cdot (m_e)^2 \ , \tag{1.2}$$

where E_γ is the energetic photon's energy, $E_{\hat{\gamma}}$ the background photon's energy and m_e the electron rest mass. This condition is derived in section B.2. As can be seen from figure 1.2, distances above a redshift z of a few 10^{-2} are thus invisible for photons of TeV or higher energies. In particular those regions which are cosmologically interesting with respect to star formation cannot be investigated. Therefore a next generation of Cherenkov telescopes is currently under construction [123, 158, 202]. They will allow to observe γ rays down to $\sim 30\,\mathrm{GeV}$ and extend the γ-ray horizon up to the borders of the visible universe.

TeV-gamma ray astronomy is already very successful: It has detected several confirmed galactic and extra-galactic point sources [244]. The interpretation of these sources with respect to potential cosmic ray acceleration sites is still open.

Neutrons and other electrically neutral cosmic rays: Just like photons, electrically neutral cosmic ray hadrons are not deflected in magnetic fields. However, unlike photons, none of these particles (neutrons, π^0,...) is stable. Instead, all decay on rather short timescales. The most long-lived among them is the neutron with a lifetime of 887 seconds. For energies of $10^{15}\,\mathrm{eV}$, the distance neutrons can travel (γct) is equivalent to the distance from earth to the galactic center. Even neutrons of higher energies will not travel cosmological distances. Neutrons may, however, play a role as mediator particles by escaping sources inside strong magnetic fields and decaying outside of these fields. They thereby initialize fluxes of protons, electrons or other charged particles. The secondary particles are then not strongly affected by the magnetic fields of the source any more.

Neutrinos: Since they interact only weakly, neutrinos are neither deflected in magnetic fields, nor absorbed as strong as the before mentioned messengers. Furthermore, they can escape from the core of dense source materials, whereas photons and nucleons can only escape from the source's outermost layers. On the other hand, their reluctancy to interact imposes a great challenge for their detection: Only a tiny fraction of incident neutrinos can be observed. As will be shown later, the goal to achieve an angular resolution of one degree (necessary for astronomy), can only be achieved when measuring high-energy neutrinos (above a few hundred GeV). Other advantages of this energy range are the increase of the neutrino interaction cross section and of secondary muon ranges with energy. To compensate the tiny fluxes (compared to neutrino beams from accelerators or low energy fluxes from reactors), it is of vital importance to build large detectors. Most long-term plans for new *neutrino telescopes* therefore aim at the construction of cubic-kilometer scale detectors [46].

In comparison to the well-established techniques described before, neutrino telescopes are the youngest class of telescopes to be actually built (though they had been proposed more than 40 years ago [109, 164]). Thus they could not contribute to the solution of the question "Where do the high energy cosmic rays come from?" – yet. In fact only two extraterrestrial sources of neutrinos have been observed so far: The sun (seen for example by SNO [3] and Super-Kamiokande [225]) and the Supernova 1987A (Seen by Kamiokande-II [122] and IMB [36]). Nevertheless neutrinos seem to be a promising tool to help answering the question about the cosmic ray origin eventually.

Historically, the search for the origin of the charged cosmic rays was the foundation of the young field of astro-particle physics. Therefore and because it is closely linked to one goal of this work, this introduction concentrated on this single topic only. By now, astro-particle physics has become a rich discipline of physics combining many different studies associated with the very largest (cosmology & astrophysics) and the very smallest (particle physics). Once large neutrino telescopes are built, they are expected to contribute not only to the question of cosmic ray sources, but also to many further open questions. Several of them are listed in section 3.2.

In the following section 2, potential sources of extraterrestrial high energy neutrinos are presented. Especially the so-called AGNs are discussed in section 2.2. After the discussion of sources, the AMANDA neutrino telescope, its technology and its detection principle are introduced in section 3. In section 4, the experimental and the Monte Carlo simulated data which entered the analysis described in this work are presented. Following is a discussion about the calibration of these data sets in section 5. The reconstruction algorithms are introduced in section 6. While the before mentioned sections introduce the theory, the experiment and the tools, the following sections all refer to the analysis performed by the author.

The analysis starts with the processing of the calibrated data as outlined in section 7. It cumulates in the selection of candidates for atmospheric neutrino events. Three sets of various purity are defined. It is shown that experimental data follows predictions for the selections chosen. This is the single most important indication that the detector performs as expected. At the same time, the selection criteria implicitly accumulate well reconstructed events as shown in section 9.1.

The data sets defined can therefore be used to search for extraterrestrial neutrinos. First, the sensitivities towards extraterrestrial neutrino fluxes are calculated via the parameter "effective area" in section 8. Then the optimal size of search bin cones is derived in section 9. The search for point sources of high-energy astrophysical neutrinos is then presented in section 10. Based on the non-observation of any significant source, flux limits are finally derived in section 11.

Definitions are moved to the appendices: In appendix A, astrophysical parameters (units of distance and energy as well as coordinate systems) are explained. The kinematic requirements for the absorption processes already discussed (electron pair creation and the formation of the Δ resonance) are derived in appendix B. Appendix C lists often occurring AGN nomenclature and acronyms. Several details of the data processing and the events finally selected are given in appendix D. The question of how the muon energy is defined in AMANDA is answered in appendix E. In appendix F finally, the dependencies on source spectra, incident angles and energy intervals of the detector efficiencies and sensitivities are tabulated.

2 High Energy Neutrino Point Sources

One task of this work is the search for extraterrestrial neutrino point sources. Potential sources of energetic neutrinos can be divided into two classes:

Bottom-up scenarios: Charged low energy particles are accelerated to high energies. Energetic neutrinos are then produced from interactions of accelerated hadrons with a "beam dump". Here, a beam dump is a matter or photon field, whose column density is large enough for the accelerated beam to interact but whose density is small enough for pions (and muons) to decay rather than interact.

Top-down scenarios: The decay or annihilation of super-heavy particles (e.g. topological defects) or of the (less heavy) so called WIMPs produces particles with high initial energy. Energetic neutrinos can be decay products themselves or can be produced by the decay products' interactions.

Top-down scenarios are able to model the highest energy cosmic rays observed, but they are nevertheless highly speculative: The existence of the heavy particles required has yet to be verified. This work will thus predominantly consider bottom-up scenarios.

Such scenarios are typically based on the so-called "Fermi acceleration" of electrically charged particles. It is described in the next section. In theories describing neutrino point sources, protons, helium-nuclei or other hadrons are accelerated by some mechanism at the "source" and then interact with a "beam dump" field. If this field contains protons, a neutrino can be produced in the following reaction chain:

$$\begin{aligned} p_{acc} + p_{dump} \rightarrow N_1\pi^0 + N_2\pi^+ + N_3\pi^- + X \qquad & N_1 \approx N_2 \approx N_3 \\ \pi^0 \rightarrow 2\gamma & \\ \pi^+ \rightarrow \mu^+ + \nu_\mu & \\ \mu^+ \rightarrow e^+ + \nu_e + \bar{\nu}_\mu & \\ \pi^- \rightarrow \mu^- + \bar{\nu}_\mu & \\ \mu^- \rightarrow e^- + \bar{\nu}_e + \nu_\mu & \end{aligned} \tag{2.1}$$

Equivalent reaction chains also exist with other hadrons (He,...) replacing the accelerated proton p_{acc}, with other hadrons or a photon field γ replacing the beam dump p_{dump}, with $K^\pm$ replacing $\pi^\pm$ or with K^0_L decays. A sample of specific models together with neutrino fluxes from the atmosphere and from the galactic disk is given in figure 2.4.

2.1 Fermi Acceleration

Many astrophysical sources have X-ray and γ-ray spectra characteristic for conditions far from thermodynamic equilibrium. They indicate efficient particle acceleration. Often the non-thermal emission is accompanied by powerful supersonic outflows containing shock waves, like it is the case in radio jets, gamma ray bursts or supernova remnants. Diffuse shock acceleration is proposed to occur in these outflows. The theory describing diffuse shock acceleration [15, 145] is based on Fermi's suggestion of multiple scattering between magnetic "mirrors" [90, 91] and Parker's discovery of the importance of shock waves in the interstellar medium for increasing the efficiency of the mechanism [190].

The two crucial ingredients for the so called *first order Fermi acceleration* are the shock front and (random) elastic scattering processes in front of it and behind it. If both are present, a particle can cross the out-flowing shockwave, scatter, cross the shockwave in the other direction, scatter again, again cross the shockwave, scatter again and so on, see figure 2.1.

If the particle enters the shocked region with energy E_1 (frame outside the shocked region), this translates to an energy $E_1' = \gamma \cdot E_1 \cdot (1 - \beta \cdot \cos(\theta_1))$ in the shocked frame of reference. (The formula is only true if one already assumes relativistic energies where $E \approx p \cdot c$.) Here, $\gamma = (\sqrt{1-\beta^2})^{-1}$ and $\beta = v/c$ are defined via the average velocity $|\vec{v}|$ of the shocked material ("downstream") in the frame of the un-shocked material ("upstream"). Elastic scattering leads to a new trajectory but the energy in the shocked frame remains constant: $E_2' = E_1'$. When the particle enters the non-shocked region again, it has the new energy $E_2 = \gamma \cdot E_2' \cdot (1 + \beta \cdot \cos(\theta_2))$. In total, there is a net energy difference ΔE, which is proportional to the already acquired energy E_1:

$$\begin{aligned} \Delta E &= E_2 - E_1 \\ \Delta E &= E_1 \cdot \left(\frac{1-\beta\cdot\cos(\theta_1)+\beta\cdot\cos(\theta_2)-\beta^2\cdot\cos(\theta_1)\cdot\cos(\theta_2)}{1-\beta^2} - 1 \right) \\ \Delta E &= \epsilon E \end{aligned} \tag{2.2}$$

Averaging over all possible angles θ_1 and θ_2, one finds that the constant $\epsilon = \frac{4}{3}\beta$ for non-relativistic flows [95]. There is thus a net energy gain. For relativistic flows, the resulting equation is more complicated but still $\epsilon \propto \beta$, see [242]. After n iterations (scattering forward and backward through the shock wave), the total energy is:

$$E = E_0(1+\epsilon)^n \tag{2.3}$$

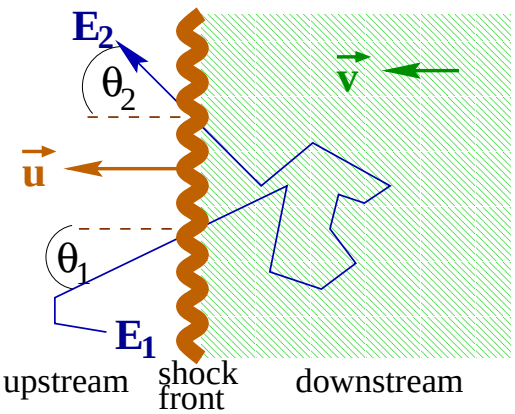

Figure 2.1: Concept of the first order Fermi acceleration: The shock front moves with velocity $\vec{u}$, the shocked material with $\vec{v}$. The particle enters with energy E_1 under an angle θ_1 from the un-shocked region, scatters inside the shocked region and leaves with an energy E_2 under the angle θ_2.

This mechanism is often compared to the case of a ball bouncing between a pair of approaching walls. Here, scattering processes at magnetic fields replace the walls. The conditions for this acceleration to proceed are:

- The energy gain per unit time must be larger than the energy loss due to synchrotron radiation and during scattering.
- The scattering length must be smaller than the shock radius.
- The sideways diffusion timescale must be longer than the acceleration time scale.
- There is no scattering within the shockwave, i.e.: the shock thickness must be much smaller than the particle gyroradius, which in turn must be smaller than its Coulomb mean free path.

If all these conditions are fulfilled, first order Fermi acceleration occurs. The spectrum produced can easily be understood: The number of iterations to increase the energy from E_0 to E is then given by

$$n = \frac{\ln(E/E_0)}{\ln(1+\epsilon)} \ . \tag{2.4}$$

If the escape probability per iteration is P_e, then the probability that the particle remained in the acceleration mechanism for n iterations is $(1-P_e)^n$. Inserting equation 2.4 into this yields

$$\frac{dN}{dE} \propto \left(\frac{E}{E_0}\right)^{\frac{\ln(1-P_e)}{\ln(1+\epsilon)}} = N_0 E^{-\gamma} \ . \tag{2.5}$$

Equation 2.5 defines the (differential) spectral index γ. It can also be written as

$$\gamma = 2 + \frac{4}{M^2} \ . \tag{2.6}$$

Equation 2.6 is derived for example in [95][1]. Here, $M \equiv \sqrt{(v/c_*)}$ is the Mach number, v is the particle velocity and c_* the speed of sound, or "Alfvén speed", in the plasma. In simple models of the Fermi acceleration, where the influence of the accelerated particles on the accelerating fields is ignored, the Mach-term is ignored and one obtains a "generic" spectral index of 2. In realistic models, the Mach number diverges for non-relativistic shocks only, but has finite values for (moderately) relativistic shocks [149]. Typical source spectra have thus $2.1 \leq \gamma \leq 2.4$. The interaction cross-section of the accelerated particles with our galaxy (magnetic, photon, and particle fields) rises with energy. Furthermore, energetic particles have larger gyroradii and thus escape our galaxy more often than particles of lower energies. A so-called leakage of $0.6 \geq \Delta\gamma \geq 0.3$ therefore modifies the source spectrum to the observed value of $\gamma = 2.7$.

The acceleration mechanism described so far is called "first order" Fermi acceleration, since it has a linear dependency on v/c_*. There also exists a so-called "second order" Fermi acceleration, which requires magnetic or plasma clouds rather than a shock front and which depends on $(v/c_*)^2$. A discussion of that (less efficient) second order Fermi acceleration can be found for example in [95].

Alternative acceleration processes may exist. Reconnections of magnetic flux tubes cause the acceleration of charged particles during solar flares. Equivalent processes are also predicted for other astrophysical sites [27]. Such, or other alternative acceleration models will not be considered any further in this work.

2.2 Active Galactic Nuclei

Active Galactic Nuclei, or simply *AGNs*, are a class of extragalactic objects whose properties (e.g. spectra) are dominated by non-stellar processes: No model describing stars predicts their properties. The AGN locations can sometimes clearly be associated with the cores of galaxies. It is believed that this association always exists, but present telescopes

[1] Note that in [95], the integral spectral index is calculated. It is correspondingly one unit smaller than the differential index used throughout this work.

are not always capable to resolve a host galaxy. An important AGN feature is the fact that their emission covers a very large fraction of the electromagnetic spectrum: From radio waves to gamma rays photons, all frequencies have been observed.

2.2.1 The Unified Scheme

Before it was realized that various objects in different wavelength intervals probably all belong to the same class, a rich nomenclature based on observational characteristics had already been established. This "zoo" has been simplified by the *unified scheme* developed in recent years [28, 187, 232]. That scheme is a consistent picture of AGNs and thereby simplified the previous classifications, see table 2.1. In the unified scheme, several observational details can be understood by a combination of source properties and selection effects such as relative source orientation and distance, see figure 2.2. By now, there is growing experimental support for these schemes, see for example [159] and references therein.

Radio Loudness	Optical Emission Line Properties		
	Type 2 (Narrow Line)	Type 1 (Broad Line)	Type 0 (Unusual)
Radio-quiet	Seyfert 2	Seyfert 1 QSO	
Radio-loud	NLRG { FR 1 FR 2	BLRG Quasars { SSRQ FSRQ	Blazars { BL Lacs FSRQ

Table 2.1: The unified scheme according to [187]. Sources are classified according to observational properties: Whether the host galaxy is resolved (top line of each box) or not (lower line), their radio loudness (top or bottom row) and emission line properties (columns). Definitions of the acronyms and terminology used here are given in appendix C

The main source of AGN energy is supposed to be gravitational energy freed when matter is accreted onto a super-massive ($M \gg 10^6 m_\odot$) black hole. For matter of mass m falling from infinity onto a black hole of mass M, this energy can be estimated to $E = GMm/R_S^2$, where R_S is the Schwarzschild radius. $R_S = GM/c^2$ and therefore $E = 1/2mc^2$: This process is much more efficient than nuclear fusion or fission. Due to conservation of energy and angular momentum, this process has to be an-isotropic – i.e. the black hole of an AGN is rotating.[2] Due to the same conservational arguments, the accreting matter then forms an accretion disk and bi-polar, relativistic plasma jets perpendicular to the accretion disk. The jets need not be connected to the accretion disk by a matter field. Instead, they can originate in a region where the (electro-)magnetic field density is sufficiently high for pair production. This is then called a *Poynting flux driven $e^\pm$ wind* extracting rotational energy from the central black hole [48, 162]. At the outer end of the accretion disk, a region of dust clouds called *torus* exists.

[2] For a rotating black hole the Schwarzschild radius is not an appropriate measure of the event horizon any more. The calculation given above for the energy released can nevertheless be used to approximate the true value.

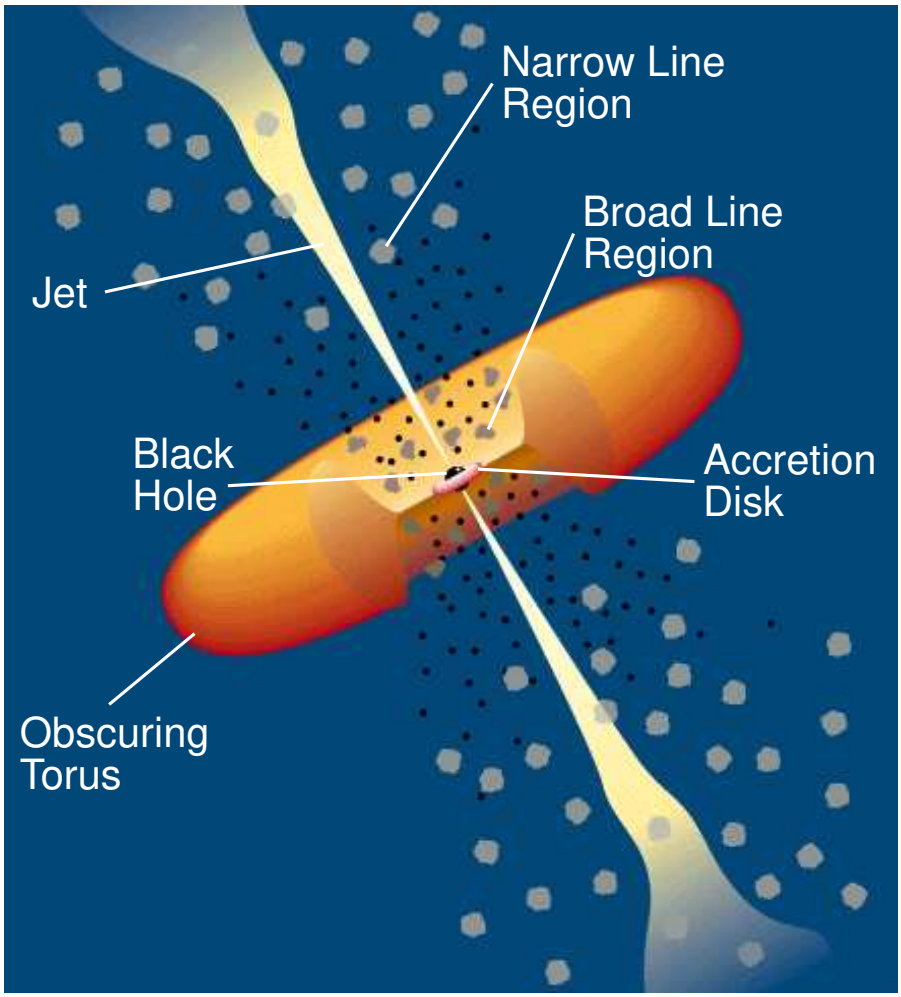

Figure 2.2: Schematic representation of a radio-loud AGN. Depending on the angle between AGN jet and line of sight, the AGN observation is determined by different phenomena. At small angles, the relativistically boosted jet dominates the observation ("observer looks into the jet"; AGNs are called blazars). At intermediate angles, the hot broad line region is observed ("observer looks into the gap between torus and jet"; AGNs are called Quasars). At large angles, the narrow line region is observed ("the torus obscures the AGN core"; AGNs are called narrow line radio galaxies). Figure taken from [232].

Due to interactions between jet and interstellar medium (ISM), the ISM is compressed to clouds and excited. Close to the AGN core, the excitation is strong, and the hot "broad emission line clouds" emit strongly Doppler-broadened emission lines. Further out, the emission lines are narrower and one speaks of "narrow line clouds" [88].

In this simplest picture, it is already evident that the AGN orientation relative to the line of sight will lead to very different observations on earth, see figure 2.2:

- Those objects classified as type 2 in table 2.1 are seen edge on, i.e. the torus obscures the hot core. The photons emitted in the jet or in the hot AGN core

have been absorbed and re-emitted, so that the observation is dominated by the more distant, non-obscured and cooler clouds - leading to rather narrow absorption lines from forbidden transitions. The so-called "radio-lobes" at the outer end of the jet dominate the total detected energy output.

- Type 1 objects of the unified schemes, are those, where the line of sight lies in the gap between torus and jet. The observer can thus see the hot center and strongly Doppler-broadened emission lines can be found in the electromagnetic spectrum.

- Type 0 (or "unusual") AGNs finally are those, where the jet is pointing towards the observer. Violently and rapidly varying spectra without clear emission or absorption lines are observed. For type 0 AGNs, the effects of relativistic boosting are important: The observed photon flux is increased by values $\sim (2 \cdot \gamma^3)$, the energy of the observed photons by γ, where γ is the Lorentz factor of the jet [187].

One thus has a decreasing angle between line of sight and jet axis in table 2.1 from left to right. The difference between quasars and radio-galaxies or between Seyfert galaxies and QSOs (top line versus bottom line entries within one box) is a distance effect: Quasars and QSOs are distant AGNs where the host galaxy cannot be resolved any more, while in radio-galaxies and Seyferts, it can be resolved. The radio-loudness in contrast (top row versus bottom row) seems to be an intrinsic source property, see appendix C.

Apparent population gaps in the unified schemes are explained by selection effects, insufficient sensitivities of present instruments and correlations between the total AGN power and the torus opening angle [87, 209].

One remark needs to be made on how frequent AGNs are: Recent measurements show that there seems to be a fundamental relation between black hole masses and their host galaxy properties like velocity dispersions [93, 104]. It thus seems very natural to assume super-massive black holes in at least a significant fraction of standard galaxies – if not in all. It has, however, also been shown that galaxies containing black holes need not be active, but can also be quiet [92]. So the ingredients for AGNs (super-massive black holes, host galaxy) seem to be very frequent. A single cause initiating (or terminating) an AGN does not seem to be identified so far.

2.2.2 Leptonic and Hadronic Acceleration Models

One of the much debated questions about AGNs concerns the nature of the particles accelerated inside the jet. It could be that the jets form as a Poynting flux driven $e^{\pm}$ wind extracting rotational energy from the central black hole [48, 162]. This leads to the so called leptonic models. Here the particle population in the jet is purely formed by pair creation out of the energy stored in the magnetic field. The main characteristic of leptonic models is the absence of hadrons in the jet. Another possibility is that the jet is footed in a hydrodynamic $e^- p^+$ wind from the relativistic inner accretion disk [60]; leading to the so called hadronic models. Here the term "hadronic" is confusing, as it stands for a process where both leptons and hadrons are accelerated. Baryon contamination [167] could, however, add hadrons also to originally purely leptonic models and thereby wash our the differences between the two classes.

So far, all observations are compatible with both classes. The main arguments in favor of leptonic mechanisms is their natural description of observed multi-wavelength spectra and of correlations between the dynamics in various wavelength regions. The latter is true especially for X-ray/TeV gamma ray correlations which have drawn much attention recently [131, 141]. The main arguments for hadronic models is their natural ability to describe detected multi-TeV gamma rays. Additionally, they make use of the naturally occurring particle populations and do not accelerate only one species. Moreover, leptonic processes also occur at least partially in hadronic models. So the before mentioned arguments in favor of leptonic processes are not as severe as they appear. E.g. correlated X-ray/TeV gamma ray flares can also be explained in a hadronic model [203]. Another more heuristic argument is that AGNs are plausible candidates of hadron acceleration above 10^{15} eV [212]. Such accelerators are believed to be needed to explain the highest energy cosmic rays.

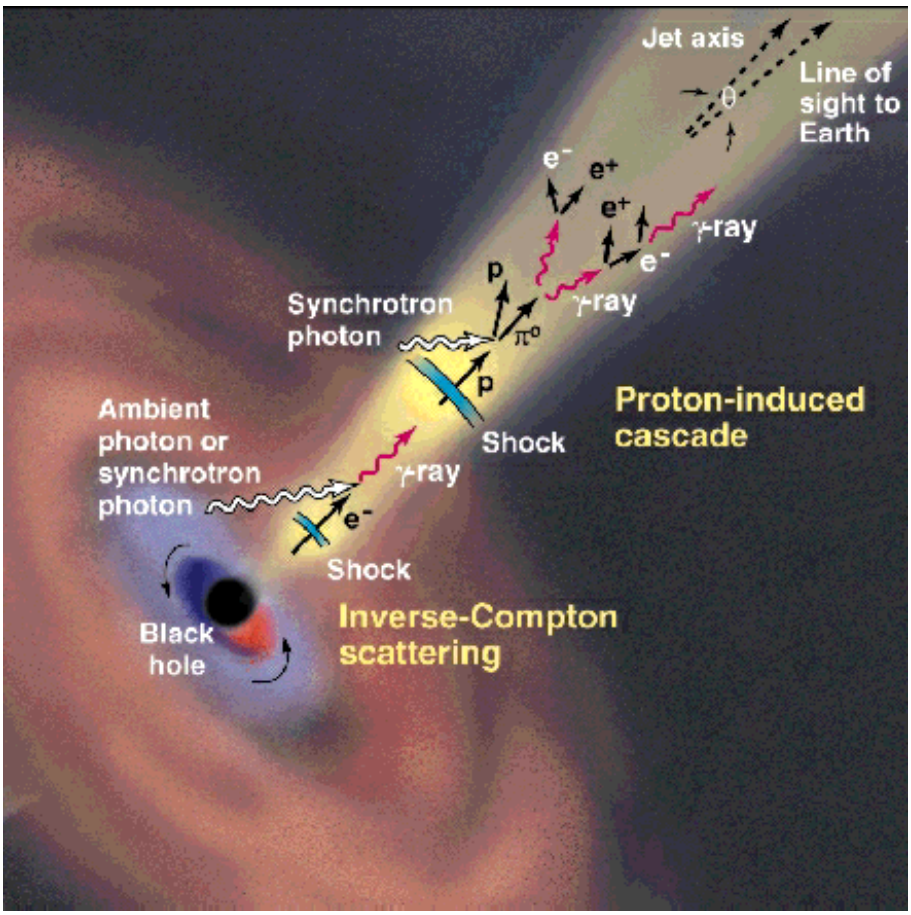

Figure 2.3: Schematic representation of AGN acceleration processes. The origin of gamma ray photons in a leptonic picture is indicated in the inner part of the jet. The outer jet shows their origin in a hadronic picture. Not shown: charged pion production and the subsequent neutrino production. Figure taken from [58].

AGNs are a potential source of high energy neutrinos only, if hadron acceleration occurs (most likely inside the jet), see figure 2.3. The acceleration itself is generally considered to be due to Fermi acceleration. Depending on the kinetic energies of the particles in the frame co-moving with the jet, one distinguishes cold beam (non-relativistic speeds) or hot beam flows [162].

The observed gamma ray spectra of AGNs can be described by four different classes of models: external and internal models, each time in a leptonic and a hadronic variant [162]. The external leptonic model is usually abbreviated as "EC" (for "External Compton"). In this model, the highest energy gamma rays are produced by inverse Compton scattering of photons outside the acceleration region. The hadronic variant is called E-PIC (for "External Proton Initiated Cascade"). Here, the hadrons are assumed to initiate high-energy secondaries by interacting with external photons. In synchrotron-self-Compton models (SSC), the electrons first emit synchrotron radiation, which is inverse-Compton scattered to γ-ray energies by the same electron population. Again, there is a hadronic analog: the proton-initiated synchrotron cascade model (S-PIC). All these models have their specific (dis-)advantages at explaining observational facts. In any case, it seems doubtful that nature has realized a pure version of any of these models.

The jet does not accelerate particles homogeneously. Instead, shock fronts travel through the jet. This leads to the observation of so called knots, regions of intense photon emission. The knots are thought to be associated with the shock waves. An interesting recent observation revealed that the knots are not located at the same position for all wavelengths [193]. This behavior can be explained by different cooling times of the particles emitting in these wavelengths. Within a leptonic framework, this result seems to prefer the synchrotron-self-Compton description as compared to the external Compton models.

It is still debated which sources yield the highest neutrino fluxes. Purely leptonic models are excluded. Theories for neutrino efficient hadronic models range from "photomeson processes in FSQRs" (E-PIC) [12] to "synchrotron-proton-LBLs" (S-PIC) [177, 178]. So-called model-independent upper bounds on diffuse neutrino fluxes have been calculated by two groups: Waxman and Bahcall argue for a constant upper bound of a few $10^{-8}\,\mathrm{GeV\,cm^{-2}s^{-1}sr^{-1}}$ for the neutrino flux multiplied with the square of the neutrino energy for energies between $10^3\,\mathrm{GeV}$ and $10^{11}\,\mathrm{GeV}$ [16, 240]. Mannheim, Protheroe and Rachen claim that this limit is only valid in a narrow energy range of 10^7 to $10^9\,\mathrm{GeV}$ and set limits up to 2 orders of magnitude larger in the other energy ranges [163, 204]. Both their calculations are based along the following line of arguments: The charged cosmic ray spectrum is measured. This can be used as an upper limit on the flux of charged cosmic rays from AGNs. Assuming a specific correlation between the emission of charged cosmic rays and neutrinos at the source, this limit translates into a limit on the neutrino fluxes.

2.3 Supernova (Remnants)

A young star balances its own gravitational attraction by fermionic pressure from the degenerate electrons and by the thermodynamic pressure obtained from the fusion of hydrogen in its core. Once the hydrogen content has decreased significantly inside the core, the fusion region slowly moves outwards. After a while, the thermodynamic parameters

have changed in such a way that helium fusion starts in the core. Again the helium content decreases in the center and the helium "burning" region moves outwards. This eventually leads to an onion-like state with subsequent shells of burning H, He, C, O and Si and an iron "ash" core. Once iron is produced, no further fusion process is energetically favored any more. The timescales of the fusion processes decrease rapidly for the heavier elements: In the case of a 20 solar masses star for example, hydrogen burning takes $\sim 10^7$ years, while silicon burning lasts just two days [63].

Low-mass stars (less than eight solar masses) do not produce sufficient gravitational pressure to ignite all of the above mentioned fusion processes. In this case the fusion chain will stop within the evolution outlined before. The end product is called a *white dwarf*. In massive stars on the contrary, the combined fermionic and thermodynamic pressure eventually cannot resist the gravitational pull any more and the star collapses. A neutron plasma is formed by protons capturing the previously degenerate electrons. The implosion of the inner core stops at a density when the strong force becomes repulsive. The inner core then bounces back and sends a shock wave through the further infalling material. The resulting explosion is called a *supernova*[3] [63].

The short supernova-explosion itself yields a large flux of neutrinos in the MeV-energy range. It is not expected to be a source of high energy neutrinos. But the shock front from the supernova propagates for long timescales through the stellar wind of the predecessor star and through the interstellar medium. With suitable magnetic fields (e.g. from the predecessor star), it can store and accelerate ambient hadrons. These supernova remnants (SNR) are expected to be responsible for the majority of the (galactic) cosmic rays below the "knee" of the cosmic ray spectrum shown in figure 1.1 [35].

If the environment, through which the shock propagates, is dense enough, it can act as a beam dump for a part of the accelerated hadrons. High energy neutrinos could thus be produced by supernova remnants. However, their flux is limited to timescales of years, during which the stellar wind of the predecessor star is still dense enough to act as an efficient beam dump. High energy neutrinos from certain types of supernova explosions are reviewed for example in [241].

2.4 Microquasars

Microquasars are a subclass of the so-called X-ray binary systems. They are objects observed within our galaxy which mimic many phenomena seen in quasars, but on a much smaller scale: They consist of a spinning central compact massive object (typical mass for a microquasar: 1 solar mass, for quasars: 10^9 solar masses), which accrete matter. This leads to an accretion disk (size for microquasars: $\sim 10^3$ km, quasars: $\sim 10^9$ km), and bipolar relativistic jets (microquasars: ~ 1 pc, quasars: $\sim 10^6$ pc) terminated by radio lobes. Contrary to quasars, where the matter is accreted from a host galaxy which circumfences the accretion disk, microquasars absorb mass from a companion star.

[3] The supernova scenario described here will leave a neutron star behind. For very massive initial stars, even the neutron degeneracy is not enough to resist the self-gravitational pull of the star: It will collapse even further into a black hole, a process which is sometimes referred to as a "hypernova" [63]. This second collapse might be relevant for objects known as Gamma Ray Bursts, see section 2.5.

Microquasars are so far the only source, where superluminal motion (see appendix C) of extended structures ("blobs") has been observed directly. For AGNs or other objects, it has so far only been inferred from spectral information. Emission from radio to soft gamma rays has been observed and is typically highly variable. The black body temperature of the accretion disk surrounding a black hole of mass m is approximately given by $T \sim 2 \cdot 10^7\, m^{-1/4}$. This leads to strong optical/UV emission of AGNs, but to strong X-ray emissions form microquasars [172, 173]. It is an open debate whether the compact object has to be a stellar mass black hole, or whether it can also be a neutron star. It is also debated whether these systems could be sources of the highest energy cosmic rays observed [171].

If microquasars do produce high energy cosmic rays, their dense environment would offer a suitable beam dump to also produce high energy neutrinos. In [153], it is argued that it is possible that observed radio flares are preceded by outbursts of 1–100 TeV neutrinos produced by photo-meson interaction. Thus microquasars are a potential (possibly transient) high energy neutrino point source.

2.5 GRBs and Transient Sources

The sources discussed so far are typically assumed to be steady or at most variable neutrino sources. In the case of gamma ray observations, additional "one-time" sources exist: the gamma ray bursts (GRBs) [139]. They are the most prominent class of potential transient sources of high energy neutrinos, and thus are the only such class introduced here[4].

GRBs are short eruptions of intense high energy photons and are randomly distributed over the sky. The likely cause of this signal are ultra-relativistic electrons and protons that have been accelerated in a relativistically expanding fireball and radiate away their kinetic energy. One class of GRB-models assumes a supernova explosion, where the resulting neutron star is gravitationally instable but initially hindered from collapse due to its angular momentum [139]. After radiating away enough rotational energy it collapses along its axis, forming bipolar jets which then will interact with the shock wave of the initial supernova explosion.

Such GRBs represent a potential class of transient sources of neutrinos with energies up to 10^{18} eV [239]. These could arise e. g. from the interaction of the accelerated jet protons with synchrotron gamma-ray radiation from the first shock wave. The average gamma ray burst is not expected to give a detectable amount of neutrinos in a neutrino detector [189,241]. Burst-to-burst fluctuations, however, could yield individual close GRBs with low Lorentz boost factors of the bulk shock, which then could be detected in future neutrino telescopes like IceCube [6, 112].

A very neutrino-strong GRB could give enough neutrinos to be detected in a search for (steady) point sources – like the one presented in this work. But in practice, one should make use of the GRB "time stamp" (taken from the gamma ray observations) in

[4] Blazar flares are also often defined to be transient sources. But since the actual sources (the blazars) are not transient and have already been discussed, blazar flares are not considered to be transient sources for the purpose of this section.

a dedicated analysis. One then can achieve a much improved signal passing rate at the same background suppression. This was performed for the same data investigated in this work and no GRB signal was found [23]. Independent of external time stamps, one can search for multiple neutrino events from one direction within a small time period. The work presented here focuses on steady sources. A dedicated search for transient sources (making use of their specific properties) will only play a minor role in this work.

2.6 Hidden Sources

"Hidden" neutrino sources are those not detectable by photons of any wavelength. Models for possible hidden neutrino sources are attractive since they do not have to adhere to any flux limits obtained from gamma ray and/or cosmic ray experiments.

One example is a recent prediction of high energy neutrinos from "pre-AGN" objects [30]. In that model, the central super-massive black hole of the AGN is required to arise from gravitational collapse of the host galactic nucleus during the galactic evolution. In the course of the collapse, stars collide destructively, thereby producing gas clouds. Only compact objects like neutron stars and stellar mass black holes survive. That residual galactic nucleus continues collapsing. Eventually neutron stars collide, forming so-called fireball explosions. The first few of these push all gas outward – including the remainder of the former regular stars. This leads to a gaseous envelope, which encloses a gas-free cavity. Inside that cavity, protons from further fireballs are effectively accelerated. High energy neutrinos arise from the collision of the accelerated protons with the gas envelope. While neutrinos escape, the other interaction products are absorbed inside the optically thick envelope. The heating of the envelope leads to IR radiation, but it is too weak to outshine the cosmic IR background over large distances.

This pre-AGN phase is assumed to exist for ~ 10 years. Depending on the cosmological model, up to 10 of these pre-AGN objects exist at any given moment. The neutrino-flux from these objects is predicted to lead to $\sim 10\,\mathrm{y}^{-1}\mathrm{km}^{-2}$ muon events above 1 TeV per average source. Crucial to this model is that the central galactic black hole forms after the galaxy formed. As mentioned in section 2.2.1, there is experimental evidence that this might not be the case.

In the past, also other models of hidden neutrino sources were discussed, but none of these is presently "en vogue":

- Very young supernova shells [32] are optically thick, but neutrinos arising from them are predicted to occur only in the MeV range.
- Thorne-Żytkow objects [227], where a pulsar is orbiting inside a red giant star, are also unlikely to produce neutrinos of TeV energies.
- Cocooned massive black holes inside AGNs [31] are in contradiction to the presently favored unified AGN schemes. In particular it is not evident how cocoons can exist in the presence of AGN jets.
- AGNs with standing shock fronts in the core regions [219, 220] locate the particle acceleration dominantly in the AGN disk. But observations in the optical and radio frequency range are best explained by jet-based acceleration models.

2.7 WIMPs and Top-Down Sources

A special class of potential neutrino sources are accelerator-free (top-down) sources. Most top-down scenarios (like the decay of topological defects) are not expected to yield significant neutrino fluxes from individual source regions [46]. A prominent exception are the neutrino fluxes expected from the annihilation of so-called *weakly interacting massive particles (WIMPs)*.

Several extensions of the standard model of particle physics propose the existence of new massive particles which only interact weakly or via new forces suppressed at energies below $\mathcal{O}(1)$ TeV. They are prime candidates for the astrophysically required dark matter halo of galaxies. These WIMPs can make any massive celestial body become a neutrino source [133]: When traversing the gravitational field of an object like the earth, WIMPs can scatter via neutral current interaction and loose enough energy to become gravitationally bound. The WIMP-orbit shrinks with time due to energy losses in subsequent scattering processes (especially when scattering within the massive object). Hence, the WIMP density increases towards the center of the gravitational potential. Once this density is large enough, WIMP annihilation counter-balances the density-increase due to accumulation. The annihilation leads to decay products, of which only neutrinos can escape through the large distances of dense matter within the celestial body.

Details of the neutrino production processes in these sources ($\equiv$ centers of celestial bodies) depend on the assumptions of the theory describing the WIMPs, see [33]. For example scattering (accumulation) resonances exist when the WIMPs have the same mass as chemical elements in the celestial object. Typical WIMP-candidates are SUSY-neutralinos. In a first approximation, the neutrino flux from a source is proportional to the mass of the celestial body and inversely proportional to the square of the detector distance from the celestial body center. For earth-based detectors, the three most relevant WIMP-neutrino sources are therefore the center of the earth, the sun and our galactic center. As will be shown in section 10, AMANDA-B10 has negligible sensitivity towards neutrinos from the sun or from the center of our galaxy, but has sensitivity for neutrinos from the center of the earth. Limits on neutrino fluxes from this source have already been derived with AMANDA [117].

2.8 Unexpected Sources

Cosmic rays of energies beyond 10^{20} eV have been observed in large air shower arrays, see figure 1.1. Their lower energy counterparts have been shown to be hadrons via direct (satellite) observations. The experimental data registered indirectly by air shower arrays is also compatible with a dominantly hadronic nature. Therefore it is a common (though not the only possible) assumption, that also the highest energy cosmic rays are hadrons. Without proposing new exotic (relic) particles or new physics, it is difficult to construct source-free models for the origin of these cosmic rays. So even if they do not originate from supernovae or their remnants (not powerful enough to yield the highest energies?), AGNs (purely leptonic?) or GRBs (too distant?), they should come from a so far undiscovered class of sources. Sources typically are surrounded by dense matter and/or photon fields.

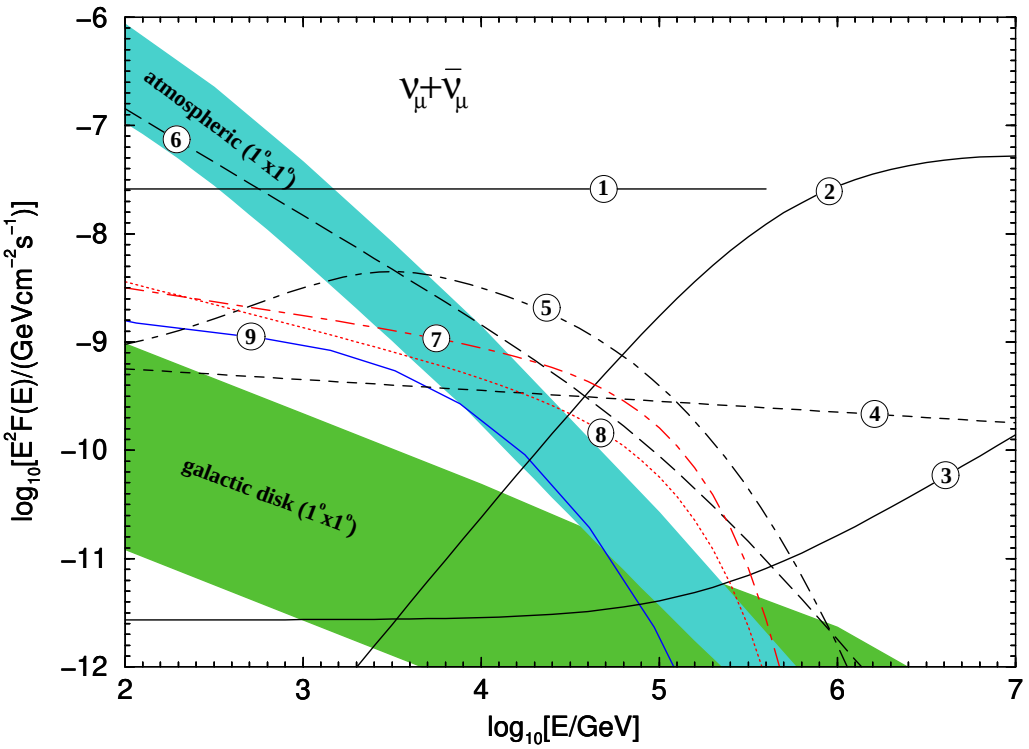

Figure 2.4: Summary of expected $\nu_\mu + \bar{\nu}_\mu$ fluxes from point sources. The diffuse flux of atmospheric neutrinos and of galactic disk neutrinos are integrated for an angular resolution of $1^\circ \times 1^o$. The width of the corresponding bands indicate the uncertainty of these guaranteed sources. The lines represent specific cosmic ray accelerator models: (1) Nellen et al. model for the core emission from 3C273 due to pp interactions (accelerated protons and proton beam dump) or similarly for Mrk501 during its outburst in 1997 if it emits half of its TeV gamma ray flux in neutrinos [182]. (2) Stecker & Salomon model for the core emission from 3C273 due to $p\gamma$ interactions (photon beam dump) [218]. (3) Mannheim model for the relativistic jet of 3C273 including pp and $p\gamma$ interactions [161]. (4) Colafrancesco et al. model for the Coma cluster [69]. (5) Bednarek & Protheroe model I for the crab nebula [26] . (6) Ingelman & Thunman model for cosmic ray induced neutrinos from the sun [127] . (7) Gaisser et al. model for supernova remnant IC444 [99] . (8) same model for supernova remnant γ Cygni [99]. (9) Atoyan et al. model for supernova remnant CasA (adopting $L_\nu = L_\gamma$ and $E_\nu = 0.5E_\gamma$) [13]. Figure taken from [149].

These can then act as "beam dumps" with which a fraction of the energetic cosmic rays will interact. From these interactions one will expect neutrinos. Thus, so-far undiscovered sources of ultra-high energy cosmic rays should be neutrino sources.

Neutrino telescopes are a new tool for astronomers and physicists. They probe different properties of the sky as compared to any previous method. The past has shown that new detection techniques often yield unexpected discoveries. Hope is that similar surprises might happen again. Unexpected neutrino point sources would be one potential surprise discovery.

2.9 Neutrino Oscillations

In 1998, the Super-Kamiokande collaboration published evidence for neutrino oscillations in atmospheric neutrinos [94]. These results were confirmed by the MACRO [175] and SOUDAN 2 [107] collaborations. Oscillations between all neutrino flavors have to be considered in a correct treatment. The present measurements favor three flavor oscillations (no sterile neutrino). Such oscillations are described by the unitary Maki-Nakagawa-Sukata matrix. For an atmospheric neutrino analysis it is, however, valid to consider only two-flavor oscillation between ν_μ and ν_τ as a first approximation. Reason is that limits published by the Super-Kamiokande [49,225] and SNO [236] collaborations on the admixture of $\nu_e \leftrightarrow \nu_\mu$ are very low.

The probability to detect a muon-neutrino of energy E after a distance L in its original flavor state is then given by

$$P_{\nu_\mu \to \nu_\mu} = 1 - \sin^2(2\theta) \cdot \sin^2\left(1.27 \cdot \Delta m^2/\mathrm{eV}^2 \cdot \frac{L/\mathrm{km}}{E_\nu/\mathrm{GeV}}\right) , \tag{2.7}$$

see for example [95]. It is parameterized by the mixing angle θ and the difference of the mass squares of the neutrino-mass eigenstates Δm^2. The recently announced most likely parameters characterizing the oscillation are $\Delta m^2 \approx 2.5 \cdot 10^{-3}\,\mathrm{eV}^2$ and maximal mixing (i.e. a mixing angle of $\sin^2(2\theta) \approx 1.0$). At 90 % confidence level, the differences of the mass squares are limited to $1.6 \cdot 10^{-3}\,\mathrm{eV}^2 \leq \Delta m^2 \leq 3.8 \cdot 10^{-3}\,\mathrm{eV}^2$ and $\sin^2(2\theta) > 0.90$ [134]. The suppression of atmospheric muon neutrinos is strongest for low energy, vertical upgoing events, as can be seen from formula 2.7.

At present, maximal mixing scenarios are also favored for $\nu_\mu \leftrightarrow \nu_e$ oscillations. Moreover, distances to astrophysical neutrino production sites are much larger than oscillation lengths for $\mathcal{O}$(TeV)-energy neutrinos. This leads to an equipartition distribution of all three neutrino flavors at the detector. So rather than typical source flux ratios of approximately $1:2:0$ for ν_e, ν_μ, ν_τ, ratios of $1:1:1$ are expected at the detector. Therefore, neutrino oscillations have to be taken into account if one compares measured neutrino fluxes to source production models. This is why neutrino oscillations are introduced in this section on neutrino sources.

3 The AMANDA Neutrino Telescope

3.1 Detection Principle

Since neutrinos only interact weakly, they cannot be observed directly. Instead, neutrino telescopes aim to detect charged leptons (l) produced in the vicinity of the detector via a charged current interaction of the neutrino (ν) with a nucleon (N):

$$\nu + N \rightarrow l + X \ . \tag{3.1}$$

Since astrophysical neutrino sources dominate the total neutrino flux at high energies only, see section 3.4, neutrino telescopes have to detect these high energy neutrinos. With the expected fluxes and interaction cross sections for high energy astrophysical neutrinos, process 3.1 is rare. Neutrino telescopes thus have to monitor a large volume. Due to cost requirements, a large detector cannot be densely equipped. With the resulting detectors, it is easier to correctly reconstruct the long tracks of minimally ionizing muons than to try to reconstruct the hadronic and electromagnetic showers resulting from ν_τ or ν_e interactions. So the standard detection mode of neutrino telescopes is the search for muon tracks.

3.1.1 Cherenkov Light

Cherenkov radiation is emitted by charged particles traveling through transparent media at velocities $\vec{\boldsymbol{v}}$ which exceed the speed of light in the medium:

$$|\vec{\boldsymbol{v}}| = \beta c > c/n \ , \tag{3.2}$$

where β is defined via the left part of equation 3.2, c is the speed of light in vacuum and n the refractive index of the medium [192].

In the following, n is considered constant[1], with $n = 1.32$ (ice at 400 nm [238]). Then the velocity threshold corresponds to a muon energy of $E_\mu^{thresh} \sim 160\,\mathrm{MeV}$. The angle θ_{cher} under which Cherenkov photons are emitted is

$$\theta_{cher} = \arccos(1/\beta n) \ . \tag{3.3}$$

The Cherenkov photons form a cone with an opening angle of

$$\alpha = \operatorname{arccot}\left((\beta^2 n^2 - 1)^{1/2} + \frac{dn}{d\omega} \frac{n\omega\beta^2}{(\beta^2 n^2 - 1)^{1/2}} \right) \ , \tag{3.4}$$

where ω is the photon's angular frequency [176]. So only in the case considered here (constant n) is α the complement of θ_{cher} and the Cherenkov photons are exactly normal to the Cherenkov cone. Neutrino telescopes typically have detection thresholds $E_\mu \geq 10\,\mathrm{GeV}$ (c.f. section 3.1.2), at which $\beta \approx 1$ and thus $\theta_{cher} \sim 40^\circ$ and $\alpha \sim 50^\circ$.

One can describe the number of photons emitted by the Frank-Tamm formula [128]:

$$\frac{d^2N}{dxd\lambda} = \frac{2\pi\alpha}{\lambda^2} \cdot \left(1 - \frac{1}{\beta^2 n^2}\right) \ , \tag{3.5}$$

[1] The dependency of n on phase- or group velocity, wavelength, pressure and temperature is discussed in [199].

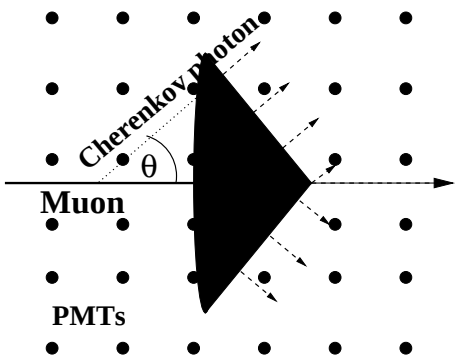

Figure 3.1: Cherenkov cone with opening angle α of a muon traveling through a 3 dimensional PMT grid. The angle under which the muon emits Cherenkov photons is θ_{cher}.

where $\alpha \approx 1/137$ is the fine-structure constant. This yields $\frac{dN_{eff}}{dx} \approx 200\,\text{photons/cm}$ with an effective transparent wavelength interval for ice and detector from approximately $300 - 500\,\text{nm}$.

Direct Cherenkov light emission is not the dominant energy loss process of muons. Muons loose energy continuously due to ionization of the detector medium. In addition, stochastic energy loss processes occur due to the production of δ-electrons, muon-nucleus interactions bremsstrahlung and pair production. All these processes lead to further (Cherenkov) photons from secondary particles. These additional photons are much more numerous than the Cherenkov photons of the muon itself – and thus more important for its detection.

While the continuous energy loss is almost constant, the energy loss (and thus the Cherenkov light) from the stochastic processes rises approximately linear with energy:

$$-\frac{dE}{dx} = a + b \cdot E \ . \tag{3.6}$$

Here, $a \approx 2\,\text{MeV}\,\text{cm}^{-1}$ represents the continuous energy losses and $b \approx 3.4 \cdot 10^{-6}\,\text{cm}^{-1}$ the stochastic processes [246]. At $E_c \equiv \frac{a}{b} \approx 600\,\text{GeV}$, the two contributions are equal. At $E > E_c$, the energy of the muon can be estimated from its energy loss due to the second term in equation 3.6. For smaller energies, the energy loss becomes less dependent on the total energy. Below $E \sim 200\,\text{GeV}$ this scheme does not allow a good estimation of the muon energy any more.

3.1.2 Basic Neutrino Telescope Design

As will be discussed in section 3.4, the suppression of atmospheric muon background requires the neutrino telescopes to be constructed under a massive radiation shield. The task is thus to detect light in a large ($\sim 1\,\text{km}^3$) transparent volume at great depth. This is achieved by deploying a three dimensional grid of large *photomultiplier tubes* (PMTs) in deep water or ice. In order to shield the PMTs from the pressure at their depths, they are contained inside transparent glass pressure spheres. The entity of pressure sphere, PMT and accompanying electronics inside the sphere is called *optical module* (OM). The OMs are attached to support strings which also contain cables for read-out and power supply.

3.2 History

Neutrino-telescopes have originally been proposed approximately 40 years ago [109, 164]. 25 years ago, the first such experiment, DUMAND [150], was initialized. The meanwhile terminated project was an effort to build a telescope in the pacific ocean. Since then, several new projects were started: The BAIKAL experiment [19] is located in Lake Baikal in

Siberia, AMANDA [9] at the *Amundsen-Scott South Pole Station* in the antarctic ice shield. Both are running and have detected atmospheric neutrinos [8,9,18,29]. ANTARES [61,77], NESTOR [110] and NEMO [62] all plan to build telescopes in the Mediterranean sea, whereas IceCube [46,248] is the planned successor of the AMANDA project.

The parameters characterizing the sites include:

Sky Coverage: It is similar for all water projects, since they are all located within less than 20° latitude. AMANDA is complementary to the other projects.

Depth: Ocean sites can be as deep as 4 km. This is an advantage over ice (~ 2 km) and Lake Baikal (~ 1 km).

Scattering: Ice shows stronger scattering than water, resulting in a worse angular resolution, but better calorimetry for energy measurements.

Absorption: The absorption is smallest in ice and at deep ocean sites.

Deployment: Stable deployment platforms exist for AMANDA and for Lake Baikal (which is frozen during the winter). Ocean deployments are performed from specialized ships, which can remain at a constant position above seabed. In all cases, the deployment is only possible during 2–4 months per year.

Maintenence: The BAIKAL group has proven its capability to repair all parts of the detector. In contrast, AMANDA components frozen into the ice cannot be accessed any more. Depending on their design, ocean detectors can either be completely recovered (NESTOR) or in parts (ANTARES). In the later case, the recovered strings might have to be redeployed to new locations.

Detector Geometry: It is constant for AMANDA. The water detectors have to constantly monitor it via sonar as it changes with changing water currents.

Environmental Noise: It is negligible for ice. Radioactive ^{40}K is dominant for ocean detectors, bioluminescence is present for all water detectors.

Surface Arrays: For calibration purposes, AMANDA can use coincident events with the (high resolution) South Pole Air Shower Experiment SPASE. At Lake Baikal such an option only exists temporarily while the lake is frozen. The ocean detectors do not have such an option.

On-Site Infrastructure: Due to a large science station, it is very good at South Pole. For the water detectors only their own infrastructure exists at the coastline. On the other hand, transport capacities to the South Pole are limited. The laboratory sites of the ocean detectors in comparison are readily accessed.

The AMANDA history began 10 years ago. In the austral summer 1991/92, preliminary site studies and drilling tests were performed at the South Pole. Two years later, the first four strings, called AMANDA-A, were deployed at depths between 810 m and 1000 m. A scattering length of ~ 25 cm due to residual air bubbles at that depth proved to be too

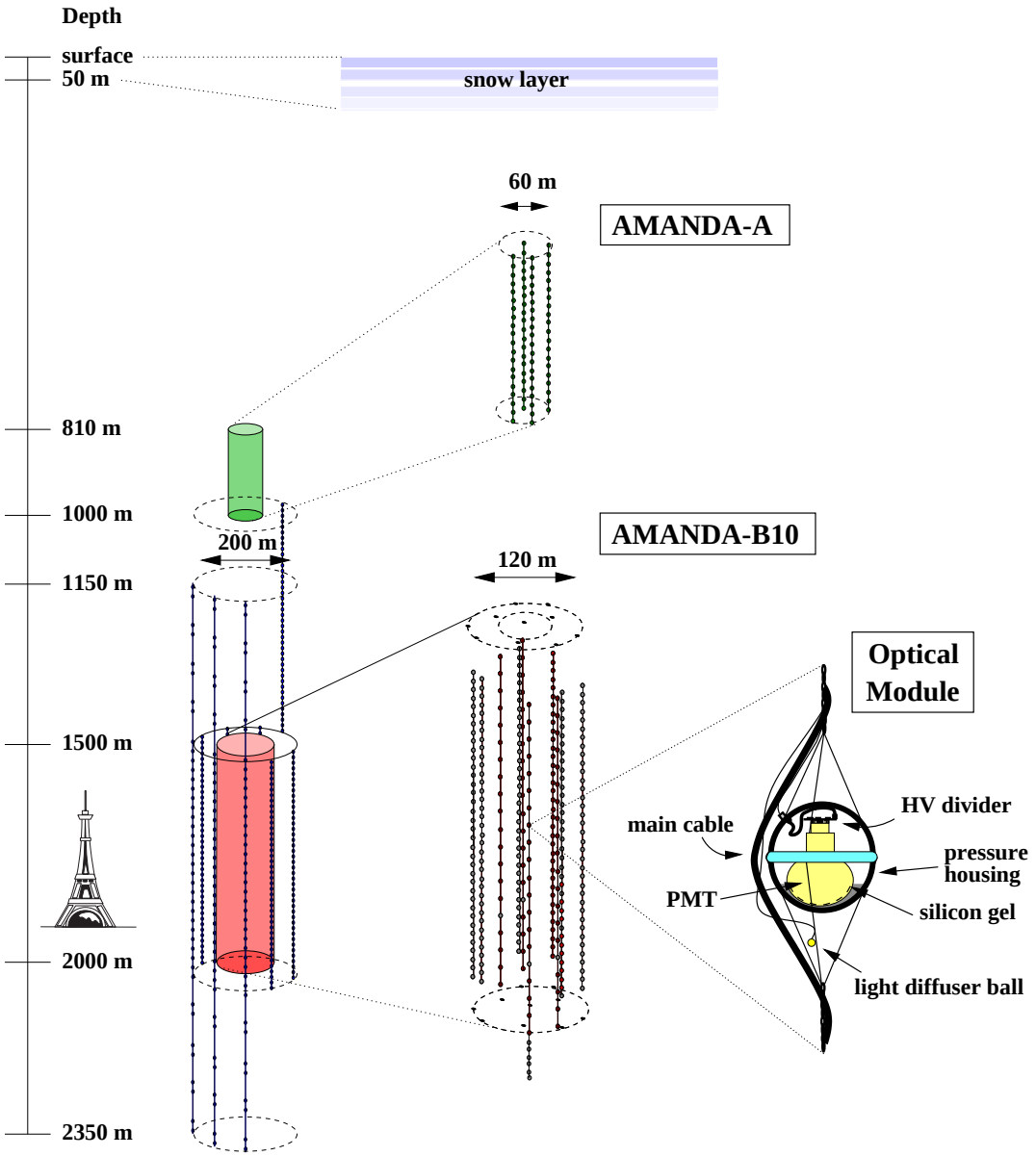

Figure 3.2: The present AMANDA-II detector. The AMANDA-B10 detector, which took the data analyzed in this work in 1997, is located at depths between 1500 m and 2000 m below the surface. It consists of 302 optical modules.

small to perform track reconstructions. In 1995/96, four new strings, called AMANDA-B4, were therefore deployed at depths between 1500 m and 1950 m. AMANDA-B10 was completed by deploying six additional strings around AMANDA-B4 the following year. In

1997/98 three long strings were deployed between 1100 and 2350 meters depth to probe the optical properties above and below AMANDA-B10. Two years later, six additional strings were deployed at depths between 1450 and 2000 meters. (In fact, string 17 did not reach its designated depth but got stuck between 1000 and 1500 meters). That is still the present status. The detector is called AMANDA-II and consists of 677 OMs. A schematic drawing of AMANDA-II is given in figure 3.2.

For the future, it is planned to construct a cubic-kilometer sized detector called IceCube, building on the knowledge gained with AMANDA [46]. The work presented here will be restricted to data taken with AMANDA-B10 in the year 1997.

3.3 AMANDA-B10

The AMANDA-B10 detector (AMANDA as of 1997) consists of 302 modules deployed on 10 strings. All OMs consist of pressure spheres, housing an 8 inch hemispherical PMT (Hamamatsu R5912-0) with 14 dynodes and operated at a gain $\sim 10^9$. The high voltage is transmitted from the surface and no active electronics are located inside the OMs. The PMT's photo cathode is in mechanical and optical contact with the pressure sphere via transparent silicon gel. The OMs of strings 1–4 are read out via coaxial cables, those of strings 5–10 via twisted pairs. The latter solution reduces dispersion. It improves the rise time of surface signals from $\sim 180\,\text{ns}$ to $\sim 60\,\text{ns}$ and the pulse width from FWHM $\sim 600\,\text{ns}$ to FWHM $\sim 210\,\text{ns}$ [44]. It thus offers a much better multi-pulse separation. As a drawback, twisted pair cables are subject to cross talk and thus 1-PE pulses can be faked on strings 5–10. The future IceCube detector will digitize the PMT pulses within the OMs and then send them to the surface.

The time resolution Δt of each channel depends on the PMT-jitter, on the errors of the calibration of the cable transmission time and on the cable dispersion. Uncertainties in the relative detector geometry are equivalent to timing uncertainties and thus can also be considered to contribute to Δt. While the PMT jitter and the dispersion can be measured prior to deployment, the other two calibration errors are difficult to determine. An estimate for the combined effect of all timing uncertainties can for example be found by optimizing a parameter of the reconstruction algorithm, which accounts for the timing uncertainties, see section 6.6. This leads to an estimation for the time resolution of $10\,\text{ns} \lesssim \Delta t \lesssim 20\,\text{ns}$. The lower bound is in accordance with the combination of three individual contributions: A time calibration uncertainty of $\sim 8\,\text{ns}$ (see section 5.1 and [38]), a relative geometry calibration uncertainty of the order of $\sim 50\,\text{cm}$ (see section 5.4 and [249]) and a combined PMT-jitter plus cable dispersion error of $\sim 5\,\text{ns}$ (see [44]).

For in situ calibration of optical properties of the ice, several light emitting devices like laser- and LED-modules were deployed together with the OMs. The most important device for timing calibration is, however, a tuneable dye laser in the surface laboratory. Its light is transmitted to the ice via optical fibers terminated by a diffuser ball. The diffuser balls isotropize the light and thereby can illuminate a neighboring PMT. On strings 1–4, every OM is connected to the surface via such a calibration fiber and has the diffuser ball below the PMT. This case is illustrated in the right-most part of figure 3.2. In the case of strings 5–10, the ball is above the OMs but only every second module has such a

calibration device. The others need to be calibrated with light from the diffuser ball of the OM below.

The glass used for the pressure spheres of strings 1–4 are contaminated by very small quantities of radioactive elements like ^{40}K. This results in an average noise rate of $\sim 300 \pm 26$ Hz. In 1996 the glass had an improved transmissivity [224], but also an increased potassium content, leading to an average noise rate of $\sim 1100 \pm 80$ Hz for OMs on strings 5–10 [213]. For comparison: Ocean experiments typically have ^{40}K induced noise rates of 100 kHz per OM plus additional bioluminescence.

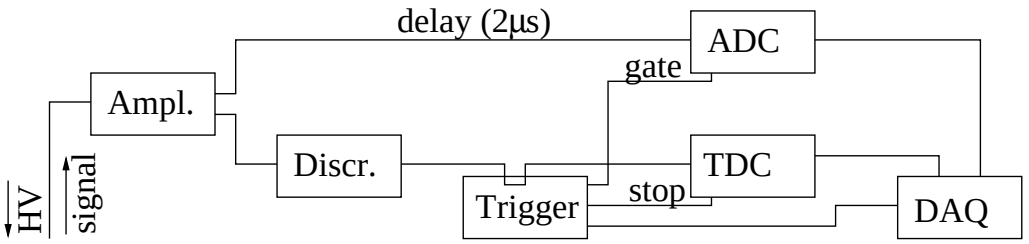

Figure 3.3: Surface electronics of the AMANDA-B10 detector: Amplifier, discriminator, trigger unit, ADC, TDC and DAQ.

The PMT signal is transported to the surface via the same cable which also supplies the high voltage. At the surface, the pulse is amplified and split in two parts. One is delayed by 2 μs and is fed into the "Analog to Digital Converter" (peak ADC). The ADC determines the pulse maximum of the delayed amplifier output to estimate the number of photoelectrons registered by the optical module. The other pulse passes a discriminator, is picked up by the trigger logic and fed into the "Time to Digital Converter" (TDC). The TDC stores a time stamp for the leading edge of the pulse.

In 1997, the trigger condition was fulfilled when at least 16 hits occurred within a time window of 2 μs. Once this simple majority condition was fulfilled, a signal activated the ADC for amplitude measurements. Another signal (delayed by 10 μs) stopped the time measurements of the TDC. Finally, the trigger unit sends a signal to the Data AcQuisition system (DAQ). After another delay, the DAQ then read out the full array over a time window of 32.0 μs. An outline of this system can be seen in figure 3.3.

3.4 Background and Signal

The dominant background in neutrino telescopes are atmospheric muons. The atmosphere of the earth acts like a beam dump for cosmic rays. Just like in equation 2.1, muons are produced in interactions of cosmic rays with the atmosphere. If they are energetic enough, the muons can penetrate the earth down to great depths. Since atmospheric muons are indistinguishable from muons induced by neutrinos, down-going muons have to be rejected as background[2]. To suppress them it is thus of vital importance to build neutrino detectors at great depths. But even at the depths suitable for neutrino telescopes, the downward

[2]In fact, there is some prospect for neutrino astronomy in using down-going neutrino-induced muons of highest energies ($> 10^3$ TeV). At these energies, atmospheric muons practically do not occur any more and the earth becomes opaque to up-going neutrinos [22].

flux of atmospheric muons is nevertheless much larger than that predicted for any neutrino source: In [1], it is approximated as

$$\begin{array}{ll} I_\mu(x) = A(\frac{x_0}{x})^\alpha \exp(-\frac{x}{x_0}) & \text{with} \\ A = (2.15 \pm 0.08) \cdot 10^{-6}\,\mathrm{cm}^{-2}\mathrm{s}^{-1}\mathrm{sr}^{-1} & , \\ \alpha = 1.93^{+0.20}_{-0.12} & \text{and} \\ x_0 = 1.155^{+0.060}_{-0.030}\,\mathrm{km\,we} & . \end{array} \tag{3.7}$$

At a depth of 2 km, this is still up to a factor of 10^6 times higher than the flux of atmospheric neutrinos (depending on zenith angle and energy). Upward moving muons in contrast evidently arise from neutrino interactions: The neutrino is the only known particle capable of traversing the earth. A neutrino telescope is therefore "looking down". AMANDA for example is located at the South Pole and monitors the northern hemisphere.

Atmospheric neutrinos, arising from atmospheric muon production and decay, are a special case. In a strict sense, they have to be considered background, since the task of neutrino telescopes eventually is the search for extraterrestrial neutrinos. They are, however, a very important calibration tool. Though their fluxes are uncertain in shape to 5 % and in absolute magnitude to 30 % [59, 96], they are well understood as compared to extraterrestrial neutrinos. Their detection is thus the necessary proof of concept for any neutrino telescope. Above 1 TeV, they have a spectrum proportional to $\sim E^{-3.7}$ [97, 98]. They dominate predicted celestial neutrino fluxes at low ($\lesssim 10$ TeV) energies, but extraterrestrial sources are expected to have harder spectra, see figure 2.4. Atmospheric neutrinos can thus be rejected with cuts on energy-dependent variables. Angular cuts can select directions towards potential point sources to further enhance their signal over atmospheric neutrino background.

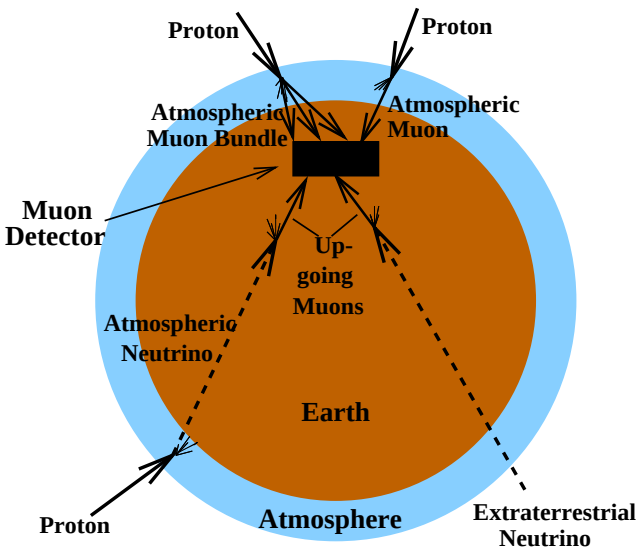

Figure 3.4: The different origins of extraterrestrial neutrinos, atmospheric neutrinos and atmospheric muons. A single air shower can produce several coincident muons, called a muon bundle.

Atmospheric neutrinos could also be produced by γ-rays from strong multi-TeV gamma ray sources such as the Crab nebula. This would result in a point-source-like signal. In such a scenario, the signal has to be separated into the γ-ray induced and the source neutrino fractions. To do this, one would have to rely on direct γ ray measurements from air shower arrays and theoretical calculations about the $\gamma \to \mu \to \nu$ chain. The onset of this effect is expected at effective telescopes areas of $10^5\,\mathrm{m}^2$ and with a space angular resolution of 1° [149].

A second class of a diffuse, but rather certain neutrino flux is expected from similar sources, but with different beam dumps: Neutrinos from the interaction of cosmic rays

with the hadrons inside our galactic disk. They are expected to have a harder spectrum than that of atmospheric neutrinos[3], see figure 2.4. These neutrinos are extraterrestric but do come from a "diffuse source" and can thus also be considered background for telescopes. The diffuse flux from many, unresolved point-like neutrino sources on the other hand is considered signal, see section 2. As can be seen, an exact definition of the term *signal* thus depends on the exact investigation performed.

3.5 Other Physics Potential

In section 2, only the aim to detect point sources of neutrinos was mentioned (AGNs, GRBs, sites of WIMP annihilation, etc). Beyond this, there are many more interesting topics which have been addressed by AMANDA:

- The search for a diffuse flux of extraterrestrial neutrinos [151].
- The search for electron or tau-neutrino events by searching for shower (or "cascade") topologies [143].
- The search for MeV neutrinos from supernova explosions in our galaxy [4, 213].
- The search for relativistic magnetic monopoles, a class of topological defects [183].
- Studies of AMANDA's sensitivity for the determination of neutrino oscillation parameters [53].
- Studies of glaciological parameters like the determination of optical properties or of the temperature profiles for the South Polar ice [10, 11, 114, 198].

Analyzes which are not finalized yet, or which will not be started before IceCube is commissioned, include:

- The participation in the SuperNova Early Warning System SNEWS [111].
- The search for slowly moving bright particles [34].
- The measurement of low x charm cross-sections via the flux of energetic "prompt" atmospheric neutrinos from the decay of charmed mesons [72, 174].
- The search for ultra high energy neutrinos from the evaporation of primordial micro-black holes due to Hawking radiation in the vicinity of the detector [105, 230].
- The search for extremely high energy neutrinos from the decay of magnetic monopoles, other topological defects or other ultrahigh-energy relic particles [149].

Since all these topics are of no direct relevance for this work, they are not presented in more detail here.

[3] Muons produced in the galactic disk always decay, the resulting neutrino spectrum is then that of the cosmic rays. Atmospheric muons can interact before they decay - the higher their energy the less likely is a decay. Hence the atmospheric neutrino spectrum is steeper than the cosmic ray spectrum.

4 Data Sets Analyzed

4.1 Experimental Data

The experimental data analyzed in this work was taken by the AMANDA detector in the year 1997, during the 252 days between March 9^{th} and November 15^{th}. The runs taken within this period contained $1.45 \cdot 10^9$ events, which were accumulated during a life-time of 224.6 days, see tables D.4 to D.8. An event was recorded when any one of five experiments triggered: AMANDA-B10 itself, AMANDA-A [194] (see section 3.2), SPASE 2 [84] (the present SPASE array, see section 3.2), SPASE 1 [24] (the old SPASE array, now dismantled) or GASP [20] (a small Cherenkov telescope, now dismantled). In this work, only those $1.29 \cdot 10^9$ events fulfilling at least the standard AMANDA-B10 trigger (see section 3.3) were analyzed. Quality criteria which will be introduced in section 7.1.1 further reduced the experimental set. E.g. all runs before run 500 (April 3^{rd}) failed the run quality criteria. In total, $1.18 \cdot 10^9$ events (any triggers) passed the run quality criteria, $1.05 \cdot 10^9$ events passed the subsequent event quality criteria (in particular the AMANDA-B10 trigger) and $1.00 \cdot 10^9$ events also passed the hit quality criteria. Those $1.00 \cdot 10^9$ events combine to a detector lifetime of 130.1 days (dead-time corrected), see appendix D.

4.2 Monte Carlo Simulation

A necessary step in the analysis of experimental data is the comparison to the expectation. The expectation is in general not calculable - neither analytical nor numerical. Instead, a statistical simulation of the relevant physics processes and the detector response is performed. But since the term *simulation* is defined in the English language as "willful deception: collusion, misrepresentation" [108], another term is also used: "Monte Carlo", often abbreviated as "MC". It is derived from the Mediterranean town of the same name which is famous for its casino. Since random (chance) processes are as important for the simulation as for gambling, the motivation of that name is apparent. In the remainder of this work, the expressions "simulation", "Monte Carlo" or "Monte Carlo simulation" are used interchangeably.

4.2.1 Event Generation

For the AMANDA detector, the simulation is split in four parts: The initial part is the so-called *generation*. It is based on a given flux of primary particles. When for example, atmospheric muon background is simulated, the primary particles are cosmic rays and their spectra are taken from other experiments. The *generator* (the program performing the generation) then simulates the interactions of the primaries with the earth (neutrino generation) or its atmosphere (atmospheric muon generation) and writes out all muons produced. During the simulation of AMANDA-B10, various generators have been used:

nu2mu **[75, 76]** was developed within the AMANDA collaboration. It is a generator which uses atmospheric neutrinos as primaries. It is based on theoretical prediction of the atmospheric neutrino flux performed by Lipari [155]. The neutrino interaction cross sections are taken from Gandhi et al. [101]. The interaction itself is simulated with

PYTHIA 5.4 [214] and uses the structure functions CTEQ3 [147]. Three years lifetime of AMANDA-B10 atmospheric neutrino statistics have been simulated. To save CPU time, only neutrino zenith-angles larger than 80° (i.e. no down-going neutrinos) have been simulated. *nu2mu* does not include effects of neutrino oscillations.

nusim **[119]** was also developed within the AMANDA collaboration, uses the same atmospheric neutrino flux predictions [155] as *nu2mu*, simulates the same zenith angular range and also ignores neutrino oscillations. The neutrino propagation within *nusim* takes into account the density profile of the earth as given by the "Preliminary Reference Earth Model" [86]. The neutrino interaction cross sections are taken from [120] and the MRSG parton distribution functions [165] are applied.

nusim incorporates zenith angular and energy importance sampling. This allows to describe arbitrary energy and zenith angular spectra with the same generated events by simply applying appropriate weights. So the same files could be used to analyze atmospheric neutrinos and extraterrestrial neutrinos of a given power-law spectrum. The concept of importance sampling in AMANDA is described in more detail in [118].

nusim is the standard muon-neutrino generator for AMANDA. If nothing else is specified, neutrino simulations referred to in this work are always based on *nusim*. The equivalent statistics of ~ 5 years of AMANDA-B10 lifetime have been simulated using *nusim*. At present *nusim* (wrongly) simulates the muon as to have the same direction as the initial neutrino. Wherever this angle is significant for this work, a correction factor is used which is derived from *nu2mu*.

CORSIKA **[115]** is the present standard program for the simulation of air showers. In AMANDA it is used to generate the atmospheric muon background. *CORSIKA* allows to use various high- or low-energy interaction models. AMANDA uses *QGSJET* for high-energy interactions and *Geisha* for low energies. The latter choice is in practice irrelevant, since the low energy regime in *CORSIKA* is defined to be below 70 GeV, but AMANDA has an energy-cutoff at $\sim$ 400 GeV at the surface of the Earth.

The *CORSIKA* generation is by far the slowest part of the AMANDA simulation chain. Since the flux of cosmic rays is homogeneous, an over-sampling technique can be (and was) applied: Each simulated air shower was used 10 times. Every time the azimuthal angle and the horizontal distance between simulated air-shower and the AMANDA array was randomly chosen. A later test revealed that this over-sampling did not change the simulation results at any cut level. For the analysis of data taken in 1998 and later, this over-sampling has even been increased from 10 to 100 times. In total $22.4 \cdot 10^6$ AMANDA events have been simulated by *CORSIKA* (version 5.70).

basiev **[57]** is a significantly faster, but slightly less accurate generator for atmospheric muons. It only simulates cosmic ray protons. To compensate for not simulating helium or heavier nuclei, it uses a differential spectral index of -2.67, which is slightly harder than that usually assumed for protons in that energy range. Like in the case of *nusim*, importance sampling in zenith angle is possible for *basiev*. $38.8 \cdot 10^6$

$(29.0 \cdot 10^6)$ events have been generated without (with) importance sampling. Those generated with importance sampling correspond to $215.5 \cdot 10^6$ AMANDA events.

Despite the differences in physical input, no strong deviations between results obtained from *CORSIKA* or *basiev* have been found. If nothing else is stated, atmospheric muon simulations referred to in this work are based on a combination of events obtained from *CORSIKA* and *basiev*.

muo0 **[223]** is a special generator not based on any primary flux. It directly generates any desired muon-energy spectrum. The muons start at random positions on a plane or within a volume. The angular spectrum can again be chosen arbitrarily, but is typically selected to be isotropic. *muo0*-generated events are useful for systematic investigations of energy-dependent detector properties. However they do not represent physically existing events. They were used during the analyzes presented here, but will not be mentioned any further in this work.

4.2.2 Muon Propagation

The main aspect of the muon propagation are the muon energy losses. The muon looses its energy via ionization of the ice, the production of δ-electrons, muon-nucleus interactions, bremsstrahlung and pair production. The Cherenkov radiation of the muon itself gives a very small contribution. Two propagation programs were used. Both are based on tables calculated by Lohmann et al. in [157]. *mudedx* [142] was a program originally optimized for mono-energetic experiments. It was modified for use in AMANDA [125] and now also serves as a wrapper for the other propagation program: *propmu* [156]. The latter program was specifically designed for underground experiments, but does not simulate δ-electrons. Now existing, additional muon propagation codes like MMC [68] (developed within the AMANDA collaboration) or MUM [215], both of which contain the latest muon interaction cross sections, were not available yet for this work.

The propagation is split in two parts. Far away from the vicinity of the detector, only the muon energy loss is determined. The light produced from secondaries from the energy loss processes will be absorbed before reaching the detector. This is different in case of energy losses in the vicinity of the detector. Hence, a so-called *active volume* is defined around the detector. It is a cylinder of 800 m height and a radius of 400 m. Inside the active volume, information about each energy loss process is stored.

4.2.3 Photon Propagation

All muon energy loss processes lead to the production of photons. The propagation of those photons, which are emitted inside the active volume, towards the PMTs is performed with the program *PTD* [135]. It describes the wavelength dependency of the absorption length based on a three component absorption model [10]. It also takes into account a reduced scattering length in the re-frozen AMANDA drill holes.

The photon propagation is not performed on an event by event basis. Instead, *PTD* is run prior to the main simulation and produces multi-dimensional tables. These tables contain the probability that a PMT receives a signal from a muon energy loss process depending on process, distance, relative orientation, amount of energy loss and time delay.

During the main simulation, the table entries are just read out and interpolated. One error still exists in the correct treatment of the various processes: Hadronic vertices are presently treated like electromagnetic ones though they produce $\sim 20\,\%$ less light [246].

The depth dependency of the scattering coefficient cannot easily be included into the simulation: Another two dimensions to the tables (PMT depth and depth of energy loss vertex) would increase the table size (required RAM-memory) too much. Instead, it was assumed that all photons registered by an OM only travel through ice which has a scattering coefficient close to that of the environment of the OM. The OMs were divided into four groups of similar local scattering coefficient. For each of these four groups, one *PTD*-table was produced. Though this is obviously an insufficient description of the scattering processes, it proved to be a significant improvement over the use of one global scattering coefficient [126]. A new program called *photonics* has been developed by the AMANDA collaboration [170]. Its main advantage in comparison to *PTD* is the correct treatment of the scattering coefficient. For this work it was not available yet.

4.2.4 Detector Response

Though all software discussed above has been modified or even designed for AMANDA, the only truly AMANDA-specific part of the simulation chain is the simulation of the detector response. *AMASIM* [124] is the program which simulates all hard- and software components: from PMT to DAQ. It also is the program which looks up the PMT hit probabilities in the tables produces by *PTD*. The so-called "masspro00" version of *AMASIM* was used to simulate the data analyzed here. For the atmospheric muon simulation, the five subversions "v000"–"v004" were used[1]. For the neutrino simulation, only the latest subversion v004 was used.

As can be seen from table D.2, 17 OMs were not operating stable during the year. A run-dependent OM cleaning had to be performed for these. Rather than trying to simulate the various run periods, a year-average detector status was simulated. 11 OMs which were operating stable for most of the year were simulated as always alive and stable. In contrast, 6 OMs which were removed from experimental data most of the time, were simulated as always dead, see table D.3. All the other OMs where simulated according to their experimental status as always dead (19 OMs) or always alive and stable (265 OMs).

One of the main uncertainties in the analysis of AMANDA-B10 is the absolute and angular dependent acceptance of the detector, see section 7.3. Uncertainties in the muon propagation (section 7.3.4), in the description of the optical parameters of the re-frozen ice in the AMANDA drill holes (section 7.3.5) or on the sensitivity of the optical module (section 7.3.6) all contribute to the uncertainty of the acceptance. In [184], it was tried to measure the angular and absolute acceptance by using well reconstructed down-going atmospheric muons. Furthermore, comparisons between up-looking and down-looking PMTs have been performed. From this, a correction factor for the optical properties of the ice immediately surrounding the OM and the OM sensitivities was derived. In particular, it corrects the acceptance for up-going (neutrino-induced) events. This correction modifies the angular sensitivity of the modules. Though most analyzes of the 1997 data use this

[1] In [45], older simulations (version "masspro98") of similar statistics were also used. These have been removed from the analysis presented here.

correction, the AMANDA collaboration has not yet decided to define it as the official simulation standard.

This new hole ice/angular sensitivity model was not available at the time when most of the atmospheric muon simulation was performed. Hence, the background simulations used in this work do not incorporate it. The neutrino simulation requires fewer CPU resources and could be repeated with the new model. Since it describes experimental data much better, all neutrino simulations used for this work are based on it.

5 Calibration

5.1 Timing Calibration: T_0 and α

This work describes two main tasks: The selection of atmospheric neutrinos and the search for extraterrestrial neutrino point sources. Both tasks strongly depend on the quality of the reconstruction: A good zenith angle resolution simplifies the rejection of down-going atmospheric muon background. Likewise, a good space-angular resolution allows the use of small search windows during the search for neutrino point sources. And small search windows again suppress random background from atmospheric neutrinos. The reconstruction will be described in section 6. There, it will be shown that it mostly relies on the timing information acquired. Hence, a good timing calibration is important for a good reconstruction and correspondingly required to obtain good results for the analyzes presented here.

The electronic signals from muons in the ice originate at the PMTs. They are transmitted via an electrical cable to the surface electronics and are recorded by the DAQ. This has been described in more detail in section 3.3. The effect of the cable and the electronics on the time-structure of the pulse is two-fold: It is delayed (due to its finite propagation speed) and it is smeared out (due to dispersion). For each pulse, the DAQ records a time stamp at time t_{LE}, when the leading edge crosses the threshold of the discriminator. In order to derive the time t_{ice} (when the PMT emitted the pulse) from t_{LE}, two calibration parameters are needed: "T_0" and "α". T_0 describes the total time delay for a virtual pulse of infinite amplitude $A \ggg 1$, where A is measured in mV. α describes the first order correction to the time delay with respect to the pulse amplitude. Since weak pulses cross the discriminator threshold slightly later than strong pulses, their time delay is larger. The time of the pulse in the ice t_{ice} is thus given by:

$$t_{ice} = t_{LE} - T_0 - \frac{\alpha}{\sqrt{A}} \; . \tag{5.1}$$

The fact that the leading correction of T_0 depends on $A^{-0.5}$ is derived for example in [210].

The two calibration parameters have to be determined for each channel. For an individual channel, they are obtained as follows: A tuneable surface laser sends light pulses down to the OM via an optical calibration fiber. At the end of the fiber, a light diffuser ball isotropizes the light pulses. Such a diffuser ball is shown in the right part of figure 3.2. The light pulses then initiate PMT signals which are read out like other PMT signals during standard detector operations. But in this case, a single pulse recorded from the PMT is sufficient to fulfill the calibration trigger condition. The α-correction is obtained from varying the strength of the laser pulses. Typical values are $300\,\mathrm{ns}\,(\mathrm{mV})^{0.5} \leq \alpha \leq 700\,\mathrm{ns}\,(\mathrm{mV})^{0.5}$ for strings 1–4 (coax cables) and $200\,\mathrm{ns}\,(\mathrm{mV})^{0.5} \leq \alpha \leq 400\,\mathrm{ns}\,(\mathrm{mV})^{0.5}$ for strings 5–10 (twisted pairs).

To determine T_0, one additionally needs the knowledge of t_{Laser}, T_{OTDR} and T_{corr}[1]. The absolute time of the laser pulses is given by t_{Laser}. T_{OTDR} is the passage time of the

[1] In this section, absolute times are represented by small letters "t", whereas capital letters "T" correspond to time delays.

light between the laser and the end of the glass fiber. T_{corr} finally is the passage time between the end of the glass fiber and the PMT. T_0 can then be obtained from

$$T_0 = t_{LE} - \frac{\alpha}{\sqrt{A}} - t_{ice} = t_{LE} - \frac{\alpha}{\sqrt{A}} - t_{Laser} - T_{OTDR} - T_{corr} \ . \tag{5.2}$$

t_{Laser} is determined by splitting the laser signal and only sending one part into the ice. The other part is producing an electric signal in a photo-diode, which is triggering a delay generator. That in turn is triggering the DAQ readout. t_{Laser} is hence obtained from the delay generator setting. T_{corr} is obtained from the known velocity of light in ice [238] and the geometric distance between PMT and isotropizer ball. T_{OTDR} finally, the passage time in the fiber is determined by measuring the surface arrival time of that part of the light which is reflected at the end of the fiber. These Optical Time Domain Reflectometer (OTDR) measurements are performed in a separate calibration scheme (using a different wavelength which is stronger reflected) prior to the timing calibration. Knowing the results of the OTDR calibration and using the laser to trigger the DAQ, one can then determine the T_0 constant. This calibration is performed for each channel of AMANDA prior to and after each data-taking period. In between the calibrations for consecutive years, hard- and/or software modifications can alter the calibration constants. The timing calibration after the 1997 season was double-checked and proven to be reliable by repeating it with an alternative dedicated DAQ system. Although the author participated in that alternative calibration, the calibration constants found with the standard calibration will be used in this work. The accuracy of the timing calibration for 1997 was estimated to be better than ± 7 ns for T_0 and better than $\pm 30\,\%$ for α [38].

5.1.1 Necessary Accuracy

In a dedicated analysis, the effects of relative timing calibration errors on the final analysis results were analyzed for this work [38]. This was achieved by using experimental as well as simulated data and calibrating them multiple times. Once the best known calibration constants were taken, whereas they were modified for the other calibrations. A total of seven potential timing calibration errors were investigated:

Random error on the T_0 calibration: This arises from individual measurement errors for each channel.

Random error on the α calibration: This arises due to the same reasons.

Random string-wise shifts of T_0 constants: Since the strings are usually calibrated one at a time, a persistent systematic error introduced at any time, can make all T_0-constants of the subsequently measured strings being shifted with respect to those already measured.

Random error on α for some modules only: The optical fibers and the light diffuser balls were not deployed for every OM. They are missing for the odd-numbered modules on strings 5–10. For these OMs, the fibers of neighboring channels have to be taken to transmit the light down into the ice. Hence, the light has to travel a distance of ~ 10 m (rather than ~ 30 cm) through the ice, being subject to diffusion.

This increases the amplitude dispersion slightly and hence worsens the α calibration for these channels.

Depth dependent systematic T_0 shifts: The results of the OTDR measurements have to be translated to the laser-wavelength used for the T_0 calibration. If this transformation is wrong, then the T_0 constants will by systematically wrong. The error will be directly proportional to depth. Shifts causing reduced and increased T_0-differences were investigated.

Systematic errors for α: For a while it was suspected, that there was a factor of 2 difference in the definition of α between the programs used to determine it during calibration and those used to apply it during data processing. Such a difference would be equivalent to a systematic error of a factor of 2. Later it turned out that this difference did not exist. Since it has been investigated, it is nevertheless listed here.

1998 calibration: The potential calibration errors mentioned so far were all investigated individually. Correlations between them were not taken into account. But especially the first two errors discussed (random T_0 and random α error) are probably highly correlated. A realistic model of all the errors can be obtained by comparing the constants obtained by two fully independent calibrations. So the data was also calibrated once with the calibration for AMANDA-B10 modules in 1998 data. Prior to the 1997 data taking period, no calibration of AMANDA-B10 had been performed due to limited time after the deployment of six strings. So the 1998 calibration was the first alternative calibration of AMANDA-B10.

After the calibration, the data sets passed the full processing chain outlined in section 7. For all cut levels introduced there, three parameters were investigated: The cut passing rates as well as the mean and the RMS of the zenith angle mismatch between true and reconstructed track. The passing rates of the various cut levels were available for experimental and simulated data. In contrast, the two parameters requiring information of the true track could only be obtained for simulated data (background and signal).

The three parameters chosen were investigated for the two/three data sets available and for all cut levels. Particular emphasis was put on analyzing the results for the final cut levels, which select the final neutrino candidate events, see section 7.2. For most of the calibration uncertainties, five values of increasing severeness have been simulated. The random error on the T_0 calibration was for example simulated with Gaussian distributions of widths $\sigma = 2$, 5, 10, 20 and 50 ns. By comparing the results for these different values, it was possible to set a limit on "acceptable" calibration errors. Here, "acceptable" was defined as

- at maximum an increase in the RMS of the zenith angle mismatch of 5 %,
- at maximum an increase in the mean of the zenith angle mismatch of 0.5° and
- at maximum a loss of 5 % in neutrino candidate events.

Class	Investigated Values	Acceptable Error	Estimated Error
Random T_0 Error	± 2, 5, 10, 20, 50 ns	± 15 ns	$\leq \pm 7$ ns
Random α Error	± 10, 20, 30, 50, 100 %	± 100 %	$\leq \pm 30$ %
Random String Shifts: T_0	± 2, 5, 10, 20, 50 ns	± 20 ns	$< \pm 1$ ns
Random α Error for some OMs	± 10, 20, 30, 50, 100 %	± 100 %	$\leq \pm 30$ %
Vertical T_0 Shift	$+/-2$, 5, 10, 20, 50 $\frac{\text{ns}}{100\,\text{m}}$	$+/-20$ $\frac{\text{ns}}{100\,\text{m}}$	< 1 $\frac{\text{ns}}{100\,\text{m}}$
Systematic Shift of α	-50, $+100$ %	~ -25, $+50$ %	$< \pm 1$ %
1998 Calibration	1997, 1998	difference is well acceptable	

Table 5.1: Investigated potential errors for the timing calibration. Given are the seven classes of potential errors investigated, the investigated values (how large the errors are), the maximum acceptable errors (as defined in the text) and the estimated size of these errors.

The results are summarized in table 5.1. The table also gives an estimation of the size of the individual errors. Motivations for these error estimations can be found in [38]. From the error estimations, one sees that all the uncertainties investigated are of acceptable size. This result is also relevant for the planning of future calibration efforts. Since the planned IceCube detector (see section 3.2) will contain on the order of 5000 OMs, the present calibration scheme seems inappropriate. It would be very expensive to equip a significant fraction of those channels with optical fibers for calibration purposes only. Also the time required to calibrate the array would exceed the time available during the South Polar summer. Instead, a calibration with down-going muons is being developed [74]. Such an alternative calibration has not been available for AMANDA-B10 yet.

5.2 Geometry Calibration

The geometry calibration is performed in two steps. Prior to the deployment, a survey determines the surface positions of the holes. During the deployment, the momentum of the drill is continously monitored. Combining both, the geometry of the hole can be derived. Together with the knowledge of the positions of the OMs along the string and the length of the string deployed, the OM positions in the ice can be determined. These first order approximations on the OM positions are, however, not accurate enough. The drill log information has a certain degree of inaccuracy and the integration over depth leads to uncertainties increasing with depth.

Hence, an additional calibration of the relative geometry is undertaken after deployment. It is performed by flashing light emitting devices deployed in the ice. The LED and/or laser pulses are recorded by many optical modules. When the propagation speed of the light pulses is known, triangulation allows to calculate the relative distances between the OMs. Strong pulses are needed for two reasons: They are seen by many optical modules, and time delays of the leading edge due to light scattering are small. The speed of light in ice is taken from data tabulated in [238].

After combining all information in a global fit, the relative geometry is obtained. The uncertainty on the individual OM position is dominated by uncertainties on the horizontal position and estimated to be smaller than 50 cm [249]. This uncertainty is equivalent to

an uncertainty $\Delta t < 2.5\,\mathrm{ns}$ on the T_0 calibration, since the group index of refraction in ice is $n \sim 1.36$ (see section 5.4). As can be seen from the discussion of timing uncertainties in section 5.1, such a knowledge of the detector geometry is sufficient for the purpose of this analysis. The absolute depth of the detector cannot be determined by this method. It is taken from pressure measurements during the deployment. The accurate knowledge of the depth is, however, of lesser importance for the performance of the detector.

5.3 Amplitude Resolution

A single photon hitting a photomultiplier tube can release an electron in the PMT cathode. The electron is accelerated strongly enough towards the first dynode to knock off several electrons. These in turn are accelerated towards the next dynode and so on. AMANDA-B10 PMTs have a design gain of 10^9, i.e. the avalanche finally produced should contain $\sim 10^9$ electrons. Likewise, photons causing n photo-electrons should give a signal of $\sim n \cdot 10^9$ electrons. From measuring the signal at the surface, it is thus possible to deduce the number of photons seen by the OM.

During normal detector operations, most hits are caused by single photons. They all cause a signal of similar size in the ADC. One therefore sees a prominent "1 PE-peak" when superimposing the ADC-output voltage of many hits. For the accuracy presently required, it is sufficient to assume a linear detector response. Identifying zero PE with the pedestal position of the ADC output, one thus has an amplitude calibration up to the maximal output of the ADC.

The 1 PE-peak has a half width at half maximum of $\sim 35\,\%$ [205, 210], the uncertainty on the amplitude measurement is thus $\sim 35\,\%$. The width is dominated by dependencies of the gain at the first two dynodes on the point of emission of the first photoelectron. The value of $\sim 35\,\%$ corresponds to the intrinsic uncertainty of the amplitude measurement. In addition, the assumption of a linear response is probably not valid for pulses $\geq 5\,\mathrm{PE}$. Such strong hits are, however, rare in the data sets passing the analysis presented her. The amplitude resolution is therefore considered accurate to $\sim 35\,\%$ for the purpose of this work.

5.4 Calibration of the Optical Properties

In open neutrino detectors like AMANDA, the transparent medium surrounding the installed hardware components is an inherent part of the detector. The reason is that the Cherenkov light is propagating inside that medium. Only the knowledge of the optical parameters of the medium allows a full description of the performance of the detector. The AMANDA collaboration uses the following parameters to approximate the optical properties of the ice: The effective scattering coefficient b_e, the absorption coefficient a, the group speed of light $|\vec{v_g}|$ and the phase speed of light $|\vec{v_p}|$ in the ice (or, alternatively, the corresponding two refractive indices n_g and n_p).

The effective scattering coefficient is defined as $b_e = b \cdot (1 - < \cos(\theta_s) >)$, where θ_s is the scattering angle and b is the scattering coefficient. The scattering coefficient itself is the inverse of the length along which a fraction e^{-1} of photons remain un-scattered. The depth-dependency of the effective scattering coefficient is shown in figure 5.1 (left). At

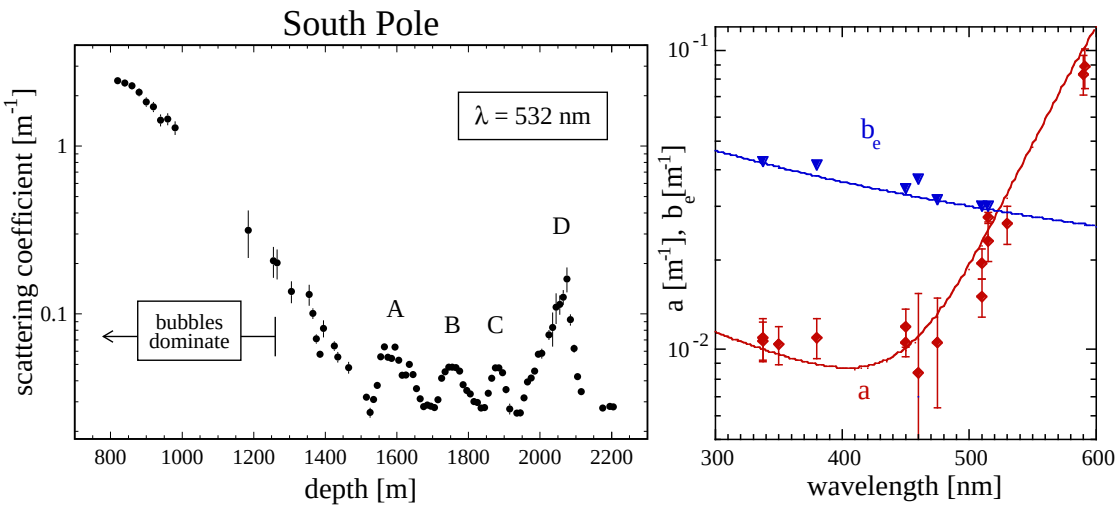

Figure 5.1: Optical properties of the ice. (Left:) Effective scattering coefficient versus depth. Data taken at a wavelength of 532 nm. (Right:) Effective scattering and absorption coefficient versus wavelength, averaged over depths between 1550 m and 1900 m. The curves are no fits but obtained from theoretical predictions [114]. Remember that the Cherenkov spectrum is proportional to λ^{-2}, see equation 3.5.

depths shallower than ~ 1300 m, residual air bubbles dominate b_e. At larger depths, the scattering coefficient displays structures. In a glacier like the South Pole ice cover, depth corresponds to age. The structures are thus caused by climate changes in the past. In particular the four peaks labeled A–D correspond to four identified glacial maxima [201]. In figure 5.1 (right), the wavelength dependency is shown. b_e decreases slowly and roughly linear with wavelength.

The absorption coefficient a is the inverse of the length of the path of a photon signal, along which a fraction e^{-1} of the photons are *not* absorbed. Due to temperature increases, a increases roughly linear with depth. The total change is approximately 10 % within AMANDA-B10 [200]. The wavelength dependency of a can be seen in figure 5.1 (right). It slowly decreases from 300 to 400 nm and increases rapidly for larger wavelengths.

The optical properties of the South Polar ice can be described using Mie theory and considering the combination of pure ice plus dust (consisting of insoluble mineral grains, acid droplets, salt grains and soot) [114]. The corresponding model leads to the two curves in figure 5.1 (right). It ascribes the increase of a with wavelength above ~ 400 nm to the ice itself. In contrast, the dust constituents cause the dominant contributions to the absorption coefficient for shorter wavelengths.

The absorption and scattering coefficients are obtained from the same data set used to calibrate the detector geometry. This time, the distribution of delayed (scattered) hits with distance and the number of hits with distance are measured versus the original light output. The results are compared to Monte Carlo simulations for various combinations of values for a and b_e. That pair of a and b_e which results in the best description of experimental data is taken as approximation to the true values of a and b_e. The wavelength dependency can be obtained from repeating this procedure using different laser/LED wavelengths. The

depth dependency is determined from restricting the analysis to modules within certain depth layers.

A special case is the re-frozen hole ice: During the melting and re-freezing of AMANDA-holes, the ice structure is destroyed. So far, there are no indications that the absorption coefficient is significantly different in the hole-ice as compared to the bulk ice. The hole-ice scattering coefficient $b_{e,\,hole}$ is, however, larger than that of the bulk ice. Bubbles and other impurities introduced during the re-freezing seem to cause this effect. In the current simulation, it is assumed that the hole-ice has a constant scattering coefficient throughout its radius. Alternative theories expect the scattering to be strongest in the center of the hole where the water re-freezes last. The scattering coefficient of the hole-ice can then be determined as a first order correction to the global scattering coefficient. The value presently used is $b_{e,\,hole} \sim 2\,\mathrm{m}^{-1}$.

The group velocity determines the speed at which Cherenkov photons travel through the ice and correspondingly all timing information. The phase velocity on the other hand describes the angle under which the Cherenkov cone forms. The difference between the two is less than 2 % for AMANDA, as was pointed out in [146]. A discussion about the role of group and phase velocity for the case of AMANDA can be found in [199]. The velocities of $|\vec{v_g}| \approx c/1.36$ and $|\vec{v_p}| \approx c/1.32$ (ignoring the slight wavelength dependencies) are taken from tabulated data for ice [238]. The numbers are wavelength averages for a Cherenkov spectrum convoluted with the PMT quantum efficiencies and the glass transmissivities [250]. The value $|\vec{v_g}|$ can be roughly verified when choosing emitter and receivers (OMs) along one string. Since the distances between OMs on one string is known, the time difference between their pulses yields the speed of light at the corresponding depth.

The calibration uncertainties are estimated to be $\leq 20\,\%$ for a and b_e and $\leq 50\,\%$ for $b_{e,\,hole}$. They are de-facto negligible for $|\vec{v_g}|$ and $|\vec{v_p}|$, but averaging over their wavelength dependency introduces small errors ($\leq 2\,\%$).

6 Reconstruction

Since a neutrino's direction cannot be measured directly, it has to be inferred from secondary information – i.e. from the muon it produces via the reaction given in equation 3.1. The neutrino direction can then be approximated by the muon direction. The error of this approximation is given by the mean angle between neutrino and muon. It can be parameterized as:

$$\begin{aligned}
\sphericalangle(\vec{r_\mu}, \vec{r_\nu}) &\approx \frac{1.8^\circ}{(E_\nu/\mathrm{TeV})^{0.5}} && \text{for} && E_\nu < 3\,\mathrm{TeV} \\
\sphericalangle(\vec{r_\mu}, \vec{r_\nu}) &\approx \frac{0.65^\circ}{(E_\nu/\mathrm{TeV})^{0.48}} && \text{for} && 3\,\mathrm{TeV} < E_\nu < 100\,\mathrm{TeV} \\
\sphericalangle(\vec{r_\mu}, \vec{r_\nu}) &\approx \frac{0.33^\circ}{(E_\nu/\mathrm{TeV})^{0.32}} && \text{for} && 100\,\mathrm{TeV} < E_\nu
\end{aligned} \tag{6.1}$$

Here, $\sphericalangle(\vec{r_\mu}, \vec{r_\nu})$ is the mean angle between neutrino and muon [185]. The distribution is non-Gaussian with low-energy *muons* dominating the tails. After an event selection, the numerators can thus shrink by factors of up to two or three. The natural goal for the muon direction resolution of neutrino telescopes is therefore $O(0.1)^\circ$.

The process of extracting the muon direction from gathered data is called *reconstruction*. One can distinguish two classes of reconstruction modes used in AMANDA: *first guess approximations* and *likelihood reconstructions*.

In the AMANDA convention, a *first guess approximation* is a fast analytical track approximation. It can also be used for a first level data reduction. During this work, the data was processed with three different first guess approximations: The *line-fit* (section 6.1) and the *dipole approximation* (section 6.2) both assume a (muon) track-like event, whereas the *tensor of inertia* (section 6.3) does not make an ad-hoc assumption about the nature of the event.

The other class are the more accurate *likelihood reconstructions*. They are based on algorithms maximizing multidimensional likelihood functions by minimizing $-\log(\mathcal{L})$. Likelihood reconstructions are too time-consuming to be applied to all data. Furthermore they give the best results if the minimization algorithms are initialized with reasonable starting values, e.g. from a previous first guess approximation. Due to these two arguments, likelihood reconstructions are always performed after an appropriate first guess approximation and a first data reduction based on its results.

The likelihood reconstructions used in this work are several variations of the *track likelihood reconstruction* (section 6.4) and the *shower likelihood reconstruction* (section 6.5). The first one assumes the event to be caused by a single muon track, whereas the other one considers the source of the event to be a cascade (or "shower"), e.g from a ν_e interaction.

So far, the track reconstructions assume a single infinitely long muon track, which generally is a good approximation. Starting muons (with their hadronic vertices) or stopping muons, muon bundles (multiple atmospheric muons from one air shower) or roughly coincident muons from independent causes can lead to reconstruction errors. However, these need not be big: The width of muon bundles from an air shower is typically around 5 m (on trigger level) and therefore comparable to AMANDA's vertex resolution. Additionally, due to the large OM spacing and due to the intrinsic probabilistic nature of hit detections,

a through-going muon can give hit patterns which are very similar to those expected from starting or stopping muons along the same direction. But independent muons from coincident air showers can fool the reconstruction. They can be mis-reconstructed and have to be rejected by dedicated cuts.

6.1 Line-fit

The *line-fit* [221] is the standard first guess approximation in AMANDA. It ignores amplitude information and produces a fit solely on the basis of hit times. The fit ignores the refractive index and all other optical properties of the ice. Instead, it assumes light traveling with a velocity $\vec{\boldsymbol{v}}$ through a 1-dimensional projection of the detector. $\vec{\boldsymbol{v}}$ is a fit parameter. Hence the speed $|\vec{\boldsymbol{v}}|$ of the light propagating through this 1-dimensional projection does not necessarily correspond to the speed of light (or of the muon) within the 3-dimensional ice.

The fit assumes the i-th PMTs to be located at $\vec{\boldsymbol{r}}_i$ and to be hit at t_i:

$$\vec{\boldsymbol{r}}_i \approx \vec{\boldsymbol{r}} + \vec{\boldsymbol{v}} \cdot t_i \ , \tag{6.2}$$

with the light at $t = 0$ being at $\vec{\boldsymbol{r}}$. A χ^2 is defined as:

$$\chi^2 \equiv \sum_{i=1}^{N_{hit}} (\vec{\boldsymbol{r}}_i - \vec{\boldsymbol{r}} - \vec{\boldsymbol{v}} \cdot t_i)^2 \ , \tag{6.3}$$

where N_{hit} is the number of hit PMTs. The χ^2 is minimized by differentiation, first with respect to $\vec{\boldsymbol{r}}$. This yields:

$$\vec{\boldsymbol{r}} = < \vec{\boldsymbol{r}}_i > - \vec{\boldsymbol{v}} \cdot < t_i > \ , \tag{6.4}$$

where $< x_i > \equiv \frac{1}{N_{ch}} \sum_i^{N_{ch}} x_i$ denotes the mean of parameter x with respect to all hit channels i. Differentiating χ^2 with respect to $\vec{\boldsymbol{v}}$ yields:

$$0 = < \vec{\boldsymbol{r}}_i \cdot t_i > - \vec{\boldsymbol{r}} \cdot < t_i > - \vec{\boldsymbol{v}} \cdot < t_i^2 > \tag{6.5}$$

$$\rightsquigarrow \vec{\boldsymbol{v}} = \frac{< \vec{\boldsymbol{r}}_i \cdot t_i > - < \vec{\boldsymbol{r}}_i > \cdot < t_i >}{< t_i^2 > - < t_i >^2} \ , \tag{6.6}$$

where the second equality is derived from inserting equation 6.4 into equation 6.5.

The line-fit thus yields a vertex $\vec{\boldsymbol{r}}$, a speed $|\vec{\boldsymbol{v}}_{LF}|$ (or simply v_{LF}), a direction $\vec{\boldsymbol{e}} = \vec{\boldsymbol{v}}/|\vec{\boldsymbol{v}}|$ and a χ^2_{LF}. The direction $\vec{\boldsymbol{e}}$ is usually expressed via its zenith angle ($\theta_{LF} \equiv \arccos(v_z/v)$) and its azimuth angle ($\phi_{LF} \equiv \arctan(v_y/v_x)$). The zenith angle θ_{LF} is used as a first veto against atmospheric muons in this work. The "speed of the line-fit"[1] v_{LF} is a measure for the topology of the event: Spherical events (showers) have low v_{LF} values, whereas thin, long events (muon tracks) have large values. Consequently v_{LF} is also used as a first filter – e.g. in the analysis presented here.

[1] People that are not familiar with the line-fit often consider "speed of the line-fit" an unfortunate name. Reason is that they sometimes understand it as to refer to the CPU-time used to calculate the line-fit. An expression like "speed obtained from the line-fit" might indeed seem more appropriate. But changing a more than 10 year old terminology used in many experiments initiates more problems than it solves. So the name persists and is also used in this work.

6.2 Dipole Approximation

The *dipole approximation* [103,206] again is a first guess approximation suitable for track-like events. It is calculated in two steps. First, all hits i are sorted according to their hit times. Then a *dipole-moment* $\vec{\boldsymbol{M}}$ is calculated:

$$\vec{\boldsymbol{M}} \equiv \frac{1}{N_{ch}-1} \cdot \sum_{i=2}^{N_{ch}} \frac{\vec{\boldsymbol{r}}_i - \vec{\boldsymbol{r}}_{i-1}}{|\vec{\boldsymbol{r}}_i - \vec{\boldsymbol{r}}_{i-1}|} \ . \tag{6.7}$$

This approximation considers the *unit* vector from one hit OM to the subsequently hit OM as an individual dipole moment. Averaging over all individual dipole moments yields the global moment $\vec{\boldsymbol{M}}$. It can be expressed via an absolute value $M \equiv |\vec{\boldsymbol{M}}|$ and the two angles θ_{DA} and ϕ_{DA}. These angles are used to approximate the true track.

The dipole approximation does not give as good an approximation of the true muon track as the line-fit. But it can be useful as a veto for a specific class of background events: Almost coincident atmospheric muons from separate air showers. If the first muon traverses downward through the bottom of the detector and the second muon downward through the top, other reconstructions assuming a single muon event can wrongly deduce an upward moving particle as cause.

6.3 Tensor of Inertia

The *tensor of inertia* [40] approximation is used to initialize shower reconstructions. It is based on a mechanical picture: Assuming that PMTs i at $\vec{\boldsymbol{r}}_i$ being hit with amplitudes a_i PE correspond to masses a_i at $\vec{\boldsymbol{r}}_i$, one can define the tensor of inertia $\mathbf{I}$ of this virtual mass distribution. Its components are given by:

$$I^{k,l} \equiv \sum_{i=1}^{N_{ch}} a_i^w \cdot (\delta^{kl} \cdot (\vec{\boldsymbol{r}}_i)^2 - r_i^k \cdot r_i^l) \ , \tag{6.8}$$

where the amplitude weight $w \geq 0$ can be chosen arbitrarily. The most common settings are $w = 0$ (the amplitude information is ignored) or $w = 1$. The origin of the tensor of inertia is at the center of gravity (COG) of the mass distribution. The tensor of inertia has three eigenvalues I_j, $j\epsilon\{1,2,3\}$, corresponding to its three main axis e_j. The smallest eigenvalue I_1 corresponds to the longest axis e_1. In case of a long track-like event $I_1 \ll I_2, I_3$ and e_1 approximates the direction of the track. Contrary, in case of a shower-like event, $I_1 \approx I_2 \approx I_3$ and e_1 approximates the direction of the primary particle which caused the shower. An ambiguity of the direction along the e_1 axis remains in both cases.

The ratios between the I_j determine the sphericity of the event. They were used as veto parameters in the analysis presented here. The center of gravity, is used to initialize the likelihood shower reconstruction.

6.4 Likelihood Track Reconstruction

The *likelihood track reconstruction* [247] is based on the minimization of the likelihood parameter L. It is defined as

$$\mathsf{L} \equiv -\frac{\log(\mathcal{L})}{N_{free}} = \frac{-1}{N_{free}} \cdot \log(\prod_{i=1}^{N_{ch}} \mathcal{L}_i) = \frac{-1}{N_{free}} \cdot \sum_{i=1}^{N_{ch}} \log(P(t_{res,i}, \mathrm{OM}_i)) \ , \tag{6.9}$$

where $N_{free} \equiv N_{ch} - 5$ is the number of free parameters (5 reconstructed parameters), $\mathcal{L}$ is the likelihood and $P(t_{res,i}, \mathrm{OM}_i)$ is the probability density for the OM i to be hit at time $t_{res,i}$. The term $t_{res,i}$ denotes the *time residual* of OM i. This is the difference between recorded photon arrival time $t_{hit,i}$ and $t_{exp,i}$, the expected arrival time for a pure Cherenkov model without scattering:

$$t_{res} \equiv t_{hit} - t_{exp} = t_{hit} - \left[T_0 + \frac{\rho}{\sin(\theta_{cer}) \cdot c_{ice}} \right] \ . \tag{6.10}$$

Here, T_0 is the calibration constant defined in section 5.1, ρ is the distance between OM and muon track, θ_{cer} is the Cherenkov angle and c_{ice} is the speed of light in the ice. t_{res} is dominated by delays due to scattering and by the time resolution of the detector.

The expression $P(t_{res}, \mathrm{OM})$ is analytically calculable in the case of an isotropic and monochromatic point-like light source:

$$P(t_{res}, \mathrm{OM}) \equiv \frac{1}{N(\rho)} \frac{\tau^{-(\rho/\lambda)} \cdot t_{res}^{(\rho/\lambda - 1)}}{\Gamma(\rho/\lambda)} \cdot exp\left[-(t_{res}/\tau + c_{ice} \cdot t_{res}/\lambda_a + \rho/\lambda_a)\right] \ , \tag{6.11}$$

where

$$N(\rho) = e^{-\rho/\lambda_a} \cdot \left(1 + \frac{\tau \cdot c_{ice}}{\lambda_a}\right)^{-\rho/\lambda} \tag{6.12}$$

is the normalization coefficient. It represents the probability that OM i detects a single photon at any time within the trigger window. λ_a is the absorption length of the ice, whereas τ (unit time) and λ (unit length) are free parameters. Both depend on the distance ρ and on the relative orientation between OM and track η. $P(t_{res}, \mathrm{OM})$ is called the *pandel-function* [188]. It describes the probability that a photon reaches OM i from a distance ρ_i under given relative orientations η at a time delay of $t_{res,i}$ compared to an un-scattered photon. Other attempts to parameterize $P(t_{res}, \mathrm{OM})$ were performed in [55] and yielded comparable results.

In $P(t_{res}, \mathrm{OM})$, the term "OM" represents the dependency on the distance between track and OM and on their relative orientation. Scattering reduces the latter dependency. So in homogeneous ice and at large distances, $P(t_{res}, \mathrm{OM}) \rightarrow P(t_{res}, \rho)$. In a first order approximation, the orientation dependency is decoupled from the distance dependency. This can be described by replacing the true distance ρ with an effective distance

$$d = d_\eta(\eta) + d_\rho(\rho) \tag{6.13}$$

In this approximation, $P(t_{res}, \mathrm{OM}) \rightarrow P(t_{res}, d)$. Here, η is the angle between the PMT axis and the Cherenkov cone. The parameters defining the pandel-function were fitted [247] using data simulated with *PTD* (see section 4.2.3). The results are:

$$\begin{aligned} &\tau = 557\,\mathrm{ns} \\ &\lambda_a = 96\,\mathrm{m} \\ &\lambda = 33.3\,\mathrm{m} \\ &d_\rho(\rho) = 0.84 \cdot \rho \\ &d_\eta(\eta) = 3.1\,\mathrm{m} - 3.9\,\mathrm{m} \cdot \cos\eta + 4.6\,\mathrm{m} \cdot \cos^2\eta \end{aligned} \tag{6.14}$$

The effective distance approximation best describes the data at distances where $\rho/\lambda \not\approx 1$. The pandel-function is not defined for negative t_{res} and has a pole at $t_{res} = 0$. The likelihood parameter based on it can thus not be minimized numerically. To compensate this, the expression for $P(t_{res}, d)$ has to be modified for small t_{res}. Since the convolution of $P(t_{res}, d)$ with a Gaussian is not analytically solvable, it is patched with a Gaussian $G(t_{res},\, d)$:

$$\hat{P}(t_{res}, d) \equiv \begin{cases} G(t_{res},\, d) = \dfrac{N_g(d)}{\sqrt{2\pi}\sigma_g} \cdot \exp\left[-\dfrac{(t_{res} - t_1)^2}{2\sigma_g^2}\right] & \text{for} \quad t_{res} < t_1 \\ T(t_{res}, d) = \sum\limits_{j=0}^{3} a_j \cdot t_{res}^j & \text{for} \;\; t_1 < t_{res} < t_2 \\ P(t_{res}, d) & \text{for} \;\; t_2 < t_{res} \end{cases} \tag{6.15}$$

The spline $T(t_{res}, d)$ is necessary to smoothly interpolate between the Gaussian and the pandel-function. $\hat{P}(t_{res}, d)$ is called *upandel-function*. The transition points are chosen to be at $t_1 \equiv 0$ and $t_2 \equiv \sqrt{2\pi} \cdot \sigma_g$. The a_j are chosen such that the upandel-function and its first derivative are continuous at t_1 and t_2 ($\rightarrow$ four conditions for the four a_j). The normalization of $\hat{P}(t_{res}, d)$, yields a condition for N_g, so that the only free parameter is σ_g. The resulting equations for the a_j and N_g can be found in [247]. The free parameter σ_g describes the convolution of all timing uncertainties – in particular the PMT jitter. It is often (incorrectly) simply called "jitter", thereby neglecting other causes of a smeared out time information. In this work it will be called *pseudo-jitter*. For the analysis presented here, it had been optimized to 15 ns, see section 6.6.

A new reconstruction which does not use the *upandel-function*, but reconstructs directly from tabulated *PTD* output is being tested at present. It was not available for the analysis presented here.

6.4.1 Iterative Reconstruction

Though several different minimization algorithms have been tested for the likelihood reconstruction (see section 6.6), the standard likelihood reconstruction can still be improved by repeating it several times. The starting value for each iteration is then the result of the previous best reconstruction (the one with the best likelihood) plus a random fluctuation on the two angles only. The point of the track which is closest to the center of gravity of hits is not modified. After this re-initialization, the minimization is performed in all five dimensions again. The reason for the improvement obtained with this iterative

approach is, that the minimization algorithms typically have more problems finding the correct direction than finding a vertex close to the detector center.

The drawback of this *iterative reconstruction* is the enhanced CPU time, which is proportional to the number of iterations performed. Multiple iterations are thus only performed with strongly reduced data sets of higher cut levels. Unless specified, reconstructions in this work are not performed multiple times (i.e. use only one iteration).

6.4.2 Multi-PE Reconstruction

The probability density 6.11 describes only the arrival times of single photons. In case of a multi PE signal, AMANDA PMTs record as time stamp the arrival time of the first photon. The first photon is usually less scattered than average, so its arrival time is earlier than that expected for a 1 PE signal. To describe the time of a N PE signal in OM i, one thus has to replace $\hat{P}(t_{res}, d)$ by

$$\hat{P}_N^{1st}(t_{res}, d) \equiv N \cdot \hat{P}(t_{res}, d) \cdot \left(\int_{t_{res}}^{\infty} \hat{P}((\tilde{t}_{res}, d) d\tilde{t}_{res} \right)^{N-1} . \tag{6.16}$$

The value of N is derived directly from the amplitude information delivered by the corresponding ADC. The resulting reconstruction is then called *multi*-PE *reconstruction*. Reconstructions using $\hat{P}(t_{res}, d)$ rather than $\hat{P}_N^{1st}(t_{res}, d)$ are sometimes called *single*-PE *reconstructions*. If nothing particular is specified, AMANDA reconstructions always refer to the *single*-PE *reconstructions*, since they do not require a precise amplitude calibration.

6.4.3 $P_{hit}P_{nohit}$ Reconstruction

In all reconstructions mentioned so far, only hit information was used. But a PMT which was *not* hit also delivers information, especially if it is close to the assumed track. An approach utilizing this fact is the $P_{hit}P_{nohit}$ *reconstruction*. It is not based on the hit times and yields complementary information to the track reconstructions previously defined.

The upandel function describes single PE hits. As mentioned in equation 6.12, the probability to detect a single photon at any time is $P_1^{hit}(d) \equiv N(d)$. If n photons are emitted, one can calculate the probabilities not to detect a single one of them ($P_n^{nohit}(d)$), or to detect at least one of them ($P_n^{hit}(d)$):

$$P_n^{nohit}(d) \equiv \left(1 - P_1^{hit}(d)\right)^n \tag{6.17}$$

$$P_n^{hit}(d) \equiv 1 - P_n^{nohit}(d) = 1 - \left(1 - P_1^{hit}(d)\right)^n \tag{6.18}$$

The number of photons n depends on E_μ, the energy of the muon: $n = n(E_\mu)$. Moreover, the assumption of a point-like light source (emitting isotropic light) has to be replaced by that of a track-like muon event emitting light along a Cherenkov cone. Therefore, the number of photons $n(E_\mu)$ has to be replaced by an orientation dependent effective number of photons $n(E_\mu, \eta)$. In [247], $n(E_\mu, \eta)$ is parameterized as:

$$n(E_\mu, \eta) = 2 \cdot (1 + 9.4 \cdot 10^{-4} \cdot E_\mu/\mathrm{GeV}) \cdot (1 + 0.35 \cdot \cos(\eta)) . \tag{6.19}$$

Noise is easily incorporated:

$$\begin{aligned} \tilde{P}^{nohit}(d) &= P^{nohit}(d) \cdot P^{nonoise} \ , \\ \tilde{P}^{hit}(d) &= 1 - \tilde{P}^{nohit}(d) \end{aligned} \tag{6.20}$$

The likelihood parameter for this reconstruction is then

$$\mathsf{L} = \frac{-1}{N_{free}} \left(\sum_{i=1}^{N_{ch}} \log(\tilde{P}^{hit}(d)) + \sum_{i=N_{ch}+1}^{N_{OM}} \log(\tilde{P}^{nohit}(d)) \right) \tag{6.21}$$

The $P_{hit}P_{nohit}$ reconstruction is thus only based on the appearance or non-appearance of hits. In particular, it does not depend on the hit times. The appearance of an explicit energy dependence in equation 6.19 allows an energy reconstruction to be performed via this likelihood parameter [247].

6.4.4 Zenith-angle-weighted Reconstruction

In an effort to improve the reconstruction, an idea from Bayesian statistics [129] was optionally included in the reconstruction: zenith-angle-weights [121]. According to the Bayes theorem [21], the probability $P(A, B)$ for the combined occurrence of events A and B is

$$P(A, B) = P(A|B) \cdot P(B) = P(B|A) \cdot P(A) \ , \tag{6.22}$$

where $P(A|B)$ is the probability of A given that B is occurring. Thus

$$P(A|B) = \frac{P(B|A) \cdot P(A)}{P(B)} \ . \tag{6.23}$$

In a Bayesian perspective of AMANDA events, one can now identify A with the true track and B with the registered hit pattern. Then $P(A|B)$ is the probability for some track A given the observed hit pattern B. This is exactly the term one is interested in, when reconstructing an event. $P(B|A)$ is the probability for some hit pattern B given the track A. $P(B|A)$ is therefore described by the upandel function. $P(A)$ is the probability to have a certain track (irrespective of the hit pattern) and $P(B)$ is the probability of the hit pattern (irrespective of any tracks). Thus $P(B) \equiv 1$ when reconstructing a *given* (*observed*) hit pattern. In order to obtain $P(A|B)$, one thus has to define a probability distribution $P(A)$ (called prior in Bayesian statistics) on how likely the various possible track directions are a priori (irrespective of any observed hit pattern). Having defined such a prior, one does not maximize the likelihood derived from the upandel function any more, but a likelihood derived from the product of the upandel function and the prior.

In the case of a uniform prior, this approach would not change anything. But in general, the prior is non-uniform and the reconstruction results change when a prior is used. Only slight changes occur for individual events with sharp maxima in their likelihood space or for events which lie in a region where the prior is locally flat.

A choice for the prior can for example be taken from theoretical models on the combined flux of atmospheric muons and neutrinos, parameterized as a function of the zenith angle. The effect of such a prior is to introduce a zenith angle dependent weight to the likelihood

function. The zenith angle is then the only reconstruction parameter altered in comparison to unweighted reconstructions. Critics of this approach argue that the weight (prior) is somehow arbitrary: It is not evident whether to put in assumptions about the total particle flux, the triggering flux or the flux remaining at the filter level at which the reconstruction is used. Furthermore, the reconstruction does not reproduce the zenith-angle distribution of the prior.

The weight function used so far is a parameterization of the total atmospheric muon flux at trigger level for down-going tracks and is uniform for up-going tracks [83]. As a result, tracks which are reconstructed as up-going with an unweighted reconstruction are either unaffected or shifted to down-going directions. Since in most analyzes, down-going events are rejected, this zenith-angle-weighted reconstruction can simply be considered as a normal reconstruction plus a cut on a (complicated) combination of likelihood and reconstructed zenith angle. In this perspective, the prior parameterization can be optimized just like any other cut – irrespective of any Bayesian interpretations. Unless explicitly stated, reconstructions referred to in this work are not zenith-angle-weighted.

6.4.5 Combined Reconstructions

In equation 6.21, the individual probabilities for the P_{hit} and the P_{nohit} functions were combined to obtain a single likelihood parameter. Accordingly any two (or more) of the likelihood functions mentioned before, can be added to obtain a combined likelihood for a more sophisticated reconstruction. In section 9.1, it will be shown that for this analysis, the reconstruction yielding the best resolution was such a combination of the multi-PE reconstruction and the $P_{hit}P_{nothit}$ reconstruction. Its likelihood parameter is defined by

$$\mathsf{L}^{\mathsf{P_{hit}P_{nothit}\oplus MPE}} = \mathsf{L}^{\mathsf{P_{hit}P_{nothit}}} + \mathsf{L}^{\mathsf{MPE}} \ . \tag{6.24}$$

This reconstruction will be referred to as the $P_{hit}P_{nothit} \oplus MPE$ reconstruction in the text. The pure multi-PE reconstruction was not used during the analysis presented here. The subscript "MPE" can and is therefore used henceforth in equations and figures to abbreviate the term "$P_{hit}P_{nothit} \oplus MPE$" reconstruction.

6.4.6 Track and Energy Reconstruction

A muon track is characterized by a vertex $\vec{r}$, a direction described by θ and ϕ and an energy E, i.e. by six parameters. Since a minimization in a six-dimensional space is much slower than in a five-dimensional space and since the energy information is often not required, the reconstruction is performed in two steps: A first reconstruction ignores the energy parameter and reconstructs the muon track only. A second reconstruction then takes the track and reconstructs the energy as its only free parameter. In the AMANDA convention, if nothing else is specified, a reconstruction always refers to the track reconstruction only. An *energy reconstruction* is specifically noted as such. Typically the track reconstruction only uses the hit times, while the energy reconstruction can for example also use amplitude information. The only energy reconstruction used in this work is the $P_{hit}P_{nohit}$ reconstruction described in section 6.4.3.

6.5 Shower Reconstruction

Not all events registered by the AMANDA detector have a track-like topology. Shower-like topologies, arising for example from ν_e interactions, are best reconstructed with a *shower reconstruction* [143]. It tries to fit events from a point-like light source with photons propagating isotropically from it. It is initialized by the center of gravity calculated in the tensor of inertia first guess method and only reconstructs the vertex of the shower. The direction of the initial particle can be considered to be along e_1 from the tensor of inertia. Just like in the case of a track reconstruction, the shower reconstruction is also based on the upandel-function (see equation 6.15). Due to the different topology of the light emission, it uses a different coordinate system and has a slightly different parameterization: $\lambda = 47\,\mathrm{m}$, $\tau = 98\,\mathrm{ns}$ and $\lambda_a = 450\,\mathrm{m}$ [143]. In this work, the shower reconstruction is only used to provide veto information.

6.6 Optimization of Reconstruction Parameters

All types of reconstructions in AMANDA are combined in the program *recoos* [223]. The reconstruction methods described above just define the various classes of reconstructions which *recoos* can handle.

The program does handle various options which have not been discussed before. They refer for example to physical quantities which are not well known, like the pseudo-jitter σ_g introduced in equation 6.15. Other options refer to free parameters, for example parameters defining the "hit cleaning" procedure. The hit cleaning (selection of hits which enter the reconstruction) can influence the result of a reconstruction.

Such parameters have to be optimized. This optimization was the starting point of the analysis presented here. A few parameters to which particular attention was paid during this work are described in the following:

Pseudo-jitter The pseudo-jitter σ_g describes the convolution of all timing uncertainties in the experiment. It enters the reconstruction via $G(t_{res},\, d)$ and via the transition point t_2, see equation 6.15. The uncertainties arise from the true PMT-jitter, from timing calibration errors, from slight instabilities of the detector performance during the data-taking period, etc. In case of small timing uncertainties (small pseudo-jitter), only a small fraction of the pulses are allowed to arrive earlier than expected (have negative time residuals) and vice versa. From laboratory measurement of the true PMT-jitter ($\sim 5\,\mathrm{ns}$), a lower bound for the pseudo-jitter was known. During the optimization, values between $\sim 4\,\mathrm{ns}$ and $\sim 24\,\mathrm{ns}$ were compared. Criteria were:

- A small angular reconstruction error for MC events. This criterion by itself is best fulfilled when the pseudo-jitter best describes all timing uncertainties of the Monte Carlo simulation. It is irrespective of unsimulated experimental effects.

- The reconstructed zenith angle distribution of experimental events on trigger level best matches the distribution expected from direct measurements.

- The reconstructed signal+background Monte Carlo distributions agree best with the reconstructed experimental distributions in various angular regions and after various cut levels.

- Other criteria like the distribution of hit times can be considered, but were not analyzed due to limited time available.

A broad optimum between ~ 10 ns and ~ 20 ns was found. The pseudo-jitter was chosen to be 15 ns.

Minimization method In a likelihood reconstruction, one crucial aspect is to find the global minimum of the likelihood function. The main challenge is the following: One can only probe individual points in the multi-dimensional likelihood space. A good algorithm has to test the likelihood space at points distant enough from each other to avoid local minima, but close enough to each other in order not to miss a sharp global minimum. In AMANDA, local likelihood minima can for example arise due to the anisotropies of the detector - especially with respect to the azimuth angle or due to scattering (causing unexpected hit times). In general, the more likelihood values one calculates, the more often one will actually find the global minimum – but the more CPU time one has to spend for each reconstruction.

Two different minimization techniques were tested: Powell's [197] and Minuit [130], with Minuit being tested in a fast, a standard and an accurate mode. The tests were performed according to the same criteria as mentioned before. While the fast Minuit mode was insufficient for the challenging 5-dimensional AMANDA likelihood space, the others gave similar results. Powell's was finally chosen since it was the fastest code (allowing to run the most iterations of the reconstruction). This result was tested at trigger level and confirmed on cut levels 2 and 3. (These cut levels are defined in section 7.1.) Other minimization procedures like simplex [197] or simulated annealing [197], which are now implemented in the AMANDA software were not available at the time this analysis was performed.

ADC assignment In case of bright events or OMs close to a muon track, AMANDA OMs can receive more than one hit within one event. In such a case, the 1997 AMANDA DAQ recorded timing information for the first 8 hits per event and OM, but only the largest amplitude of any of the hits. Since amplitude information was required for a hit to pass hit cleaning criteria (c.f. section 7.1.1) and since it was used for the multi-PE reconstructions, care had to be taken which hit(s) to assign the registered amplitude to.

The options investigated were to assign it to:

- All hits: At least the strongest hit will get its correct ADC. The disadvantage of this assignment is that the weaker hits get an amplitude assigned which is known to be too large.

- The first hit: Large hits usually come first since they are less affected by scattering and later hits can be due to after-pulses. The danger is to assign the amplitude to an accidental early noise hit.

- The hit with the largest time over threshold: Large hits typically have long durations. But a large time over threshold might also arise from two overlapping low-amplitude hits. Such an overlap typically arises from the dispersion in the $\sim 2\,\mathrm{km}$ long cable.

The best result was depending on the reconstruction method: While the first guess approximations gave best results when assigning the ADC to the first hit only, the likelihood reconstructions gave the best and most stable results when all hits got the amplitude assigned. The ADC assignment was performed accordingly.

Hit Cleaning Prior to the reconstruction, likely noise-hits are removed from the data stream. One criterion in identifying such noise-hits is the isolation criterion (c.f. section 7.1.1): Each hit which does not have a "neighboring" hit in space and time is rejected as a likely noise hit. For the definition of "neighbor", distances between 60 m and 100 m and time differences from $\pm 300\,\mathrm{ns}$ to $\pm 600\,\mathrm{ns}$ were tested. $\pm 500\,\mathrm{ns}$ and 100 m (70 m for the line-fit) were the values chosen according to the criteria listed above.

Hole Ice As will be outlined in more detail in section 7.3.5, the scattering length of the re-frozen ice inside the AMANDA drill holes (the "hole ice") is not very well known. Strong scattering close to the OM isotropizes the incident light signal - irrespective of the relative orientation between OM and track. The angular acceptance of the combined entity OM plus hole ice inside *recoos* thus have to be initialized with the correct hole ice scattering length. Values of 10 cm, 30 cm, 50 cm, 100 cm and an infinite scattering length have been tested. In accordance with dedicated hole ice analyzes, a scattering length of 50 cm gave the best results. So far, no angular dependency of this parameter has been optimized. Also dependencies of the locations of the optical module with respect to the hole ice column or inhomogenousities of the hole ice scattering coefficient have not been investigated yet.

7 Data Processing

7.1 Processing of 1997 AMANDA Data

Data processing was governed by two principles. First, experimental and MC simulated data were treated exactly the same way. Wherever this principle was not (could not) be obeyed, it is clearly marked in this work. Secondly, the processing details should not be biased by the experimental data to be analyzed. Therefore most of the processing scheme was defined according to Monte Carlo simulated data. This was not always possible due to insufficient quality of the simulation of experimental data, or due to insufficient background Monte Carlo statistics. In these cases, only the data taken on odd numbered days was analyzed. Half of the experimental data set therefore remained untouched until all processing details had been finalized. It turned out that there was no significant difference between the two experimental data sets. Actually, the blindly processed even days showed a slightly higher passing rate for final cuts, see table D.14. Apart from that table, the presentation in this work does not distinguish between the two experimental data sets.

7.1.1 Preprocessing

Before the data could be reconstructed, several initialization steps were necessary:

OM and Run Selection: For each experimental run, a selection was performed in order to identify the usable OMs. An OM was considered usable (or "stable") if it was

1 alive,

2 calibrated,

3 its TOT and ADC distributions were stable for that run and

4 its average noise rate within the run deviated from its average noise rate for the full year by less than two (strings 1–4) or four (strings 5–10) standard deviations.

Runs were rejected as "bad" when fewer than 220 out of the total 302 optical modules were passing these criteria. For the remaining ("good") runs, those OMs failing the before mentioned criteria were flagged. Their hit information did not enter the following analysis. As explained in section 4.2.4, the simulation tried to describe a "year-average" detector and not individual runs. Hence all OMs in the simulation were either simulated as dead (45 OMs) or as always stable (257 OMs). Correspondingly, all simulated runs passed the run selection criteria. Details on the selected OMs (experimental and simulated data) and runs (experimental data) are given in appendix D.1 and D.2.

Event Selection: Each event within an accepted run had to pass the standard AMANDA-B10 16-fold majority trigger. This explicit requirement was necessary since there were additional coincidence triggers from external experiments causing $\sim 10\,\%$ of all triggers. These additional triggers had not been included in the Monte Carlo simulation.

Calibration: For each selected event, the timing and amplitude information of the hits was calibrated. In 1997, the AMANDA DAQ could store up to 8 leading edge times in the TDCs. However, only the largest amplitude had been registered in the peak ADC for each OM. If an OM was hit multiple times inside its ADC gate, it was unknown which hit had caused the ADC signal. The decision on how to assign the amplitude information was based on the corresponding optimization analysis described in section 6.6. All hits within the ADC gate were calibrated as if they all had the same maximal amplitude. In the case of the line-fit, however, only the first hit per OM got the amplitude assigned.

Hit-Cleaning: After the calibration, a hit-cleaning procedure was performed in order to reject noise hits, cross-talk hits and those hits which were caused by severely delayed (scattered) photons. Cross-talk hits arise when an electric signal in one channel causes a current in another channel by electromagnetic induction. Severely scattered hits were suppressed since they worsen the track reconstruction results. The hit-cleaning requirements had been optimized, see section 6.6. They were:

Timing: The leading edge time of the hits had to be within a time window of 4.5 μs. The time over threshold of each hit had to be between 125 ns and 2000 ns. The second criterion was optimized to efficiently remove cross-talk hits [140]. A later analysis revealed that for some channels, slightly tighter TOT cuts would have been needed to remove all cross-talk hits [83].

Amplitude: The calibrated amplitude had to be between 0.1 PE and 1000 PE, the uncalibrated one larger than 50 mV. This was not demanded for energy reconstructions.

Isolation: Each hit needed at least one neighboring hit within $\pm$500 ns at another OM not further than 100 m away. For first guess approximations, the maximum distance was reduced to 70 m. This anti-isolation criterion was not required for energy reconstructions.

Multiple Hits: Only the first hit of an OM was used for first guess approximations. Likelihood reconstructions used all hits.

Less stringent hit-cleaning criteria were applied for the energy reconstructions, since one tries to make use of the calorimetric effect of photon scattering for these reconstructions. For track reconstructions in contrast, scattering smears out time information and thus leads to worse results. The analytic first guess approximations are based on assumptions ignoring scattering. Correspondingly, the tightest hit-cleaning requirements were chosen for first guess approximations. Cleaned hits were flagged only. I.e. they were not removed from the data stream and later reconstructions could use hits not used in previous reconstructions.

After the analysis of this work was finished, the neutrino candidates found here were compared to those found in an independent analysis [83]. It turned out that hit-cleaning in AMANDA is rather crucial: A significant fraction of neutrino candidate events found in only one analysis (A) would have also been found in the other analysis (B), if analysis (B) would have used the hit-cleaning of analysis (A). This was true for experimental and simulated signal data. However, no simple conclusions could be drawn: For one event a

modified hit-cleaning would make it pass later filter stages it formerly did not pass, while for another event the opposite would be true.

A track is defined by five parameters: Three giving a point on the track $\vec{x}$ plus two defining the direction via two angles (θ and ϕ). So, only events which had at least five hits left after hit-cleaning were kept in the processing chain. The combined passing rate of the preprocessing (after run selection) was 84.7 % for experimental data and 99.8 % for simulated data (background and signal). As explained, ~ 10 % of the 15.3 % difference in experimental data arises from the not simulated external triggers. The remaining ~ 5.3 % difference is mainly attributed to the removal of un-simulated cross-talk in experimental data.

7.1.2 Level 1

Main aim of the level 1 processing was to

1. reduce the data sets to a size reconstructible with a likelihood reconstruction by the available CPU resources and

2. to provide an initialization for the likelihood reconstruction.

Thus, level 1 processing consisted of a first guess approximation and an event selection (filter) depending on the results. As initial first guess approximation, a line-fit was used.

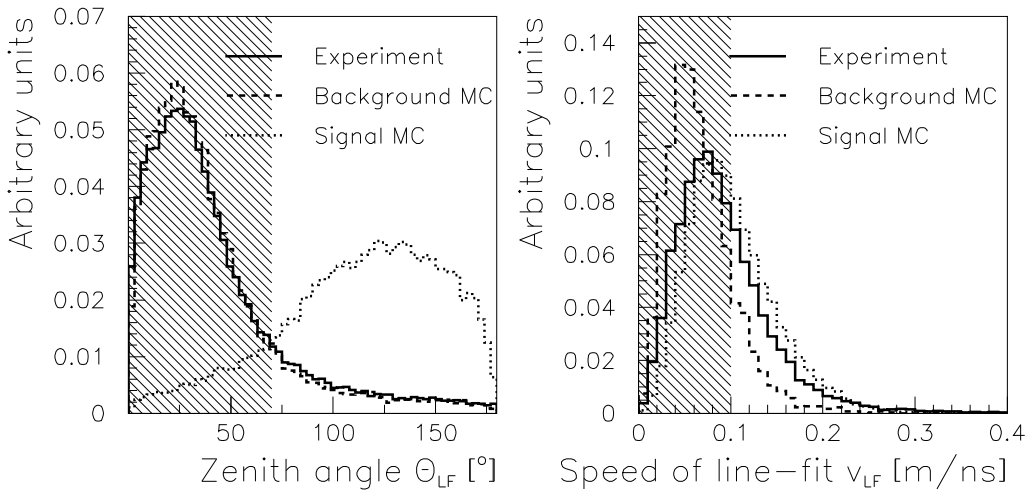

Figure 7.1: (Left:) Minimum bias data: Zenith angle θ_{LF}. (Right:) Speed of the line-fit v_{LF} after cut $\theta_{LF} > 70$. Solid line: experimental data, dashed line: *CORSIKA* background simulation, dotted line: *nusim* signal simulation. Shaded area: Removed by level 1 cut.

Figure 7.1 displays the two cut parameters obtained from it: The zenith angle θ_{LF} and the speed of the line-fit v_{LF}. θ_{LF} shows a good agreement between experimental and background MC data. The dominant fraction of events of the three data samples shown is reconstructed as to originate from the correct hemisphere. But a significant fraction of events is mis-reconstructed. The cut was set at $\theta_{LF} = 70°$.

For v_{LF}, the agreement is not satisfactory. Simulated signal data shows just marginally better (larger) values than experimental data. The background simulation yields the worst (smallest) values and cannot describe the experimental data. The effect of low v_{LF}-values in simulated signal data is due to low energy neutrino events. In these cases, the muon does not travel far from the hadronic vertex. In addition, the light output from the hadronic vertex is comparable to that from the muon. The total light distribution of such events is therefore approximately spherical. These low-energy events are practically impossible to reconstruct, so they have to be cut away at some stage. Nevertheless, a strong cut on this parameter is certainly not optimal and discarded for future analyzes.

The discrepancy between simulated background and experimental data is attributed to a wrong description of either the optical properties of the ice or of the OM sensitivity, see sections 7.3.5 and 7.3.6. It is correlated with a systematic shift in the N_{ch} distribution between experimental and simulated background data [42]. Both are attributed to the same insufficiencies of the simulation.

There were two reasons to cut on v_{LF} in this analysis: First, the cut was defined in 1998. The version of the Monte Carlo simulation available at that time showed larger v_{LF} values for the signal simulation than the present version. Secondly, no alternative first guess approximations (yielding alternative cut parameters) were available at the time of data processing. The alternative of an even tighter θ_{LF} cut (at $\sim 110^\circ$) would have rejected too much well reconstructible signal. Since CPU-time requirements restricted the passing rates of level 1 cuts, the cut at $v_{LF} = 0.1$ was applied to 1997 data.

It should be noted that although v_{LF} is not an explicit angular cut, it has an implicit angular dependency. Likewise, all other AMANDA cuts modify angular distributions. This is mainly due to the anisotropic geometry of the detector.

The level 1 cuts are thus:

$$\begin{array}{lcl} \theta_{LF} & > & 70^\circ \\ v_{LF} & > & 0.1\,\mathrm{m/ns} \end{array} \tag{7.1}$$

The total passing rates after these cuts are 4.8 % for experimental data, 3.5 % for the *CORSIKA* background simulation sample and 36 % for the *nusim*-simulated atmospheric signal sample. The data samples passing the level 1 cuts were then reconstructed with a standard likelihood reconstruction.

7.1.3 Level 2

The aim of the level 2 processing was to base cuts on the likelihood reconstruction and select only events which were passing two basic quality cuts. Afterwards the reconstruction could be improved by using it in an iterative mode and applying a few more basic cuts. Finally, several additional reconstructions were performed.

An error of the calibration was discovered after the level 2 processing had been performed: Up-looking PMTs had been calibrated as down-looking and vice versa. This affected the reconstruction via the orientation angle η, see equation 6.13. The effect of this error on the passing rates of already applied cuts was small [42], but the error had to be corrected. The data was thus re-calibrated and the level 2 processing was repeated. Therefore a level 2a (with the wrong calibration) and a level 2b (correct calibration) exists.

The text of this section does not always distinguish between the two. Unless stated otherwise, it refers to level 2b. The full details of levels 2a and 2b are given in appendix D.3, tables D.10 and D.11.

Level 2 processing started with selecting only those events which had a reconstructed zenith angle from the likelihood reconstruction of at least 70 degrees (level 2a). This parameter can be seen in the left frame of figure 7.2. Experimental data and background simulation agree well. Much of the background data which was reconstructed as up-going by the line-fit is now correctly identified as down-going.

The remaining data set was filtered to contain at least eleven hits after hit-cleaning. The corresponding N_{ch} distributions can be seen in figure 7.2 (right). Simulated signal data clearly shows the highest number of hit channels. There is a shift of about 4 hits between experiment and background simulation. The reason for this shift is attributed to the earlier mentioned simulation insufficiencies (see discussion of the v_{LF} parameter). It persists through all cut levels when using the standard simulation. It is removed by a new model of the angular OM sensitivities (see sections 7.3.5 and 7.3.6), which has only been included in the signal Monte Carlo simulation for this analysis. Re-simulating a large background statistics would have required too much CPU-time.

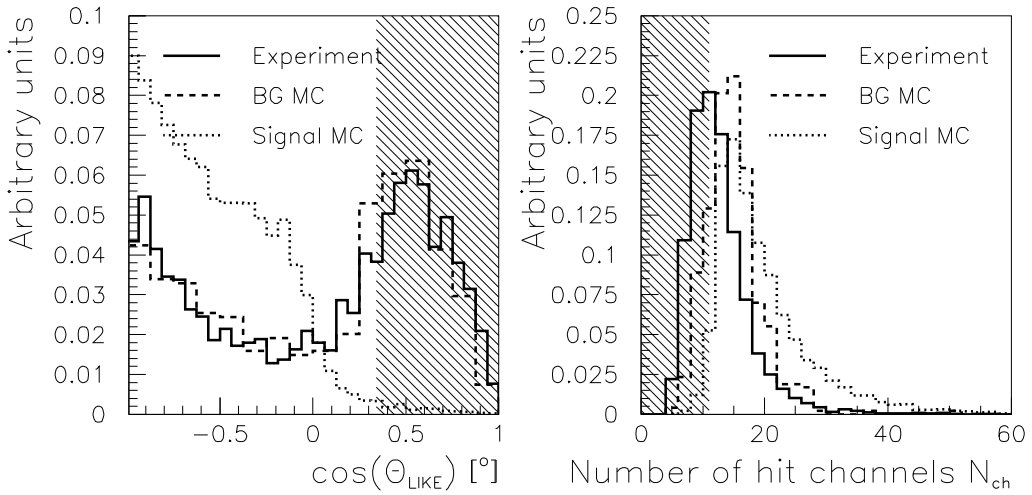

Figure 7.2: Data after cut level 1: Zenith angle of level 2a likelihood reconstruction θ_{LIKE} (left) and number of hit channels N_{ch} (right). Solid line: experimental data, dashed line: *CORSIKA* background simulation, dotted line: *nusim* signal simulation. Shaded area: Removed by level 2 cut.

The data was then passed through an iterative likelihood reconstruction with 16 iterations. This time, a cut on the reconstructed zenith angle was set at 80 degrees, see figure 7.3 (left). One can compare the result to that from the non-iterative reconstruction in the left frame of figure 7.2. Both distributions are shown after cut level 1. The improvement introduced by the iterative reconstruction are evident. Experiment and background Monte Carlo simulation are in nice agreement.

As can be seen in figure 7.3 (right), the number of direct hits $N_{dir,ITER}(-15..25)$ was required to be larger than three. A direct hit is a hit which has a low time residual T_{res} (as defined in equation 6.10). In case of $N_{dir}(-15..25)$, it is demanded that

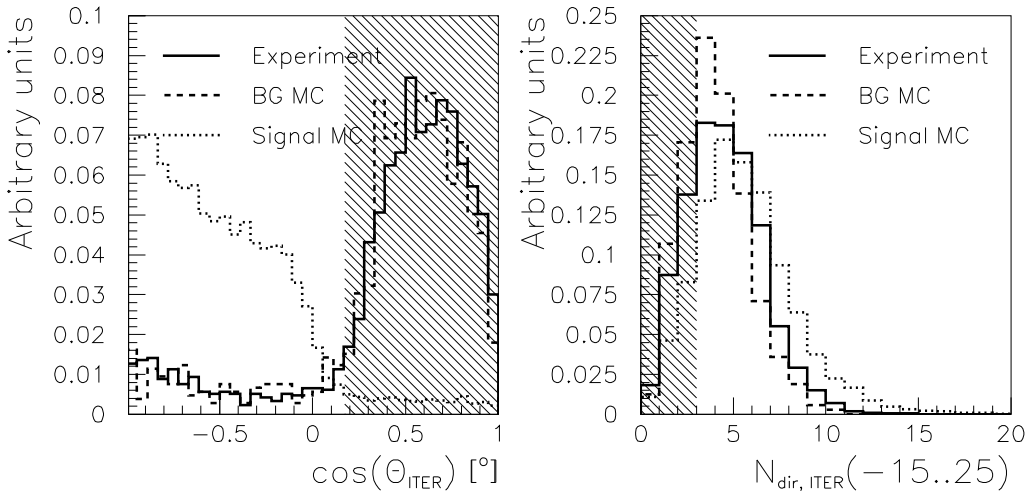

Figure 7.3: Data after cut level 1: Zenith angle of the iterative reconstruction θ_{ITER} (left) and the number of direct hits of that reconstruction $N_{dir,\,ITER}(-15..25)$ (right). Solid line: experimental data, dashed line: *CORSIKA* background simulation, dotted line: *nusim* signal simulation. Shaded area: Removed by level 2 cut.

$-15\,\mathrm{ns} \leq t_{res} \leq +25\,\mathrm{ns}$. Simulated signal data shows the highest number of direct hits. There is a slightly larger number of direct hits in experiment than in background simulation. Again this discrepancy persisted through all cut levels [43]. And again it can be overcome with the new model on the angular OM sensitivity.

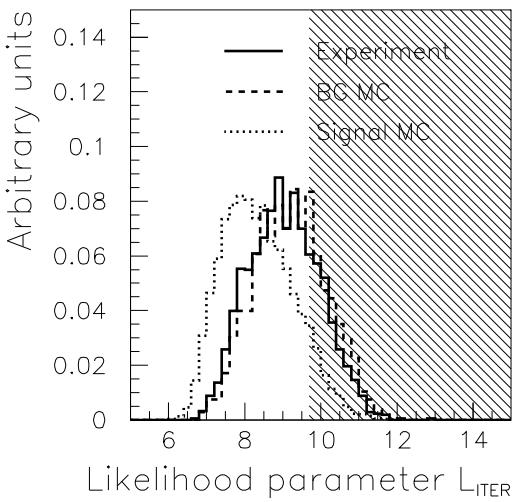

Figure 7.4: Data after cut level 1: Likelihood parameter of iterative reconstruction: L_{ITER}. Solid line: experimental data, dashed line: *CORSIKA* background simulation, dotted line: *nusim* signal simulation. Shaded area: Removed by level 2 cut.

Finally, the value of the likelihood parameter was used to estimate the quality of the reconstruction. A likelihood parameter of at most 9.5 was demanded, see figure 7.4. Signal events have clearly better likelihoods than background and experimental events on this cut level. There is a reasonable agreement between background simulation and experimental data, although experiment has slightly better likelihood parameters.

To summarize, the level 2 cuts are:

$$\begin{aligned} \theta_{LIKE} &> 70^\circ \\ \theta_{ITER} &> 80^\circ \\ \mathsf{L}_{ITER} &< 9.5 \\ N_{dir,\,ITER}(-15..25) &> 3 \\ N_{ch} &> 11 \end{aligned} \tag{7.2}$$

Here, a subscript $LIKE$ represents cuts on the first likelihood reconstruction and a subscript $ITER$ represents cuts on the 16-fold iterative reconstruction. The total passing rates

including these cuts are $0.44 \cdot 10^{-3}$ for experimental data, $0.38 \cdot 10^{-3}$ for the *CORSIKA* background simulation sample and 15 % for the *nusim*-simulated atmospheric signal sample. The data samples passing the level 2 cuts were then reconstructed with an energy reconstruction, fitted by a tensor of inertia first guess approximation and reconstructed with a shower reconstruction.

7.1.4 Level 3

The (non-angular) level 2 cuts were designed to select events fulfilling basic quality criteria. The level 3 cuts were supposed to additionally reject specific classes of background events. Furthermore, it was aimed to reduce the full data sets to sizes appropriate for interactive (*PAW* [67]) analyzes.

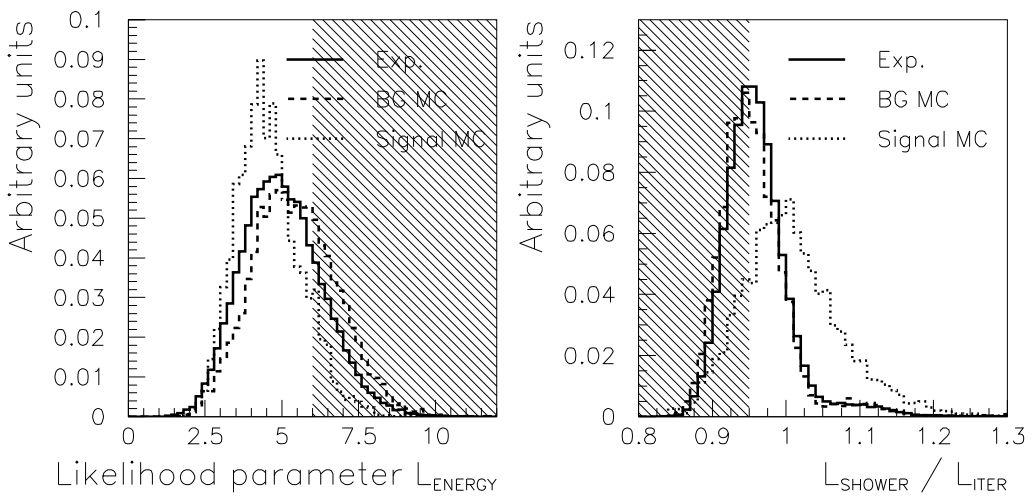

Figure 7.5: Data after cut level 2: The likelihood parameter of the energy reconstruction L_{ENERGY} (left) and the ratio of the likelihood parameters for the shower and the track reconstructions $\mathsf{L}_{SHOWER}/\mathsf{L}_{ITER}$ (right). Solid line: experimental data, dashed line: *CORSIKA* background simulation, dotted line: *nusim* signal simulation. Shaded area: Removed by level 3 cut.

Level 3 processing started by cutting on several parameters of the reconstructions performed before. The cut on the iteratively reconstructed zenith angle was tightened to 90° to remove only slightly mis-reconstructed, almost horizontal atmospheric muons (c.f. figure 7.3 (left)). The likelihood parameter of the iterative reconstruction was also tightened, this time to a value of 8.7 (see figure 7.4), to reject all those events where the reconstruction did not find a high probability for the reconstructed direction.

In addition, a cut on the likelihood parameter of the energy reconstruction was set at 6.0, see figure 7.5 (left). The reason for this cut was that the energy reconstruction is severely hindered (and gets a bad likelihood) if the corresponding track reconstruction does not find the true muon track. Although there is a slight shift between experiment and background, the signal is clearly separated. As a last likelihood cut, the ratio between the likelihood parameters of the reconstruction with the shower hypothesis and the track hypothesis was cut at $\mathsf{L}_{SHOWER}/\mathsf{L}_{ITER} > 0.95$. The cut is displayed in figure 7.5 (right). The signal is evidently much better described with a track hypothesis than background.

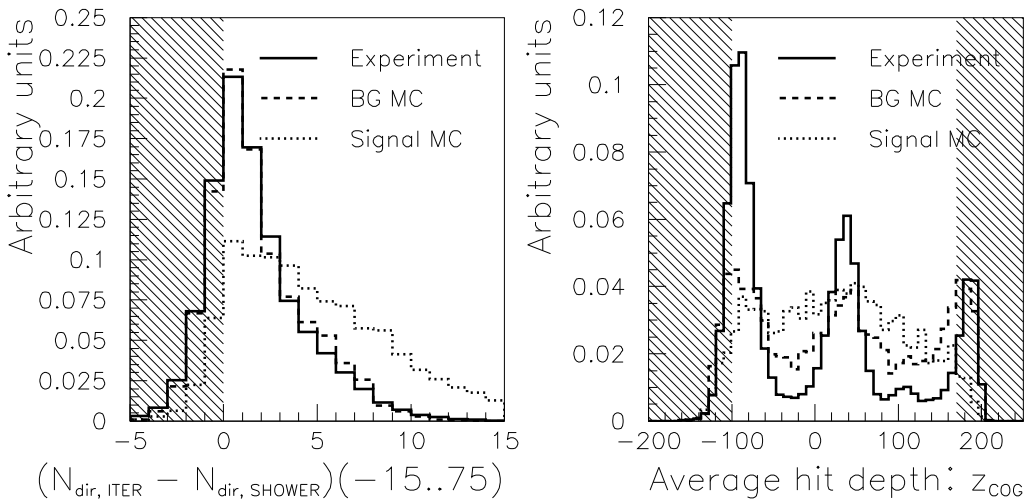

Figure 7.6: Data after cut level 2: The difference between the number of direct hits in the track assumption $N_{dir,\,ITER}(-15..75)$ and the number of direct hits in the shower assumption $N_{dir,\,SHOWER}(-15..75)$ (left). The vertical component of the center of gravity of the hits within an event z_{COG} (right). Note the increased time window for the number of direct hits as compared to the cut on $N_{dir,\,ITER}(-15..25)$ in level 2 processing. Solid line: experimental data, dashed line: *CORSIKA* background simulation, dotted line: *nusim* signal simulation. Shaded area: Removed by level 3 cut.

Again there is a marginal shift between simulated background and experiment, the latter have "better" (larger) values of the cut parameter. The events which were suppressed as shower-like by this cut were dominantly atmospheric muons with associated bright bremsstrahlung events.

Another cut compared the number of direct hits obtained from two reconstructions (shower and track hypothesis). It is shown in figure 7.6 (left). The reconstruction based on a track hypothesis was required to have more direct hits than that assuming a shower-like event. Experiment and background simulation are in good agreement. Signal simulation clearly prefers the track hypothesis.

Another parameter is displayed in figure 7.6 (right): z_{COG}, the vertical component of the center of gravity of hits (c.f. section 6.3). Regarding this parameter, one sees a prominent effect: a triple peak structure in experimental data. The background simulation does not yet fully reproduce this feature. Older Monte Carlo simulations, assuming homogeneous ice, could not reproduce the peaks at all. The vertical ice structures, perhaps in combination with electronic artifacts, are believed to cause these features.

The cut $z_{COG} > -100\,\mathrm{m}$ was applied to remove so-called *corner clippers*: An atmospheric muon which passes below the detector induces upward traveling light. This can easily mimic an upward moving muon. Such a corner clipper only induces light in the lowest OMs, while only a small fraction of neutrino-induced events deposits all its light in these OMs. A similar effect exists for corner clippers at the top of the array: An atmospheric muon traveling approximately at the Cherenkov angle introduces an almost horizontal light-pattern. This can be reconstructed as an horizontal neutrino event. Selecting only events from the top z_{COG}-peak, one sees that they are dominantly reconstructed

to horizontal directions. So the cut on $z_{COG} < +150\,\mathrm{m}$ effectively removes these upper corner clippers.

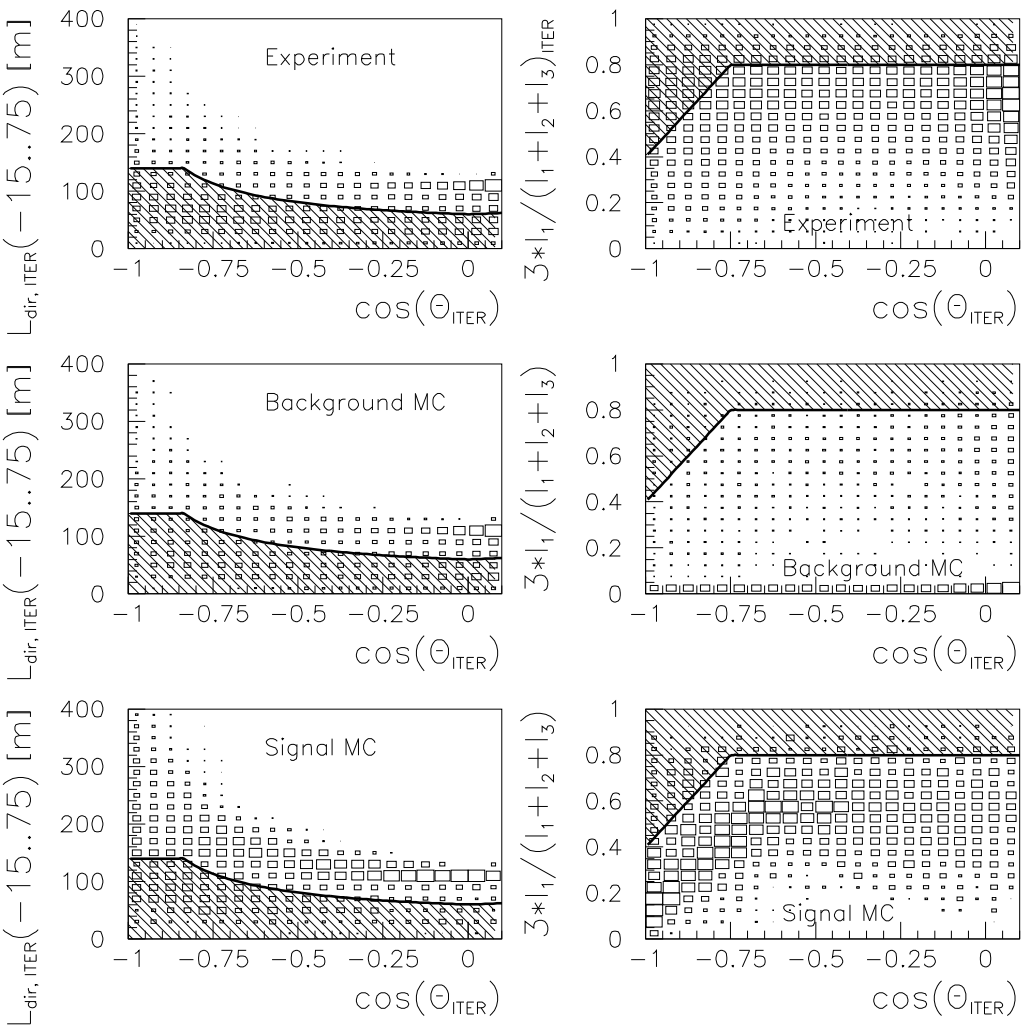

Figure 7.7: Data after cut level 2: 2-dimensional cuts on the direct length $L_{dir,\,ITER}(-15..75)$ (left column) and on the ratio of the eigenvalues of the tensor of inertia $3 \cdot I_1/(I_1 + I_2 + I_3)_{ITER}$ (right column), both dependent on the reconstructed angle. Top: experimental data; center: *CORSIKA* simulation; bottom: *nusim* simulation. Shaded area: Removed by level 3 cut. The area of the boxes is linearly proportional to the number of events within the corresponding bin.

Two more parameters were used to remove another specific class of background: Cuts on the ratio of the eigenvalues of the tensor of inertia $3 \cdot I_1/(I_1 + I_2 + I_3)_{ITER}$ and on the direct length $L_{dir,\,ITER}(-15..75)$, see figure 7.7. The direct length is the largest distance between any two direct hits when they are projected onto the track. In both cases the cut is not at a specific value but depends on the reconstructed zenith angle, see definitions 7.3. Reasons for these zenith angle dependencies of the cuts are:

- The long slim geometry of AMANDA-B10. Large L_{dir} or $I_1/(I_1+I_2+I_3)$-values can not be produced by horizontal events.
- The poorer quality of the reconstruction for horizontal events, see figure 9.7 (left).
- The larger background contamination at the horizon.

The cuts are based on a simple topological model relating the two parameters to the zenith angle for reasonable tracks. This topological model is explained in [103], but shall not be discussed here. The two cuts were effective in removing that part of the background which is located at the bottom and center peak regions in z_{COG} (see figure 7.6 (right)) and which shows strong $\cos(\theta)$ dependency. It is probably caused by a combination of regions of extreme scattering length and electronic artifacts. See [41, 45] for more details on the z_{COG} background.

The level 3 cuts thus were:

$$\begin{gathered}
\theta_{ITER} > 90^\circ \\
\mathsf{L}_{ITER} < 8.7 \\
\mathsf{L}_{ENERGY} < 6.0 \\
\mathsf{L}_{SHOWER}/\mathsf{L}_{ITER} > 0.95 \\
N_{dir,\,ITER}(-15..75) - N_{dir,\,SHOWER}(-15..75) > 0 \\
+170\,\mathrm{m} > z_{COG} > -100\,\mathrm{m} \\
3 \cdot I_1/(I_1+I_2+I_3) < f_{INERT}(\theta_{ITER}) \\
L_{dir,\,ITER}(-15..75) > f_{L_{dir}}(\theta_{ITER})\ ,
\end{gathered} \tag{7.3}$$

$$\begin{aligned}
\text{where } f_{INERT}(\theta_{ITER}) &\equiv \min(\ 0.8\,,\ 2.0 - 1.6 \cdot |\cos(\theta_{ITER})|\ ) \\
\text{and } f_{L_{dir}}(\theta_{ITER}) &\equiv \min\left(140\,\mathrm{m}\,,\ \frac{w + 2 \cdot L_v \cdot |\cos(\theta_{ITER})|}{\sin(\theta_{ITER})}\right)
\end{aligned}$$

The parameters $w = 60\,\mathrm{m}$ and $L_v = 10\,\mathrm{m}$ correspond to the approximate detector radius and a typical distance along which most of the Cherenkov light is un-scattered.

The total passing rates after the level 3 cuts were $0.13 \cdot 10^{-4}$ for experimental data, $0.70 \cdot 10^{-5}$ for the *CORSIKA* background simulation sample and 6.9 % for the *nusim*-simulated atmospheric ν-signal sample. This corresponds to 14776 remaining experimental events, out of which ~ 380 are expected to be neutrino-induced.

7.1.5 Level 4

The aim of the level 4 cut selection was very different from that of the previous cut levels. Rather than trying to find a set of individual cuts, it was tried to find one single combination of cuts. This combined cut should take into account the correlations between the individual cut parameters. Another task was that this combined cut should be simpler to understand than the output of a neural net analysis [37], but more flexible than the simple linear combination obtained in a discriminant analysis [76]. Moreover it was aimed to achieve the highest possible signal passing rate. Finally, the level 4 cuts had to be determined with a very limited statistics of background simulation.

CUTEVAL**:** The CUTEVAL routine offers an algorithm to fulfill all these requirements. It is described in detail in [102]. It is a program allowing the optimization of signal with respect to background as a function of a set of cut parameters. CUTEVAL is run in several steps. First, the single most sensitive cut parameter for the optimization is determined. Then the second, third, etc. most sensitive cut parameters are determined. Finally the optimization is performed with a limited number of the most sensitive cut parameters. The full procedure is now outlined in slightly more detail:

In a first step, CUTEVAL takes a list of potential cut parameters and automatically finds for each parameter the cut value which optimizes the ratio *signal to square root noise* ($S/\sqrt{N}$). This optimization is performed by taking a single parameter $\mathcal{C}$ at a time, cutting at $\mathcal{C} = x$ for various cut values x and calculating $S/\sqrt{N}(x)$ for each x. To calculate $S/\sqrt{N}$, the signal is generally defined as the number of simulated signal events passing the cut. Alternatively it can be the number of residual experimental events when selecting down-going rather than up-going events. (For this, all zenith angle cuts of all previous cut levels are changed correspondingly). Noise is typically the number of remaining simulated background events. But it can also be defined as the difference between the number of experimental and signal events passing. In this analysis, all four combinations of theses definitions for signal and noise were used. For each one of the four choices (CUTEVAL modes), the optimization yields the one cut parameter $\mathcal{C}_1$ which gives the best ratio: $(S/\sqrt{N})_1$. This cut-parameter is the result of the first step of running CUTEVAL.

In a second step, $(S/\sqrt{N})_i$ is then optimized in the 2-dimensional space spanned by $\mathcal{C}_1 \otimes \mathcal{C}_i$ for all other cut parameters i. I.e. the cut value for $\mathcal{C}_1$ is not fixed to the value found during the first CUTEVAL step. A certain number of the $(S/\sqrt{N})_i$ is not better than $(S/\sqrt{N})_1$. The corresponding cut parameters $\mathcal{C}_i$ therefore possess no complementary information to $\mathcal{C}_1$. From now on, they are discarded during the CUTEVAL analysis. Out of the remaining parameters, $\mathcal{C}_2$ gives the best 2-dimensional $S/\sqrt{N}$, now called $(S/\sqrt{N})_2$. The result of the second step is a set of two selected cut parameters and a reduction of the remaining cut parameters to be analyzed.

In a third step, the optimization is performed in the three-dimensional space spanned by $\mathcal{C}_1 \otimes \mathcal{C}_2 \otimes \mathcal{C}_j$. Again, one selects another cut-parameter ($\mathcal{C}_3$) and discards several others. Equivalent steps are repeated until all parameters are either selected or discarded. This leads to a minimal set of n cut parameters yielding the best $S/\sqrt{N}$ achievable.

These parameters $\mathcal{C}_1..\mathcal{C}_n$ span an n-dimensional space. A point $\vec{\boldsymbol{x}}$ within this space defines a certain combination of cut values with corresponding values of S, N and $S/\sqrt{N}$. One can now maximize S for fixed values of N within this space. For each value N, this leads to a set of optimal cut values $\vec{\boldsymbol{x}}$.

One thus obtains values of $\vec{\boldsymbol{x}}_N$ for each tested value of N. The corresponding individual cut values $x_{i,\,N}$ (i.e. the projections of $\vec{\boldsymbol{x}}_N$ onto the individual cut parameters) have been fitted to $x_{i,\,fit} = a + b \cdot \log(N)$ for two ranges of N separately. These fits can be found in table D.12. They are based on the CUTEVAL mode using Monte Carlo simulated data only. The fits define a path $\vec{\boldsymbol{x}}_{\boldsymbol{fit}}(N)$ through the cut parameter space for all N. It can be transformed to $\vec{\boldsymbol{x}}_{\boldsymbol{fit}}(Q)$ via the variable transformation

$$Q \equiv \log N_0/N \ . \tag{7.4}$$

Here, $N_0 = 1.05 \cdot 10^9$ is the number of triggers and N is the CutEval parameter N. The variable Q is defined via equation 7.4. It is called *quality* or *event quality*. A cut on Q is now defined as the set of cuts on the individual parameters $\mathcal{C}$ defined by $\vec{\boldsymbol{x}}_{\boldsymbol{fit}}(Q)$.

Care has to be taken when interpreting the parameter N. N is an estimate for the number of residual background events after applying a cut on $\vec{\boldsymbol{x}}_{\boldsymbol{fit}}(Q(N))$. But $\vec{\boldsymbol{x}}_{\boldsymbol{fit}}(Q)$ is the result of fitting simple functions to a discrete set of points $\{\vec{\boldsymbol{x}}_{\boldsymbol{N}}\}$. As can be expected, not all these points lie exactly on the fitted path. Since N is now used to parameterize the fit, it does not need not be equivalent to the true residual number of experimental background events any more.

Since Q only depends on logical AND combinations of simultaneously applied cuts, it is considered as simpler (to understand) than a neural net output. On the other hand, since the CutEval combination of parameterized cut values offers more free parameters than a simple linear combination, it is considered more powerful than a straight forward discriminant analysis. More details on this procedure can be found in [103]. In particular the method of how to define and optimize $S/\sqrt{N}$ in cases where the Monte Carlo simulation does not describe the experiment accurately is discussed.

Before CutEval was run in this analysis, the zenith angle cuts were tightened. These pre-CutEval cuts were called level 4a cuts. The cut values were:

$$\theta_{ITER} = 95^\circ \tag{7.5}$$

$$\theta_{MPE} = 95^\circ. \tag{7.6}$$

After these cuts, experimental data is believed to contain already $\sim 10\,\%$ signal neutrino-induced events.

Altogether 130 parameters were fed into CutEval. The minimal set of optimal cut parameters found were the following five parameters. They are called level 4b cut parameters.

- $\Psi(ITER, LF)$: The space angle between the track from the line-fit and that from the iterative likelihood reconstruction. As can be seen from figure 7.8 (left), the results of the two reconstructions agree best for simulated signal data. The experimental distribution is still well described by the background simulation.

- $|S^{van}_{MPE}|$: The *vanilla smoothness* of the multi-PE reconstruction. The *vanilla smoothness* compares the distribution of hits projected onto the track with that of a perfectly homogeneous distribution in a similar way as a Kolmogorov-Smirnov test. $S^{van} \equiv -1/+1$ corresponds to scenarios where all hits are at the beginning/end of the track and $S^{van} \equiv 0$ when the distribution is perfectly homogeneous[1]. The cut is shown in figure 7.8 (right). Simulated signal has clearly better (smaller) smoothness values than background. Experimental data is at an intermediate stage, but is still dominated by background. Cutting on the absolute value of the smoothness has proven to be sufficient for this analysis, although background events with different signs of S^{van}_{MPE} correspond to different classes of background.

[1] Like in the case of "speed of the line-fit", the term "smoothness" is not chosen very luckily. Its absolute value is high when the hits are *not* distributed smoothly. The smoothness parameter thus measures the deviation from a smooth distribution. A name like "coarseness" would be more appropriate. But again: The name "smoothness" has been established and is used in this work.

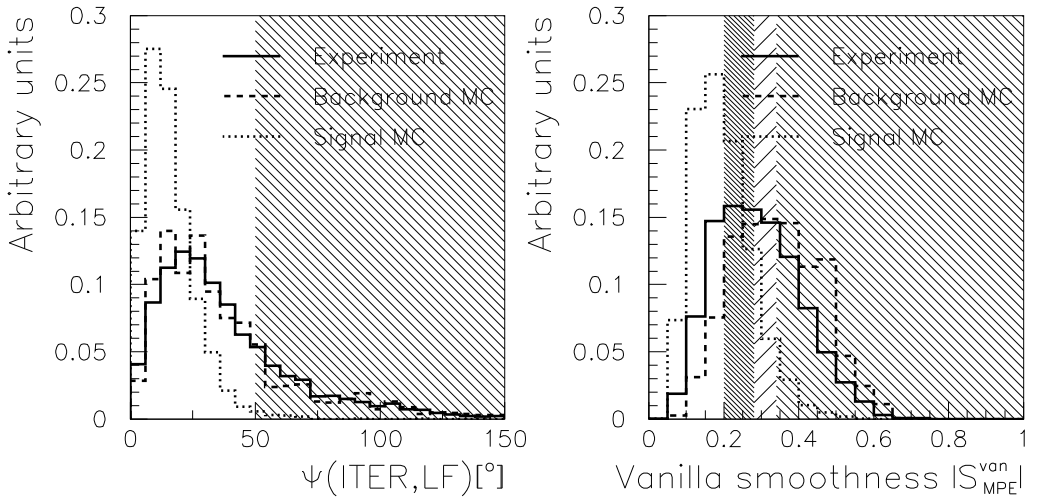

Figure 7.8: Data after cut level 3: Space angle between results from line-fit and iterative reconstruction $\Psi(ITER, LF)$ (left) and *vanilla* smoothness $|S^{van}_{MPE}|$ (right). Solid line: experimental data, dotted line: *nusim* signal simulation, dashed line: combined *basiev* and *CORSIKA* background simulation. Normal shaded area: removed by cuts for CutEval parameter $N = 100$, less intense shaded area: additionally removed for BG-10 sample, dark shaded area: additionally removed for BG-1 sample.

- $|S^{P_{hit}}_{ITER}|/(\theta_{MPE} - 90°)$: The ratio between the P_{hit} smoothness and the zenith angle from the multi-PE reconstruction. The P_{hit} *smoothness* is obtained from the *vanilla* smoothness by weighing the comparison distribution with the hit and no-hit probabilities of the optical modules (see section 6.4.3 how these probabilities are calculated). For the cut, the angle is shifted by 90° in order to measure the "distance" from the horizon (the boundary between signal and background region). The cut requires tighter smoothness values for horizontal events as compared to vertical ones. The distribution of this parameter is displayed in figure 7.9 (left). It shows a very nice separation between signal and background events. As with the other distributions after cut level 3, the experimental events are distributed similarly to the background events and only show a small signal content.

- $(N_{dir,\,MPE}(-15..75) - 2) \cdot L_{dir,\,MPE}(-15..75)$: The product of the number of direct hits and the direct length. The reduction of the direct hits by two was motivated by the fact that the two outermost direct hits are required to define L_{dir}. Additional information can thus only be provided by the additional direct hits in between. The corresponding distributions are shown in figure 7.9 (right). Signal events have clearly larger values of this parameter than background. In a dedicated analysis, this cut proved to be particular powerful against coincident muons from independent air showers [52].

- $\log(\mathcal{L}_{down,\,ITER}) - \log(\mathcal{L}_{up,\,ITER})$: During the minimization process of the reconstruction, likelihood values are calculated in the full parameter space. Even for events finally reconstructed as up-going, likelihood values for down-going directions are calculated. Both the best likelihood values in the down- and in the up-going

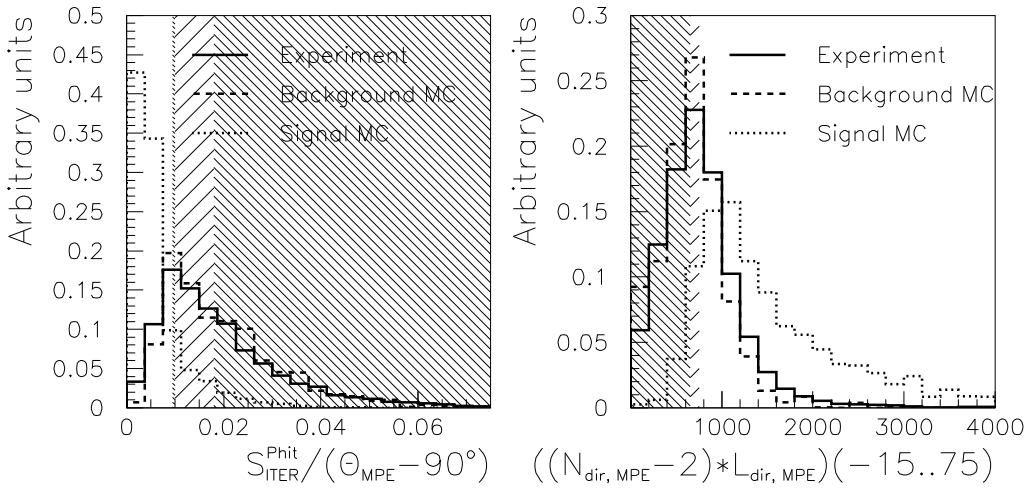

Figure 7.9: Data after cut level 3: Ratio between the P_{hit} smoothness and the reduced zenith angle $|S^{P_{hit}}|/(\theta_{MPE} - 90°)$ (left) and the product of the reduced number of direct hits and the direct length $(N_{dir}(-15..75) - 2) \cdot L_{dir}(-15..75)$ (right). Solid line: experimental data, dotted line: *nusim* signal simulation, dashed line: combined *basiev* and *CORSIKA* background simulation. Definition of shaded areas like in caption of figure 7.8.

hemispheres are stored (one of them being the best overall likelihood). The ratio of these two likelihoods gives an estimate of how much more likely the up-going track is with respect to a down-going track. Rather than cutting on this likelihood ratio, the cut is applied to the difference of the log-likelihoods. The parameter is shown in figure 7.10 (left). Signal clearly has higher likelihoods to be up-going than background events. Note that the difference is in log (likelihood), not in the likelihood parameter L defined in equation 6.9.

After selecting the "level 4b" cuts at the CutEval parameter $N = 10$, two residual classes of background were found by visually inspecting the remaining experimental events. For these, dedicated cuts were developed outside the CutEval regime:

- It was discovered that the few z_{cog} events remaining could be eliminated by a cut on the space angle between the $P_{hit}P_{nothit} \oplus MPE$ and the line-fit reconstruction at $\Psi(MPE, LF) < 35°$. It was double checked whether this cut could replace the $\Psi(ITER, LF)$ cut found by CutEval, but this was not the case. The $P_{hit}P_{nothit} \oplus MPE$ and the iterative reconstruction seem to contain complementary information. The parameter is displayed in figure 7.10 (right). The cut clearly removes a significant fraction of the background events, but only few signal events.

- A few seemingly coincident muons from independent air showers persisted. To reject them, a dedicated cut was developed: $R_{S,\,dir,\,ITER}$. It is the "radius" in the space spanned by the two smoothness flavors P_{hit} and *vanilla*, both taken from the iterative reconstruction and calculated for direct hits only. The cut was set at $R_{S,\,dir,\,ITER}(-15..75) \equiv \sqrt{S^{P_{hit}}_{dir,\,ITER}(-15..75)^2 + S^{van}_{dir,\,ITER}(-15..75)^2} < 0.55$. The

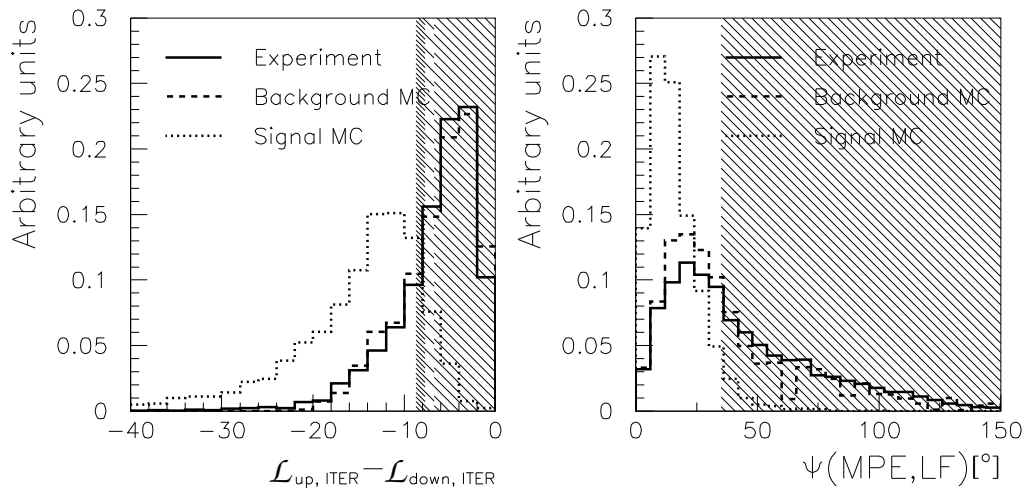

Figure 7.10: Data after cut level 3: (Left:) The difference between the best log (likelihood) in the down-going and the up-going parameter space $\log(\mathcal{L}_{down,\,ITER}) - \log(\mathcal{L}_{up,\,ITER})$. (Right:) Space angle between the $P_{hit}P_{nothit} \oplus MPE$ and the line-fit reconstruction results $\Psi(MPE, LF)$ Solid line: experimental data, dotted line: *nusim* signal simulation, dashed line: combined *basiev* and *CORSIKA* background simulation. Definition of shaded areas like in caption of figure 7.8.

cut is shown in figure 7.11 (left). Monte Carlo simulated background has larger smoothness radii than signal.

Both cuts were not determined by CutEval. Correspondingly the cut values were fixed for any value of the CutEval parameter N.

Figure 7.11 (right) shows the number of events for experiment, background and signal Monte Carlo simulations versus the quality parameter Q. With the definition of Q as given in equation 7.4, Q is only defined when the CutEval parameter N is defined. On cut levels prior to the CutEval regime this is not the case. In order to obtain Q for all processing levels, the definition of Q is expanded to

$$\begin{array}{ll} Q = \log(N_0/N_{BG-MC}) & \text{for cut-levels prior to cut level 4a} \\ Q = \log(N_0/N) & \text{for later (CutEval) cut levels,} \end{array} \tag{7.7}$$

where N_{BG-MC} is the number of Monte Carlo simulated background events. The separation between both areas is at cut level 4a, which corresponds to $Q = 5.4$, i.e. to a background suppression of $10^{5.4}$. The left part of the curves in the figure (up to $Q = 5.4$) thus represents the cuts up to cut level 4a. Here, the background curve is by definition a straight line. The right part shows the regime where the cuts were obtained from the CutEval fits. In that region, the background curve fluctuates. The experiment follows the background simulation on low cut levels (but has a slightly higher passing rate), turns over and follows the signal simulation for tight cut values.

There was no obvious solution as how to include the two "post-CutEval" cuts into this figure. Since they are applied to all data processed after level 3 cuts, it was decided to apply them after cut level 4a, but prior to CutEval in that figure. This causes the downward bend of all data curves between the points calculated at $Q = 5.4$ (cuts not applied) and the next one at $Q = 5.8$.

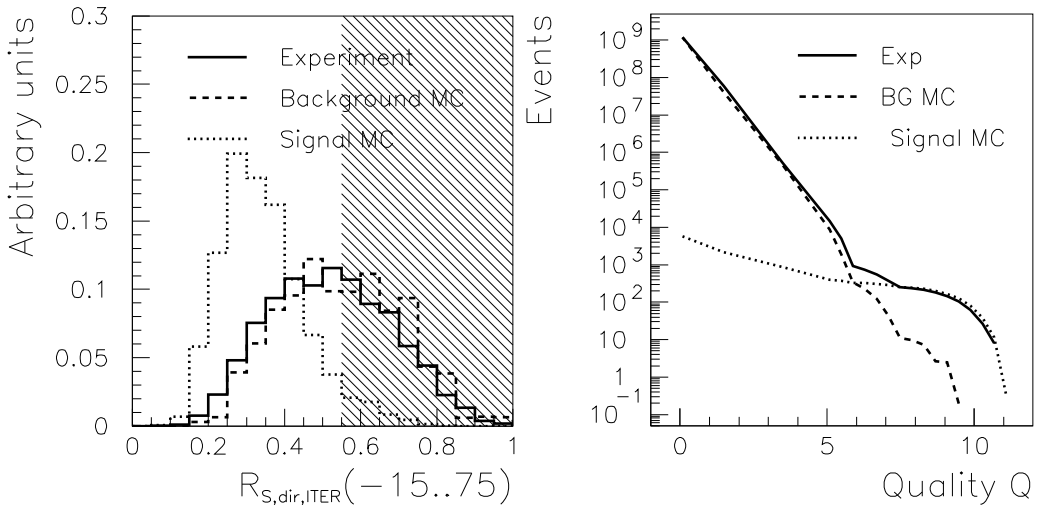

Figure 7.11: (Left:) Data after cut level 3: The "smoothness-radius" $R_{S,\,dir,\,ITER}$. Definition of shaded areas like in caption of figure 7.8. (Right:) Number of events versus quality parameter Q. Curves defined by cut levels 0 (trigger),1, 2, 3 and 4a (at $Q = 0$, 1.4, 3.4, 5.0 and 5.4) and by further points calculated in steps of $\Delta Q = 0.4$. Solid line: experimental data, dotted line: *nusim* signal simulation, dashed line: combined *basiev* and *CORSIKA* background simulation.

7.2 Final Data Samples

7.2.1 Sample Definitions and Properties

The level 4 cuts can now be set according to the CutEval parameterization and the additional cuts. The details of the CutEval parameterization are given in appendix D.4. The standard cut for the atmospheric neutrino analysis is set at $N = 10$ ($Q = 8.1$; for a list of the corresponding cut values, see table D.13). The resulting experimental sample consists of 223 neutrino candidates. This corresponds to a total passing rate of $0.17 \cdot 10^{-8}$ for this analysis. The numbers for background (*basiev* and *CORSIKA*) and atmospheric signal MC are: $0.59 \cdot 10^{-10}$ and 4.2 %. The selected experimental sample is the default sample for the atmospheric neutrino analysis. In figure 7.12 (left), the zenith angle distribution of that sample is compared to the expectations from Monte Carlo simulations. The simulated neutrino signal in that figure is corrected for neutrino oscillations with parameters $\Delta m^2 = 2.5 \cdot 10^{-3}\,\mathrm{eV}^2$ and $\sin^2(2 \cdot \theta) = 1.0$, see section 2.9. The agreement between simulated atmospheric neutrinos and the experimental data sample is remarkably good.

In addition to the default sample "BG-10", two further samples were defined: At CutEval parameter $N = 100$ ($Q = 7.1$), the "BG-100" sample is derived from relaxed cuts. It contains 369 experimental events. The corresponding passing rates are $0.28 \cdot 10^{-8}$, $0.29 \cdot 10^{-9}$ and 5.1 % for experiment, simulated background and simulated signal respectively. The zenith angle distribution of events with this selection can be seen in figure 7.12 (right). In comparison to the left figure, two features are evident. On the one hand, the experimental distribution contains a significantly larger fraction of events from horizontal directions. On the other hand, the description of the experimental data by the

sum of simulated background and signal is slightly worse. The first observation is mainly caused by the relaxed cut on $\mathsf{L}_{up,ITER} - \mathsf{L}_{down,ITER}$. This cut, shows a strong zenith angle dependency, which is expected from its definition. The poorer description of experiment by simulated data is due to statistical fluctuations in the background simulation. The bin at $-0.6 \leq \cos(\theta_{MPE}) \leq -0.5$ for example contains more simulated background events than expected, while the neighboring bins contain fewer events than expected. Furthermore, the absolute number of background events is slightly too low. This is related to the question of the absolute background normalization, which is addressed in appendix D.6.

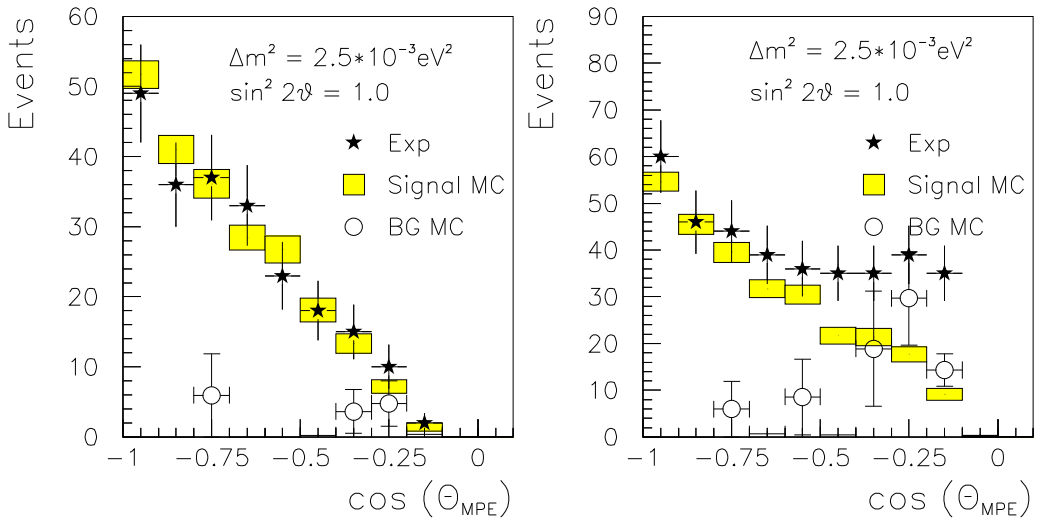

Figure 7.12: Final event selection: Zenith angle distribution after BG-10 cut selection (left) and after BG-100 selection (right). Stars: Experiment, boxes: signal, open circles: background simulation.

"BG-1" at CutEval parameter $N = 1$ ($Q = 9.1$) is a third sample obtained by tightening the cuts. It leaves 138 experimental data events (passing rate: $0.11 \cdot 10^{-8}$). The passing rates of simulated background and signal are: $0.72 \cdot 10^{-11}$ and 2.9 % respectively. The tables D.16 to D.18 list all experimental events which are contained in any of the three finally extracted samples. Given are the times of the events, their reconstructed directions and energies and which samples they are contained in. Further samples can be defined for any other value of CutEval parameter N.

The agreement between experimental and simulated data is good ("BG-100" sample) or even very good ("BG-1" and "BG-10") with respect to all (cut) parameters tested (`HDIFF`$\leq$ 20 or 10 %, [66]). Many of the parameters tested were "unbiased", i.e. they have not been cut upon. This agreement indicates that the samples indeed are neutrino-rich.

The change of the reconstructed zenith angle distribution of experimental events with cut level is presented in figure 7.13 (left). At trigger level it is dominated by well reconstructed down-going atmospheric muons. At intermediate stages, only the misreconstructed atmospheric muon events remain. At final cut levels, the samples are dominated by atmospheric neutrino-induced muon events in the up-going hemisphere. While the total flux of atmospheric neutrinos is isotropic to within a factor of two [155], the spectrum of experimental events on cut level 4 is dominated by almost vertical events.

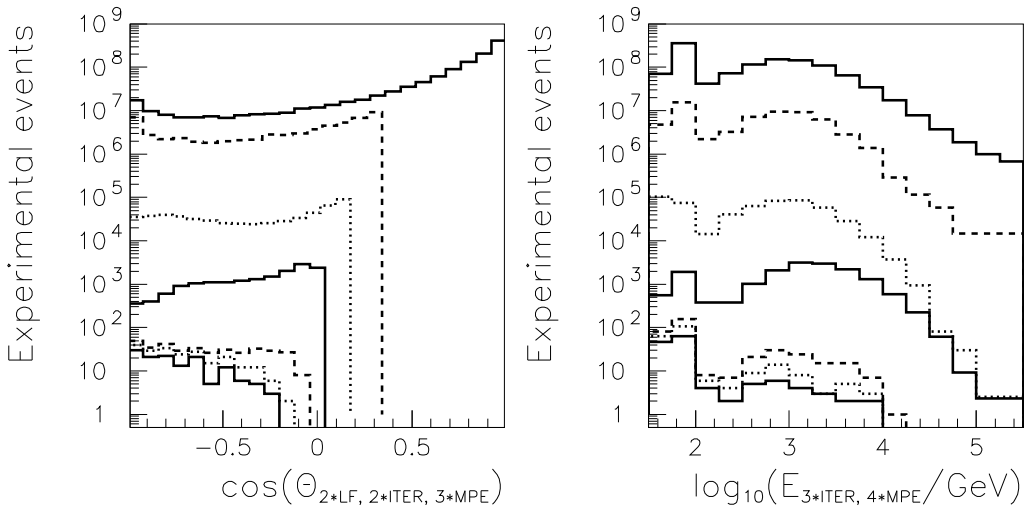

Figure 7.13: The reconstructed zenith angle (left) and reconstructed muon energy (right) for various cut levels. From top to bottom: Trigger level, cut level 1, cut level 2, cut level 3, final samples BG-100, BG-10 and BG-1. The reconstructions chosen in this figure were always the best ones available on the corresponding cut level. Since the energy reconstruction was not performed for the line-fit or likelihood reconstruction, later reconstructions were used for the two upper-most curves here, as compared to the zenith angle distributions.

This is due to the higher sensitivity of the long and slim AMANDA-B10 detector towards vertical events.

The right frame of figure 7.13 shows the reconstructed energy of the events passing the various cut levels. Muons with energies $10\,\mathrm{GeV} \leq E_\mu \leq 100\,\mathrm{GeV}$ are minimally ionizing. The difference in their light output is so small that they are de-facto indistinguishable. The peak at $E \leq 100\,\mathrm{GeV}$ is an artifact of the reconstruction. The reconstruction (arbitrarily) reconstructs all events as to have energies of 100 GeV when their light output can be described with the hypothesis of minimally ionizing particles. Only events with a smaller light output (due to stochastic fluctuations) are reconstructed as to have lower energies.

One notices a slight change in the shape of the curves of figure 7.13 (right): Energies of $1\,\mathrm{TeV} \leq E_\mu \leq 2\,\mathrm{TeV}$ are reconstructed most efficiently. In this range, the total passing rates (from trigger) are approximately a factor of two higher than the average passing rate for the full simulated energy range ($10^{1.0}$ to $10^{5.5}$ GeV). The reason is that muons in the $\mathcal{O}(1)\,\mathrm{TeV}$ energy range best fulfill the assumptions of the reconstruction and of the cuts. Muons of lower energies are poorly approximated by infinitly long tracks. Muons of higher energies cause so much light in the detector that their hit topologies show a certain level of sphericity and the events are then stronger removed by the anti-shower cuts (see section 7.1.4).

Though neutrinos with energies as low as 10 GeV have been simulated, low energy events are largely suppressed. The energy thresholds of this analysis are at $E_\mu = 45\,\mathrm{GeV}$ and $E_\nu = 64\,\mathrm{GeV}$ (BG-1), at $E_\mu = 44\,\mathrm{GeV}$ and $E_\nu = 63\,\mathrm{GeV}$ (BG-10), or at $E_\mu = 43\,\mathrm{GeV}$ and $E_\nu = 63\,\mathrm{GeV}$ (BG-100)[2]. Here, *threshold* is defined such that 95 % of the simulated

[2]Please see appendix E for the convention which defines the term "muon energy" for this work.

signal events passing the corresponding selection criteria have larger true energies (figure 7.13 (right) shows reconstructed – not true energies). The range of 45 GeV muons in ice is $\sim 220\,\mathrm{m}$, see equation 8.8. As a comparison: The height of AMANDA-B10 is $\sim 500\,\mathrm{m}$. This explains why low energy neutrino-events are difficult to reconstruct: The corresponding muon tracks are too short to be well reconstructed.

High energy neutrinos ($E > 10\,\mathrm{TeV}$) also do not pass the cuts very efficiently. Reason is that they emit so much light that the hit-topology is very spherical compared to a minimally ionizing muon. So upper energy limits of this analysis are at $E_\mu = 2.0\,\mathrm{TeV}$ (all samples) and $E_\nu = 3.7\,\mathrm{TeV}$ (BG-1 and BG-10) or at $E_\nu = 3.6\,\mathrm{TeV}$ (BG-100). The term *upper energy limit* is defined correspondingly to *threshold*: only 5 % of the signal events passing have larger energies than the *upper energy limit*. The range of 2.0 TeV muons in ice is $\sim 4.4\,\mathrm{km}$.

The average (mean) event energy is dominated by the tail of high energy events. The typical event energy is therefore measured by the median energy of the simulated events. It is at $E_\mu = 0.22\,\mathrm{TeV}$ (all samples) and $E_\nu = 0.32\,\mathrm{TeV}$ (BG-1 and BG-100) or at $E_\nu = 0.33\,\mathrm{TeV}$ (BG-10). The range of 0.22 TeV muons in ice is $\sim 0.94\,\mathrm{km}$.

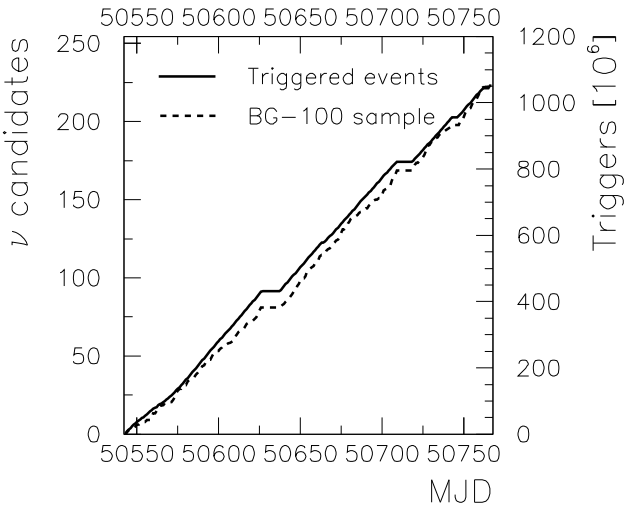

Figure 7.14: Number of events versus modified julian day number. Dashed line: triggered events passing the run and event selection, see section 7.1.1. dotted line: neutrino candidates obtained from the BG-10 selection.

The accumulation of the neutrino candidate events over time is shown in figure 7.14 for the BG-10 sample. The other curve in that figure is the number of triggers passing the run and event selections as defined in section 7.1.1. The horizontal axis is given in modified julian days (MJD can be transformed to the day number of the year 1997 by subtracting 50448.) In this integral representation, a slight deficit of neutrino candidates in the first half of the season as compared to the second half can be seen.

This effect appears more prominent than it is. It is dominated by the period MJD 50595–50608. This period corresponds to runs 707–738, i.e. a period where almost all runs taken passed this work's run selection, see tables D.4 to D.8. During these 14 days, only five neutrino candidate events were found, whereas 16 were expected from the year average. The chance probability to have 5 or less events when 16 are expected is $1.38 \cdot 10^{-3}$ from Poisson statistics. After run selection, but before dead-time correction, the life-time of the detector was slightly larger than 175 days, see section 4.1 and table D.9. There are 162 (correlated) possibilities to select a continuous period of 14 out of 175 days. The probability to observe at least one continuous 14 day period with 5 or less events has been simulated to be 8.8 %.

Another time dependency which was analyzed is the time differences between the detection of neutrino candidate events. When correcting for run selection effects, these time differences agree with Poisson distributions. From the timing information, there is hence no indication of systematic contaminations in the selected data set.

7.2.2 Background Estimations

As mentioned, the CutEval parameter N is just an estimator for the background. It can only be as accurate as the background simulation which CutEval was based on. It is in general *not* a measure of the true background. The background is instead estimated from various methods. These are summarized (including numbers for the "BG-10" sample) in the following:

- Residual simulated background events. As it is very common in astro-particle physics, the great problem in the case of AMANDA is the lack of sufficient simulated air shower statistics for final cut levels. This most straight forward background estimation is thus not very accurate here. Moreover, the normalization of the background is debatable, see section D.6. Nevertheless, this method can be used and gives an estimate of $16^{+4}_{-8}(syst.) \pm 8(stat.)$ events, see table D.15.

- The CutEval parameter N. This gives an estimation of 10 events.

- The "excess" in experimental data as compared to the signal expectation, see table D.14. This gives a value of -1.0 ± 1.7 events.

- "N-1 Cuts": When applying all but one cut, one expects background to appear in the background region of the cut not applied. One can then obtain correction factors for the background simulation by

$$\eta = \frac{N^{BG-region}_{Experiment} - N^{BG-region}_{Sig-MC}}{N^{BG-region}_{BG-MC}} \ . \tag{7.8}$$

  The assumed background in the signal region is $\eta \cdot N^{Sig-region}_{BG-MC}$. This is performed for every level 4 cut and yields a combined estimate of 14 ± 4 background events.

- z_{COG} shape: At cut level 3, the background is dominated by the z_{COG} class of background events. One can parameterize the experimental z_{COG} distribution on a lower cut level. At the final cut level one then fits the z_{COG} distribution by the signal expectation plus the previous z_{COG} background parameterization times a normalization factor. This normalization factor then allows a background estimation for this specific class of background. This estimation is compatible with zero z_{COG} background with an upper limit of 35 events.

- Visual inspection: This method should not be used to place cuts, but can be used to estimate background. Efficiencies were determined beforehand via a blind analysis performed by several persons. The two persons who could best separate simulated signal and background performed the visual inspection of experimental events. Background was estimated to 13^{+23}_{-9} events.

More details on these individual methods can be found in [45]. In summary, the various background estimations agree reasonably well. Though each single one of them is inappropriate as a sole estimate, the combination of all of them are convincing. For the "BG-10"sample, the background is estimated at $\sim$ 15 events (7 % of the 223 events) or can be limited to 15 % of the events. In case of the "BG-100" sample, the number of atmospheric muon background events is estimated to be approximately 100. The tighter "BG-1" sample has a background contamination of 3–5 events.

7.2.3 Sample Motivations

One of the great challenges in the field of neutrino astronomy is the determination of the absolute sensitivity of the detectors. The first difficulty is that open water/ice Cherenkov neutrino telescopes use their natural environment as an inherent part of the detector. Hence there is no possibility to calibrate all detector components in a laboratory. Furthermore, there is no calibration beam available. This situation is similar to Cherenkov air shower telescopes. But in that case, the crab nebula can be used as a standard candle for cross-calibrations among the various experiments. What comes closest to such a standard candle for neutrino telescopes is the flux of atmospheric neutrinos. It offers the possibility for cross-calibrations among neutrino telescopes. It is also reasonably well understood from theory. This allows to investigate systematic effects of individual experiments (like AMANDA-B10).

Only when the flux of atmospheric neutrinos is understood, it is possible to draw absolute conclusions about the flux of extraterrestrial neutrinos. This is the reason why the point source search presented in sections 10 and 11 is based on an atmospheric neutrino analysis: In this analysis, the comparison to atmospheric neutrino predictions offers a handle on the absolute sensitivity and its uncertainties. A comparable feature is not available for a different AMANDA-B10 point source analysis [251], which does not try to separate atmospheric neutrinos.

The data set dominantly discussed so far (the "BG-10" set) is used as the one defining an atmospheric neutrino selection. It is supposed to represent a good balance between a high atmospheric neutrino passing rate and a low atmospheric muon contamination.

The "BG-1" sample has only a very small background contamination. It has been used for systematic cross checks as an almost "background-free" sample. It will only be of minor importance for the remainder of this work.

The default sample for the neutrino point source search introduced in section 10 of this work is the "BG-100" sample. In such a point source search, atmospheric muon and atmospheric neutrino events are both background events. This combined background can be considered approximately isotropic in the vicinity of a potential point source. Within such a vicinity (or search cone), relaxed cuts can significantly enhance the number of signal events, while the combined background is only increased slightly. A potential gain of very few neutrinos from an astrophysical point source more than compensates the challenge of an increased diffuse background.

7.3 Systematic Uncertainties

A first simple systematics check is seen in figure 7.11 (right): At any cut level, the experimental data follows the sum of signal and background simulated data. There seems to be a difference between the passing rates of simulated background and experimental data. This topic is addressed in appendix D.6. Since it does not influence the uncertainties in the signal regime, it is of lesser importance for the systematic uncertainties on the atmospheric neutrino prediction.

Figure 7.15 shows the reconstructed zenith angle versus the reconstructed azimuth angle of the "BG-10" sample. A dedicated analysis did not find any indications for the existence of significant clusters or voids in this distribution. This leads to the conclusion that the detector (and the reconstruction) are not severely malfunctioning with respect to angular acceptance.

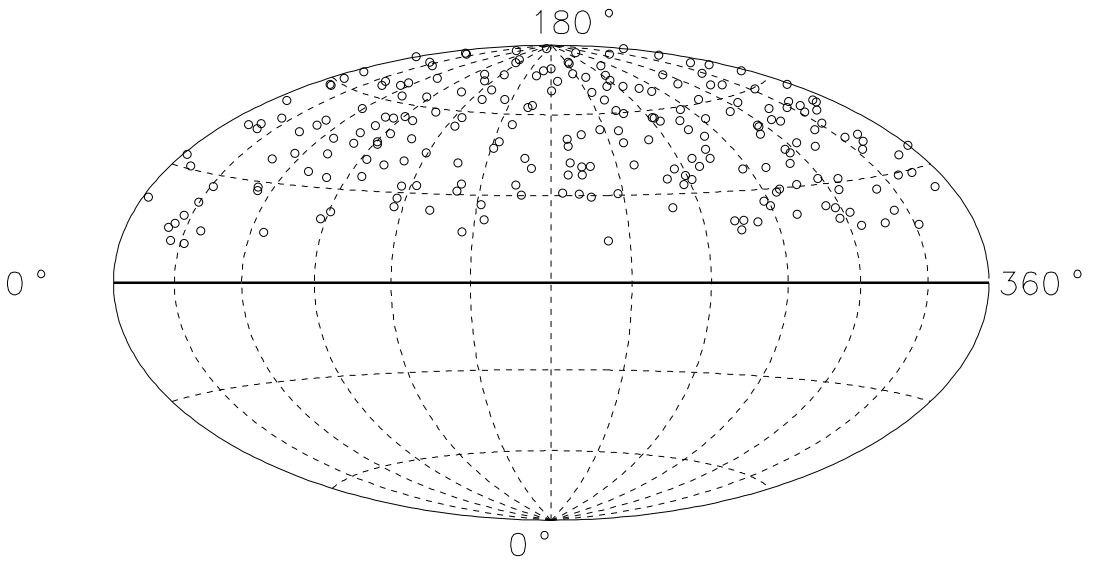

Figure 7.15: The celestial distribution of the BG-10 sample in detector coordinates. The projection used is the Hammer-Aitoff equal area projection, see appendix A.2.4.

Both these tests do not allow any quantitative estimation of the systematic uncertainty. A more detailed investigation is thus needed. Quantitative statements in the following discussion of individual uncertainties all refer to the "BG-10" samples. The other two samples will be discussed during the summary of the systematic uncertainties in section 7.3.11.

7.3.1 Neutrino Flux Predictions

A recent review investigated the theoretical uncertainties on the present neutrino flux predictions [96]. The conclusion was that the absolute uncertainty is $\lessapprox \pm 30\,\%$ (mostly arising from uncertainties on the Kaon production), but that the actual calculations differ by less than $\pm 10\,\%$. The uncertainty on the shape of the energy distribution is estimated to be around $\pm 5\,\%$ by the author of that review. Here, the total uncertainty due to neutrino flux predictions is estimated to be up to $30\,\%$.

7.3.2 Neutrino Interaction Cross Section

As stated in section 4.2.1, two independent neutrino simulation codes (*nusim* and *nu2mu*) are used in AMANDA. Both are based on the same theoretical flux model. The difference between the two simulations allows to estimate the effect of different simulation techniques and interaction models to less than $\pm 6\,\%$ in absolute event numbers. Shapes of distributions agree very well with each other.If one would compare even more interaction models, one might see a slight increase in the differences between the models. The neutrino flux uncertainty due to different interaction models is thus estimated conservatively to be less than $10\,\%$.

7.3.3 Neutrino Oscillations

AMANDA Monte Carlo simulations do not include neutrino oscillations at present (see section 4.2.1). But with the true track information available in the simulation, it is simple to include the effect a posteriori into the analysis by calculating the neutrino flight path L. From the geometry of a triangle, it follows that:

$$\begin{aligned} &L^2 = (R_\oplus + h)^2 + (R_\oplus - d)^2 - 2 \cdot (R_\oplus + h) \cdot (R_\oplus - d) \cos(\gamma), \text{ where} \\ &\gamma \equiv 180^\circ - \alpha - \beta, \text{ with} \\ &\alpha \equiv 180^\circ - \theta, \text{ and} \\ &\sin(\beta) \equiv \sin(\alpha) \cdot \frac{R_\oplus - d}{R_\oplus + h} \end{aligned} \tag{7.9}$$

Here, $R_\oplus = 6378\,\text{km}$ is the radius of the earth, $d \approx 1.75\,\text{km}$ is the average depth of the AMANDA-B10 array and θ is the zenith angle of the incoming neutrino. The average height above ground of the neutrino production vertex in the atmosphere h is given by a broad distribution. The neutrinos from pion and kaon decay peak at 15 km. Neutrinos from muon decay are roughly equally distributed at lower altitudes but give softer spectra [100]. In this work, $h = 12\,\text{km}$ is taken as an average value for all neutrinos.

Δm^2	$\sin^2(2\theta)$	Sample BG-100	Sample BG-10	Sample BG-1
No oscillation		285.9	236.9	163.0
$1.6 \cdot 10^{-3}\,\text{eV}^2$	0.90	280.4 (-1.9 %)	231.8 (-2.2 %)	159.5 (-2.2 %)
$1.6 \cdot 10^{-3}\,\text{eV}^2$	1.0	279.7 (-2.1 %)	231.2 (-2.4 %)	159.1 (-2.4 %)
$2.5 \cdot 10^{-3}\,\text{eV}^2$	1.0	271.9 (-4.9 %)	224.0 (-5.4 %)	154.0 (-5.5 %)
$3.8 \cdot 10^{-3}\,\text{eV}^2$	1.0	257.7 (-9.9 %)	211.1 (-10.9 %)	145.0 (-11.0 %)

Table 7.1: Oscillation effects on level 4 passing rates. Given are the absolute predicted event numbers for the three selected samples for the case of no oscillations and at different values of Δm^2 and $\sin^2(2\theta)$. The relative changes between the no-oscillation and oscillation cases are given in parentheses. The Δm^2 and $\sin^2(2\theta)$ values shown correspond to the preferred value from Super-Kamiokande and to the values limiting their central 90 % confidence interval [134].

Quantitative results are summarized in table 7.1. Since the BG-100 sample contains relatively more horizontal events than the other samples, it is least affected by neutrino

oscillations. Depending on the selected sample, AMANDA atmospheric neutrino expectations are reduced by 4.9 % to 5.5 % due to oscillations. The uncertainty on this reduction ranges from $^{+3.0\,\%}_{-5.0\,\%}$ (for the BG-100 sample) to $^{+3.3\,\%}_{-5.5\,\%}$ (for the BG-1 sample) at the 90 % confidence level of Super-Kamiokande. (It is given by the differences between the third and the first or fourth row in table 7.1.) For atmospheric neutrinos, the uncertainty on the oscillation effect is dominated by the uncertainty on Δm^2. It should be noted that for astrophysical neutrinos, the uncertainty on the oscillation effect is only given by the uncertainty of the oscillation angle. The uncertainty on Δm^2 is irrelevant due to the long flight path L.

7.3.4 Muon Propagation

Below a muon energy of 600 GeV, ionization dominates the muon energy loss. This energy range is accessible to accelerators and the corresponding cross sections are reasonably well known. Above 600 GeV, radiative processes like bremsstrahlung and pair production dominate. Since accelerators data is energy-limited, the uncertainties are much larger in this regime. Comparisons between different muon propagation codes applied to atmospheric muons in AMANDA and in the Fréjus experiment have been performed in [78], for the BAIKAL experiment in [222]. Comparisons of *propmu* and *mudedx* for neutrino-induced muons have been performed in [83]. Uncertainties of up to 25 % were found for final event samples. The uncertainties on the muon propagation are thus considered to be 25 %.

7.3.5 Optical Properties

A specific challenge for AMANDA is the determination of the optical properties of the South Polar ice cap. The bulk ice has been studied in detail in [201], using light emitters of various technology deployed in the ice. In [126], it has been shown that changing from one set of global parameters for the bulk ice to a simulation including ice layers, the change in predicted absolute event rates is $\sim$ 15 %. The effects are larger for background than for signal events. The uncertainty with the improved ice layer Monte Carlo simulation is thus estimated to be less than 15 %. The new simulation describes several experimental distributions better than the old one - especially the hit frequencies of the individual modules and the z_{COG} distribution.

In contrast to the bulk ice, the re-frozen ice in the AMANDA holes (hole ice) is less well understood. The fast re-freezing process is very different from the adiabatic millenia-long process during which the bulk ice had formed. A video camera deployed in 1997/1998 showed very strong scattering in the hole ice, but questions arose whether the camera was operating properly. Recent studies of the angular OM sensitivities [184] corrected the combined effects of scattering hole ice just below the optical module and the angular sensitivity of the optical module. This lead to a new model, which is discussed in sections 4.2.4 and 7.3.6. With the new model, the combined error (including bulk ice, ice layer and hole ice uncertainties) should be less than 30 % (with respect to absolute neutrino numbers) and the remaining uncertainties should not strongly affect distribution shapes any more.

7.3.6 OM Sensitivity

The individual components of the absolute sensitivity of the optical modules can be measured in the laboratory. The combined transmissivity of pressure sphere glass, optical gel and PMT glass has recently been re-measured [224]. The result was that the simulations used for AMANDA-B10 so far (also for this work) underestimate the number of photoelectrons by 37 %.

The PMT specific properties are the "quantum efficiency" (fraction of photons that yield a photoelectron) and the "collection efficiency" (fraction of photoelectrons that hit the first dynode). They are measurable in the lab prior to deployment. But the corresponding data is not available for AMANDA-B10. Furthermore, aging effects of the PMT or of the gel inside the OM, temperature or pressure effects could alter in situ properties from those measured in the laboratory.

An analysis of the absolute OM sensitivities deployed in the ice showed that the uncertainties on this parameter could be large enough to *reduce* predicted neutrino fluxes by 40 % [43]. This is exactly the opposite effect of what is expected from the transmissivity measurements. This lead to another investigation, this time of the angular sensitivities of deployed OMs [184]. It has been described in slightly more detail in section 4.2.4. It confirmed that the OM sensitivities were overestimated by approximately 40 % for upward moving muons. Since the absolute and angular OM sensitivities are closely related, these two in situ analysis are in nice agreement. But both these analyzes could only determine the combined effects of optical parameters of the ice, OM transmissivities and PMT efficiencies. It thus seems that wrong assumptions on the optical properties, the quantum and the collection efficiency of the PMT over-compensated the underestimation of the OM transmissivity.

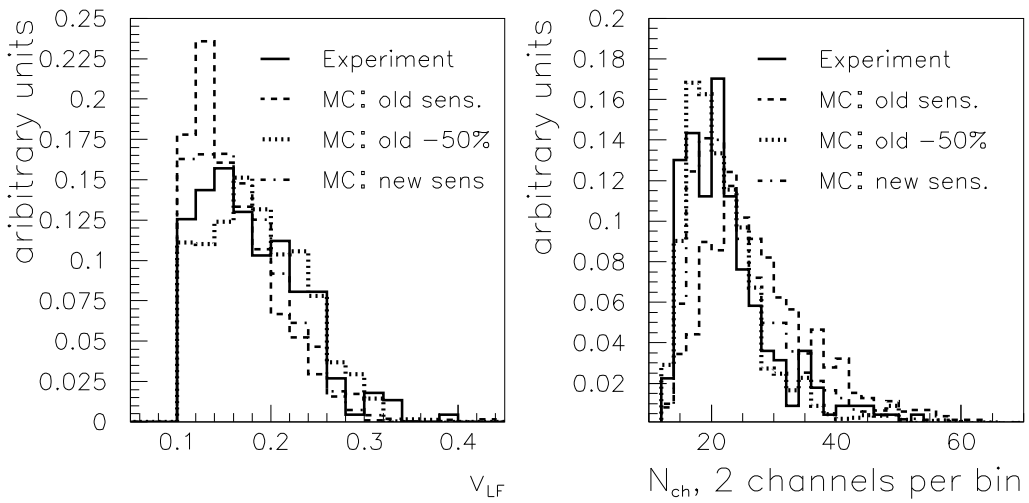

Figure 7.16: Final event selection: v_{LF} (left) and N_{ch} (right) for various OM sensitivities. Solid line: experiment; dashed line: simulation with old hole ice/OM sensitivity model; dotted line: simulation with old model but OM sensitivity reduced by 50 %; dash-dotted line: simulation with new hole/ice OM sensitivity model. All data: BG-10 selection.

A new hole ice/angular sensitivity model was derived from the angular sensitivity analysis. That model can be considered a correction factor for the combined effect of wrong optical parameters, transmissivities and efficiencies. That model contained angular-dependent corrections on the OM sensitivity of $\sim -40\,\%$. In figure 7.16, it is compared to the experiment as well as to the old ice/OM sensitivity model with standard and a 50% reduced OM sensitivity for the BG-10 selection. For both parameters shown (speed of the line-fit v_{LF} and number of hit channels N_{ch}), the new model describes the experiment better than the old model. The simulation with a 50% reduced OM sensitivity in the old model seems to overcompensate previous errors. Though the new model is not perfect, it significantly improved the description of experimental data by signal simulation for level 4 data. In particular the three previously problematic distributions are described much better: the speed of the line-fit v_{LF} (already shown in figure 7.1 (right)), the number of hit channels N_{ch} (already shown in figure 7.2 (right)) and the number of direct hits N_{dir} (already shown in figure 7.3 (right), but not shown in figure 7.16). Furthermore, the absolute normalization of event numbers is in much better agreement. This is the reason why the new hole ice/angular sensitivity model was used for the simulation of the signal data for this work, see section 4.2.4. As mentioned in that section, CPU limitations prevented the simulation of large background statistics with this model.

When using this new model, the remaining uncertainty on the absolute OM sensitivity should effect neutrino predictions by less than 30 %.

7.3.7 Hardware Simulation

Changes in the simulation of the detector hardware can affect the predicted detector performance. In particular, the accuracy of modeling the event trigger and individual OM properties, such as pulse-shapes, relative gains and thresholds may affect the results [126]. In a dedicated test it has been shown that a 30 % systematic error in the description of the thresholds of the surface electronics can lead to a change on the predicted flux of maximally 15 % [71].

An estimation of the total size of the hardware simulation errors can be achieved by comparing present and past (2 years old) hardware simulations. Differences on trigger level can reach up to 40 % for neutrino simulations. At final cut levels the differences have decreased to $\sim$ 20 %. Interestingly, these differences partly cancel with changes in the ice simulation. After improving the accuracy in both fields (hardware and ice simulation), the event numbers agree well between the old and the new simulation. The difference is only 3 % for neutrino events simulated with the generator *nu2mu* and less than 5 % for those generated with *nusim*. No strong effects are visible in the shapes of characteristic distributions. The absolute neutrino-flux uncertainty from the detector simulation is estimated to be less than 20 %.

7.3.8 Timing and Geometry Calibrations

As mentioned in section 5, three further calibrations exist for the AMANDA array: Timing, amplitude and geometry calibration. Uncertainties in the geometry calibration can be directly translated to timing calibration uncertainties. The combined uncertainties are

estimated to less than 10 ns. It has been shown that event rate uncertainties due to such timing uncertainties are below 5 %, see [38] and sections 5.1 and 5.2. Distribution shapes are also not affected by these timing uncertainties.

7.3.9 Amplitude Resolution

The amplitude measurement has a larger uncertainty: $\sim 35\,\%$, see section 5.3. The amplitude information is used during the hit-cleaning, for the multi-PE reconstruction and for the $P_{hit}P_{nohit}$ reconstruction and therfore also for the $P_{hit}P_{nothit} \oplus MPE$ reconstruction. The $P_{hit}P_{nothit} \oplus MPE$ can be compared to the normal reconstruction, showing that the effect of using amplitudes is small with respect to event rates or distribution shapes. The uncertainty on the neutrino event rates due to amplitude measurement uncertainties is therefore considered to be $< 5\,\%$. Distribution shapes should not be affected by these uncertainties.

7.3.10 Peaks in z_{COG}

The parameter z_{COG} shows a triple peak structure in experiment after cut level 2 processing which is not fully reproduced in the simulation, see section 7.1.4. From various investigations, it is assumed that the peaks are mainly caused by (un-simulated) details of the vertical ice structures, perhaps in combination with electronic artifacts [41,45,83]. The question thus arises, whether the simulation can describe experimental data on neutrino level, when it cannot correctly describe experimental data after cut level 2.

The answer is: "Yes it can": Experimental data after cut level 2 is dominated by those 0.04 % of the background events which are the most difficult ones to reconstruct or simulate. Experimental data after cut level 4 in contrast is dominated by those 4 % of the signal events, which are best reconstructed and simulated.

To double-check the description of experimental data with the signal simulation, down-going data was taken. From trigger to cut level 4 (up-down inverted cuts), down-going experimental data could well be described with down-going signal simulation. In particular, no z_{COG} triple-peak structure appeared. The other distributions were also in good agreement and the passing rates agreed. The agreement was not expected to be so good, since (experimental) down-going atmospheric muons are by far not as isotropic or homogeneous as (simulated) down-going atmospheric neutrinos. Nevertheless, this test shows that there is no significant problem contained in the simulation of the neutrino samples. A similar conclusion is drawn from the estimation of the z_{COG}-background in the final data samples, see section 7.2.2. Uncertainties for signal due to the unexplained z_{COG} effects are hence considered small ($\leq 5\,\%$) in comparison to the other systematic uncertainties.

7.3.11 Summary of Systematic Uncertainties

To summarize the systematic uncertainties: The shapes of characteristic distributions are mostly well understood. A few distributions depend critically on the OM sensitivity (and hole ice model). But since they are in good agreement between new Monte Carlo signal simulation and experiment, the residual uncertainty on the OM sensitivity (and hole ice model) seems to be small. Quadratically adding the above mentioned uncertainties leads

to a total systematic uncertainty of 63 %. Other important systematic uncertainties than those mentioned above have not been identified or even quantified yet. Nevertheless they can be expected. The good agreement between absolute numbers in experiment and atmospheric neutrino simulation can hint either at over-conservative error estimations or at a cancellation effect between the dominant errors.

The above statements were made for the "BG-10" sample. But they are also true for the "BG-1" sample. In case of the "BG-100" sample, a significant fraction of the experimental events ($\sim 30\,\%$) are atmospheric muons events. Correspondingly, distributions of experiment and simulated signal data do not agree any more. A few parameters are not correctly described by the background simulation on high cut levels, see for example the discussion of z_{COG} in section 7.1.4. For the many other parameters, experimental data of the "BG-100" sample is well described by the sum of simulated atmospheric neutrinos and muons. The prediction of the absolute passing rates ($\sim$ 270 neutrinos predicted by the simulation and $\sim$ 100 muons predicted by CutEval) is in better agreement with experimental data (369 events) than expected. The systematic uncertainties for this sample are equivalent to those for the "BG-10" sample; at least in a first approximation. Therefore the absolute rate prediction on the atmospheric neutrino content is again estimated to be correct to 63 %.

No.	Parameter	Uncertainty [%]	Remarks
1.	Flux prediction	30	Theoretical uncertainties
2.	ν-interaction cross section	10	Different models
3.	ν-oscillations	$^{+3.3}_{-5.5}$	Uncertainty on Δm^2
4.	Muon propagation	25	Software comparison
5.	Optical parameters	30	AMANDA measurements
6.	OM sensitivity	30	AMANDA analysis
7.	Hardware simulation	20	AMANDA analysis
8.	Timing and geometry calibration	5	AMANDA analysis
9.	Amplitude resolution	5	Estimation
10.	Neutrino-z_{COG} events	5	Below sensitivity
	Combined	63	Quadratic summation

Table 7.2: Summary of systematic uncertainties on the atmospheric neutrino flux.

Extraterrestrial neutrinos are the same particles as atmospheric neutrinos. They just come from different locations and might have different energy spectra. In section 7.2.1, it has been shown that the energy interval covered by events from the "BG-100" sample is equivalent to those of the "BG-10" sample. Since the locations of potential astrophysical neutrino sources are unknown, their systematic uncertainties should be determined for an average incident direction. The differences between the systematic uncertainties for an isotropic neutrino flux and one with an atmospheric angular spectrum are considered negligible. Due to these three arguments, the systematic uncertainties for extraterrestrial neutrinos in the "BG-100" sample can be considered the same as those of atmospheric neutrinos in the "BG-10" sample.

But now one can make use of the fact that the point source search is based on the atmospheric neutrino analysis. The atmospheric neutrino analysis showed that the sensitivity towards atmospheric neutrinos was within 10 % of expectation (depending on sample). The absolute sensitivity towards atmospheric neutrinos can thus be considered as "calibrated" with an accuracy of 10 %. The only remaining uncertainty is the uncertainty on the "calibration beam", i.e. the 30 % uncertainty on the absolute flux of atmospheric neutrinos.

Some parameters have different uncertainties with respect to an atmospheric or to an extraterrestrial neutrino spectrum. These can be considered new, additional uncertainties. They are:

- The uncertainty on the effects of neutrino oscillations due to $\sin^2(2\theta)$. In comparison to the uncertainty on Δm^2, this is a second order effect for atmospheric neutrinos. But for extraterrestrial neutrinos it becomes important due to the long flight-path of the neutrinos. Its uncertainty is 10 % [134].

- The uncertainty on the neutrino interaction cross section, as it rises with energy. The same is true for the uncertainty on the muon propagation and on the amplitude resolution. If measurable, extraterrestric neutrino fluxes have hard spectra. It is estimated that these parameters give an additional contribution to the uncertainty for high energy events or hard spectra. The additional uncertainty on these parameters is estimated to be of similar size or smaller as compared to their uncertainty for atmospheric neutrinos.

No.	Parameter	Uncertainty [%]	Remarks
1.	Calibration accuracy	10	Atmospheric neutrino analysis
2.	Atm. flux prediction	30	Theoretical uncertainties
3.	ν-oscillations	10	Uncertainty on $\sin^2(2\theta)$
4.	ν-interaction cross section	10	Energy scaling
5.	Muon propagation	25	Energy scaling
6.	Amplitude resolution	5	Energy scaling
	Combined	43	Quadratic summation

Table 7.3: Summary of systematic uncertainties on the sensitivity towards astrophysical neutrinos.

These uncertainties can again be added added quadratically, see table 7.3. This yields an uncertainty on the sensitivity towards extraterrestrial neutrinos of 43 %. It is estimated to apply for the spectra investigated (atmospheric to E_ν^{-1} and all energies investigated ($10^{1.0}$ GeV to $10^{5.5}$ GeV). Again one might invoke a contingency argument to give a conservative uncertainty of 65 %.

8 The Effective Detector Size

Apart from the physical size of the detectors, there are two other important parameters describing the size of the detectors: The effective area A_{eff} and the effective volume V_{eff}. Both depend on those parameters on which the detector acceptance depends: In particular the energy and the zenith angle of the particles registered.

8.1 General Definitions

The effective area: The effective area A_{eff} is defined as

$$A_{eff} \equiv \frac{\mathcal{R}_{det}}{\Phi} \ , \tag{8.1}$$

where $\mathcal{R}_{det}$ is the detected count rate and Φ is the incident particle flux. The count rate can be taken at trigger level or after cuts. Correspondingly, one distinguishes effective areas at various cut levels. The benefit of the effective area is this simple correlation of a flux (e.g. from a theoretical prediction) with a detected count rate. The effective area of a detector can be considered the size of a virtual, equivalently efficient 2-dimensional detector, which detects all particles *passing through* it and none passing outside.

Caution has to be used to which particle species the effective area refers to: Detectors like AMANDA can specify a muon effective area $A_{\mu,\,eff}$ as well as a neutrino effective area $A_{\nu,\,eff}$. Both are proportional to $\mathcal{R}_{det}$. But the neutrino-induced muon flux is orders of magnitude smaller than the neutrino flux itself (at least in the $\mathcal{O}$(TeV) energy range). The neutrino effective area will therefore be orders of magnitude smaller than the muon effective area. In the literature it is more common to refer to the (large) muon effective area than to refer to the (small) neutrino effective area. This is justified by the fact that the muon is the particle actually registered in the detectors. But the neutrino interaction cross sections are different in different detector environments. The ratio of muon to neutrino flux therefore depends on the environment of the experiment. Hence, it is useful to additionally give the neutrino effective area.

A flux like Φ in equation 8.1 is a rate per area. So for Monte Carlo simulation studies, the effective area can easily be computed. One has to define a "generation plane" of size A_{gen} and count the "generation rate" $\mathcal{R}_{gen}$ of particles passing through it (or which are starting on it). The effective area is then given by:

$$A_{eff} = A_{gen}\frac{\mathcal{R}_{det}}{\mathcal{R}_{gen}} \ , \tag{8.2}$$

where $\mathcal{R}_{det}$ is the detected count rate. In simulations of atmospheric muons or neutrinos, the generation area is typically taken to be either the earth surface or a virtual plane in front of the detector. The effective areas obtained are then $A_{atm.\,\nu,\,eff}$ or $A_{atm.\,\mu,\,eff}$.

The effective volume: In the case of a neutrino signal, one can not only determine the flux of neutrinos through a plane. Alternatively one can count the number of neutrino

interactions that produce muons inside a certain "interaction volume" V_{int}. This leads to the definition of the *effective volume* V_{eff}:

$$V_{eff} \equiv V_{int} \frac{\mathcal{R}_{det}}{\mathcal{R}_{\nu \to \mu}} \ , \tag{8.3}$$

where $\mathcal{R}_{\nu \to \mu}$ is the rate of charged current neutrino interactions inside the volume and $\mathcal{R}_{det}$ again is the detected (muon) rate. Equivalently to the interpretation of effective areas, V_{eff} can be thought of as the size of a fully efficient 3-dimensional detector which detects all neutrino-induced muons *starting* inside its volume and none starting outside.

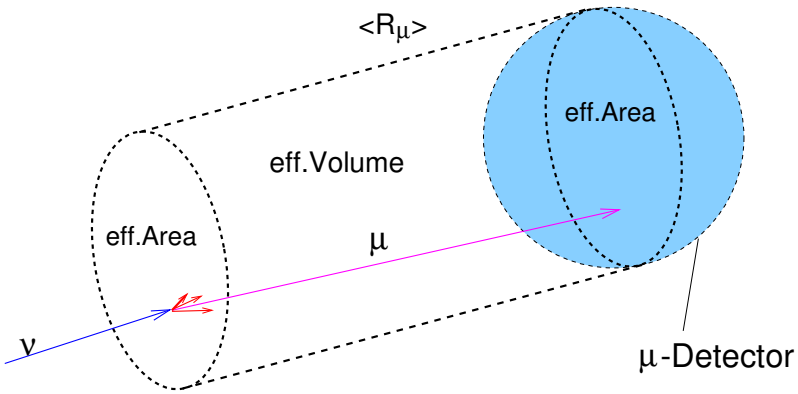

Figure 8.1: The muon effective area $A_{\mu,\,eff}$, the effective volume V_{eff}, the average range of a muon $< R_\mu >$ and the detector volume of a neutrino telescope.

The rate of neutrino to muon conversions per unit volume ($\mathcal{R}_{\nu \to \mu}/V_{int}$ in equation 8.3) can also be expressed as $\Phi_\nu \cdot P_{\nu \to \mu}$. Here, Φ_ν is the incident neutrino flux and $P_{\nu \to \mu}$ is the neutrino to muon conversion probability per unit track length for an individual neutrino. From equation 8.3, it thus follows that

$$V_{eff} = \frac{\mathcal{R}_{det}}{\Phi_\nu \cdot P_{\nu \to \mu}} = A_{\nu,\,eff} \cdot \frac{1}{P_{\nu \to \mu}} \ . \tag{8.4}$$

Equation 8.1 was used here. The effective volume is thus the product of the neutrino effective area and the length $\frac{1}{P_{\nu \to \mu}}$.

The average neutrino range: It might seem straight forward to identify the length $\frac{1}{P_{\nu \to \mu}}$ with a characteristic length of the neutrino inside the (sufficiently large) detector medium. But it is not evident which characteristic length to use: The average range, the median range, the range until the flux is reduced by a factor $\exp(-1)$, or another length. In the following, $\frac{1}{P_{\nu \to \mu}}$ is calculated as a function of the average range $< R_\nu >$ of the neutrino inside the (sufficiently large) detector medium before converting to a muon. Let

the probability $P_{\nu\to\mu}$ and the neutrino path length l be measured in dimensionless units. Then:

$$\begin{aligned}
&\Phi_\nu(l) = \Phi_\nu(0)\cdot(1-P_{\nu\to\mu})^l \\
&\rightsquigarrow < R_\nu > = \int_0^\infty 1\cdot(1-P_{\nu\to\mu})^l dl = \int_0^\infty \exp\left[l\cdot\ln(1-P_{\nu\to\mu})\right]dl = \tfrac{-1}{\ln(1-P_{\nu\to\mu})} \\
&\rightsquigarrow P_{\nu\to\mu} = 1-\exp\left(-<R_\nu>^{-1}\right) = <R_\nu>^{-1} + \mathcal{O}(<R_\nu>^{-2}) \\
&\rightsquigarrow \tfrac{1}{P_{\nu\to\mu}} = <R_\nu> \\
&\rightsquigarrow V_{eff} = A_{\nu,\,eff}\cdot <R_\nu>
\end{aligned} \tag{8.5}$$

Here, the assumption was made that $P_{\nu\to\mu}$ is independent of l and hence independent of the muon energy. This is only a (valid) assumption since the neutrino has a finite (but small) neutral current interaction cross section and the charged current cross section depends on energy. Within this approximation, the effective volume is then the product of the neutrino effective area and the average distance a neutrino travels. $< R_\nu >$ in turn can be expressed via the neutrino interaction cross section with ice molecules $\sigma_{\nu,\,ice}$, the ice density ρ_{ice} and the mass of an ice molecule μ_{ice}:

$$< R_\nu > = \frac{1}{P_{\nu\to\mu}} = \frac{\mu_{ice}}{\sigma_{\nu,\,ice}\cdot\rho_{ice}}\ . \tag{8.6}$$

The average muon range: The effective volume cannot directly be defined for atmospheric muons. But it allows the definition of an alternative expression for the muon effective area via the flux of neutrino-induced muons $\Phi_{\mu(\nu)}$. Canceling $\mathcal{R}_{det}$ from equations 8.4 and 8.1 yields:

$$V_{eff} = \frac{A_{\mu,\,eff}\cdot\Phi_{\mu(\nu)}}{\Phi_\nu\cdot P_{\nu\to\mu}} = A_{\mu,\,eff}\cdot\frac{\Phi_{\mu(\nu)}}{\Phi_\nu}\cdot <R_\nu> = A_{\mu,\,eff}\cdot <R_\mu>\ , \tag{8.7}$$

where $< R_\mu >$ is the mean muon range. $< R_\mu >$ can for example be expressed via the muon energy loss coefficients a and b when integrating equation 3.6:

$$< R_\mu > = < R_\mu(E_\mu) > = \frac{1}{b}\cdot\ln\left(\frac{bE_\mu}{a}+1\right)\ , \tag{8.8}$$

with $a = 2\,\mathrm{MeV/cm}$ and $b \sim 3.4\cdot10^{-6}\,\mathrm{cm}^{-1}$ [246].

Combining all: From equations 8.5 and 8.7 it thus follows:

$$\boxed{V_{eff} = A_{\nu,\,eff}\cdot <R_\nu> = A_{\mu,\,eff}\cdot <R_\mu>} \tag{8.9}$$

As mentioned before, it is common to compare muon effective areas when comparing neutrino detectors. But when one wants to compare neutrino telescopes to Cherenkov-telescopes, one should compare effective areas for the primary messenger particle, i.e. gamma effective areas to neutrino effective areas. The detected rates at earth then have a ratio of

$$\frac{\mathcal{R}_{\gamma,\oplus}}{\mathcal{R}_{\nu,\oplus}} = \frac{\Phi_{\gamma,\star}}{\Phi_{\nu,\star}}\cdot\frac{\epsilon_\gamma}{\epsilon_\nu}\cdot\frac{A_{\gamma,\,eff,}}{A_{\nu,\,eff}}\ , \tag{8.10}$$

where $\mathcal{R}_\oplus$ represents rates at earth, $\Phi_\star$ fluxes at the source and ϵ the survival probability for the propagation from source to earth. A source emitting neutrinos and gamma rays then induces the same count rate in gamma ray and neutrino telescopes, when the ratios of source fluxes, survival probabilities and effective areas cancel.

8.2 Flux Limits and the Energy-Averaged Effective Area

From equation 8.1, it follows that the number of muon events $\hat{N}_S$ expected within a detector lifetime T_{life} from a source with a differential flux $\left(\frac{d\Phi_\nu}{dE_\nu}\right)_\star$ is given by

$$\hat{N}_S = T_{life} \cdot \int_{E_{\nu,\,min}}^{E_{\nu,\,max}} A_{\nu,\,eff}(E_\nu) \cdot \left(\frac{d\Phi_\nu}{dE_\nu}\right)_\star dE_\nu \ . \tag{8.11}$$

Suppose that a measurement yielded an observation of N_O events, while $\hat{N}_{BG}$ were expected from background. The upper limit on the number of signal events inside the search bin at 90 % confidence level is denoted by $\mu_{90}(N_O, \hat{N}_{BG})$. The differential flux limit at energy E_ν is then given by

$$\left(\frac{d\Phi_\nu}{dE_\nu}\right)^{limit}(E_\nu) = \frac{\mu_{90}(N_O, \hat{N}_{BG})}{\hat{N}_S} \cdot \left(\frac{d\Phi_\nu}{dE_\nu}\right)_\star (E_\nu) \ . \tag{8.12}$$

It is impossible to restrict the measurement to an infinitesimally small neutrino-energy range. Therefore, equation 8.12 is integrated over an energy interval between $E_{\nu,\,min}$ and $E_{\nu,\,max}$. The resulting flux limit is then the integral flux limit within that energy range:

$$\Phi_\nu^{limit}(E_{\nu,\,min} \le E_\nu \le E_{\nu,\,max}, \left(\frac{d\Phi_\nu}{dE_\nu}\right)_\star) = \frac{\mu_{90}(N_O, \hat{N}_{BG})}{\hat{N}_S} \cdot \int_{E_{\nu,\,min}}^{E_\nu,\,max} \left(\frac{d\Phi_\nu}{dE_\nu}\right)_\star dE_\nu \ . \tag{8.13}$$

This expression can be simplified by introducing the energy-averaged effective area $\bar{A}_{\nu,\,eff}$:

$$\bar{A}_{\nu,\,eff}(E_{\nu,\,min} \le E_\nu \le E_{\nu,\,max}, \left(\frac{d\Phi_\nu}{dE_\nu}\right)_\star) = \frac{\int_{E_{\nu,\,min}}^{E_\nu,\,max} A_{\nu,\,eff}(E_\nu) \cdot \left(\frac{d\Phi_\nu}{dE_\nu}\right)_\star dE_\nu}{\int_{E_{\nu,\,min}}^{E_\nu,\,max} \left(\frac{d\Phi_\nu}{dE_\nu}\right)_\star dE_\nu} \tag{8.14}$$

Inserting this in equation 8.13 yields:

$$\Phi_\nu^{limit}(E_{\nu,\,min} \le E_\nu \le E_{\nu,\,max}, \left(\frac{d\Phi_\nu}{dE_\nu}\right)_\star) = \frac{\mu_{90}(N_O, \hat{N}_{BG})}{T_{life} \cdot \epsilon_{bin} \cdot \bar{A}_{\nu,\,eff}} \ . \tag{8.15}$$

Here, the reconstruction efficiency of the corresponding search bin ϵ_{bin} has already been included. It will be discussed in more detail in section 9.3. Since formula 8.15 contains the energy-averaged effective area, the integral limit calculated by it is sometimes called *energy-averaged limit*, e.g. in [251].

The formulae 8.14 and 8.15 only referred to the neutrino. The corresponding expressions for the muon are basically equivalent. They are therefore not explicitely given. The formulae how to determine the energy-averaged effective areas from Monte Carlo simulated data can be obtained by inserting equation 8.2 into equation 8.14[1].

[1] The resulting formulae can be rewritten using *nusim* specific parameters in case of Monte Carlo data simulated with *nusim*. The results are given in [251] (equations 6.14 and 6.15) when identifying A_{GEN} with "$r14$". Care has to be taken since the calculation of $N_{GEN}(\gamma)$ has to distinguish between $\gamma \neq -1$ and $\gamma = -1$.

8.3 The Energy-Averaged Effective Areas in AMANDA

For this work, the calculation of the effective area is no task by itself. Instead, flux limits shall be derived. The appropriate parameter is thus not the effective area by itself, but the energy-averaged effective area. This is therefore the parameter whose properties shall be investigated in slightly more detail in this section.

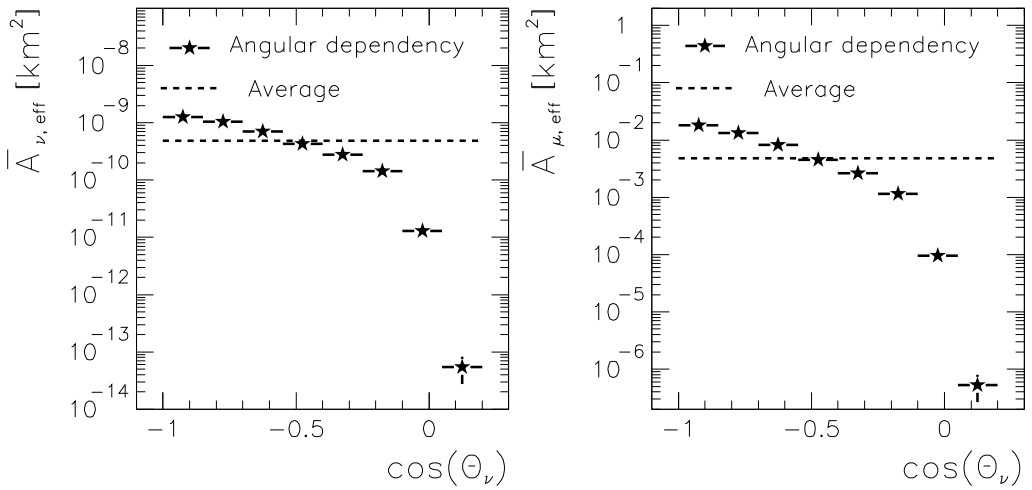

Figure 8.2: The dependency of the energy-averaged effective area $\bar{A}_{eff}$ on the neutrino zenith angle. (Left:) energy-averaged neutrino effective area. (Right:) energy-averaged muon effective area. All data: Monte Carlo simulation, BG-100 selection. Data shown for a differential E_ν^{-2} neutrino spectrum with energies in the range $10^{1.0}\,\mathrm{GeV} \leq E_\nu \leq 10^{5.5}\,\mathrm{GeV}$. The simulated flux is isotropic in the zenith angle range $80^\circ \leq \theta_\nu \leq 180^\circ$. Dashed line: Average over all data; Points: data binned in $\cos(\theta_\nu)$. Vertical error bars show statistical errors only.

Figure 8.2 shows the dependency of the energy-averaged neutrino and muon effective areas on the cosine of the true neutrino angle. The numbers entering the figure were derived for an E_ν^{-2} neutrino spectrum with neutrino energies between $10^{1.0}\,\mathrm{GeV}$ and $10^{5.5}\,\mathrm{GeV}$ with an isotropic neutrino flux between 80° and 180°. The most prominent effect is the difference in the absolute scale between energy-averaged neutrino and muon effective areas. The energy-averaged neutrino effective area is seven orders of magnitude smaller than the energy-averaged muon effective area. The cause of this difference is the small neutrino interaction cross section.

Within each sub-figure, one sees a higher sensitivity towards events induced by vertically up-going neutrinos as compared to those induced by horizontal neutrinos. $\bar{A}_{eff}$ changes by approximately one order of magnitude from $\theta_\nu \sim 180^\circ$ to $\theta_\nu \sim 95^\circ$. For angles $\theta_\nu \leq 95^\circ$, the drop is significantly stronger. This latter effect is a direct result of the level 4a cuts (equation 7.6) that remove all events which are correctly reconstructed as to originate from that range. Only few, severely mis-reconstructed events survive. Hence, the effective area for angles $\theta_\nu \leq 95^\circ$ is very low (and likewise $\bar{A}_{eff}$).

The behavior of $\bar{A}_{eff}$ within the region not affected by the level 4a cuts is explained by two effects: First, the long and slim geometry of AMANDA-B10 makes the detector more sensitive to vertical events. Furthermore, the (mis-reconstructed) background is

stronger at horizontal than at vertical up-going directions. Correspondingly, the cuts applied to suppress the background are tighter for horizontal events. Both effects lead to a reduction of the effective area for incident horizontal directions. $\bar{A}_{\nu,\,eff} = 4.81\,\mathrm{cm}^2$ and $\bar{A}_{\mu,\,eff} = 4.83 \cdot 10^7\,\mathrm{cm}^2$ are the values averaged over the zenith angle. They are close to what is expected for neutrinos with incident angles of $\theta_\nu \sim 125°$.

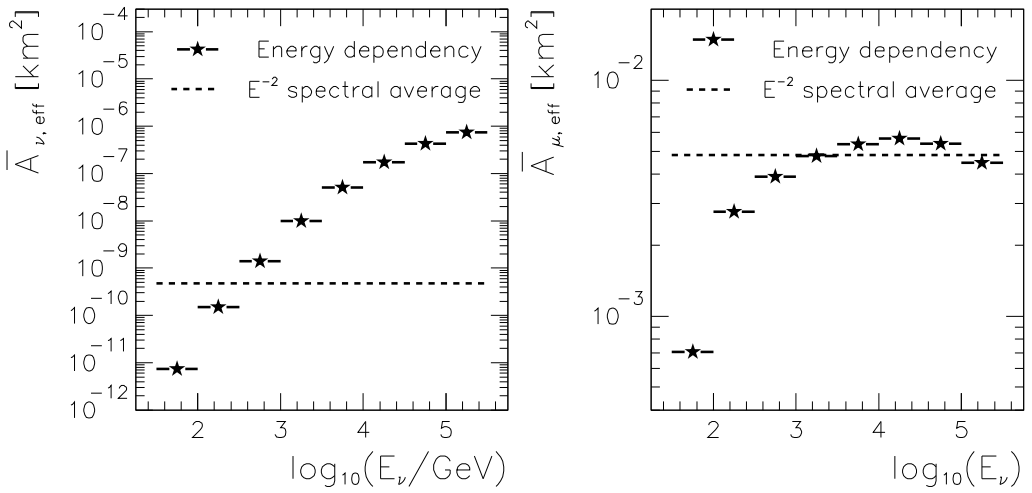

Figure 8.3: The energy dependency of the energy-averaged effective area $\bar{A}_{eff}$. (Left:) energy-averaged neutrino effective area. (Right:) energy-averaged muon effective area. All data: Monte Carlo simulation, BG-100 selection. Data shown for an E_ν^{-2} neutrino spectrum. The simulated flux is isotropic in the zenith angle range $80° \leq \theta_\nu \leq 180°$. Dashed line: Average over all data; Points: data binned in E_ν. Vertical error bars show statistical errors only.

Figure 8.3 shows the dependency of $\bar{A}_{eff}$ on the true neutrino energy. The numbers entering the figure were derived for the same spectrum (E_ν^{-2}), angular range (between 80° and 180°) and energy range ($10^{1.0}$ to $10^{5.5}$ GeV) as in figure 8.2. While $\bar{A}_{\nu,\,eff}$ and $\bar{A}_{\mu,\,eff}$ have a remarkably similar dependence on the neutrino angle, their energy dependencies are very different. $\bar{A}_{\nu,\,eff}$ depends very critically on the neutrino energy. At energies below $E_\nu = 10^4$ GeV, it changes over almost four orders of magnitude while the neutrino energy changes over two orders of magnitude. At higher energies, it changes by another order of magnitude, while the neutrino energy changes over 1.5 orders of magnitude. $\bar{A}_{\mu,\,eff}$ in contrast increases with neutrino energy until $E_\nu \sim 10^4$ and shrinks for higher energies. Altogether the dependency on the neutrino energy is much weaker: The changes are only within 1.5 (0.5) orders, when including (excluding) the first bin.

The rise in $\bar{A}_{\mu,\,eff}$ from the first to the second bin is dominated by the low passing rates of the cuts for low energy events. This effect persists on a much smaller scale until $E_\mu \sim 10^4$ GeV. This maximum corresponds to a neutrino energy of $E_\nu \sim 10^{4.3}$ GeV, i.e to the same bin in the figure. The effect of shrinking muon-sensitivity at very large energies has already been explained during the discussion of figure 7.13 (left) in section 7.2.1: Very energetic muons cause so much light that their event topology is more spherical than that of minimally ionizing muons. The anti-shower cuts (see section 7.1.4) then reduce the cut passing rates and hence the effective areas.

When explaining $\bar{A}_{\nu,\,eff}$, one has to consider two additional effects. First, the muon range increases with energy (approximately linearly until $E_\mu \sim 10^3\,\mathrm{GeV}$ and logarithmically above, see equation 8.8). This "critical" energy of $E_\mu \sim 10^3\,\mathrm{GeV}$ corresponds to a neutrino energy of $E_\nu \sim 10^{3.3}\,\mathrm{GeV}$. Secondly, the neutrino interaction cross section rises approximately linearly with energy until $E_\nu \sim 10^{4.5}\,\mathrm{GeV}$ and logarithmically with energy afterwards [101]. The energy dependency of $\bar{A}_{\nu,\,eff}$ is the convolution of these two dependencies with the energy dependency of $\bar{A}_{\mu,\,eff}$.

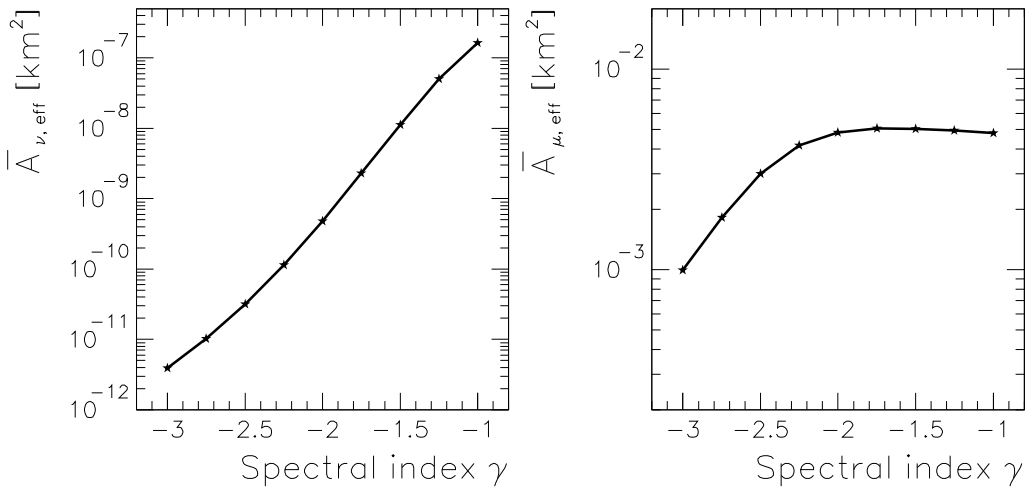

Figure 8.4: The spectral index dependency of the energy-averaged effective area $\bar{A}_{eff}$. (Left:) energy-averaged neutrino effective area. (Right:) energy-averaged muon effective area. All data: Monte Carlo simulation, BG-100 selection. The neutrino energies are in the range $10^{1.0}\,\mathrm{GeV} \leq E_\nu \leq 10^{5.5}\,\mathrm{GeV}$. The simulated flux is isotropic in the zenith angle range $80° \leq \theta_\nu \leq 180°$. Points: data for specific γ values. Line: No fit, just to guide the eye.

The dependency of $\bar{A}_{eff}$ on the spectral index γ is shown in figure 8.4. $\bar{A}_{\nu,\,eff}$ increases over 5 orders of magnitude for spectral indices hardening from -3 to -1. $\bar{A}_{\mu,\,eff}$ in contrast only increases by a factor of 5 for spectral indices hardening from -3 to -2 and is slowly shrinking for harder spectral indices.

The reason for the γ-dependencies is the varying contribution of the high-energy neutrinos with respect to the low energy neutrinos. E.g. an increase in the spectral index of 1 increases the population of highest-energy neutrinos ($10^{4.5}\,\mathrm{GeV} \leq E_\nu \leq 10^{5.5}\,\mathrm{GeV}$) by approximately three orders of magnitude with respect to events of the lowest energies ($10^{1.5}\,\mathrm{GeV} \leq E_\nu \leq 10^{2.5}\,\mathrm{GeV}$). Since events of various energy pass the cuts with different efficiencies, the transformation from the energy-dependency to the spectrum dependency is not simple. But in any case, hard spectra cause a larger fraction of high energy events than soft spectra and thus figure 8.4 shows the same trends as figure 8.3. The arguments interpreting these trends are not repeated here.

Appendix F lists the energy-averaged effective areas (for neutrino and muon) for all combinations of the θ_ν-intervals, E_ν-intervals and spectral indices investigated.

8.3.1 Uncertainties

The statistical errors on the numbers given in appendix F are on average $\sim 3.3\,\%$. They increase towards the horizon and for low energies. For the most extreme combinations of δ and E_ν, the uncertainties can be as high as $\sim 14\,\%$, or as low as $\sim 1.0\,\%$. The statistical errors on those numbers which average over several declination and/or energy bins are correspondingly lower. The statistical uncertainty on declination-averaged numbers for example is on average $\sim 1.4\,\%$. The dependency of the uncertainty on the spectral index is small.

Table 7.3 in section 7.3.11 already discussed the uncertainty on the sensitivity towards extraterrestric neutrinos (43 %). There, it was noted that this is a conservative estimate which applies to all spectra investigated (atmospheric to E_ν^{-1} and to all energies investigated ($10^{1.0}$ GeV to $10^{5.5}$ GeV). Since the sensitivity is proportional to the effective area, 43 % is also the uncertainty on the effective area. And since it is an energy-independent estimate, this is then also the uncertainty for the energy-averaged effective areas.

9 Resolution, Bin-size and Efficiency

Before one can start searching for point sources, one has to determine the optimal size of the search cones (or search bins). If their size is too large, the number of random background events N_{BG} becomes too large. On the other hand, if the bin-size is too small, signal events might be lost due to the finite detector resolution. So the goal of the bin-size optimization is to find the bin-size which fulfills the following property: *If a signal exists within a bin, then the optimal size of that bin minimizes the chance probability P_c that the total flux within the bin can be explained by background only.*

In case of Gaussian probability distributions, probabilities are often measured in units of standard deviations from the expectation. This concept can also be generalized for non-Gaussian distributions. The probability P_c is then denoted to have a *significance* $\mathcal{S} = n\sigma$ or a significance of n *standard deviations* with $n \geq 0$ if

$$P_c = \int_n^\infty \frac{dy}{\sqrt{2\pi}} \exp\left(\frac{-y^2}{2}\right) . \tag{9.1}$$

Here, the terms "σ" or "standard deviation" are solely defined as the unit of the significance.

9.1 The Detector Resolution

9.1.1 Determination of the Detector Resolution

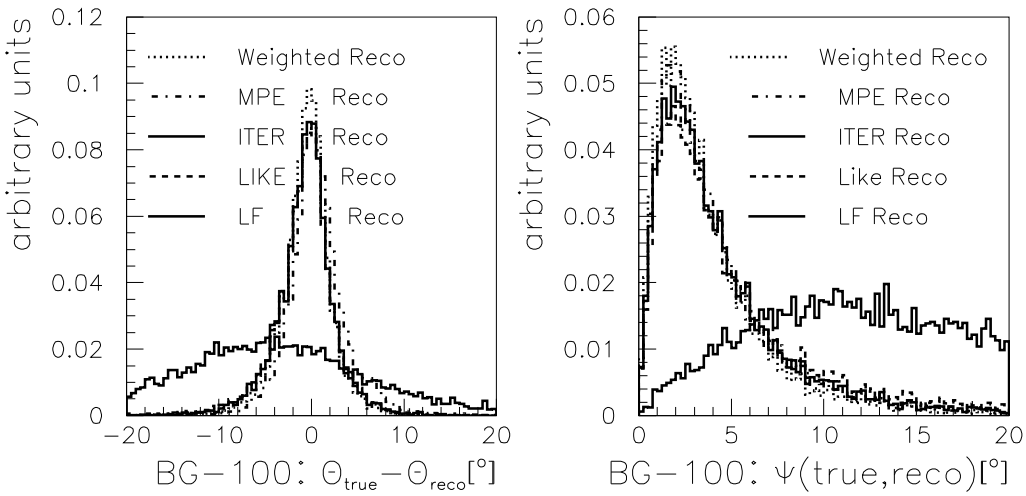

Figure 9.1: The mismatch of various reconstructions. (Left:) Zenith angle mismatch. (Right:) Space angle mismatch. All data: Atmospheric neutrino simulation after BG-100 selection.

Since the background events can be considered as being randomly distributed, the optimal bin-size mostly depends on the detector resolution. In AMANDA, the detector resolution depends on various parameters like energy, zenith angle, cut level or reconstruction algorithm used. The properties of individual events (like energy or zenith angle) are fixed and cannot be selected. Likewise, the event selection has been defined (in section 7.2) and

is not altered any more. The only selection possible to obtain a good detector resolution is the choice of an appropriate reconstruction among the various reconstructions which have been applied during the data processing.

The various reconstructions used during the analysis presented here have been introduced in section 6. In figure 9.1, the space angular and zenith angle mismatches of several of these reconstructions are shown for Monte Carlo simulated atmospheric neutrinos. The resolution given there is the muon resolution only. It does not include the angle between muon and neutrino of formula 6.1.

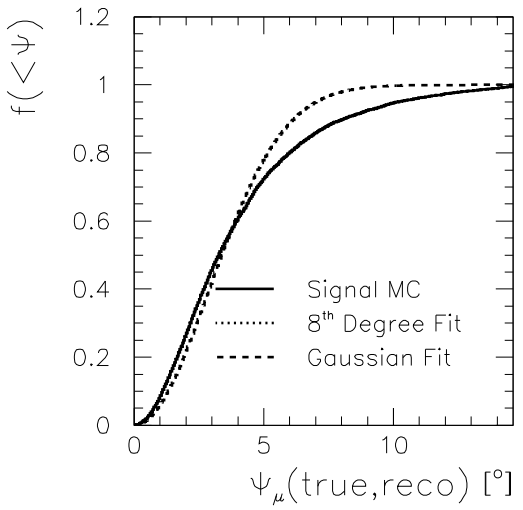

Figure 9.2: Parameterization of the detector resolution for muons. Shown is the number of events with a reconstruction error smaller than a certain value versus that value. Solid line: simulated signal, dashed line: Gaussian fit, dotted line: 8^{th} degree polynomial fit, see table 9.1 for the values of the fit parameters. In black and white copies of this figure, one might not see the difference between the solid and the dotted line, since the 8^{th} degree polynomial fit fits the simulated signal so well.

It is evident that the line-fit gives the worst approximation of the true track. All the other reconstructions are of much better quality. The zenith angle resolution is best for the $P_{hit}P_{nothit} \oplus MPE$ reconstruction (see section 6.4.5). It yields the lowest systematic offset and the smallest RMS. Second best is the weighted reconstruction (see section 6.4.4). This in turn gives the best space angular resolution (lowest mean and median), while the $P_{hit}P_{nothit} \oplus MPE$ reconstruction is second best. Overall, these two reconstructions give comparable results. Here, the choice was made to use the $P_{hit}P_{nothit} \oplus MPE$ reconstruction henceforth. Reason is that the weighted reconstruction introduces additional systematic uncertainties arising from the arbitrariness in the definition of its prior.

The zenith angle resolution thus achieved ($P_{hit}P_{nothit} \oplus MPE$ reconstruction) is given by a RMS of 3.3° (FWHM = 4.4°). The reconstructed zenith angles are systematically slightly smaller than the true angles (mean of difference: 0.56°, median: 0.36°). All other reconstructions show a systematic shift of larger amplitude into the opposite direction. The azimuth angle mismatch is given by a RMS of 5.9° (FWHM = 7.4°). The space angular mismatch has a mean of 4.1° and a median of 3.2°. The typical angle between muon and neutrino is smaller than the angle between true and reconstructed muon track. The neutrino resolution is thus only marginally ($\sim 10\,\%$) worse than the muon resolution.

For the determination of the optimal bin-size, it is necessary to parameterize the resolution. A Gaussian approximation is insufficient as can be seen from figure 9.2. It shows an integral distribution of the space angular reconstruction errors. The curve obtained from the atmospheric signal simulation is compared to an 8^{th} degree polynomial fit and to the hypothesis of a Gaussian resolution. The width of the Gaussian is taken from an unrestricted fit of an exponential curve to the distribution of the half-squares of the space angular mismatches, yielding $\sigma = 2.83°$.

The 8^{th} degree polynomial fit describes the simulated data well, while the Gaussian hypothesis can be rejected. Even when using a different width for the Gaussian (e.g. from restricting the fit), the Gaussian hypothesis cannot simultaneously describe the data for small and large angular mismatches. The sum of two Gaussian distributions also does not match the data satisfyingly. Henceforth, the resolution is therefore parameterized by an 8^{th} degree polynomial fit. The parameterization is limited to the range between 0° and five times the Gaussian width σ. The fit is restricted to be positive in that region. The tail containing data with even worse mismatches is ignored. The asymptotic behavior of the polynomial for very large absolute values is thus not crucial.

9.1.2 Analysis of the Space-angular Resolution

The resolution depends on various parameters. One of them, the dependency on the reconstruction algorithm, has already been shown in figure 9.1 and has been discussed in section 9.1.1.

Figure 9.3 (left) shows the dependency of the resolution on the cut level. One sees that the resolution improves from trigger level to final cut selections by a factor of 2. One notices an approximately exponential decrease of the reconstructed space angle mismatch with cut level. The filters defining these levels were originally defined in section 7 to enhance the signal from atmospheric neutrinos with respect to the background from atmospheric muons. Figure 9.3 (left) proves that these filters also implicitly select well reconstructed events.

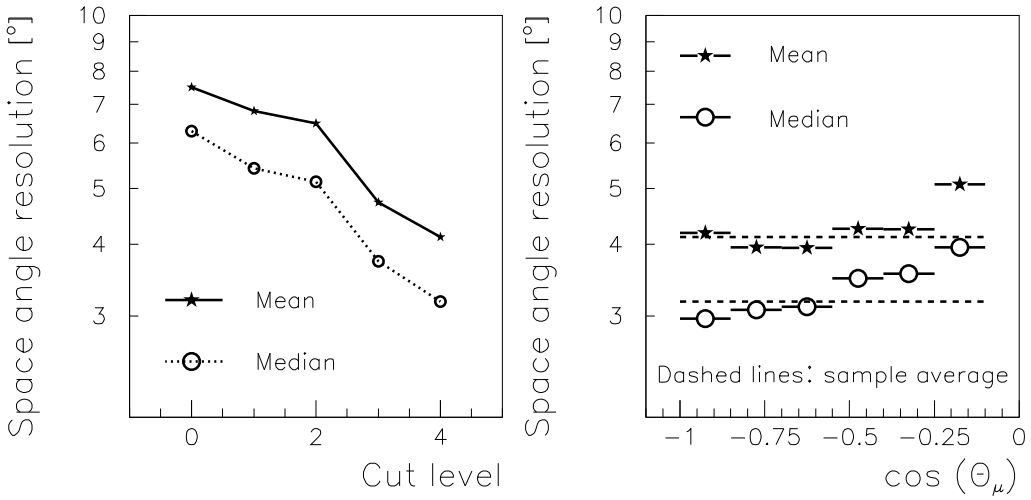

Figure 9.3: (Left:) The dependency of the space angular resolution on the cut level. Here, cut level 4 corresponds to the BG-100 selection. (Right:) The dependency of the space angular resolution on the incident muon zenith angle measured in bins of width 0.2 in $\cos\theta_\mu$. Dashed lines: mean (top) and median (bottom) for all angles of the simulated atmospheric neutrinos after the BG-100 selection.

In the right sub-figure, the dependency of the resolution on the zenith angle of the muon track is shown. One notices a systematic improvement of the resolution with increasing zenith angle. The slight increase in the leftmost bin for the mean of the space angle

mismatch is not significant. Reason for the systematic trend is the geometry of the slim AMANDA-B10 detector, which offers a good "lever arm" for the reconstruction only in case of vertical events. The average resolution for the selected sample is only slightly smaller than the resolution obtained for the most favorable (near vertical) incident angles. This is explained as follows: The triggered atmospheric neutrino flux is almost isotropic. Due to the cuts applied, the passing rate of near vertical events is enhanced with respect to vertical events. The dominant fraction of events in the BG-100 sample (dashed lines) is thus near vertical. This has already been shown with figure 7.12 (right).

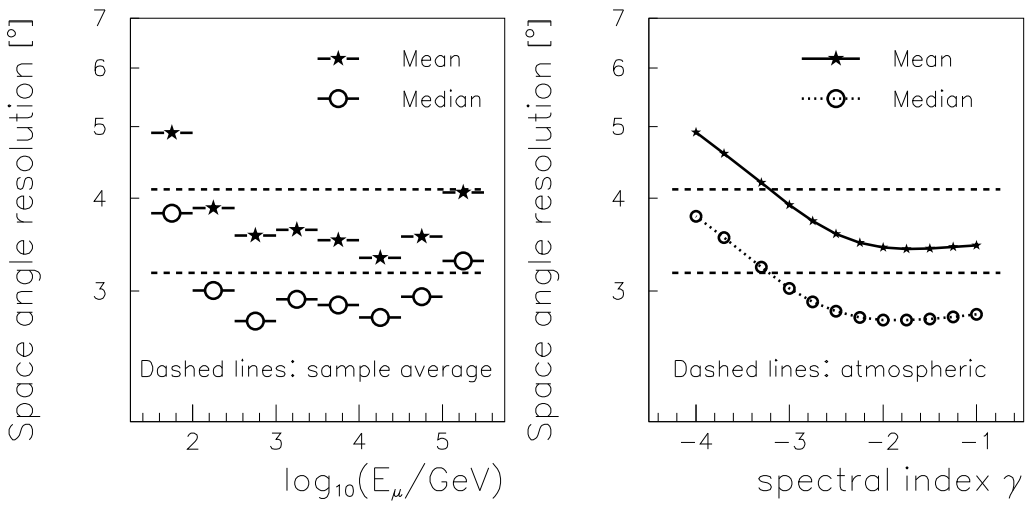

Figure 9.4: (Left:) The dependency of the space angular resolution on the muon energy measured in intervals of width 0.7 in $\log(E_\mu)$. (Right:) The dependency of the space angular resolution on the neutrino energy spectrum (left). Dashed lines: mean (top) and median (bottom) for all energies of the simulated atmospheric neutrinos after the BG-100 selection.

This is very different for the case of the dependency on the neutrino energy, which is displayed in figure 9.4 (left). Low energy events are worst reconstructed. But they are so much more abundant than high energy events that they significantly affect the average resolution of the full sample. In general, the resolution improves with muon energy until $E_\nu \sim 10^3\,\mathrm{GeV}$, stays approximately constant and worsens for the highest energies again. The worsening at high energies is due to the increased sphericity of the hit topology.

The average in the logarithm of the muon energy of simulated signal after the BG-100 selection is given by $< \log(E_\mu/GeV) >= 2.4$. One sees that this energy corresponds approximately to the interaction point between the dashed lines and a curve through the data points in figure 9.4 (left). One can thus argue that the average resolution of the BG-100 sample is close to that expected for muons of energies $E_\mu \sim 10^{2.4}\,\mathrm{GeV}$. The argument here concerned the average of the logarithm of the energy $< \log(E_\mu/GeV) >$. The logarithm of the average energy $\log(< E_\mu > /GeV) \approx 3.4$ is obviously very different. So one should not stretch the argument mentioned above.

A closely related dependency is presented in figure 9.4 (right): the dependency on the neutrino spectrum. So far, the resolution was only investigated for an atmospheric neutrino spectrum. This figure now compares the resolution of an atmospheric spectrum

(dashed lines) to those obtained for various harder spectra (points). The hard spectra on the right yield better angular resolutions than the soft spectra on the left. This is explained by their larger fraction of high energy events. These in turn are reconstructed better than average events - as can be seen in figure 9.4 (left). Furthermore, one sees that atmospheric neutrino events yield resolutions which are comparable to an $E^{-3.2}$ spectrum; Atmospheric neutrinos above $E_\nu = 1\,\mathrm{TeV}$ are expected to have a spectrum $\sim E^{-3.7}$. The spectrum is harder for lower energies. The dominant contribution in AMANDA-B10 comes from neutrinos of energies below $E_\nu = 1\,\mathrm{TeV}$. The resolution of the atmospheric neutrino spectrum is thus better than that of an $\sim E^{-3.7}$ spectrum.

9.1.3 Cross-Checks of the Simulation Results

So far, the determination and analysis of the detector resolution has solely been based on simulated signal data. An effort undertaken during the analysis presented here was the search for the "shadow" of the moon in down-going atmospheric muons. Since cosmic rays do not travel through the moon, their flux should be reduced from the direction of the moon. Correspondingly, the flux of atmospheric muons coming from the direction of the moon should also be reduced. The observation of this *shadow of the moon* would allow an independent determination of the absolute offset and of the angular resolution of the muon reconstruction. It would not depend on the standard AMANDA simulation, but only on the cosmic ray deflection between moon and earth and on the angular difference between atmospheric muons and initial cosmic rays. Both can be simulated with higher precision than atmospheric neutrinos in AMANDA.

However, this effort was non-successful. At South Pole, the moon did not reach altitudes higher than 14° above the horizon in 1997. The atmospheric muon flux from these regions is very low compared to the vertical down-going flux. Furthermore, the diameter of the moon ($\sim 0.5°$) is small compared to the AMANDA resolution. The "shadow" can therefore at most reduce the atmospheric muon flux by $\mathcal{O}(10\,\%)$. Altogether, several years of AMANDA-B10 data would be needed to significantly detect the shadow of the moon. In [185], it was estimated that the proposed ANTARES experiment would need five years statistics for a $3\,\sigma$ "discovery" of the moon with an angular resolution of better than 1°.

But a similar analysis can be performed using coincidence data with the SPASE array [17, 169, 207]. The *South Pole Air Shower Experiment* is located at the surface, close to the AMANDA detector. It can reconstruct the direction of the air shower axis with a space angular resolution of 0.8° (RMS) [207]. This is significantly better than the resolution of the AMANDA-B10 detector. Muons of sufficient energy to penetrate the ice to the depth of the AMANDA detector are closely aligned to the axis of the air shower they were produced in. Coincidence data between the two experiments can hence be used to estimate the reconstruction resolution of AMANDA. This calibration yields an absolute offset of the reconstructed zenith angle of experimental events in AMANDA of $\sim 1.5°$. The resolution agrees with that obtained from simulated data to within $\sim 10\,\%$ for cut levels corresponding to level 2 and beyond as defined in this work.

Caution has to be used interpreting this result. From the simulated data, there is strong evidence that the AMANDA resolution shows a certain angular dependency, see figure 9.3. But the SPASE array can only calibrate a small zenith angle direction. The straight line

connecting the detector centers is at $\theta = 12°$. To apply the SPASE calibration to AMANDA neutrino data, it has to be assumed that the AMANDA resolution for atmospheric muons is the same as that for atmospheric neutrinos. Arguments against this assumption include

- The sensitivity of the AMANDA detector is not up-down symmetric since most optical modules have their PMTs oriented downwards.
- Atmospheric muons may appear in bundles, neutrino events do not appear in bundles.
- Atmospheric neutrino events can have (bright) muon-production vertices within the AMANDA array, atmospheric muons cannot.
- The atmospheric neutrino flux is isotropic to within a factor or two. The atmospheric muon flux increases over 6 orders of magnitude from horizontal to down-going directions.
- The flux of muons induced by atmospheric neutrinos is homogeneous. The flux of atmospheric muons shrinks by a factor of 2 from top to bottom of the AMANDA-B10 array.

Furthermore, the atmospheric muon spectrum is fixed. It is thus difficult to determine energy or spectrum dependencies with the SPASE coincidence analysis.

It is therefore impossible to determine the AMANDA resolution on neutrino events from down-going muons alone. But the SPASE coincidence analysis is sufficiently accurate to cross-check the resolution obtained from simulated data. This cross-check does not indicate any severe error in the determination of AMANDA's detector resolution. The offset seen in the SPASE-AMANDA coincidence analysis is reproduced in the Monte Carlo simulation of atmospheric muons for the corresponding zenith angular range. Since the Monte Carlo simulation of neutrinos only shows an offset of 0.56°, it is estimated that the true offset is only of approximately that size.

9.1.4 Systematic Uncertainties of the Resolution

Table 7.2 lists those parameters which influence the prediction of the absolute neutrino flux. Several of these do not influence the resolution of the reconstruction. The parameters that do influence the resolution are the calibration parameters and the description of the neutrino-interaction cross section (since this modifies the energy spectrum).

The systematic uncertainty of the resolution due to uncertainties on the neutrino-interaction cross section can be estimated from comparing the resolution obtained with *nusim* to that obtained from the *nu2mu* simulation (see section 4.2.1). The resolution obtained with *nu2mu* is better than that obtained from the standard simulation (*nusim*), but the difference is less than 10 % (or 0.3° for the RMS).

The uncertainties on the timing and amplitude calibration (see sections 5.1 and 5.3) affect the MPE contribution of the $P_{hit}P_{nothit} \oplus MPE$ reconstruction. The uncertainty on the resolution due to the timing calibration uncertainties is negligible [38]. The uncertainty due to amplitude calibration is estimated to be less than 5 %. Several AMANDA

parameters depend crucial on the OM sensitivities, see for example section 7.3.6. However it only causes an uncertainty on the angular resolution of less than 5 % [43]. Other calibration uncertainties are not expected to contribute significantly either.

The SPASE coincidence analysis gives a resolution uncertainty for AMANDA-B10 reconstructed data of $\leq 10\,\%$. As mentioned before, this is only determined in a certain angular range and for an atmospheric muon spectrum. Combining this with the previous arguments, one can estimate the total systematic uncertainty on the resolution to be $< 15\,\%$.

9.2 The Optimal Bin-Size

9.2.1 Basic Assumptions

When looking for optimal bin-sizes, one often has to start with assumptions simplifying the problem investigated. An example are the following assumptions:

1. The background distribution is flat.
2. The signal distribution is Gaussian.
3. The background and signal events are not distinguishable any further.
4. Statistical fluctuations are negligible: $\{N_{BG}, N_S\} \gg \{\sqrt{N_{BG}}, \sqrt{N_S}\}$. Here, N_{BG} and N_S are the number of background and signal events respectively. In a search for a signal, the total background is much larger than the total signal. Hence, this assumption can be rewritten as $N_{BG} \gg N_S \gg \sqrt{N_{BG}} \gg \sqrt{N_S} \gg 1$.

These assumptions are not valid for the point source search in the AMANDA experiment. They are introduced here to illustrate basic concepts of the optimal bin-size. The assumptions which are appropriate for AMANDA-B10 will be discussed in section 9.2.3.

As follows from equation 9.1, the significance can be easily expressed in case of a normal distribution. It is then the difference between observed number of events and expected number of background events measured in units of the uncertainty on the expected number of background events:

$$\mathcal{S} \equiv \frac{N_O - \hat{N}_{BG}}{\sigma(\hat{N}_{BG})} = \frac{(N_S + N_{BG}) - \hat{N}_{BG}}{\sigma(\hat{N}_{BG})} \approx \frac{N_S + \hat{N}_{BG} - \hat{N}_{BG}}{\sqrt{\hat{N}_{BG}}} \approx \begin{cases} \frac{N_S}{\sqrt{N_{BG}}} \\ \frac{N_S}{\sqrt{\hat{N}_{BG}}} \end{cases} , \qquad (9.2)$$

where $\hat{N}_{BG}$ is the expected number of background events, while N_O, N_S and N_{BG} are the total number of observed events, of true signal events and of true background events respectively. Assumption 4 has been used repeatedly here. It has to be emphasized that the formula $\mathcal{S} = N_S/\sqrt{(N_{BG})}$ is only correct under the above mentioned assumptions. Either only observed - though not necessarily distinguishable - quantities (top row) or only predicted quantities (bottom row) remain in equation 9.2. From this, one can then calculate the optimal bin-size in two typical cases:

Circular Bins: Circular search bins might for example be used when searching for pre-selected sources. In this case, and under the above mentioned assumptions, the number of expected signal or background events within a bin of radius R are proportional to

$$\begin{array}{lll} \hat{N}_S & \propto \int_0^R \left(\sigma\sqrt{(2\pi)}\right)^{-1} \cdot \exp\left(-r^2/2\sigma^2\right) & r\ dr \\ \hat{N}_{BG} & \propto \int_0^R 2\pi & r\ dr\ . \end{array} \tag{9.3}$$

The assumptions 1 and 2 were used here. The optimal bin size has the radius $R = R_o$ and maximizes the significance $\hat{N}_S/\sqrt{(\hat{N}_{BG})}$, see equation 9.2:

$$0 = \frac{d}{dR}\left\{\frac{\hat{N}_S}{\sqrt{(\hat{N}_{BG})}}\right\}\ . \tag{9.4}$$

Substituting $x = r^2/\sigma^2$, $X = R^2/\sigma^2$ and canceling the constants, one obtains for $X = X_o$:

$$0 = \frac{dX}{dR}\frac{d}{dX}\left\{\frac{\int_0^X \exp\left(-x/2\right)\ dx}{\sqrt{(\int_0^X dx)}}\right\}\ . \tag{9.5}$$

For non-zero bins, $\frac{dX}{dR}$ is never zero, therefore (at $X = X_o$):

$$0 = \frac{d}{dX}\left\{\frac{2\left(1 - \exp\left(-X/2\right)\right)}{\sqrt{X}}\right\}\ . \tag{9.6}$$

$$\rightsquigarrow 1 + X_o = \exp\left(X_o/2\right)\ . \tag{9.7}$$

Equation 9.7 is solved numerically, giving

$$X_o = 2.513,\ \text{or}\ R_o = 1.585 \cdot \sigma\ . \tag{9.8}$$

Square bins: Square bins are typically used when a large fraction of the sky shall be covered with a grid of search bins. In this case,

$$\begin{array}{lll} \hat{N}_S & \propto \int_{-W}^{+W}\int_{-W}^{+W} \left(\sigma\sqrt{(2\pi)}\right)^{-2} \cdot \exp\left(-x^2/2\cdot\sigma^2\right)\cdot\exp\left(-y^2/2\cdot\sigma^2\right) & dxdy\ , \\ \hat{N}_{BG} & \propto \int_{-W}^{+W}\int_{-W}^{+W} 1 & dxdy\ . \end{array} \tag{9.9}$$

The optimal search bin has a half-width of $W = W_o$. One then gets

$$\begin{aligned} 0 = &\ \frac{d}{dW}\left\{\frac{\hat{N}_S}{\sqrt{(\hat{N}_{BG})}}\right\}\ , \\ 0 = &\ \frac{d}{dW}\left\{\frac{\mathrm{erf}(W/(\sqrt{2}\cdot\sigma))^2}{2W}\right\}\ , \\ 0 = &\ \frac{\sqrt{2}\ \mathrm{erf}(W_o/(\sqrt{2}\cdot\sigma))\exp\left(-W_o^2/(2\cdot\sigma^2)\right)}{W_o\sqrt{\pi}} - \frac{1}{2}\frac{\mathrm{erf}(W_o/(\sqrt{2}\cdot\sigma))^2}{W_o^2}\ . \end{aligned} \tag{9.10}$$

Numerically this can be solved, giving

$$W_o = 1.40 \cdot \sigma \approx \sqrt{2} \cdot \sigma \ . \tag{9.11}$$

Comparing equation 9.11 to equation 9.8, one notices that the area of an optimal circular bin is larger than the area of the optimal square bin, but the difference is less than 1.0 %. It might be surprising that the optimal bin-size depends on the search bin shape. But the original assumptions of a flat background and a Gaussian signal distribution in 2 dimensions contain a spherical symmetry. It is convincing that search bin shapes which reflect this symmetry have larger optimal sizes than those that don't reflect it.

Excursion: $\sigma_{63\,\%}$: As shown in equation 9.11, the optimal half-width for square bins is $W_o \approx \sqrt{2}\cdot\sigma$. This value is often referred to as $\sigma_{63\,\%} \equiv \sqrt{2}\cdot\sigma$. While 68 % of a 1-dimensional Gaussian distribution are contained in the region $[-\sigma..+\sigma]$, a circle of radius $\sigma_{63\,\%}$ contains 63 % of a 2-dimensional Gaussian distribution. This can be derived easily from equation 9.3 with the previously used substitution $x = r^2/\sigma^2$: $N_S = \text{const.} \cdot (1 - \exp(-x/2))$. Normalizing $N_S(x = \infty) \equiv 1$, one gets const. $\equiv 1$. Then $N_S(r = \sqrt{2} \cdot \sigma) = 1 - \exp(-1) = 0.63$.

Equations 9.8 and 9.11 can then be rewritten as

$$R_o = 1.12 \cdot \sigma_{63\,\%} \quad \text{and} \tag{9.12}$$

$$W_o = 0.99 \cdot \sigma_{63\,\%} \approx \sigma_{63\,\%} \ . \tag{9.13}$$

9.2.2 Non-Gaussian Signal Distributions

In the calculations performed above, the signal was assumed to have a Gaussian distribution. In most experiments, this assumption is not valid for large errors any more. In this case, one first has to determine a function $f(< \psi)$ giving the fraction of events which are reconstructed accurately to within ψ degrees. A parameterization of $f(< \psi)$ thus allows to follow similar calculations as the ones presented above. As discussed in section 9.1.1, $f(< \psi)$ was parameterized as

$$f(< \psi) = \sum_{i=0}^{8} a_i \cdot \psi^i \ . \tag{9.14}$$

a_0 $0.51828 \cdot 10^{-03}$	a_1 $-0.24233 \cdot 10^{-01}$	a_2 0.14739
a_3 $-0.46045 \cdot 10^{-01}$	a_4 $0.72012 \cdot 10^{-02}$	a_5 $-0.66485 \cdot 10^{-03}$
a_6 $0.36765 \cdot 10^{-04}$	a_7 $-0.11275 \cdot 10^{-05}$	a_8 $0.14735 \cdot 10^{-07}$

Table 9.1: The parameterization of the resolution function $f(< \psi)$.

Here, ψ is measured in degrees and the a_i are given in table 9.1. Substituting $\hat{N}_S$ of equation 9.4 by this parameterization (table 9.1) leads to an optimal bin-size of $R_o = 3.49°$

for circular bins. Comparing the calculations of $\hat{N}_S$ from circular bins to the case of square bins, one sees that $\int_0^{W_o} \frac{df(<\psi)}{dR_o} \frac{1}{R_o} dR_o$ replaces the error function in 9.10. Hence $f(<\psi)$ can also be used to calculate the optimal half-width of square bins. The result is $W_o = 2.29°$.

Likewise, one could also incorporate a non-flat background distribution by parameterization of the background. This has not been performed here, since the assumptions are still not appropriate for the case of AMANDA-B10.

9.2.3 AMANDA-B10 Scenario: Small Statistics

When $N_S \not\ll N_{BG}$ or $N_S \not\gg \sqrt{N_{BG}}$, $\frac{N_S}{\sqrt{N_{BG}}}$ is not a valid expression for the significance any more, see the derivation of equation 9.2. In [154], a more generalized formula is given for the significance which is still valid as long as $N_S \gg 1$ and $N_{BG} \gg 1$ (formula 17 in that paper). But in cases of very low statistics, even that formula is not valid any more. Then, the fluctuations on the number of background and signal events are dominant. General simple formulae for the significance can then not be derived easily any more.

In [144] it is therefore suggested to take a different approach and directly consider the chance probability P_c from equation 9.1. Via integration by parts, one can expand P_c as follows:

$$\begin{aligned}
P_c(n) = & \int_n^\infty \frac{dy}{\sqrt{2\pi}} \exp\left(\frac{-y^2}{2}\right) = \int_n^\infty \frac{dy}{\sqrt{2\pi}} \left[y \cdot \exp\left(\frac{-y^2}{2}\right)\right] \cdot \left(\frac{1}{y}\right) \\
= & \frac{1}{\sqrt{2\pi}} \frac{1}{n} \exp\left(\frac{-n^2}{2}\right) - \int_n^\infty \frac{dy}{\sqrt{2\pi}} \frac{1}{y^2} \exp\left(\frac{-y^2}{2}\right) \\
= & \frac{1}{\sqrt{2\pi}} \frac{1}{n} \exp\left(\frac{-n^2}{2}\right) - \frac{1}{\sqrt{2\pi}} \frac{1}{3} \frac{1}{n^3} \exp\left(\frac{-n^2}{2}\right) + \int_n^\infty \frac{dy}{\sqrt{2\pi}} \frac{1}{3} \frac{1}{y^4} \exp\left(\frac{-y^2}{2}\right) \\
= & \frac{1}{\sqrt{2\pi}} \cdot \sum_{i=0}^{\infty} \left\{ \left[\prod_{j=0}^{i} (2j+1) \right]^{-1} \frac{(-1)^i}{n^{2i+1}} \right\} \cdot \exp\left(\frac{-n^2}{2}\right) \\
= & \frac{1}{\sqrt{2\pi}} \frac{1}{n} \exp\left(\frac{-n^2}{2}\right) + \mathcal{O}\left(\frac{1}{3} \frac{1}{n^3} \exp\left(\frac{-n^2}{2}\right)\right) \\
\approx & \frac{1}{\sqrt{2\pi}} \frac{1}{n} \exp\left(\frac{-n^2}{2}\right)
\end{aligned} \tag{9.15}$$

Use has been made of the rapid convergence of the series which runs over i. The last expression can then be inverted numerically. In the case of large n, an analytic approximation is possible:

$$-\ln(P_c) \approx 0.5 \cdot n^2 + \ln(n) + 0.5 \cdot \ln(2\pi) \tag{9.16}$$

$$-\ln(P_c) \approx 0.5 \cdot n^2 \text{ for large } n \tag{9.17}$$

$$\rightsquigarrow n \approx \sqrt{-2 \cdot \ln(P_c)}\,. \tag{9.18}$$

Remember that n is the significance measured in units of standard deviations. It has thus been shown that the maximization of the significance is equivalent to the maximization of the expectation for $\sqrt{-\ln(P_c)}$. As expected, this in turn is equivalent to the minimization of the chance probability P_c.

In this work, the minimization is performed with toy Monte Carlo simulations. A large number of individual experiments will be performed. For each toy simulation, the obtained chance probability p_c is calculated. It is the probability that a particular measurement can be explained by background only. P_c is then the expectation value of p_c obtained when averaging over many individual simulated measurements: $P_c =< p_c >$.

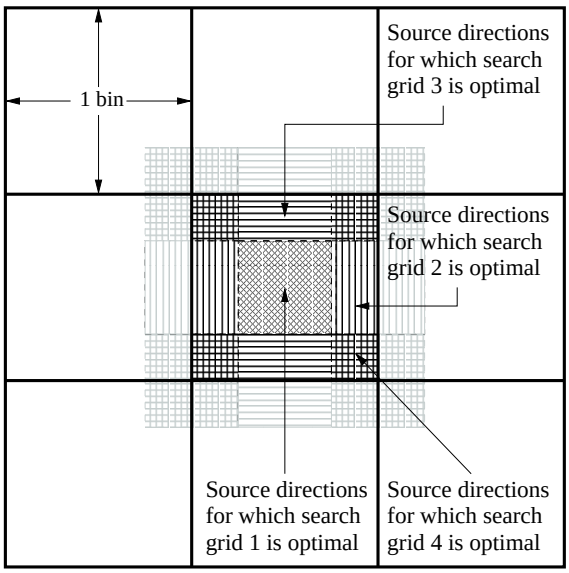

Figure 9.5: A model search grid containing 9 bins. The central bin is divided into nine subregions.

The toy simulation starts by constructing a grid of search bins. To do this, an arbitrary half-width w for the initial bins is chosen. One model search grid is then constructed with square search bins of half-width w. A 3×3 part of such a model grid is shown in figure 9.5. A second grid is then constructed by shifting all bins of the first grid by half a bin-width along their horizontal axes. A third and fourth grid are derived from the first two grids by similar shifts along their vertical axes.

Having constructed the four grids, an assumption about the source(s) has to be made. In this work, the optimization is performed for the hypothesis of a single source only. The source location is chosen at a random position. It is sufficient to consider only the source locations within the central quarter of one bin of one search grid: In figure 9.5, the central quarters of the bins of the four searches grids are shaded in four separate styles. They cover exactly the full search area. So any source location falls within the central quarter of one bin of one of the search grids. That bin is then the bin, the center of which is positioned closest to the source. It is thus expected to be most sensitive towards neutrinos from the source location.

After the source position is chosen, the detector response towards neutrinos from that source has to be defined. The detector response is assumed to be the similar to that for atmospheric neutrinos (given by $f(< \psi)$, see table 9.1). This is probably a worst-case assumption for the resolution since source spectra are generally believed to be harder than the atmospheric neutrino spectrum, and the resolution improves with spectral hardness – as can be seen from figure 9.4 (right). An error in this assumption will lead to non-optimal bin-sizes and hence to non-optimal limits.

The final assumption about the source concerns the source power in neutrinos (or the neutrino luminosity or the neutrino flux from the source). For simplicity, the source power is measured in N_S, the number of source events it causes in the data sample analyzed. N_S signal events are then randomly generated around the source according to $f(< \psi)$. So far,

N_S is a free parameter which does influence the final result. The dependency on it and the choice for it will be discussed section 9.2.4.

Finally, the background events are generated. They are generated randomly over the full grid. N_{BG}, the number of background events is the difference between total number of events observed (369 for the BG-100 selection) and N_S. The assumption of a random background distribution is actually not fully correct. Otherwise the zenith angle distribution of the BG-100 sample would have to be flat in figure 7.12 (right).

For this one set of source and background events, one now calculates p_c. It is the chance probability that the observed number of events in the source bin is arising from background only. Here, binomial statistics have to be used.

$$p_c = \binom{n}{k} \cdot (\tilde{p})^k \cdot (1-\tilde{p})^{(n-k)} \tag{9.19}$$

The parameters entering equation 9.19 are:

- n, the number of "trials". It is given by $n = N_S + N_{BG}$, the total number of events.
- k, the number of "successes". It is the number of events in the source bin
- $\tilde{p}$, the probability for an "individual success". It is the probability for an individual background event to be located inside the source bin. For the uniform background expectation assumed here, $\tilde{p}$ is simply the inverse of the number of bins.

The expected average chance probability P_c is obtained by averaging over many p_c values. This procedure described above for one source is therefore repeated 10^7 times to cover all potential source positions sufficiently often. The results were not stable when using fewer repetitions. P_c describes the expected average chance probability that the source bin has a population compatible with background.

The procedure described so far was for one bin-size only. What remains to be done is the actual optimization of the bin-size. This is achieved by systematically modifying the half-width w, as to obtain a curve $P_c(w)$. The optimal half-width w_o is then defined by the minimum of the curve. The expected average significance $\mathcal{S}$ for the optimal bin-size can be calculated via equation 9.18.

Figure 9.6 (left) shows the dependency of the expected average chance probability on the half-width of the bin-size. It can be seen that the chance probability drops rapidly with increasing bin-size for small bin-sizes. It then has a broad minimum and increases again. The optimal bin-size can readily be determined from it. The feature in $< p_c >$ at $\sim 4.6^\circ$ is not fully understood. It coincides with a vanishing second derivative of $f(< \psi)$ at that value.

9.2.4 Analysis of the Optimal Bin-Size

Figure 9.6 (right) shows the dependency of the optimal bin-size on N_S, the number of signal events simulated from the source. The smallest bin-sizes are obtained for 3–5 signal events. For smaller values, the bin-size increases. This is interpreted to be necessary to guarantee that at least one signal event is reconstructed within the source bin most of the

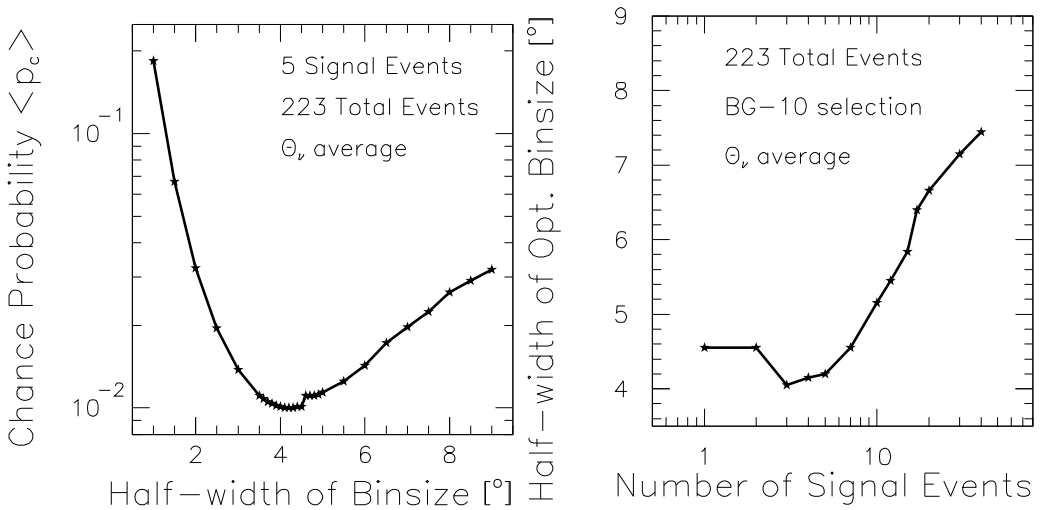

Figure 9.6: (Left:) The chance probability $< p_c >$ versus bin-size for the BG-10 selection, assuming 5 signal events from one source and averaged over angle. (Right:) The dependency of the optimal bin-size on the number of signal events for the BG-10 selection, averaged over zenith angle.
Most of the figures in this section show data for the BG-10 selection only. The search for neutrino sources shall be performed with data obtained from the BG-100 selection. A simple "bug" in the program calculating the points in the figures lead to the two data samples being mixed up. With less accuracy, all these plots have been reproduced for the BG-100 selection. Strong quantitative, but no qualitative differences were found. But only the qualitative behavior was meant to be illustrated here. To save CPU time, the figures were thus not reproduced for the data from the BG-100 selection. It was decided to show the BG-10 figures here due to their higher accuracy.

time. For larger number of signal events, the optimal bin-size rises as well. This can be understood as follows: The number of expected signal events increases, while the number of expected background events stays constant. The region where a significant fraction of the data is signal thus increases. Since aim of this optimization is to find one bin of large significance (and not several bins of mediocre significance), the optimal bin-size rises.

Figure 9.7 (left) shows the angular dependency of the optimal bin-size for the BG-1, the BG-10 and the BG-100 selection each time assuming 5 signal events. One notices two effects:

1. The optimal bin-size rises with tightened cuts. This is because the number of signal events remains fixed at 5. The leads to a relative increase in signal strength. Why this leads to larger bin-sizes has been discussed just before.

2. The angular dependency of the resolution can introduce angular dependencies of the bin-size. For tight cuts, the acceptance as well as the resolution is better for vertical events, leading to lower bin-sizes there. It is just a coincidence that the dependency is negligible in the case of the BG-100 selection (accuracy: 0.1°).

The right frame of that figure shows the dependency on the total background. Here, the total number of events (background plus signal) is varied, keeping the number of signal events fixed at 5. The optimal bin-size shrinks with increasing number of total events.

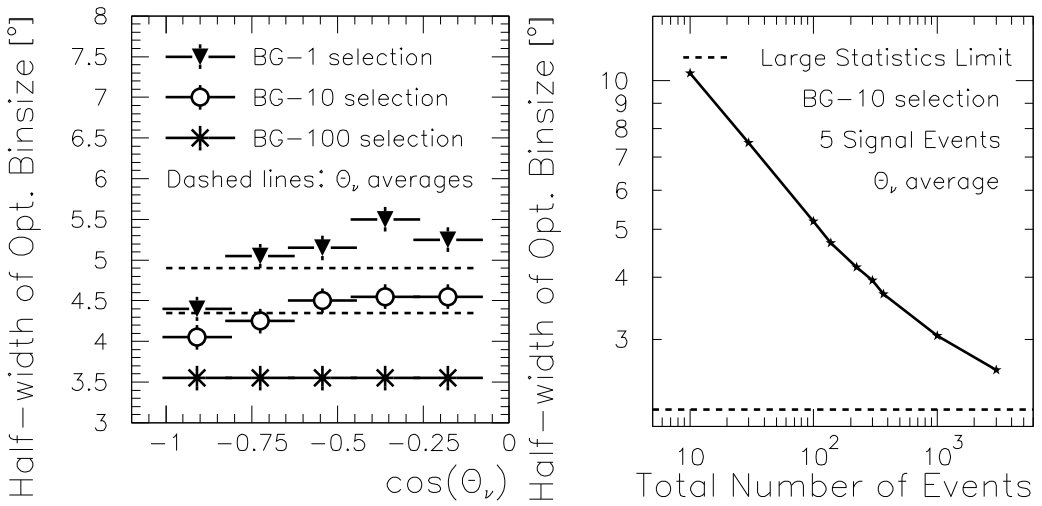

Figure 9.7: (Left:) the optimal bin-size versus reconstructed angle for the BG-1, the BG-10 and the BG-100 selection, assuming 5 signal events from one source. (Right:) The dependency of the optimal bin-size on the total number of events for five signal events, averaged over zenith angle and assuming the resolution of the BG-10 selection.

This is due to the opposite effect of what was just explained in the case of varying signal strength. This time the background level is increased, leading to a reduced region of significant signal, leading to smaller bin-sizes.

An angular dependency of the optimal bin-size could easily be included in the search for point sources. Since no such dependency was found for the BG-100 sample, this was not necessary. Since the data set has been fixed, the dependency on the total number of events is of indirect relevance only. What remains to be chosen is the signal strength for which the search should be optimized.

The analysis of data taken with the Super-Kamiokande detector uses for example source strengths of 10 signal events [166]. For a source causing 5 signal events in AMANDA-B10 data after the BG-100 selection, the minimal $< p_c >$-value obtained is 0.025. This gives an expected average significance of such a source of only $2.03\,\sigma$, see equation 9.18. With sources causing 4 or 6 signal events, the minimal $< p_c >$-values obtained would correspond to expected average expected significances of 1.76 or $2.31\,\sigma$. As a comparison: For the BG-10 selection and 5 signal events, the average expected significance would be $2.37\,\sigma$ – as can be seen when inserting the minimum $< p_c >$-value shown in figure 9.6 (left) into equation 9.18.

Due to the limited acceptance of AMANDA-B10, it had been decided in advance to optimize on low average expected significances of $\mathcal{O}(2)$ sigma. The significances obtained for sources causing five signal events (1.92) is lower than two, but comes closest. It was decided to optimize the bin-size for such signal strengths. The optimal half-width obtained from this is 3.55°.

In the literature, the optimal bin-size is sometimes defined slightly differently [144]. The parameter minimized instead of $< p_c >$ is then $\hat{p_c}$. That in turn is defined as the probability for a background only experiment to achieve a chance probability at least as

extreme as $< p_c >$ in the source bin. To calculate $\hat{p_c}$, the procedure described above to obtain $< p_c >$ is repeated for each bin-size for background only (the total number of simulated events staying constant). This approach was tested for specific settings, but did not improve the limits finally obtained. Since it is doubling the CPU requirements, it was discarded henceforth.

So far, the determination of the optimal bin-size ignored potential effects from systematic reconstruction errors and only considered the resolution σ. In [196] appendix B, the effects of a systematic reconstruction offset δ is investigated. The result is that in cases $\delta < 0.5 \cdot \sigma$, the reconstruction offset δ can simply be considered as a part of the resolution. The combined resolution is then:

$$\sigma_{combined} \approx \sqrt{\delta^2 + \sigma^2} \ . \tag{9.20}$$

In section 9.1.3 of this work, it has been discussed that despite some indications, no strong systematic offset is expected. Furthermore, such a systematic offset is only existing for the zenith angle resolution. For the optimization procedure described in this work, the space angle resolution has been used, which by definition cannot have such an offset.

Summary: The aim of this section was to calculate the "optimal" binsize. Such a task can only be achieved within a certain accuracy. The following aspects might lead to a non-optimal binsize:

- Wrong assumptions about the detector resolution towards the unknown signal neutrino spectra.
- The assumption of a flat background distribution is known to be wrong.
- The optimization has only been performed for square bins with sources at random positions in the central quarters. Such bins are appropriate for an all sky (grid) search as will be presented in section 10.4. When searching for fluxes from preselected sources (like in section 10.6), circular bins with source positions fixed at the bin centers would be more appropriate.

All this leads to non-optimal search bins. These in turn lead to non-optimal flux limits. But since non-optimal search bins can not lead to incorrectly tight flux limits, these are not considered systematic uncertainties for the flux limits finally obtained. Instead, these are aspects which might be improved in future analyzes.

9.3 Reconstruction Efficiency

Having fixed the size of the search bins to 3.55°, one further important parameter is implicitly fixed: The reconstruction efficiency ϵ_{bin}. The efficiency describes the fraction of source-events which are reconstructed within the source bin.

Figure 9.8 (left) shows the dependency of the efficiency on the incident neutrino angle for an assumed E^{-2} spectrum. It is evident that larger incident neutrino zenith angles yield larger efficiencies. This is due to the improved resolution for these angles, see figure 9.3. The average efficiency for the BG-100 sample is 0.62, which is similar to what is expected

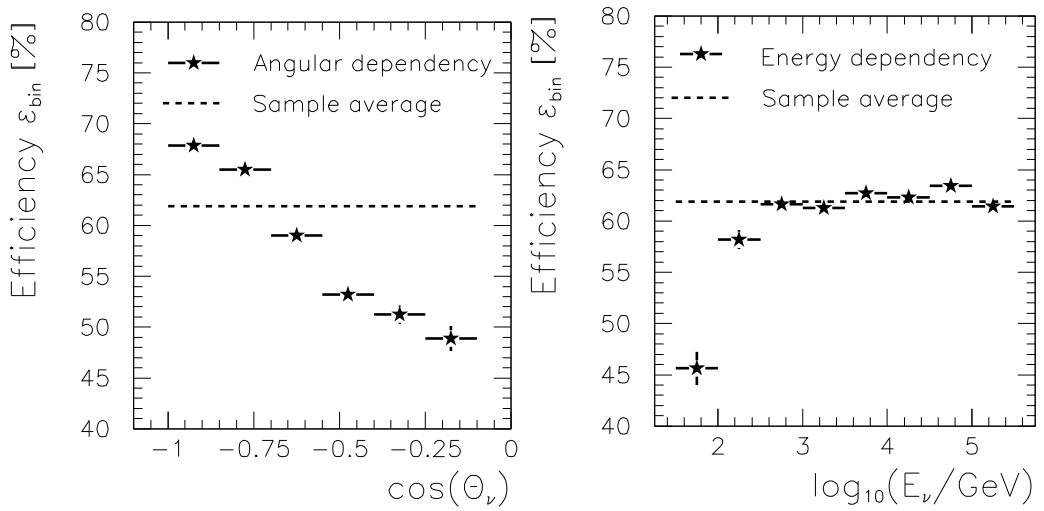

Figure 9.8: The angle (left) and energy (right) dependency of the efficiency ϵ_{bin} for arbitrary source positions within the central quarter of the source bin. Data after BG-100 selection for a simulated neutrino spectral index of $\gamma = -2$. Dashed line: Efficiency for an energy interval of $10^{1.0}\,\mathrm{GeV} \leq E_\nu \leq 10^{5.5}\,\mathrm{GeV}$ and an isotropic angular spectrum with $80^\circ \leq \theta_\nu \leq 180^\circ$. Points: Data binned in $\cos(\theta_\nu)$ (left) and $\log(E_\nu)$ (right). Vertical error bars correspond to statistical errors only.

for angles $\theta_\nu \approx 135^\circ$. The difference between average and maximum efficiency is 6.0 %. The angular dependency is strong: In the angular range shown, the efficiency varies by almost 20 % in absolute numbers.

The dependency on the neutrino energy is shown in figure 9.8 (right). The efficiency is almost constant for energies larger than $E_\nu \approx 200\,\mathrm{GeV}$. This is explained by the improved resolution with increased energy, as already discussed for figure 9.4. The efficiency averaged over an E^{-2} spectrum is dominated by this high-energy range. This is because low energy events are suppressed by the cuts applied during the data processing. This would be different for the softer atmospheric neutrino spectrum.

Figure 9.9 finally shows the dependency of the efficiency on the spectral index. For $-3 \leq \gamma \leq -2$, the efficiency increases with spectral hardness, for even harder spectra it is constant. The reason for the saturation is the saturation in the energy dependency of the efficiency: For hard spectra, the contribution of low energy neutrinos $E_\nu \leq 100\,\mathrm{GeV}$ becomes insignificant. Since the efficiency is constant for higher neutrino energies, it is constant for the hard spectra as well. For spectra softer than E^{-2}, the contribution of low energy neutrinos becomes significant. The softer the spectrum, the larger is the contribution of these low energy events with their low efficiency.

The definition of the efficiency stated above was: *The efficiency describes the fraction of source-events which are reconstructed within the source bin.* This general definition does not make any statement about where the source is located inside the source bin. But this location is important. The efficiency is obviously higher for a source in the center of a bin than for a source close to the edge of a bin.

For the following point source analysis, two separate cases have to be investigated. The first case corresponds to searches for which the source is known to be located in the

center of the search bin. The resulting efficiency $\epsilon_{bin,\,selected}$ is needed when searching for preselected sources in section 10.6.

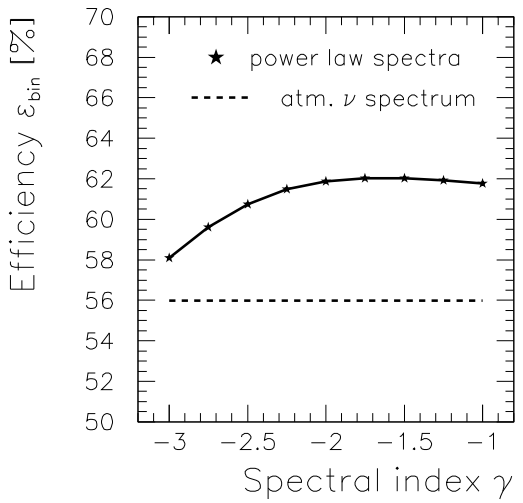

Figure 9.9: The spectrum dependency of the efficiency ϵ_{bin} for arbitrary source positions within the central quarter of the source bin. Simulated signal data after BG-100 selection. Efficiency for an energy interval of $10^{1.0}\,\mathrm{GeV} \leq E_\nu \leq 10^{5.5}\,\mathrm{GeV}$ and an isotropic angular spectrum with $80° \leq \theta_\nu \leq 180°$. Dashed line: Atmospheric neutrino spectrum. Points: Various power law spectra.

The situation is different for the case of the binned analysis which uses search grids and is presented in section 10.4. In that case, a source can be located at any position within the search bin. The corresponding efficiency $\epsilon_{bin,\,grid}$ is defined for sources at random positions within the bin. In section 9.2.3, it has already been discussed that it is sufficient to consider random source positions within the central quarter of search bins only. Reason is that four shifted grids of search bins will be used. A second order effect has been neglected here: Even within the central quarter of a bin, the efficiency is not constant but varying from the very center to the edge of the central quarter. This leads to a slight selection effect of a higher sensitivity towards sources in the very center of the bins. Correcting for this selection effect would slightly increase the values of the efficiency $\epsilon_{bin,\,grid}$ and hence yield slightly stronger flux limits. Ignoring this selection effect thus leads to conservative limits.

The efficiencies shown and quantified in this section so far were all defined according to this second definition. The systematic dependencies of $\epsilon_{bin,\,selected}$ are equivalent to those shown for $\epsilon_{bin,\,grid}$. On average, $\epsilon_{bin,\,selected}$ is 4 % to 10 % larger than $\epsilon_{bin,\,grid}$. The difference is strongest for shallow declinations.

In appendix F, both efficiencies ($\epsilon_{bin,\,selected}$ and $\epsilon_{bin,\,grid}$) are tabulated. There, efficiencies are listed for all combinations of the θ_ν-intervals, E_ν-intervals and spectral indices investigated.

The systematic uncertainty on the efficiency is considered to be of the same size, as that on the resolution: $< 15\,\%$ (see section 9.1.4). The statistical errors are given in the tables in appendix F. They are on average $\sim 4\,\%$. They increase from $\sim 1.5\,\%$ for the highest energies and largest declinations to $\sim 20\,\%$ ($\epsilon_{bin,\,selected}$) or 25 % ($\epsilon_{bin,\,grid}$) for the lowest energies and shallowest declinations. The statistical uncertainties on efficiencies which are averaged over several declination and/or energy bins are correspondingly smaller. No significant dependencies of the uncertainties on the spectral index have been identified.

10 Extraterrestrial Point Source Searches

It is a common task in high-energy astro-particle physics to look for point sources of detected individual events. Examples of other experiments which have published such searches include the HEGRA air shower array at La Palma, Spain [144, 196], the underground muon detector MACRO in the Gran Sasso Laboratory, Italy [7] or the water Cherenkov detector Super-Kamiokande in the Kamioka mine, Japan [166].

10.1 Motivation

Neutrino telescopes can only achieve detector resolutions of $\mathcal{O}(1^\circ)$ with respect to neutrinos, see equation 6.1. The angular extension of potential sources in contrast is significantly smaller. They can therefore always be considered as point-like. When looking for such point-like sources, the standard approach is to select the data such that one obtains a very good angular resolution. The better the angular resolution, the smaller search cones can be used to look for potential sources. Reason is that one typically assumes the background to be flat in the vicinity of a potential source. In small search cones, one then only has a small fraction of the total number of background events. One thus can accept a considerable total background. In a first approximation, an improvement in the (1-dimensional) signal resolution by a factor of two reduces the size of the (2-dimensional) search cones by a factor of four. The standard AMANDA point source search [137, 251] followed this approach. The passing rates of the cuts applied there, approximately correspond to the level 4a cuts of this analysis, see section 7.1.4 and table D.14. The data set analyzed there is correspondingly dominated by residual atmospheric muons.

For AMANDA, however, there are additional challenges as compared to other experiments. The AMANDA detector coordinate "zenith angle" is equivalent to the celestial coordinate "declination" ($+90^\circ$, see appendix A.2.1). Systematic effects in detector zenith therefore directly translate into systematic effects in celestial declination. An example is the "z_{COG} background" (c.f. discussion in section 7.1.4). This background causes bands of constant declination which are more densely populated than others. Likewise, uncertainties on the muon propagation (see section 7.3.4) cause uncertainties in the zenith angle distribution for atmospheric muons. Reason is that the propagation length over which the uncertainty is integrated grows with $\sec(\theta)$. This effect does not exist for the isotropic atmospheric neutrino background. A different aspect is that the background (both atmospheric muons and atmospheric neutrinos) is in general not flat. Instead, it often shows a significant zenith (i.e. declination) dependency, see figure 7.13 (right). With a non-flat background, the optimal search cone size shrinks slower than the square of the signal resolution. The benefit of an optimized angular resolution is therefore reduced and a good atmospheric muon suppression becomes more important.

It is nevertheless vital to perform the standard AMANDA point source search [251]. But the above arguments motivate a complementary alternative approach. Such an alternative is to base a point source search on an atmospheric neutrino analysis. The main advantage of the standard search are the relaxed cuts and thus the enhanced signal sensitivity. The main advantage of the alternative approach are the smaller systematic uncertainties of the data: In both cases the data set consists of nearly 100 % background. In the standard

search, the background dominantly consists of atmospheric muons, which have been reduced by a factor $\sim 10^{-6}$ from trigger level. In the alternative approach, the background is dominated by atmospheric neutrino events, which have been reduced by a factor ~ 20. While the simulation cannot describe the residual atmospheric muons any more, it does describe the atmospheric neutrinos. During data processing, the main goal of the standard point source analysis is to achieve a good angular resolution for neutrino events. The main goal during cut selection for the alternative approach is a good suppression of atmospheric muon background. These two tasks are closely related but not identical.

In [251], it has been shown that in any case and irrespective of any other (dis-)advantages, it might be necessary to perform complementary searches: One analysis can only treat a certain range of cut sets. But for each potential source spectrum, the optimal set of cuts is different. In general, soft cuts are optimal for hard spectra while tight cuts are optimal for soft spectra. The standard point source analysis [251] defined its cuts appropriate for an E^{-2} spectrum since this corresponds to the generic Fermi acceleration (see section 2.1). An atmospheric neutrino analysis in contrast implicitly optimizes cuts for spectra close to the atmospheric neutrino spectrum of $\sim E_\nu^{-3.7}$ (for $E_\nu > 1\,\mathrm{TeV}$). Realistic source spectra are *believed* to have spectral indices of $2.1 \leq \gamma \leq 2.4$, see section 2.1. Since nobody *knows* which spectra neutrino sources do have, complementary searches optimized for different spectra seem appropriate. The approach to base a point source search on an atmospheric neutrino analysis (called "alternative approach" up to now) is taken in the work presented here.

10.2 Data Sample

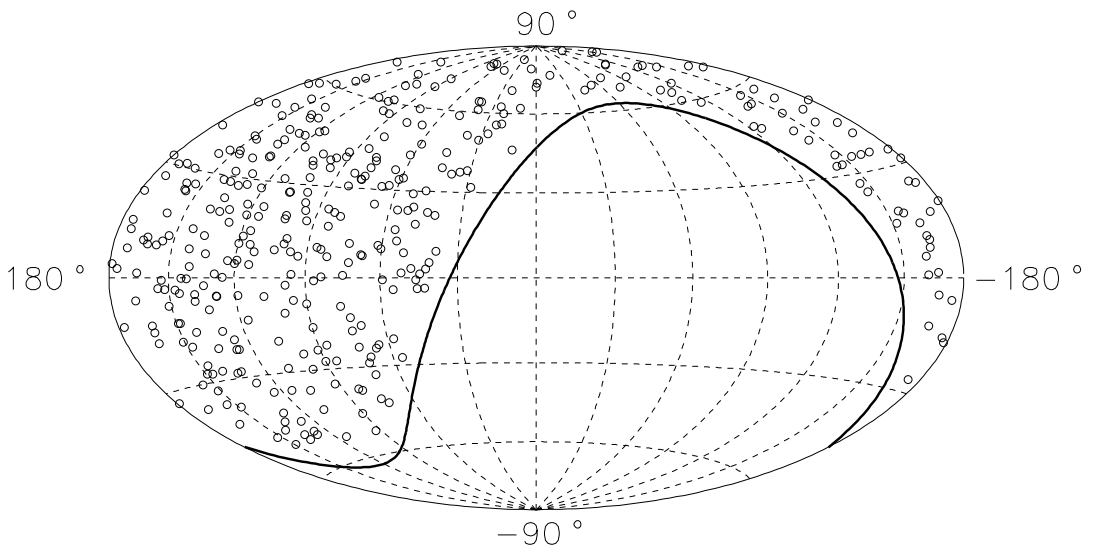

Figure 10.1: The celestial distribution of the BG-100 sample in galactic coordinates. These coordinates are defined in appendix A.2.1. The projection used is the Hammer-Aitoff equal area projection given in appendix A.2.4. The AMANDA horizon is indicated by the curved line. Mind the astronomical convention that the horizontal axis runs from right to left.

The data sample used for this search is the one defined via the "BG-100" selection in section 7.2. Unless explicitly stated otherwise, all data sets used in the following refer to that selection. The celestial distribution of these events in galactic coordinates is shown in figure 10.1. The definition of these coordinates can be found in appendix A.2.1. The bulk of the galactic matter is concentrated around the horizontal axis in this figure with the galactic center being in the center of it. The curved line indicates the horizon of AMANDA. One sees that AMANDA-B10 has zero sensitivity towards the galactic center. There is no correlation between the observed events and the galactic disk.

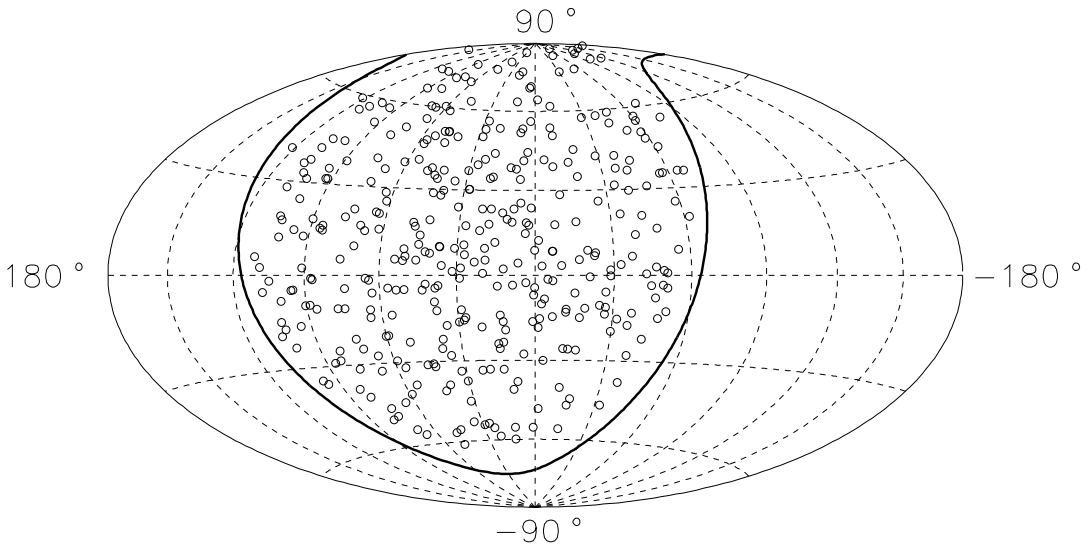

Figure 10.2: The celestial distribution of the BG-100 sample in super-galactic coordinates, as defined in appendix A.2.1. The projection used is the Hammer-Aitoff equal area projection, see appendix A.2.4. The AMANDA horizon is indicated by the curved line. Mind the astronomical convention that the horizontal axis runs from right to left.

Figure 10.2 presents the same data, this time in super-galactic coordinates. Again, the definition of these coordinates can be found in appendix A.2.1. The majority of galaxies (and AGNs) of the local super-cluster is located around the horizontal axis in these coordinates. AMANDA-B10 has a good sensitivity towards the super-galactic center. Like in galactic coordinates, there is also no obvious correlation between the observed events and the super-galactic disk.

10.3 Search Strategies

Various search strategies will be performed. They can be grouped in three categories:

Binned (grid) searches: The search cones are centered along arbitrary directions. They are adjacent and define a grid covering the whole sky.

Selected sources: The search cones are centered on selected sources.

Cluster searches: The search cones are centered on the directions of the detected events.

Each of these strategies has its own particular set of advantages and disadvantages. They are summarized in table 10.1. To benefit from all the advantages, all three strategies have been used during this work. They will be presented in the following sections 10.4 to 10.6.

Aspect	Binned (Grid) Search	Selected Sources	Cluster search
Sky Coverage	+	-	+
Flux limits	+	+	-
Bin-boundaries	-	+	+

Table 10.1: The advantages (+) and disadvantages (-) of potential search strategies. A justification of these classifications is given in sections 10.4 to 10.6, where the strategies will be discussed individually.

10.4 Binned (Grid) Search

The main challenge of a binned analysis is the non-uniform sensitivity of the search towards sources within an individual search bin: A potential source in the bin center has a higher chance to be detected than one at the borders. In order to compensate this, it is common to repeat the analysis with shifted bins. A source at the edge of a bin in one grid is then close to the center of a different bin in a shifted grid. With three grids shifted along a third of the bin-diagonal, one could guarantee that no source would lie on bin edges in all three grids. Since most grids are based on quadratic bins, it is easier to use four grids: The difference between first and second grid is a shift by half a bin-width along one axis. Likewise, the difference between third and first or fourth and second grid is a shift by half a bin-width along the other axis. One thus obtains four grids and the guarantee to have each (source) direction in the central quarter of one of the grids, see figure 9.5.

10.4.1 Definition of the Search Grids

Before being able to construct the grids, the number and size of the search bins used has to be defined. In section 9.2, it has been shown that the half-width of the optimal search bin is 3.55°, irrespective of the zenith angle. It thus covers an area of 50.41 square degrees. As follows from equation 7.6, the data set analyzed here covers regions in the sky with $5° \leq \delta \leq 90°$. This corresponds to an area of

$$2 \cdot \pi \cdot (\sin(90°) - \sin(5°))\,\mathrm{sr} = 5.7\,\mathrm{sr} = 18,829 \text{ square degrees} \quad (10.1)$$

$$\text{since } 1\,\mathrm{sr} \equiv (360/2\pi) \text{ square degrees .} \quad (10.2)$$

To fit this area with an integer number of bins, 374 search bins of half-width 3.548° (each covering an area of 50.34 square degrees) were used for the search grids.

All four grids were based on quadratic search bins. Two different projections of the first grid are shown in figures 10.3 and 10.4. The upper and lower bin boundaries correspond to lines of constant declination, whereas the right and left boundaries correspond to lines of constant right ascension, see figure 10.3. The first and second grid share the same boundaries of constant declination. Likewise, the third and fourth grid share the same

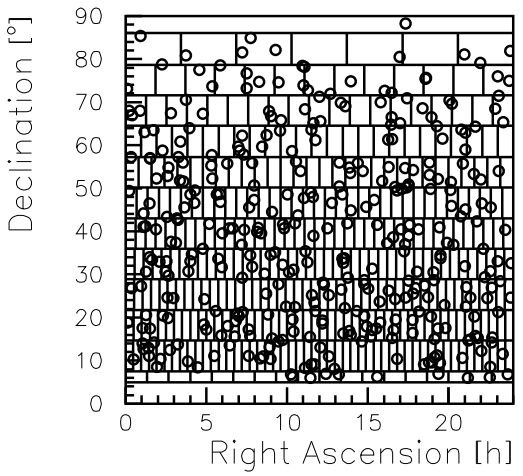

Figure 10.3: The search bins used for the first search grid in a non-equal area projection. All bins contain the same solid angle. The grids are defined in section 10.4.1.

"declination bands". The first band of the first two grids is defined by one circular bin covering all declinations larger than a certain value δ_1. Here, δ_1 is chosen such that the one circular bin defined by it covers the required search bin area of 50.41 square degrees. Hence $\delta_1 = 86.00°$ The neighboring declination band is then set to a width as close to the optimal bin width ($2 \cdot 3.548°$) as possible, so that an integer number of bins fits inside the band. The lower boundary of that second declination band is at $\delta_2 = 78.66$ and this second band contains 7 bins. Likewise, all consecutive declination bands are defined by two criteria:

1. Each declination band contains an integer number of bins.

2. The width of each declination band is as close as possible to $2 \cdot 3.548°$.

The reason for the second criterion is that it guarantees as quadratic bins as possible. This is necessary, since the bin-size optimization has only been performed for quadratic bins. The least distorted projection of their quadratic shape can be seen in figure 10.4 for right ascensions $\alpha \sim 12\,\mathrm{h}$. The only setback of this grid definition is the last declination band: The width of that band might be very different from $2 \cdot 3.548°$ and the bins inside that band are in general not quadratic. This can be seen in figures 10.3 and 10.4. This non-optimal declination band is acceptable for this analysis, since the detector performance is poorest for such shallow declinations.

Now all the declination bands for the first two grids are defined. The difference between the two grids are the locations of the bin boundaries within a band. The first grid is defined such that directions of right ascension $\alpha = 0\,\mathrm{h}$ are located on search bin boundaries, as shown in figures 10.3 and 10.4. The second grid is then obtained by shifting all bins by half a bin width in right ascension.

The third and fourth grid again share the same declination bands. This time, the criteria defining the declination bands are:

1. The band contains an integer number of bins and

2. the declination band boundaries are as close as possible to the centers of the declination bands of the first two grids.

The first two bands of these two grids are thus characterized by $\tilde{\delta_1} = 81.99$ and $\tilde{\delta_2} = 74.98$. The bands contain 4 and 10 bins respectively. The difference between search grids 3 and 4 is again the locations of the vertical bin boundaries within a band. Directions of right ascension $\alpha = 0\,\mathrm{h}$ are located on search bin boundaries for grid 3, but in the center of bins of grid 4.

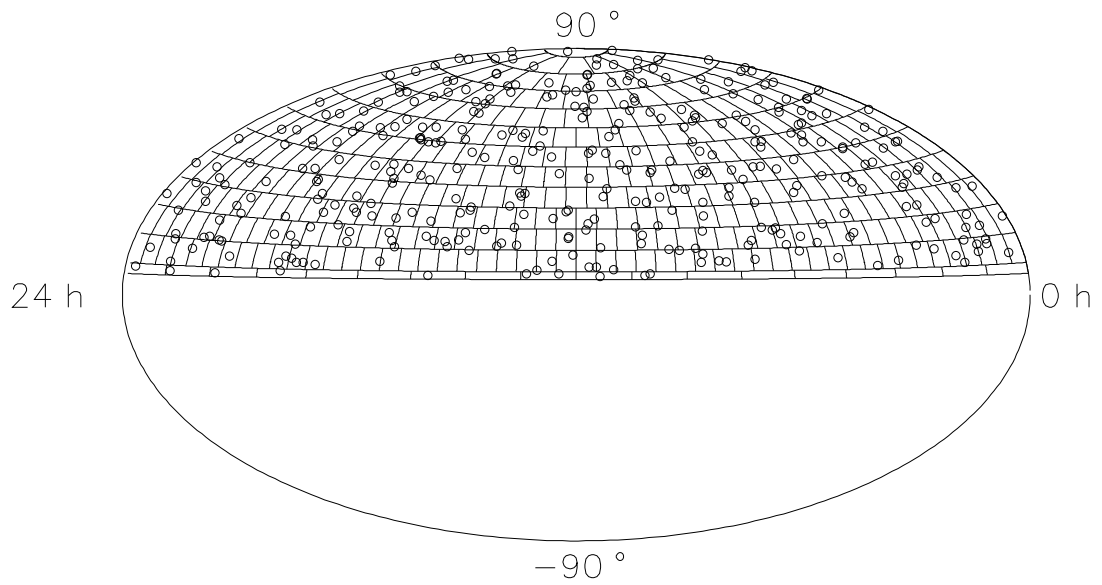

Figure 10.4: The celestial distribution of the BG-100 sample in equatorial coordinates and the search bins used for the first grid as described in section 10.4.1. The projection applied is the Hammer-Aitoff equal area projection, see appendix A.2.4. Mind the astronomical convention that the horizontal axis runs from right to left.

10.4.2 H_0 Hypotheses

Having defined the search grids (i.e. the locations of the search bins), one can then analyze the data for excess events within individual bins. The definition of an excess requires the comparison to an expectation for the distribution of background events. This expectation (or H_0 hypothesis) contains four assumptions, the first three of which are:

- The background events are *independent* from one another.
- The probability distribution for the background events is the product of two independent distributions. One distribution describes the right ascension (or detector azimuth) angle distribution and the other one the declination (or detector zenith) angle distribution.
- The probability distribution for the azimuth angle is uniform (and hence also that for the right ascension).

What remains is the assumption on the distribution of events in declination/zenith angle. Here, two slightly different assumptions (yielding two different H_0 hypothesis) were used:

Hypothesis 1 (H_0^1) *The distribution of background events in declination is described by the distribution of simulated atmospheric neutrinos.*

Hypothesis 2 (H_0^2) *The distribution of background events in declination is described by the experimentally observed distribution.*

The advantages of hypothesis 1 are that it is neither biased by statistical fluctuations of the experiment, nor by potentially existing astrophysical neutrinos in the data sample. The advantage of hypothesis 2 is that it does not rely on the uncertainties of the simulation results. It seems that hypothesis 2 is the present standard in the literature when $\mathcal{O}(1000)$ events are analyzed [5, 144, 251].

Hypothesis 2 could be modified to exclude the events inside the search bin from the determination of expected background for that search bin. But such a hypothesis 3 causes problems for bins which contain a significant fraction of the total number of events in the band. This happens in bands with low event populations or with few number of bins (e.g. in the uppermost declination bands of this analysis). Such a hypothesis 3, or any further potential hypothesis, are hence not investigated in this work.

A toy Monte Carlo simulation representing hypothesis 1 can be obtained from the experimental data sample. Each event gets assigned a random azimuth angle, but the zenith angles remain unchanged. In a similar way, a toy Monte Carlo simulation for hypothesis 2 can be produced. This time the zenith angles are also modified. They are chosen randomly, according to the simulated distribution. These toy Monte Carlo simulations then define the expectation for the population of each search bin. A comparison to the observed population allows the identification of an unexpected excess.

10.4.3 Significance of Excess

In a naive approach, one would take the number of observed events n_O within one bin and compare it to $\hat{n}_{BG}$, the number of events expected from the toy simulation. The parameter $\mathcal{S} = (n_O - \hat{n}_{BG})/\sqrt{(\hat{n}_{BG})}$ would then be considered the significance of the excess, see equation 9.2. The problem is that equation 9.2 is only valid for assumptions which do not apply to the data set analyzed, see section 9.2. One example is the identification of a standard deviation with $\sqrt{(\hat{n}_{BG})}$, which is not valid here, since the Poissonian limit is not given.

Instead, the chance probability P_c is compared between experiment and toy simulation, see [5,166]. It describes the probability that the population of one search bin is caused by a random distribution of all events within the search bin's declination band. It is calculated from binomial statistics. Let N_{bins} be the number of bins within the declination band, n_{band} be the number of events inside the declination band and n_{bin} be the number of events inside the search bin. The probability for any event within that band to be located inside the search bin is then $\frac{1}{N_{bins}}$. The chance probability P_c for a bin is therefore given by

$$P_c = \binom{n_{band}}{n_{bin}} \cdot \left(\frac{1}{N_{bins}}\right)^{n_{bin}} \cdot \left(1 - \frac{1}{N_{bins}}\right)^{n_{band}-n_{bin}} \quad \text{(binomial statistics)} \qquad (10.3)$$

A remark has to be made concerning multiple searches for sources in the same data set. Various searches within the same data set will be presented here and other searches with related data sets have been performed elsewhere [137, 251]. It is well known that throwing a dice often enough, one will eventually throw five sixes in a row. One might fear that looking at the same data often enough, one will eventually find a significant source — irrespective of the true existence of such a source. This is, however, not the case. Reason is that the various searches are not independent but use the same data set.

What would correspond to throwing the dice multiple times would be to take data year after year and each time only analyzing one year of data. In that case, one would expect to find a significant point source eventually – whether such a source exists or not.

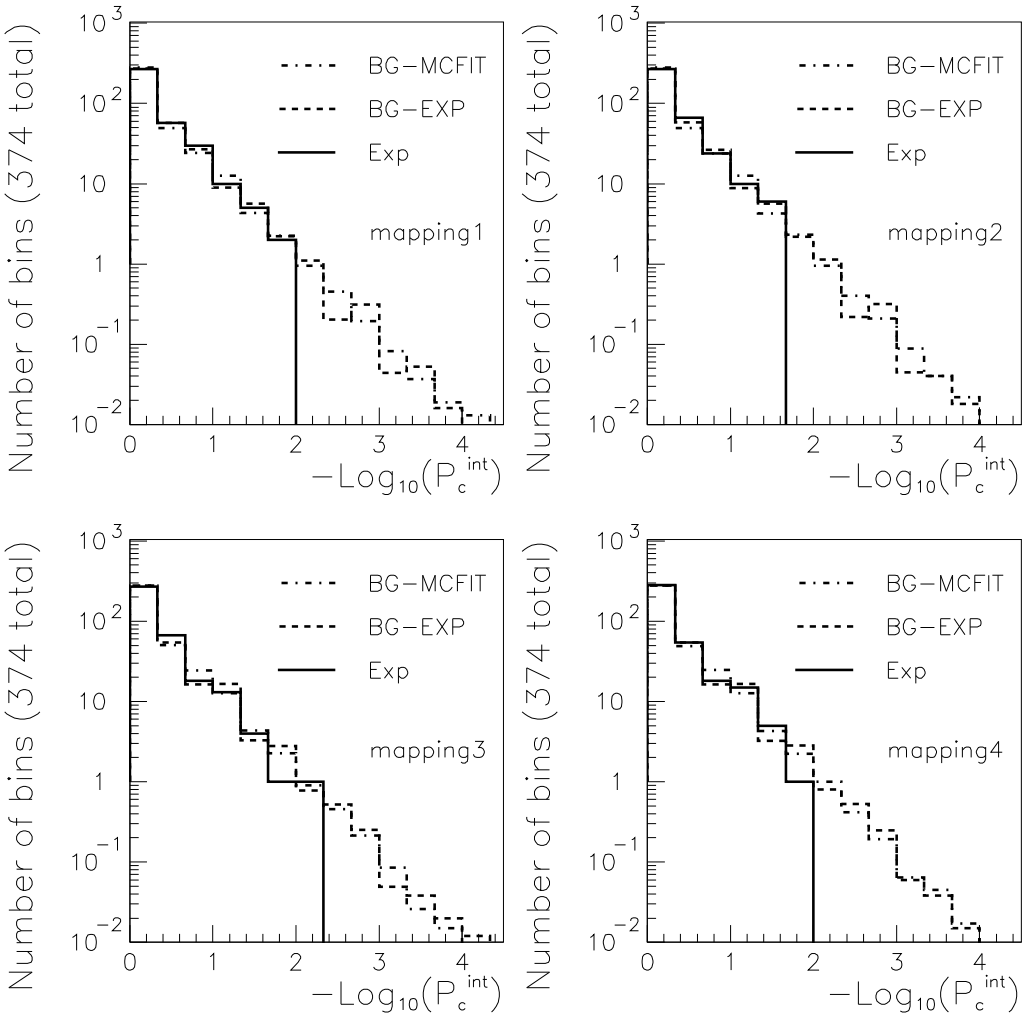

Figure 10.5: The integral distribution of chance probabilities for the binned search. Dash-dotted line ("BG-MCFIT"): Toy Monte Carlo corresponding to hypothesis 1. Dashed line ("BG-EXP"): Toy Monte Carlo corresponding to hypothesis 2; Solid line ("Exp"): Experimental distribution.

But something similar has to be considered: The 374 individual search bins within one grid are independent. It is thus expected that a few of them will give very low chance probabilities. The definition of a significant excess can therefore not simply be made by defining the minimal allowed P_c value. Such a limit instead has to depend on the number of search bins. This can for example be achieved using the *false discovery rate* method [168]. Here, a different approach is taken. Rather than setting a limit on P_c values of individual bins, the comparison between observed events and toy simulation is used for all bins simultaneously. In figure 10.5 this comparison is performed. Both toy simulations introduced in section 10.4.2 randomly distributed 369 events over the sky. The chance

probabilities were analyzed and the procedure repeated 1000 times. The distribution of simulated P_c values (scaled down by a factor of 1000) nicely matches the corresponding distribution for the experimental data. The figure actually shows the integral distribution of chance probabilities P_c^{int}, i.e. the chance probabilities for at least the observed number of events. There is no indication for unexplained low P_c^{int} values for any of the four searches with the four search grids. The most extreme P_c^{int} value in experimental data is $P_{c,\,min}^{int} = 9.24 \cdot 10^{-3}$. It is obtained for a bin which contains 5 events while 1.32 are expected from 29 events in 22 bins of the corresponding band. The bin is from search grid 3 and has the direction: $8.73\,\mathrm{h} \leq \alpha \leq 9.82\,\mathrm{h}$; $60.82^\circ \leq \delta \leq 67.94^\circ$.

A chance probability $P_c^{int} \leq P_{c,\,min}^{int}$ occurs 6361 (6841) times in the toy simulations formed according to hypothesis 1 (2). Since the toy simulations were repeated 1000 times each, the expectation for the number of bins in experimental data with $P_c^{int} \leq P_{c,\,min}^{int}$ is 6.361 (6.841). The probability to observe *at least* one such bin are larger than 99 % for both hypotheses. There is no indication of an excess of low P_c^{int}-values in experimental data as compared to the H_0 expectation. As a comparison: The average P_c^{int}-value expected from a source which causes five signal events in a bin of average declination (also containing one background event) is $P_c^{int} = 10^{-3.26}$. A corresponding entry would show up prominently in figure 10.5. It is thus concluded that none of the four searches gives any indications for the existence of a point source in the data analyzed. Based on this result, an all-sky upper limit on the flux of neutrinos from point sources is calculated in section 11.1.

10.5 Cluster Search

It is not evident how to define all-sky flux limits based on a cluster search. But a cluster search can be used to find point source candidate directions. Furthermore, it has neither the bin boundary problem of the binned search, nor the sky coverage limitations of the search for pre-selected sources (see below). Therefore a cluster search has been performed in this analysis. The search cones used were again quadratic, this time centered on the reconstructed arrival direction of the measured events (δ, α). The bins covered those directions spanned by $\{\delta \pm 3.55^\circ\} \otimes \{\alpha \pm (3.55^\circ / \sin(\delta))\}$.

Figure 10.6 (left) shows the distribution of the number of events within these 369 search windows. By definition, the minimum population in each bin is 1. As a comparison, the distribution obtained from the previously introduced toy simulations have been included. No excess of large clusters can be seen in this figure. On the contrary, a deficit of large clusters (many events within one search cone) exists, which is compensated by a slight excess of small clusters.

This indicates that the events are more evenly spread over the sky than expected from the H_0 hypotheses. This in turn is evidence that the H_0 hypotheses might not be appropriate to describe the experimental data. This interpretation is still being investigated. It is not confirmed by the distribution of chance probabilities calculated during the binned search or that calculated during the search for selected sources.

For the purpose of this work it is important to note that the cluster analysis yields no indication for an excess of large clusters, i.e. there is no indication for the existence of point sources. The corresponding distribution of chance probabilities (not shown) also does not show indications for an excess of low chance probabilities.

10.6 Selected Sources

The obvious challenge of a search for selected sources is to select the most luminous sources. Since no observations of astrophysical high-energy neutrino sources exist, this is practically an impossible task. It is thus likely that some of the strongest neutrino sources are not selected. When only pre-selected sources are searched for, such non-selected sources cannot be discovered. In other words, the strategy to search for selected sources does not "cover the full sky". Its main advantage are the optimal flux measurements/limits obtained for the selected sources.

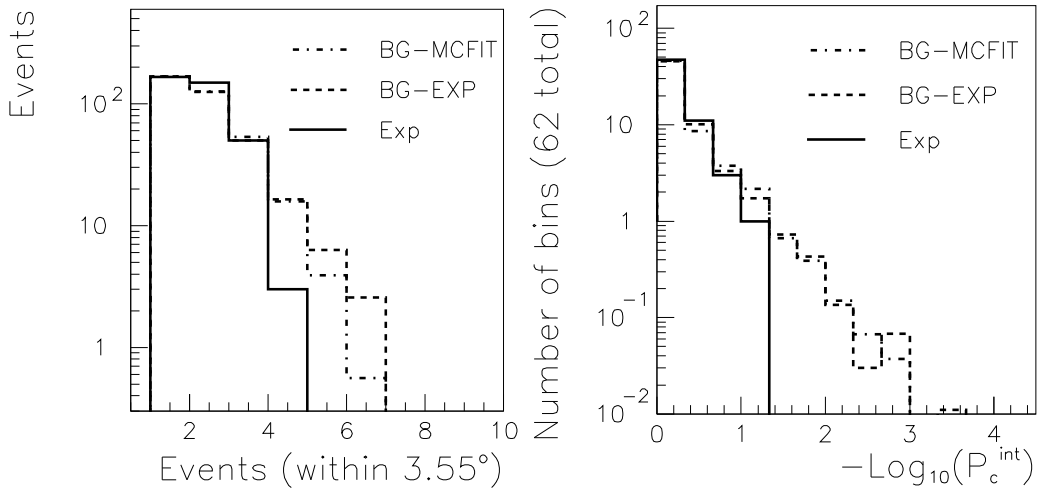

Figure 10.6: (Left:) Cluster search: Number of events within search bins around each single event. (Right:) The integral distribution of chance probabilities for the selected sources search. Solid line ("Exp"): Experimental distribution. Dashed line ("BG-EXP"): Toy Monte Carlo corresponding to hypothesis 2. Dash-dotted line ("BG-MCFIT"): Toy Monte Carlo corresponding to hypothesis 1.

There exists a great number of theories describing potential astrophysical high energy neutrino sources, see section 2. Since no sources have been discovered so far, it is not *known* which criteria define sources that yield the highest neutrino fluxes. For the purpose of this work, several classes of potential sources are defined. One example of such a source class are blazars detected in γ-rays by the EGRET satellite [113]. For each class, individual sources are selected which are "strongest" in some parameter which is characteristic for the class. In the EGRET example, the individual sources selected were the five sources strongest in the EGRET parameter "maximum detected flux". All selected classes and sources, as well as the motivations for each selection, are listed in section 11.2. In total, 10 classes containing 62 potential sources have been selected. This selection is by far not a complete list, but should indicate potential selection schemes for future neutrino point source searches.

Like in the cluster search, the search cones used were quadratic. They cover those directions spanned by $\{\delta \pm 3.55°\} \otimes \{\alpha \pm (3.55°/\sin(\delta))\}$, where (δ, α) is the source position.

Just like in the case of the binned analysis, the chance probabilities were calculated. The declination distribution of the pre-selected events is different from that of the bins in the binned (grid) search. The distributions of chance probabilities in this search (shown

in figure 10.6 (right)) can thus have a different shape from the corresponding distributions for the binned search. This time, the most extreme P_c^{int} value in experimental data is $P_{c,\,min}^{int} = 9.51 \cdot 10^{-2}$. It is obtained for the direction of an UHECR triplet called triplet 1 in table 11.12 ($\alpha = 1.28\,\mathrm{h}$, $\delta = 20.37°$). The corresponding search bin contains 3 events while 1.045 are expected from 43 events in 41.157 bins of the corresponding band. (For this search, there is no need to demand an integer number of bins in the declination band.) P_c^{int}-values at least as extreme as this are expected to occur 3.1 times (H_0 hypothesis 2) or 3.3 (H_0 hypothesis 1) times. The observation of at least one case with $P_c^{int} \leq 9.51 \cdot 10^{-2}$ is thus expected. Correspondingly, no indications for the existence of neutrino point sources can be inferred from this search. Instead, upper limits on the neutrino fluxes from these sources were calculated. They are given in section 11.2.

If several point sources exist, but their fluxes are all just below those necessary for a clear detection in telescopes, only upper flux limits can be derived. A last resort to still discover sources is then the super-positioning (or stackering) of several homogeneously selected sources [245]. The flux limit expected from stackering n sources is $\mathcal{O}(\sqrt{(n)} \cdot \Phi)$, where Φ is the average flux limit for an individual source. Without stackering, the combined flux limit would be $\mathcal{O}(n \cdot \Phi)$. This can, however, only lead to the discovery of "source classes"; not to the discovery of individual sources. Since AMANDA-B10 is not expected to detect individual sources, such stackering was performed in addition to the "conventional" point source search described before. Flux limits for the stackered sources are also given in section 11.2.

From this analysis, there is no indication of a significant difference between the properties of the experimental data and its description by the H_0 hypotheses (what had been the case for the cluster search).

10.7 Search for Neutrino Bursts

So far, only the search for steady neutrino point sources was discussed. For them, the main signature was an excess of detected events within a search cone over the expected background of atmospheric neutrinos and muons. A very different strategy is needed when searching for neutrinos from transient sources, e.g. from gamma ray bursts. In such a search, one can additionally use the timing information. Since the source only exists for a limited time δt_1, the neutrinos have to arrive within a time window $\delta t_2 = (1 + \epsilon) \cdot \delta t_1$. Here, the so far unknown absolute neutrino masses and the distance of the source determine the dispersion described by ϵ. The time scale of the neutrino production (δt_1) might be as small as that of gamma rays in GRBs ($\leq 10\,\mathrm{s}$). It might, however, be significantly larger, depending on the theory describing neutrino production in GRBs. As examples: A previous AMANDA search for neutrinos from GRBs did use time windows of 10 seconds and 2 hours [23], whereas a HEGRA search used time windows of 2^i minutes with integer $i \geq 0$ [196].

The signature of neutrinos from transient sources like GRBs are thus an excess of events coincident in arrival time and direction. The optimal search bins in space angle and time for such a search would have to be optimized for both parameters simultaneously. They are larger than individually optimized bin-sizes. Especially the previously used angular bin-size of 3.55° is tighter than necessary for transient source searches. But since such a

search is not the main task of this work, the corresponding bin-size optimization has not been performed here. Instead, a simple search was performed by investigating the product of time differences and arrival direction differences of detected neutrino candidates.

Figure 10.7 shows the tail of the corresponding distribution: The product of time difference and space angle differences between any two neutrino events of the BG-100 data set. A burst-like source like a GRB should be detected via an excess at small values in this plot. The measurement is compared to a toy simulation of what is expected from random coincidences in an equivalent experiment with 10 times the AMANDA-B10 statistics. Such an excess can not be excluded. Six coincidences show such small values of the product that they are investigated further.

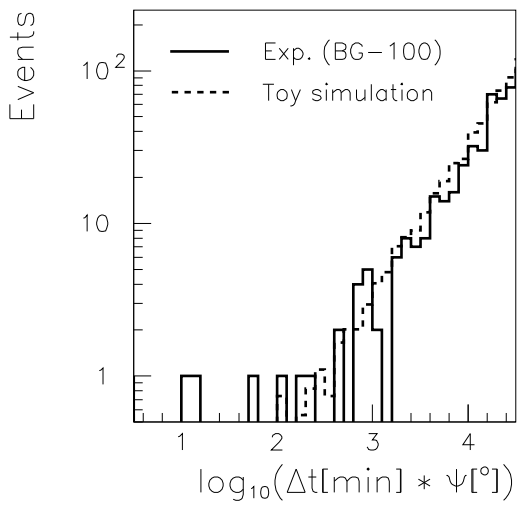

Figure 10.7: Search for GRB candidates in final experimental events: The product of time difference and space angle difference between neutrino events. Solid line: experimental data (BG-100). Dashed line: Toy simulation.

Table 10.2 lists the relevant parameters for these coincidences (or doublets). They are compared to GRBs detected by the BATSE satellite [186] on the same or on the following day. A previous dedicated analysis using only weak cuts did not find indications that single events detected by AMANDA are correlated to BATSE-GRBs in 1997 [23]. The comparison in table 10.2 also does not show any indications for coincidences between AMANDA-B10-doublets and BATSE-GRBs.

Caution has to be used when interpreting this result. First of all, BATSE had a large, but limited field of vision. I.e., in principle AMANDA could have observed GRBs which BATSE missed. In addition, AMANDA could have detected GRBs where the gamma rays have been absorbed before reaching our galaxy or even neutrino bursts from other phenomena than GRBs. However, the suspicious candidates listed above consist only of event-doublets. A triplet would be a much stronger indication for a real neutrino burst. Furthermore, the space angle between the two events of each doublets are on average significantly larger than expected for neutrinos from a common source.

Another remark concerns the units chosen in this analysis: Degrees and minutes. The only reason for them was that they are of comparable size. One could as well measure time differences in units of the average GRB duration (a few seconds) and the space angular differences in units of AMANDA resolution. Such a linear transformation would change the scale on the horizontal axis of figure 10.7, but not the relative values. But in general one could investigate

$$[\Delta(t)]^\alpha \cdot [\Delta(\Psi)]^\beta = \left(\Delta(t) \cdot [\Delta(\Psi)]^{\frac{\beta}{\alpha}}\right)^\alpha \tag{10.4}$$

with arbitrary weights α and β. The overall weight α would lead to a non-linear scale transformation, but not to a change in the ordering of the GRB burst candidates. But the

date	Exp.	t [min]	δ [°]	α [h]	$\Delta(t)$ [min]	$\Delta(\Psi)$ [°]	samples
Oct 27^{th}	AMANDA	901.7	25.2	13.4	0.24	49.2	1
Oct 27^{th}	BATSE	157.9	-7.7	8.1	-	6.6	-
Oct 28^{th}	BATSE	398.9	-1.7	13.3	-	13.1	-
Aug 2^{nd}	AMANDA	992.6	35.5	13.2	0.45	34.3	2
Aug 2^{nd}	BATSE	205.5	3.3	14.3	-	2.2	-
Aug 2^{nd}	BATSE	1015.0	-2.0	6.8	-	4.3	-
Aug 3^{rd}	BATSE	1108.9	59.8	9.8	-	2.2	-
Nov 7^{th}	AMANDA	1323.9	31.1	16.8	1.07	50.9	1
Nov 8^{th}	BATSE	172.9	-70.4	15.8	-	4.9	-
Nov 8^{th}	AMANDA	1126.3	13.2	7.5	10.57	11.3	1
Nov 8^{th}	BATSE	172.9	-70.4	15.8	-	4.9	-
Jun 26^{th}	AMANDA	525.4	53.2	3.1	14.66	11.6	3
Jun 27^{th}	BATSE	64.4	40.0	15.2	-	1.6	-
Jun 27^{th}	BATSE	432.8	42.3	8.1	-	0.9	-
Jun 27^{th}	BATSE	1213.4	-18.4	19.0	-	21.9	-
May 7^{th}	AMANDA	655.4	24.9	15.1	5.89	35.1	2
May 7^{th}	BATSE	1021.7	83.5	5.9	-	8.2	-
May 8^{th}	BATSE	1301.8	80.6	8.8	-	2.3	-

Table 10.2: Comparison between AMANDA neutrino candidate doublets and BATSE GRB detections on the same and on the following day. Given are the date of the measurement, the time t within the day (measured in minutes GMT), the declination δ (in degrees) and the right ascension α (in hours). For AMANDA data, the average value of the two events in the doublet is given. Also listed are the differences between the parameters of the two events (AMANDA) or the uncertainty on the measurement (BATSE). Here, $\Delta(\Psi)$ represents the space angle difference/uncertainty. The column "samples" indicates the doublet was contained only in the BG-100 data set (samples=1) or also in the BG-10 data set (samples=2) or even in the BG-1 data set (sample=3). Those AMANDA events where the product of the time difference in hours and space angle difference in degrees between the two neutrino events is smallest appear first in the table.

relative weight $\frac{\beta}{\alpha}$ would influence the analysis. There is no model-independent theorem preferring any relative weights. Furthermore, a GRB analysis is not the main task of this work. Hence, only the simplest case of $\alpha \equiv \beta \equiv 1$ was investigated here.

11 Flux Limits and Discussion of Results

In section 10, various methods have been employed to find neutrino sources in the data analyzed. No significant source was identified. Based on this result, flux limits shall be derived. This is the task of this section. As discussed in section 8.2, the limits given will be integral flux limits. This is in accordance to what is being published by other experiments like MACRO [7] or Super-Kamiokande [166]. If nothing else is specified, integral flux limits given always refer to the energy range between $10^{1.0}$ GeV and $10^{5.5}$ GeV.

In order to derive flux limits, one has to calculate how many events are maximally allowed from a source when N_O are observed and the expectation from background is $\hat{N}_{BG}$. In this work, the allowed number of signal events in the data is calculated at the 90 % confidence level, using the approach of Feldman and Cousins [89]. The main advantage of their approach over classical Poissonian statistics is the smooth transition between an upper limit and a central confidence belt. By this, the potential for under-coverage due to "flip-flopping" is removed. If the approach gives a true upper limit "$\mu_{90}(N_O, \hat{N}_{BG})$" for the number of signal events, one can derive an integral flux limit via:

$$\Phi(E,\gamma,\delta)^{limit} = \frac{\mu_{90}(N_O, \hat{N}_{BG}(\delta))}{T_{live} \cdot \bar{A}_{eff}(E,\gamma,\delta) \cdot \epsilon_{bin}(E,\gamma,\delta)} \ . \tag{11.1}$$

The flux limit (or measurement) depends not only on μ_{90}, but also on the lifetime T_{live} (section 4.1), the effective energy-averaged area $\bar{A}_{eff}$ (section 8.2) and the reconstruction efficiency ϵ_{bin} (section 9.3). The energy-averaged effective area and (to a lesser degree) the reconstruction efficiency both show characteristic dependencies of the AMANDA detector: The dependencies on energy E, spectral index γ and declination δ. In formula 11.1 they are given explicitely. To enhance the readability of the text of this section, the dependencies on E, γ or δ will not be stated any more, unless they are important for the text. In any case, the dependency on δ is not relevant for all flux limits: In the case of pre-selected sources, δ is defined by the source position.

In the case of central confidence belts, upper *and* lower flux limits are calculated by replacing $\mu_{90}(N_O, \hat{N}_{BG})$ in equation 11.1 with $\mu_{90}^{lower}(N_O, \hat{N}_{BG})$ and $\mu_{90}^{upper}(N_O, \hat{N}_{BG})$ respectively. In general, the existence of a lower flux limit obtained from an individual search is an indication for a potential discovery of a point source in that search. But in this work, altogether $4 \cdot 374 = 1496$ search windows were used in the binned search and 62 in the search for preselected sources. When flux limits are calculated at the 90 % confidence level, it is thus expected that ~ 110 searches will yield lower flux limits[1]. Such lower limits were observed in 77 search bins, 76 of which were in the binned analysis. This number is below what is expected. This again is an indication that the data is distributed more randomly than expected from the H_0 hypotheses (see section 10.5 for a previous indication).

[1] Due to the integer nature of the problem investigated, the tables given in the report of Feldman and Cousins [89] cannot achieve exact coverage for most of the combinations (N_0, $\hat{N}_{BG}$). The two authors of that report decided to always use over-coverage in these cases. Due to that over-coverage, the expectation for the number of sources that fall outside their 90 % confidence interval is less than 10 %. This is best illustrated by numbers. In case of pure background experiments, the fraction $f(\hat{N}_{BG})$ of experiments giving lower limits at the 90 % confidence interval for a Poissonian distributed background expectation of $\hat{N}_{BG}$ is: $f(0.5) = 9\,\%$, $f(1) = 8\,\%$, $f(1.5) = 7\,\%$, $f(2) = 5\,\%$, $f(2.5) = 4\,\%$, $f(3) = 8\,\%$, $f(3.5) = 8\,\%$, ... An average value of $f(\hat{N}_{BG}) \approx 7\,\%$ is estimated from these numbers.

The conclusion of section 10 was that there exists no significant indication for point sources in the data analyzed. Correspondingly, all the lower flux limits which were calculated for 77 search bins are treated as being due to statistical fluctuations. They will be indicated if the corresponding search bin is discussed in this text. But only the upper limits will be used to set final flux limits. These upper limits are then known to over-cover and are in that respect "conservative".

11.1 All-sky Flux Limits

Integral flux limits are calculated according to equation 11.1. Before this could be performed, a slight subtlety had to be solved: The angular dependencies of the effective areas and the efficiencies were determined for declination bands of width 0.15 in $\sin(\delta)$. The definition of the search bins for the all-sky search was independent and yielded different declination bands. This lead to an ambiguity about which effective areas and efficiencies should be used during the calculation of upper limits for search bins which covered parts of two $\bar{A}_{eff}/\epsilon_{bin}$ declination bands. Those values leading to worse limits had to be taken. Since the search grids were designed to guarantee that no declination value is on the borders of all search bins, this "problem" cannot be solved by different future definitions of the declination bands.

Table 11.1 shows the flux limits calculated for various declination bands and above two different neutrino energy thresholds. Figure 11.1 represents the same data graphically. For each search bin analyzed, a different value of μ_{90} was calculated. To obtain an upper limit applying to all search bins, the worst (largest) of all these values was taken. To indicate that it is the worst of an ensemble, it will be called μ_{90}^{limit} for the remainder of this work. It was calculated separately for all declination bands analyzed. Depending on angle, μ_{90}^{limit} varies from 7.5 to 8.7 without showing any systematic trends. The lifetime which enters the flux limit calculation is $1.12 \cdot 10^7$ s, as calculated from table D.9.

Declination	μ_{90}^{limit}	Φ_μ^{limit}	Φ_ν^{limit}	Φ_μ^{limit}	Φ_ν^{limit}
		$E_\nu \geq 10^{1.0}$ GeV		$E_\nu \geq 10^{3.0}$ GeV	
$0.85 \leq \sin(\delta) \leq 1.0$	8.67	6.25	9.11	5.14	0.100
$0.7 \leq \sin(\delta) \leq 0.85$	7.52	7.74	9.87	6.68	0.107
$0.55 \leq \sin(\delta) \leq 0.7$	7.69	14.1	16.5	12.6	0.181
$0.4 \leq \sin(\delta) \leq 0.55$	7.69	28.4	30.0	26.1	0.329
$0.25 \leq \sin(\delta) \leq 0.4$	7.66	50.6	47.5	47.0	0.516
$0.1 \leq \sin(\delta) \leq 0.25$	7.72	122	98.4	15.7	1.06

Table 11.1: Integral all sky limits on the μ and ν_μ fluxes for an assumed E_ν^{-2} spectrum. The lifetime in 1997 was $T_{life} = 1.1242 \cdot 10^7$ s. Limits are given in units of $10^{-15}\,\mathrm{cm}^{-2}\mathrm{s}^{-1}$ for muon fluxes and in units of $10^{-8}\,\mathrm{cm}^{-2}\mathrm{s}^{-1}$ for neutrino fluxes.

Assuming that AMANDA-II or the future IceCube telescope have an isotropic sensitivity larger than the vertical sensitivity of AMANDA-B10 and that they will take data for much

longer than 130 days, the potential for improvements in flux limits (especially at shallow declinations) is evident.

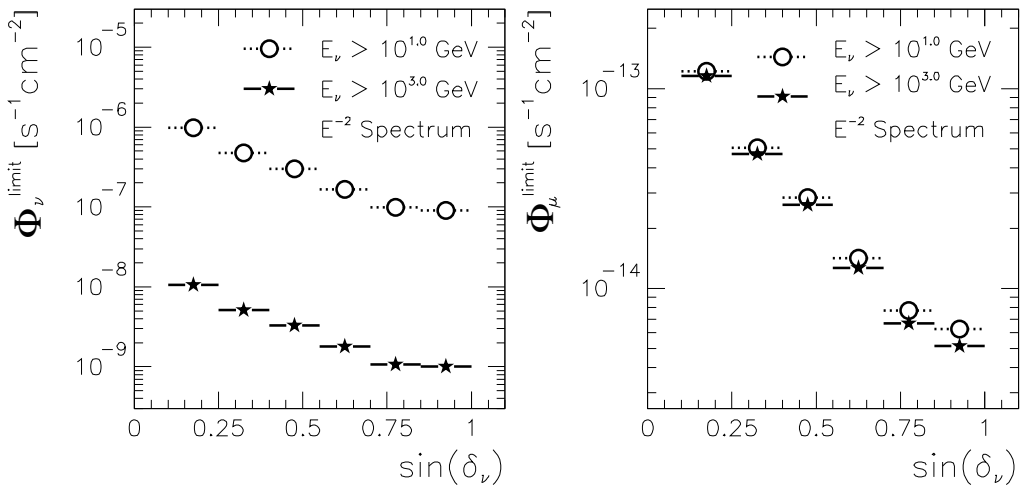

Figure 11.1: The declination dependency of the flux limits. Left: Integral limit on the neutrino flux. Right: Integral limit on the neutrino-induced muon flux. A spectral index of $\gamma = -2$ is assumed and the energy thresholds are 1 GeV or 1 TeV respectively. (The maximal simulated energy is $10^{2.5}$ TeV in both cases.)

The energy-averaged effective area and the reconstruction efficiency were shown versus declination in figures 8.2 and 9.8 respectively. The numbers in table 11.1 and figure 11.1 are simply an approximate constant (μ_{90}/T_{life}) divided by the bin-wise product of these two figures. The only difference is that this time, the parameters are also given for energies $E_\nu \geq 1\,\mathrm{TeV}$. The general trend of both sub-figures is dominated by the properties of $\bar{A}_{eff}$. The discussion of figure 8.2 therefore applies again, but shall not be repeated here. Both the muon and neutrino flux limits change by slightly more than one order of magnitude over the declination range investigated. The shape of the angular dependency of the flux limit is almost independent of the threshold.

The limits on the neutrino flux shrink by two orders of magnitude when only energies $E_\nu \geq 1\,\mathrm{TeV}$ are considered (rather than energies $E_\nu \geq 10\,\mathrm{GeV}$). This is expected for an E_ν^{-2} spectrum, since for that spectrum the number of particles above a certain threshold is inversely proportional to the threshold. This has to be kept in mind when comparisons are being performed between various experiments with different thresholds. The limit on the muon flux remains approximately constant. This is also expected for the following reasons: In the range $E_\nu < 10^4\,\mathrm{GeV}$, the neutrino interaction cross section and the muon range both increase approximately linearly with neutrino energy. As discussed for figure 8.2, this makes the muon effective area approximately independent of energy. In other words, the effective muon spectral index is two units larger than the neutrino spectral index. For a spectrum $\sim E_\mu^0$, the flux limit is dominated by the high-energy tail of the spectrum and approximately independent from the lower threshold.

Figure 11.2 and table 11.2 show the dependency of the flux limits differential in neutrino energy for an E_ν^{-1}, an E_ν^{-2} and an E_ν^{-3} spectrum. These are no true differential limits,

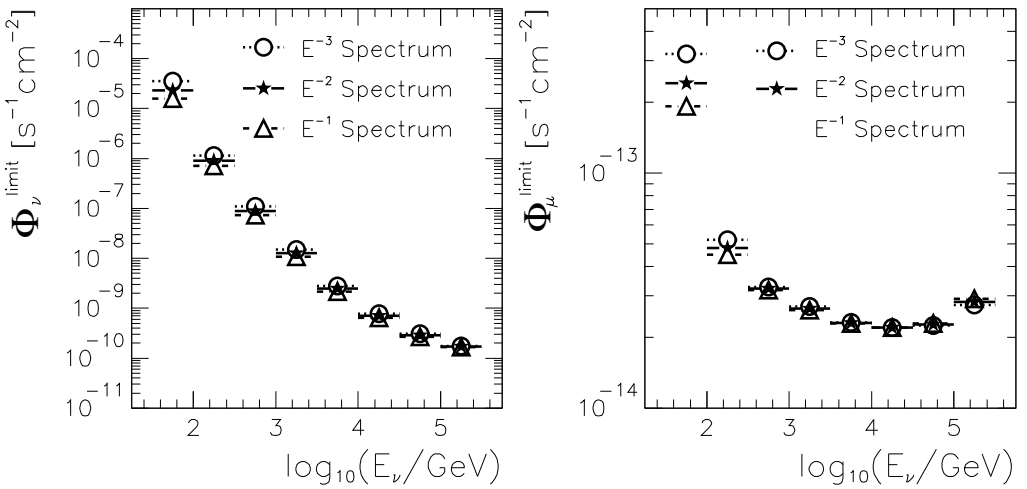

Figure 11.2: The pseudo-differential flux limits. Left: Limit on the neutrino flux. Right: Limit on the neutrino-induced muon flux. Both limits for an E_ν^{-1}, an E_ν^{-2} and an E_ν^{-3} spectrum and an average declination $5° \leq \delta \leq 90°$. (left)

Energy range	Φ_μ^{limit}			Φ_ν^{limit}		
	$\gamma = -1$	$\gamma = -2$	$\gamma = -3$	$\gamma = -1$	$\gamma = -2$	$\gamma = -3$
$10^{1.5} \leq E_\nu/\text{GeV} \leq 10^{2.0}$	192	241	321	1590	2300	3510
$10^{2.0} \leq E_\nu/\text{GeV} \leq 10^{2.5}$	45.0	48.1	52.1	70.9	89.5	114
$10^{2.5} \leq E_\nu/\text{GeV} \leq 10^{3.0}$	31.8	32.2	32.8	7.26	8.87	10.8
$10^{3.0} \leq E_\nu/\text{GeV} \leq 10^{3.5}$	26.1	26.5	27.0	1.08	1.28	1.51
$10^{3.5} \leq E_\nu/\text{GeV} \leq 10^{4.0}$	22.9	23.1	23.2	0.214	0.247	0.281
$10^{4.0} \leq E_\nu/\text{GeV} \leq 10^{4.5}$	22.0	22.0	22.1	0.0646	0.0710	0.0775
$10^{4.5} \leq E_\nu/\text{GeV} \leq 10^{5.0}$	23.0	22.7	22.4	0.0269	0.0289	0.0308
$10^{5.0} \leq E_\nu/\text{GeV} \leq 10^{5.5}$	29.1	28.3	27.4	0.0166	0.0171	0.0175

Table 11.2: Pseudo-differential limits on the μ and ν_μ fluxes for assumed E_ν^{-1}, E_ν^{-2} and E_ν^{-2} spectra for an average declination $5° \leq \delta \leq 90°$. $\mu_{90}^{limit} = 8.67$ was used for all energies. Limits are given in units of $10^{-15}\,\text{cm}^{-2}\text{s}^{-1}$ for muon fluxes and in units of $10^{-8}\,\text{cm}^{-2}\text{s}^{-1}$ for neutrino fluxes.

but rather integral limits over a sufficiently small energy range to be considered *pseudo-differential*. Again, the figure is basically a convolution of previously shown figures, this time of figures 8.3 and 9.8 (right). The detailed discussion of the general trends shall therefore not be repeated here. The main feature is a pseudo-differential neutrino flux limit, which is rapidly improving with energy, and a muon flux limit which is much more weakly improving up to energies $E_\nu \sim 10^{4.3}\,\text{GeV}$ and worsening thereafter.

An important information is the difference between the *pseudo-differential* limits for the three different spectral indices shown. The difference between the limits is a measure for the error one gets by taking these limits as real differential limits and applies them to an arbitrary source spectrum.

A very striking observation is obtained when comparing figures 11.1 and 11.2 (or the corresponding table entries) for the smallest energy bins: The (integral) flux limit over the range $10^{1.5}\,\mathrm{GeV} \leq E_\nu \leq 10^{2.0}\,\mathrm{GeV}$ is worse than the (integral) flux limit over the larger interval $10^{1.5}\,\mathrm{GeV} \leq E_\nu \leq 10^{5.5}\,\mathrm{GeV}$. This is explained as follows: Figure 11.2 shows pseudo-differential flux limits. They depend only slightly on the spectral index as they are obtained by averaging over a small energy interval. This analysis has a very poor sensitivity towards low energy events ($E_\nu \leq 10^{2.0}\,\mathrm{GeV}$) and hence the limits are poor in this energy range. But the sensitivity is much better for higher neutrino energies. The flux limits for the interval $10^{2.5}\,\mathrm{GeV} \leq E_\nu \leq 10^{3.0}\,\mathrm{GeV}$ for example are already a factor ~ 200 better. With the assumption of a spectral index of $\gamma = -2$, one knows that the neutrino fluxes in these two energy ranges only differ by a factor of 10. The flux limits for the low energy interval as obtained from the high energy interval is therfore a factor of 20 better due to the assumption about the energy spectrum. One could take this argument further and modify the limits on the low-energy intervals correspondingly. Then these new limits would, however, not be (pseudo-)differential any more. But the same argument is also the reason why it is justified that this work gives flux limits for energy thresholds of 10 GeV for fixed source spectra, although the sensitivity of the analysis is vanishing towards this threshold.

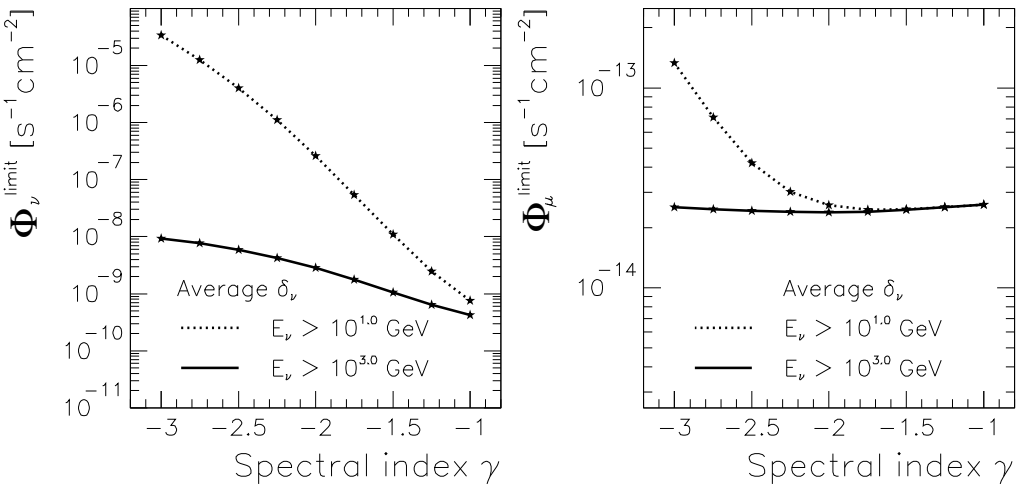

Figure 11.3: The spectrum dependency of the integral flux limits. Left: Integral limit on the neutrino flux. Right: Integral limit on the neutrino-induced muon flux. Both limits for an average declination $5° \leq \delta \leq 90°$ and two energy ranges: $10^{1.0}\,\mathrm{GeV} \leq E_\nu \leq 10^{2.5}\,\mathrm{TeV}$ and $1\,\mathrm{TeV} \leq E_\nu \leq 10^{2.5}\,\mathrm{TeV}$.

Figure 11.3 shows the dependency of the integral flux limits on the spectral index γ. It is derived from a convolution of figures 8.4 and 9.9. Again, two different thresholds on the neutrino energy are compared. In case of the neutrino flux limit, the threshold dependency is significant. As already explained, the trend is dominated by the number of particles above the threshold for each spectral index. The ratio of particles above the two thresholds for an $E^{-3,\,-2,\,-1}$ flux is $1 : 10^4,\ 1 : 10^2,\ 1 : 3$. The ratio of the two curves in the figure approximately reproduces these ratios. The additional non-dominant contributions shall not be discussed here. In case of the muon flux limit, the effect is much smaller.

As discussed for figure 11.1, the muon spectrum has a spectral index approximately two units larger than the neutrino spectrum. For spectral indices $\gamma_\mu > 0$, the threshold effect vanishes. For smaller spectral indices the threshold effect becomes more important. The curve for the lower energy threshold is basically the inverse of figure 8.4 (right) and shall not be discussed in more detail here.

The tables 11.1 and 11.2 gave flux limits for assumed E_ν^{-2} spectra only. Appendix F lists the energy-averaged muon and neutrino effective areas and efficiencies for all combinations of energies, spectral indices and declinations investigated. $T_{life} = 1.1242 \cdot 10^7$ s and the values for μ_{90}^{limit} are also given in table 11.1. It is thus easy to take these numbers and calculate pseudo-differential or integral flux limits for any desired spectrum, declination or energy range via equation 11.1. The numbers also allow to calculate integral limits for energy thresholds of $10^{1.0}$ GeV, $10^{2.0}$ GeV, $10^{3.0}$ GeV or $10^{4.0}$ GeV. The procedure outlining these simple calculations is given in appendix F. In order not to overload the text with all kind of combinations of these numbers, a selection had to be performed. As a result of this selection, only E_ν^{-2} spectra are shown here, since these spectra seem to be the present "benchmarks" in the literature. The important results of this section are thus the integral all-sky flux limits listed in table 11.1 and shown in figure 11.1, as well as the pseudo-differential flux limits shown in figure 11.2 and listed in table 11.2.

11.2 Specific Potential Sources

In the following sections, several classes of criteria for potential sources are defined. For each class, individual sources are selected according to their luminosity in photon emissions or according to other appropriate "strength" properties. The selection is by far not a complete list, but should indicate potential selection schemes for future neutrino point source searches. During the processing, a cut on the reconstructed zenith angle had been set at $\theta = 95°$, see equation 7.6. This corresponds to a declination of $\delta = 5°$, see equation A.7. Hence only potential source with $\delta \gtrsim 5°$ were selected.

The flux limits are compared to those previously achieved by various other experiments. As pointed out in section 11.1, care has to be taken to compare equivalent numbers. Especially for the neutrino flux limits, the assumed spectral index and energy threshold are important. The limits obtained in this analysis are given throughout this section for an E_ν^{-2} spectrum and a threshold of 10 GeV.

The Super-Kamiokande collaboration [166] only calculated muon flux limits. They do not specify their assumed spectral index. Their energy threshold is "around 1 GeV" [166]. As shown in section 11.1 for all sky flux limits, their flux limits are numerically approximately 7 % "worse" than flux limits calculated here, due to their different energy threshold (assuming they used an E_ν^{-2} spectrum). The term "numerically worse" is meant to denote the following: A Super-Kamiokande flux limit which is "numerically 7 % worse" than a flux limit given here is physically of equivalent quality (in the range covered by both experiments. The different absolute numbers are pure threshold effects. In the following tables, limits from Super-Kamiokande are indicated with a superscript S.

The MACRO collaboration [7] published both muon and neutrino flux limits. Their energy threshold is 1 GeV and they only investigated $E_\nu^{-2.1}$ spectra. Their different energy threshold and assumed spectrum make their neutrino flux limits a factor of 13 and their

muon flux limits 10 % "numerically worse" than those obtained here. In the following tables, limits from MACRO are indicated with a superscript M.

The IMB collaboration [25] also published muon and neutrino flux limits. Their energy thresholds are "at least 1 GeV" (it is considered 2 GeV in [97]) and they investigated an E_ν^{-2} spectrum. Also assuming a threshold of 2 GeV for them, their neutrino flux limits are expected to be a factor of 10 and their muon flux limits 7 % "numerically worse" than flux limits derived here. IMB limits will be denoted with a superscript I in the following tables.

The BAKSAN collaboration [51] only published muon flux limits. Their energy threshold is at 1 GeV and they assume an $E_\nu^{-2.5}$ spectrum. Their flux limits are expected to be a factor of 1.8 "numerically worse" than limits obtained here. Their limits will be denoted with a superscript B in the following tables.

The results obtained by the standard AMANDA point source search [251] will be discussed in the text, since there specific spectra were assumed for several sources. Like this analysis, it also has a lower energy threshold of the simulation of 10 GeV.

11.2.1 TeV γ-ray Blazars

At present, AGNs seem to be the preferred class of sources for significant predicted neutrino fluxes. AGNs have so far only been detected in the photon regime. Those AGNs which are known to emit photons with energies above the AMANDA neutrino threshold (several 10 GeV) are the TeV γ-ray blazars. In fact, they are the only class of extra-galactic sources which is known to emit any kind of particles in that energy regime. Their TeV photons have been detected by air shower Cherenkov telescopes [243]. The sources investigated are the complete set of discovered TeV γ-ray blazars [2, 244]. The only restriction was $\delta > 5^\circ$ due to the visible range of AMANDA. These highly variable sources and the year-average flux limits obtained for them are given in table 11.3.

Object	α [h]	δ [°]	redshift	N_O	$\hat{N}_{BG}$	μ_{90}	Φ_μ^{lim}	comp.	Φ_ν^{lim}	comp.
Markarian 421	11.074	38.209	0.0300	1	1.04	3.32	5.75	13^S	6.73	360^I
Markarian 501	16.898	39.760	0.0337	1	1.04	3.33	5.77	9.9^S	6.75	1070^M
1ES 2344+514	23.785	51.705	0.0440	0	1.40	1.39	1.37	—	1.74	—
1ES 1959+650	20.000	65.149	0.0470	0	1.57	1.33	0.931	—	1.30	—
3C 66A	02.378	43.036	0.444	1	1.28	3.11	5.38	—	6.31	—
1ES 1426+428	14.476	42.673	0.129	0	1.15	1.53	2.65	—	3.10	—
superposition	—	38.209	—	3	7.47	1.63	2.83	—	3.31	—

Table 11.3: Year-average Limits on integral muon and neutrino fluxes from TeV γ-ray Blazars. Energy range: $10^{1.0}\,\text{GeV} \leq E_\nu \leq 10^{5.5}\,\text{GeV}$. Object names according to [244]. Position and redshift information according to NED [180]. Number of detected events (N_O), number of expected background events ($\hat{N}_{BG}$), upper limit on number of signal events (μ_{90}) and flux limits (Φ_μ^{lim}, Φ_ν^{lim}): this analysis. Assumed spectrum: E_ν^{-2}. Comparison to other experiments (comp.): IMB [25] (I), MACRO [7] (M) or Super-Kamiokande [166] (S). Limits are given in units of $10^{-15}\,\text{cm}^{-2}\text{s}^{-1}$ for muon fluxes and in units of $10^{-8}\,\text{cm}^{-2}\text{s}^{-1}$ for neutrino fluxes.

Other collaborations have so far only published limits on the two Markarians in table 11.3. Super-Kamiokande has published slightly worse muon flux limits than this analysis [166]. The neutrino flux limits achieved here are significantly better than other previously published limits.

The standard AMANDA point source analysis assumes different specific models for the neutrino spectrum from the Markarians. The neutrino flux limit results are thus difficult to compare to those derived here for an E_ν^{-2} spectrum. But since the muon flux limits are not very spectrum-sensitive, these can be compared. The other analysis obtained limits of $\Phi_\mu^{lim}(Mrk\ 501) = 14.65 \pm 3.3$ and $\Phi_\mu^{lim}(Mrk\ 421) = 9.24 \pm 2.2$ in the units of table 11.3. Within the uncertainties, these limits agree to within a factor of two with those obtained here.

For the sources 1ES 2344+514, 1ES 1959+650 and 3C 66A that other AMANDA analysis also assumes an E_ν^{-2} spectrum. The flux limits for 3C 66A are very similar to those obtained here ($\Phi_\mu^{lim} = 6.55 \pm 1.4$, $\Phi_\nu^{lim} = 7.15 \pm 1.5$ in the units of table 11.3). The limits on 1ES 2344+514 and 1ES 1959+650 are approximately a factor of five better here, due to a μ_{90}-value which is a factor of five better than that in the other analysis.

One difference between the two AMANDA analyses is the treatment of the uncertainties. The present analysis, uses the traditional approach to calculate limits first. The uncertainties on the limits are then discussed in section 11.4. The standard AMANDA point source analysis in contrast uses a different approach. There, the full analysis is repeated multiple times. In each iteration one physics parameter is varied within its systematic uncertainties. The resulting individual flux limits are then averaged to give the final flux limit. The systematic uncertainty on the final limits is obtained from the spread of the individual limits.

The declination dependency of the flux limits lead to a subtle difficulty during the calculation of flux limits for stackered sources: It is not evident which declination to assume for the stackered source. In order to obtain true upper limits, one has to take the declination giving the worst limits. Since the limits get systematically worse with lower declinations, it is always the lowest declination of any of the stackered sources which has to be taken. The resulting (stackered) flux limit on the combined flux of the six extragalactic TeV γ-ray sources is tighter than the limit obtained for some of the individual sources. This is because the statistical fluctuations in N_O and $\hat{N}_{BG}$ partly cancel and thus μ_{90} is comparatively low for the superimposed sources. This property of a combined limit which can be better than individual limits causes criticism of the method. This work here will not attempt a justification of the stackering method. Its results are provided as additional information for those readers interested, but are not considered the main results of this work. They are not discussed in detail for the following source selections any more.

11.2.2 MeV γ-ray selected Blazars

In the highest energy range accessible to satellites, EGRET discovered various extragalactic point sources [113]. Later, most of these were identified as blazars. The five sources identified as blazars, seen by AMANDA-B10 and strongest in the EGRET parameter "maximum detected flux" were selected. They and their flux limits are given in table 11.4. Due to the shallow declinations of the sources, the limits obtained for them are significantly

Object	α [h]	δ [°]	redshift	N_O	$\hat{N}_{BG}$	μ_{90}	Φ_μ^{lim}	Φ_ν^{lim}
3EG J0237+1635	02.644	16.616	0.940	1	1.16	3.21	21.9	19.9
3EG J0450+1105	04.819	11.358	1.21	0	0.95	1.64	23.7	19.0
3EG J0530+1323	05.157	13.532	2.06	0	1.08	1.57	22.7	18.2
3EG J1635+3813	16.588	38.134	1.81	1	1.04	3.32	5.75	6.73
3EG J2254+1601	22.899	16.148	0.869	2	1.18	4.73	29.3	27.5
superposition	—	11.358	—	4	5.42	3.27	47.2	38.0

Table 11.4: Limits on integral muon and neutrino fluxes from strong MeV γ-ray AGN. Energy range: $10^{1.0}\,\mathrm{GeV} \leq E_\nu \leq 10^{5.5}\,\mathrm{GeV}$. Object names according to [113]. Position and redshift information according to NED [180]. Number of detected events (N_O), number of expected background events ($\hat{N}_{BG}$), upper limit on number of signal events (μ_{90}) and flux limits (Φ_μ^{lim}, Φ_ν^{lim}): this analysis. Assumed spectrum: E_ν^{-2}. Limits are given in units of $10^{-15}\,\mathrm{cm}^{-2}\mathrm{s}^{-1}$ for muon fluxes and in units of $10^{-8}\,\mathrm{cm}^{-2}\mathrm{s}^{-1}$ for neutrino fluxes.

worse than those on the extragalactic TeV-blazars. No other experiment has published neutrino or muon flux limits on these sources yet.

11.2.3 Infrared & X-ray selected AGNs

Object	α [h]	δ [°]	redshift	N_O	$\hat{N}_{BG}$	μ_{90}	Φ_μ^{lim}	Φ_ν^{lim}
J144207.7+352632	14.702	35.440	0.0791	0	0.89	1.68	2.91	3.40
J141759.6+250817	14.300	25.137	0.0172	0	0.88	1.69	5.85	6.17
J224239.6+294333	22.711	29.725	0.0247	2	1.10	4.81	16.7	17.6
J135304.8+691832	13.884	69.308	0.0305	2	1.68	4.23	2.96	4.32
J074232.9+494830	07.709	49.810	0.0222	2	1.34	4.57	4.49	5.73
superposition	—	25.137	—	6	5.89	5.58	20.7	21.8

Table 11.5: Limits on integral muon and neutrino fluxes from strong X-ray AGNs seen in coincidence at infrared wavelengths. Energy range: $10^{1.0}\,\mathrm{GeV} \leq E_\nu \leq 10^{5.5}\,\mathrm{GeV}$. Object names according to [235] (The string "1RXS " preceeding all objects in that catalog is omitted here for layout reasons) . Position and redshift information according to NED [180]. Number of detected events (N_O), number of expected background events ($\hat{N}_{BG}$), upper limit on number of signal events (μ_{90}) and flux limits (Φ_μ^{lim}, Φ_ν^{lim}): this analysis. Assumed spectrum: E_ν^{-2}. Limits are given in units of $10^{-15}\,\mathrm{cm}^{-2}\mathrm{s}^{-1}$ for muon fluxes and in units of $10^{-8}\,\mathrm{cm}^{-2}\mathrm{s}^{-1}$ for neutrino fluxes.

The photons of the next lower energy regime are the X-rays. Many AGNs have an emission peak in X-rays — and another one in infrared wavelengths. Such a correlation between their properties in different wavelength regions is typical for AGNs. In leptonic models, it is often attributed to the same particle species that emits (low-energy) synchrotron photons and boosts them to higher energies by inverse Compton scattering. The combined process is abbreviated as "SSC" (from Synchrotron Self Compton process). AGNs seen by both, the infrared satellite IRAS [208] and the X-ray satellite ROSAT [235] were thus selected twice. The first selection took those AGNs with the highest ROSAT count rate.

The sources selected and the flux limits obtained for them are given in table 11.5. Again, these are the first muon flux or neutrino flux limits for these sources.

Object	α [h]	δ [°]	redshift	N_O	$\hat{N}_{BG}$	μ_{90}	Φ_μ^{lim}	Φ_ν^{lim}
02483+4302	02.860	43.253	0.0514	2	1.22	4.69	4.45	5.67
12173+2953	12.335	29.281	0.00217	2	0.99	4.92	17.0	18.0
13446+1121	13.785	11.106	0.0226	0	0.91	1.67	24.0	19.4
11395+1033	11.703	10.278	0.0205	2	0.90	5.01	72.2	58.2
18210+5308	18.366	64.343	0.297	1	1.47	2.93	2.05	2.99
superposition	—	10.278	—	7	5.50	7.03	101	81.6

Table 11.6: Limits on integral muon and neutrino fluxes from strong infrared AGNs seen in coincidence in X-rays. Energy range: $10^{1.0}\,\mathrm{GeV} \leq E_\nu \leq 10^{5.5}\,\mathrm{GeV}$. Object names according to [208]. Position and redshift information according to NED [180]. Number of detected events (N_O), number of expected background events ($\hat{N}_{BG}$), upper limit on number of signal events (μ_{90}) and flux limits (Φ_μ^{lim}, Φ_ν^{lim}): this analysis. Assumed spectrum: E_ν^{-2}. Limits are given in units of $10^{-15}\,\mathrm{cm}^{-2}\mathrm{s}^{-1}$ for muon fluxes and in units of $10^{-8}\,\mathrm{cm}^{-2}\mathrm{s}^{-1}$ for neutrino fluxes.

In a second iteration, those coincident sources with the highest IRAS flux at a wavelength of $60\,\mu$m were selected. They and their flux limits are listed in table 11.6. Again, the flux limits given are the first neutrino or muon flux limits for these sources.

11.2.4 Radio selected AGNs

Object	α [h]	δ [°]	redshift	N_O	$\hat{N}_{BG}$	μ_{90}	Φ_μ^{lim}	Φ_ν^{lim}
PKS 0528+134	05.516	13.532	2.06	1	1.08	3.29	47.4	38.3
B2 0552+39A	05.925	39.814	2.37	1	1.04	3.33	5.77	6.75
B2 0923+39	09.451	39.006	0.695	1	1.03	3.34	5.79	6.77
3C 345.0	16.716	39.810	0.593	1	1.04	3.33	5.77	6.75
PKS 2145+06	21.802	06.961	0.990	0	0.62	1.86	26.8	21.6
superposition	—	06.961	—	4	4.80	3.80	54.8	44.2

Table 11.7: Limits on integral muon and neutrino fluxes from strong radio-loud AGNs. Energy range: $10^{1.0}\,\mathrm{GeV} \leq E_\nu \leq 10^{5.5}\,\mathrm{GeV}$. Object names according to [234] Position and redshift information according to NED [180]. Number of detected events (N_O), number of expected background events ($\hat{N}_{BG}$), upper limit on number of signal events (μ_{90}) and flux limits (Φ_μ^{lim}, Φ_ν^{lim}): this analysis. Assumed spectrum: E_ν^{-2}. Limits are given in units of $10^{-15}\,\mathrm{cm}^{-2}\mathrm{s}^{-1}$ for muon fluxes and in units of $10^{-8}\,\mathrm{cm}^{-2}\mathrm{s}^{-1}$ for neutrino fluxes.

One of the most prominent features of AGNs is their strong radio emission. It leads to the so-called radio knots stretching far into the intergalactic space. Consequently, a sample of strong radio-loud AGNs was selected. Since flat spectrum radio quasars tend to be more powerful in the high energy regime than other quasars, the selection rule was combining strength and steepness arguments:

- The flux at $\lambda = 11\,\mathrm{cm}$ was required to exceed $1\,\mathrm{Jy}$.

- The ratio between the fluxes at 6 cm and at 11 cm should give a spectral index flatter than 0.5.
- Out of the remaining sources, the flux should be strongest at 6 cm.

The data was taken from the Veron/Veron catalog [234]. The selected sources and the flux limits obtained are listed in table 11.7. No other limits are published on the muon or neutrino fluxes from these sources so far.

Object	α [h]	δ [°]	redshift	N_O	$\hat{N}_{BG}$	μ_{90}	Φ_μ^{lim}	Φ_ν^{lim}
0316+161	03.316	16.476	unknown	1	1.19	3.19	19.8	18.6
1323+321	13.438	31.903	0.370	3	1.13	6.29	21.8	22.9
1345+125	13.793	12.290	0.122	0	1.10	1.56	22.5	18.1
1358+624	14.008	62.178	0.431	0	1.32	1.43	1.00	1.46
2342+821	23.734	82.444	0.735	1	1.56	2.87	2.01	2.94
superposition	—	12.290	—	5	6.29	3.84	55.4	44.6

Table 11.8: Limits on integral muon and neutrino fluxes from GHz-peaked radio AGNs. Energy range: $10^{1.0}\,\mathrm{GeV} \leq E_\nu \leq 10^{5.5}\,\mathrm{GeV}$. Object names according to [217]. Position and redshift information according to NED [180]. Number of detected events (N_O), number of expected background events ($\hat{N}_{BG}$), upper limit on number of signal events (μ_{90}) and flux limits (Φ_μ^{lim}, Φ_ν^{lim}): this analysis. Assumed spectrum: E_ν^{-2}. Limits are given in units of $10^{-15}\,\mathrm{cm}^{-2}\mathrm{s}^{-1}$ for muon fluxes and in units of $10^{-8}\,\mathrm{cm}^{-2}\mathrm{s}^{-1}$ for neutrino fluxes.

A rather small, but very interesting catalog is the complete sample of thirty-three GHz-Peaked-Spectrum (GPS) radio sources [217]. This could be a list of very young sources. The five strongest sources at any wavelength within that catalog were selected and are listed (together with the flux limits obtained) in table 11.8. Like in the previous few selections, this is the first compilation of neutrino or neutrino-induced muon flux limits for these sources.

11.2.5 Close Quasi Stellar Objects.

If AGNs are neutrino sources, then objects close to the earth should yield higher fluxes than those further away. Another selection was thus taken to select close AGNs. Since previous selections were biased towards selecting blazars, this time only QSOs were selected. Thus the five closest QSOs of known redshift (NED [180] as of September 2001) were selected. Together with their flux limits, they are listed in table 11.9. Again, the flux limits given are the first limits on neutrino or muon fluxes from these sources.

11.2.6 Galactic TeV γ-ray Sources

Not only extra-galactic, but also galactic TeV γ-ray sources have been detected [244]. At present few theories predict significant ν fluxes from them. But since they are the only galactic sources known to produce any particles of energies above the AMANDA-B10 threshold, they were also investigated. They (and flux limits for them) are listed in table 11.10. These are the first non-AGNs sources selected in this work.

Object	α [h]	δ [°]	redshift	N_O	$\hat{N}_{BG}$	μ_{90}	Φ_μ^{lim}	Φ_ν^{lim}
NGC 1275	03.330	41.512	0.0176	2	1.03	4.88	8.45	9.91
[HB89] 0210+860	02.387	86.321	0.0184	1	1.06	3.30	2.31	3.37
FBQS J164018.1+384220	16.672	38.706	0.0200	1	1.08	3.29	5.70	6.67
UGC 08621	13.628	39.155	0.0200	1	1.06	3.31	5.73	6.71
KUG 1016+336	10.330	33.368	0.0245	2	1.04	4.87	8.44	9.90
superposition	—	33.368	—	7	5.27	7.26	12.5	14.7

Table 11.9: Limits on integral muon and neutrino fluxes from close quasi stellar objects. Energy range: $10^{1.0}\,\mathrm{GeV} \leq E_\nu \leq 10^{5.5}\,\mathrm{GeV}$. Object names according to [180]. Position and redshift information according to NED [180]. Number of detected events (N_O), number of expected background events ($\hat{N}_{BG}$), upper limit on number of signal events (μ_{90}) and flux limits (Φ_μ^{lim}, Φ_ν^{lim}): this analysis. Assumed spectrum: E_ν^{-2}. Limits are given in units of $10^{-15}\,\mathrm{cm}^{-2}\mathrm{s}^{-1}$ for muon fluxes and in units of $10^{-8}\,\mathrm{cm}^{-2}\mathrm{s}^{-1}$ for neutrino fluxes.

Object	α [h]	δ [°]	N_O	$\hat{N}_{BG}$	μ_{90}	Φ_μ^{lim}	comp.	Φ_ν^{lim}	comp.
Crab Nebula	05.571	22.010	1	1.01	3.35	21.0	4.1^S	19.6	470^M
Cassiopeia A	23.390	58.811	0	1.23	1.48	1.04	—	1.52	—
superposition	—	22.010	1	2.24	2.37	14.7	—	13.8	—

Table 11.10: Limits on integral muon and neutrino fluxes from galactic TeV γ-ray sources. Energy range: $10^{1.0}\,\mathrm{GeV} \leq E_\nu \leq 10^{5.5}\,\mathrm{GeV}$. Object names according to [244]. Position and redshift information according to NED [180]. Number of detected events (N_O), number of expected background events ($\hat{N}_{BG}$), upper limit on number of signal events (μ_{90}) and flux limits (Φ_μ^{lim}, Φ_ν^{lim}): this analysis. Assumed spectrum: E_ν^{-2}. Comparison to other experiments (comp.): either MACRO [7] (M) or Super-Kamiokande [166] (S). Limits are given in units of $10^{-15}\,\mathrm{cm}^{-2}\mathrm{s}^{-1}$ for muon fluxes and in units of $10^{-8}\,\mathrm{cm}^{-2}\mathrm{s}^{-1}$ for neutrino fluxes.

The muon flux limit published for the Crab nebula by Super-Kamiokande [166] is significantly better than the limit obtained here. Main reason is the shallow declination of the Crab nebula which leads to poor limits in this analysis, see table 11.1. But the neutrino flux limit obtained here is an improvement over the previous MACRO [7] limit.

The other AMANDA point source analysis [251] has derived limits for both the Crab nebula and Cassiopeia A. Its limit for the Crab nebula ($\Phi_\mu^{lim} = 4.97 \pm 1.1$, $\Phi_\nu^{lim} = 4.15 \pm 1.0$ in the units of table 11.10) is significantly better than that achieved here. But the limit of the other analysis on Cassiopeia A ($\Phi_\mu^{lim} = 7.61 \pm 2.0$, $\Phi_\nu^{lim} = 9.80 \pm 2.6$ in the same units) is significantly worse. Different μ_{90} factors are the main reason for the differences in both cases. While the number of observed events is smaller than expected from background for Cassiopeia A but within expectation for the Crab nebula in this analysis, the effect is reversed for the other AMANDA point source analysis.

All known astrophysical TeV gamma-ray sources (galactic or not) were discovered in TeV gamma-rays by Cherenkov-telescopes. These can only monitor selected regions in the sky. It is therefore conceivable that further gamma-ray sources of similar strength exist. From the MILAGRITO experiment, it is, however, known that the maximal luminosity

of steady sources in the northern hemisphere is limited to approximately 5 times the luminosity of the Crab nebula [237].

11.2.7 Microquasars

Object	α [h]	δ [°]	N_O	$\hat{N}_{BG}$	μ_{90}	Φ_μ^{lim}	comp.	Φ_ν^{lim}	comp.
GRS 1915+105	19.253	10.946	3	0.90	6.11	88.4	—	71.1	—
SS433	19.197	04.983	1	0.32	4.04	58.2	6.7^M	46.7	127^M
Cygnus X-3	20.541	40.953	1	1.00	3.36	6.17	10^S	7.23	450^I
CI Cam	04.328	55.999	0	1.26	1.46	1.43	—	1.83	—
superposition	—	04.983	5	3.48	6.51	93.8	—	75.6	—

Table 11.11: Limits on integral muon and neutrino fluxes from microquasars. Energy range: $10^{1.0}\,\mathrm{GeV} \leq E_\nu \leq 10^{5.5}\,\mathrm{GeV}$. Object names according to [171]. Position and redshift information according to NED [180]. Number of detected events (N_O), number of expected background events ($\hat{N}_{BG}$), upper limit on number of signal events (μ_{90}) and flux limits (Φ_μ^{lim}, Φ_ν^{lim}): this analysis. Assumed spectrum: E_ν^{-2}. Comparison to other experiments (comp.): either IMB [25] (I), MACRO [7] (M) or Super-Kamiokande [166] (S). Limits are given in units of $10^{-15}\,\mathrm{cm}^{-2}\mathrm{s}^{-1}$ for muon fluxes and in units of $10^{-8}\,\mathrm{cm}^{-2}\mathrm{s}^{-1}$ for neutrino fluxes.

Another class of potential galactic sources are the microquasars. Only few of them have been discovered so far, so the complete set according to [171] has been selected; see table 11.11 for a list of them and the corresponding flux limits obtained. According to its declination of $\delta = 4.983°$, SS433 should not have passed the criterion of $\delta \geq 5°$ for this selection. But since the difference is so small and only few microquasars exist, it has nevertheless been selected. In a strict sense, no flux limits could be calculated for it, since the energy-averaged effective areas and the efficiencies had only been evaluated for $\delta = 5°$. For the calculation of the limits, SS433 was considered to have a declination of $\delta = 5°$. In any case, due to this shallow declination, this analysis cannot obtain competitive limits for this source. (Remember that the MACRO limit on the neutrino flux has to be divided by 13 to be comparable to the limit from this analysis.)

For Cygnus X-3, the Super-Kamiokande collaboration [166] has published muon flux limits which are slightly worse than those obtained here. The neutrino flux limit of this analysis is significantly better than that previously published by IMB [25]. The other AMANDA point source analysis [251] has derived limits for Cygnus X3 which are even better than those obtained here: $\Phi_\mu^{lim} = 4.57 \pm 0.9$ and $\Phi_\nu^{lim} = 4.94 \pm 0.9$ in the units of table 11.11. Again the difference is mainly due to different μ_{90} values for the corresponding search bins.

11.2.8 Highest Energy Cosmic Ray Multiplets

Among the highest energy cosmic rays (above $4 \cdot 10^{19}\,\mathrm{eV}$), so-called multiplets exist. These are doublets or even triplets of cosmic rays coming from within 1°. There are significantly more multiplets than expected for a random distribution. Since the magnetic deflection at these energies is very low, speculations exist whether these multiplets point at (hadronic)

Object	α [h]	δ [°] [○]	av. energy	N_O	$\hat{N}_{BG}$	μ_{90}	Φ_μ^{lim}	Φ_ν^{lim}
Triplet 1	∼1.28	∼20.37	$10^{20.01}$ eV	3	1.04	6.38	49.6	37.2
Triplet 2	∼12.32	∼56.90	$10^{19.79}$ eV	0	1.25	1.47	1.44	1.84
Doublet 1	∼18.88	∼48.06	$10^{19.84}$ eV	1	1.26	3.13	3.08	3.93
Doublet 2	∼4.65	∼34.50	$10^{19.72}$ eV	1	0.97	3.39	5.87	6.87
Doublet 3	∼17.87	∼75.56	$10^{19.70}$ eV	2	1.92	3.99	2.79	4.07
Doublet 4	∼15.80	∼79.40	$10^{19.64}$ eV	1	1.73	2.73	1.91	2.79
Doublet 5	∼10.37	∼65.85	$10^{19.67}$ eV	0	1.61	1.31	0.944	1.38
Doublet 6	∼10.92	∼51.45	$10^{19.67}$ eV	1	1.43	2.98	2.93	3.73
Doublet 7	∼17.44	∼57.16	$10^{19.85}$ eV	2	1.22	4.69	4.60	5.88
Doublet 8	∼11.07	∼64.50	$10^{19.62}$ eV	1	1.53	2.88	2.01	2.94
superposition	—	∼20.37	—	12	13.97	5.22	32.4	30.4

Table 11.12: Limits on integral muon and neutrino fluxes from the directions of UHECR multiplets. Energy range: $10^{1.0}\,\text{GeV} \leq E_\nu \leq 10^{5.5}\,\text{GeV}$. All information according to [229] (mostly AGASA data). Number of detected events (N_O), number of expected background events ($\hat{N}_{BG}$), upper limit on number of signal events (μ_{90}) and flux limits (Φ_μ^{lim}, Φ_ν^{lim}): this analysis. Assumed spectrum: E_ν^{-2}. Limits are given in units of $10^{-15}\,\text{cm}^{-2}\text{s}^{-1}$ for muon fluxes and in units of $10^{-8}\,\text{cm}^{-2}\text{s}^{-1}$ for neutrino fluxes.

cosmic ray sources. Such sources would be interesting candidates for neutrino production. All multiplets collected in [229] were selected. They and their muon and neutrino flux limits are listed in table 11.12.

"Triplet 1" (the triplet with the higher average energy) is the only pre-selected source of this analysis, where a lower limit on the source flux was found. As explained earlier, it is expected to find such lower flux limits for some sources when a large number of sources is being investigated. These lower limits are considered to be due to statistical fluctuations only and are not considered to contain physical information on the particular source[2]. No other collaboration has published neutrino or muon flux limits for these multiplets so far.

11.2.9 BL Lacertae close to Highest Energy Cosmic Ray Directions

Another remarkable feature appears when analyzing cosmic rays of even higher energies. The number of BL Lacertae located within 2.5° around the directions of cosmic rays above $4.8 \cdot 10^{19}\,\text{eV}$ seems to be higher than expected from statistics [228]. All the corresponding BL Lacerta objects were selected and are given in table 11.13. The table also includes the flux limits obtained for these sources. Again, no previous neutrino or muon flux measurement from theses sources have been published.

11.2.10 Individual further Objects

Finally, a few other individual objects were selected. These had been discussed in the past as potential neutrino sources, but do not represent a homogeneous selection. The selection

[2]For the readers which are nevertheless interested in numbers: The lower flux limits for "triplet 1" are a factor of 115 lower than the upper flux limits given in table 11.12.

Object	α [h]	δ [°]	redshift	N_O	$\hat{N}_{BG}$	μ_{90}	Φ_μ^{lim}	Φ_ν^{lim}
1ES 0806+524	08.164	52.316	0.138	1	1.38	3.02	2.97	3.78
RX J1058.6+5628	10.977	56.470	0.144	1	1.32	3.07	3.02	3.85
2EG J0432+2910	04.560	29.140	unknown	0	0.99	1.62	5.61	5.91
OT 465	17.666	47.633	unknown	3	1.22	6.20	6.09	7.78
TXS 1428+370	14.511	36.818	0.564	0	0.85	1.71	2.96	3.47
superposition	—	29.140	—	5	4.44	5.55	19.2	20.3

Table 11.13: Limits on integral muon and neutrino fluxes from BL Lacs close to UHECR directions. Energy range: $10^{1.0}\,\mathrm{GeV} \leq E_\nu \leq 10^{5.5}\,\mathrm{GeV}$. All information according to NED [180]. Number of detected events (N_O), number of expected background events ($\hat{N}_{BG}$), upper limit on number of signal events (μ_{90}) and flux limits (Φ_μ^{lim}, Φ_ν^{lim}): this analysis. Assumed spectrum: E_ν^{-2}. Limits are given in units of $10^{-15}\,\mathrm{cm}^{-2}\mathrm{s}^{-1}$ for muon fluxes and in units of $10^{-8}\,\mathrm{cm}^{-2}\mathrm{s}^{-1}$ for neutrino fluxes.

Object	α [h]	δ [°]	redshift	N_O	$\hat{N}_{BG}$	μ_{90}	Φ_μ^{lim}	comp.	Φ_ν^{lim}	comp.
Cygnus X-1	19.973	35.202	~ 0	1	0.92	3.44	5.96	24^S	6.97	624^M
Hercules X-1	16.964	35.343	~ 0	1	0.89	3.47	6.01	8.7^S	7.03	480^I
Perseus A	03.330	41.512	0.0176	2	1.03	4.88	8.45	34^S	9.91	1399^M
M87 ($\equiv$ Vir A)	12.514	12.391	0.00436	1	1.12	3.25	46.8	6.3^S	37.7	—
Geminga	06.566	17.860	~ 0	3	1.27	6.15	38.2	$11^{S,M}$	35.8	210^M
superposition	—	12.391	—	9	6.25	9.03	130	—	105	—

Table 11.14: Limits on integral muon and neutrino fluxes from selected individual candidate sources. Energy range: $10^{1.0}\,\mathrm{GeV} \leq E_\nu \leq 10^{5.5}\,\mathrm{GeV}$. All information according to NED [65, 180]. Number of detected events (N_O), number of expected background events ($\hat{N}_{BG}$), upper limit on number of signal events (μ_{90}) and flux limits (Φ_μ^{lim}, Φ_ν^{lim}): this analysis. Assumed spectrum: E_ν^{-2}. Comparison to other experiments (comp.): either BAKSAN [51] (B), IMB [25] (I), MACRO [7] (M) or Super-Kamiokande [166] (S). Limits are given in units of $10^{-15}\,\mathrm{cm}^{-2}\mathrm{s}^{-1}$ for muon fluxes and in units of $10^{-8}\,\mathrm{cm}^{-2}\mathrm{s}^{-1}$ for neutrino fluxes.

criterion was that the source has been investigated by IMB, MACRO or Super-Kamiokande and is within the range of view of AMANDA-B10. The flux limits obtained here represent significant improvements with respect to previous limits for Cygnus X-1, Perseus A and Hercules X-1 (neutrino flux limit only). The neutrino flux limit on M87 is the first limit obtained for that source. The limits calculated here are worse than existing limits for the other sources. The best present flux limits for the Geminga pulsar come from the other AMANDA point source analysis [251]: $\Phi_\nu^{lim} = 6.81 \pm 1.7$ and $\Phi_\mu^{lim} = 9.05 \pm 2.3$ in the units of table 11.11. They are far better than those obtained here due to a μ_{90} factor which is smaller by a factor 2.5 and due to the shallow declination where the other analysis in general gives better limits.

11.3 Comparison to other Analyzes

This analysis gives limits for the neutrino and neutrino-induced muon fluxes for 62 sources. For 48 of these, no limits have previously been published. For one further object (M87),

only a muon flux limit has previously been published. For four further objects (all of which are TeV γ-ray sources), the only previously existing limits came from the other AMANDA point source analysis. For all four objects, this analysis could improve the corresponding flux limits. Muon flux limits could be significantly improved with respect to previous non-AMANDA publications for Markarian 421, Markarian 501, Cygnus X-1, Cygnus X-3 and Perseus A. Neutrino flux limits could be significantly improved with respect to previous non-AMANDA publications for Markarian 421, Markarian 501, the Crab nebula, Cygnus X-1, Cygnus X-3, Hercules X-1 and Perseus A. In the case of the Crab nebula and Cygnus X3, the other AMANDA point source analysis gives even better flux limits than those obtained here.

The author is not aware of published all-sky upper limits from other experiments for neutrino or for muon fluxes from point sources like those presented in 11.1. It is possible to obtain average limits expected from other experiments in certain declination bands by averaging over their published limits on selected sources. This is being performed in table 11.15. It shows that for assumed E_ν^{-2} spectra, AMANDA-B10 is competitive with respect to MACRO for declinations $\sin(\delta) > 0.25$ and competitive to Super-Kamiokande for declinations $\sin(\delta) \gtrsim 0.33$.

declination	Φ_μ^{limit}	Φ_ν^{limit}	Φ_μ^{limit}	Φ_ν^{limit}	Φ_μ^{limit} Super-
	this analysis		MACRO		Kamiokande
$0.85 \leq \sin(\delta) \leq 1.0$	1.8	2.6	—	—	—
$0.7 \leq \sin(\delta) \leq 0.85$	3.2	4.0	—	—	—
$0.55 \leq \sin(\delta) \leq 0.7$	5.5	6.5	52	1000	13
$0.4 \leq \sin(\delta) \leq 0.55$	9.4	9.9	60	1100	—
$0.25 \leq \sin(\delta) \leq 0.4$	30	28	36	340	7.6
$0.1 \leq \sin(\delta) \leq 0.25$	43	34	11	220	11

Table 11.15: Average expected limits on the integral muon and neutrino fluxes for not yet selected sources. The Super-Kamiokande collaboration did not select any souces inside the declination band $0.4 \leq \sin(\delta) \leq 0.55$. Limits are given in units of $10^{-15}\,\mathrm{cm}^{-2}\mathrm{s}^{-1}$ for muon fluxes and in units of $10^{-8}\,\mathrm{cm}^{-2}\mathrm{s}^{-1}$ for neutrino fluxes.

These average expected flux limits are better than the worst flux limits from all individual bins in the corresponding declination band (the "true flux upper limits"). For this analysis, the ratio is approximately a factor of three. The true all-sky flux upper limits of table 11.1 can be compared to those obtained in the standard AMANDA point source analysis [251]. That analysis used softer cuts and obtained a significantly higher acceptance, especially for shallow declinations. The comparison of all-sky flux limits obtained here and in that analysis yielded differences which significantly depend on the spectral index: For a very soft spectrum of $\gamma = -3$, this analysis gives flux limits which are on average a factor ~ 2 better than those from the other analysis. For spectra with $\gamma = -2.5$, the results obtained here are better by $\sim 15\,\%$ for vertical up-going events and equivalent to within $\sim 5\,\%$ for horizontal events with $\delta \lesssim 15^\circ$. For a spectral index of $\gamma = -2$, the two analyzes give comparable flux limits for declinations $\delta \gtrsim 35^\circ$. For the shallowest declinations, the

flux limits obtained in this analysis are worse by up to a factor of three (muon flux limits) or by up to 40 % (neutrino flux limits).

Even harder spectra were not simulated in the other analysis and hence cannot be compared. It is expected that the other analysis would give significantly better flux limits for harder spectra. These hard spectra were simulated here, since some neutrino flux models predict such hard spectra at least in parts of the energy range of this analysis ($10^{1.0}$ GeV to $10^{5.5}$ GeV). Since the systematic uncertainties of both AMANDA analyzes are approximately identical, and since the statistical errors are smaller, differences of $\gtrsim 10\,\%$ between the two analyzes are considered significant. For the case of selected sources, statistical fluctuations in the μ_{90} factor are dominantly responsible for the differences between the flux limits obtained by the two analyzes (at least for sources at declinations $\delta \gtrsim 23^\circ$).

The results from the comparison of the flux limits derived here to those obtained in the standard AMANDA point source analysis are interpreted as follows: The simulated signal used for the cut optimization for this analysis was an atmospheric neutrino signal. Atmospheric neutrinos have effective spectra similar to $E_\nu^{-3.3}$ for the energy range of this analysis[3]. Their flux is isotropic to within a factor of two. Neutrinos with a simulated $E_\nu^{-2.0}$ spectrum entered the other analysis. Since it is not known where neutrino point sources are, that flux was simulated isotropically. Apart from the spectral index, the two signal samples were thus basically identical. In both cases, the cuts were designed to best select the simulated signal. I.e. the cuts here were optimized for an $E_\nu^{-3.3}$ spectrum, the cuts in the other analysis for an $E_\nu^{-2.0}$ spectrum. It is therefore expected that this analysis yields better flux limits for soft spectra, whereas the other analysis yields better flux limits for hard spectra.

11.4 Uncertainties of the Flux Limit Calculation

Three individual uncertainties contribute to the uncertainty of the flux limit: The uncertainties on $\bar{A}_{eff}$, on ϵ_{bin} and on $\mu_{90}(N_O, \hat{N}_{BG})$. The uncertainty on the lifetime T_{live} in contrast is negligible. In sections 8.3.1, the uncertainties on $\bar{A}_{eff}$ was estimated to 43 % (systematic) plus 3 % (av. statistical). In section 9.3,the uncertainty on ϵ_{bin} was estimated to 15 % (systematic) plus 4 % (av. statistical).

It might be surprising that there is an uncertainty on $\mu_{90}(N_O, \hat{N}_{BG})$. It arises from the fact that events from the source bin are used to estimate the background contamination in the source declination band. In case of a true signal, detected signal events will thus lead to an overestimation of the true background. This in turn leads to an underestimation of the signal strength and thus gives too tight upper limits. This effect should be small for point source searches if the number of strong sources inside a declination band is small compared to the number of bins within that declination band.

An alternative background estimation scheme could remove this effect. The background for one bin would then be estimated by the events in all other bins of that band, but not

[3] Atmospheric neutrinos have spectra of $E_\nu^{-3.7}$ for energies $E_\nu \gg 1\,\text{TeV}$. But the median energy of the events in this analysis is $E_\nu = 0.32\,\text{TeV}$. The spectral index is harder for lower energies. The effective spectrum of the BG-100 sample can be estimated to $E_\nu^{-3.3}$ from comparing results for atmospheric spectra to those obtained for pure power law spectra in figures 9.4 (right) or 9.9.

by those of the bin investigated. This alternative scheme was discarded due to limitations of this alternative scheme. They are best explained for the case when only one bin within a band contains events. The estimated background for that bin would then be zero, which would automatically lead to a lower flux limit of that bin. Furthermore, this alternative scheme does impose problems for the case when the full band contains only one bin. This is the case for the top-most band in search grids 1 and 2 as described in section 10.4.1.

Nevertheless, it has been analyzed how $\mu_{90}(N_O, \hat{N}_{BG})$ changes if the alternative selection scheme is applied for 30 randomly selected bins. As expected, the change is on average zero. $\mu_{90}(N_O, \hat{N}_{BG})$ rises (the limits get worse) in cases where $N_O > \hat{N}_{BG}$, but the change was below 5 % for all bins tested. Hence, the uncertainty on $\mu_{90}(N_O, \hat{N}_{BG})$ is taken to be $< 5\,\%$ (statistical).

Combining this with the previously mentioned uncertainties, one obtains an uncertainty of 46 % (systematical) plus 7% (av. statistical) on the limits given. For the lowest energy ranges and shallowest declinations, the statistical error can reach up to 29 %; in the opposite extremes, it can be as low as 5 %. The statistical errors of the efficiency and energy-averaged effective area are listed in appendix F depending on declination, energy and spectral index. It is thus possible to calculate the statistical uncertainty on the flux for any given combination of neutrino energy and declination from the data in appendix F.

The statistical uncertainty defines the uncertainty on the ratio of flux limits obtained in this analysis. This is the reason why the flux limits are given with a higher precision than what could be considered appropriate from the total uncertainty.

12 Summary

This work covered two main tasks: An atmospheric neutrino analysis and a search for extraterrestrial neutrino point sources. During the atmospheric neutrino analysis, three event samples containing 138, 223 and 369 events have been extracted. It was shown that these samples are neutrino dominated. Their neutrino content was estimated to $\sim 97\,\%$, $\sim 93\,\%$ and $\sim 73\,\%$, respectively. The properties of these samples were discussed and no anomalies were found. The experimental data sets closely follow the expectation from Monte Carlo simulations. The uncertainties of the expectation for the absolute number of atmospheric neutrinos is estimated to $63\,\%$. The actual agreement between experimental and simulated data is far better than expected from this estimate of the maximum uncertainty. The conclusion of the atmospheric neutrino analysis is that the AMANDA-B10 detector is capable of detecting neutrinos and its sensitivity is understood within reasonable uncertainties.

A search for astrophysical neutrino sources could thus be based on the data samples extracted. In order to keep as many potential source neutrinos as possible, the analysis henceforth concentrated on the sample containing 369 events. The size of the search bins was optimized in a detailed procedure. The sensitivity of the detector and the reconstruction efficiency was determined for various combinations of declination range, neutrino energy range and source spectral index. The analysis cumulated in the calculation of upper flux limits for the neutrino- and the neutrino-induced muon fluxes from potential neutrino sources. For neutrino energies $E_\nu > 10\,\mathrm{GeV}$ and declinations $\delta > 33^\circ$, the all-sky upper limits obtained are $\Phi_\mu^{limit} = 1.41 \cdot 10^{-14}\,\mathrm{cm}^{-2}\mathrm{s}^{-1}$ and $\Phi_\nu^{limit} = 1.65 \cdot 10^{-7}\,\mathrm{cm}^{-2}\mathrm{s}^{-1}$ assuming an E_ν^{-2} source spectrum. After "calibrating" on the flux of atmospheric neutrinos, the systematic uncertainty on these limits could be estimated to be $46\,\%$ (systematic) plus $7\,\%$ (statistical).

For 62 selected potential sources, individual flux limits were derived. For 48 of these, neither muon nor neutrino flux limits had previously been published, for one further source, no neutrino flux limit had been published before. Published muon flux limits could be improved for 5, published neutrino flux limits for 7 sources. The average improvement of the flux limits for the individual sources with respect to the all-sky upper limits is approximately a factor of three. In the worst cases, this improvement is of the order of $25\,\%$, in the best cases it is a factor of six. This work provides the data to transform the explicitly stated flux limits to flux limits for potential other source spectra and for arbitrary different sources at declinations $\delta > 5^\circ$.

13 Outlook

There are several points where this analysis could be improved:

- New cut parameters or different cut values could improve the neutrino passing rate. Especially the cut on the "speed of the line-fit" should be removed, see section 7.1.2.

- During this analysis, the cuts were optimized with respect to a good atmospheric muon suppression. In the standard AMANDA point source analysis [251], the cuts have been optimized with respect to a good angular resolution. Such an approach would also improve the sensitivity of this analysis towards point sources. On the other hand it would worsen the atmospheric neutrino analysis.

- The cuts of this analysis could be further relaxed to a "BG-1000" selection. In the data analyzed here, this would, however, introduce some depth dependent ("z_{COG}") background. This background is particularly problematic since it shows zenith (declination) angle dependencies, see section 7.1.4.

- This analysis did not use any explicit cuts on the reconstructed energy of the events. Reason was that such a cut is not appropriate for an atmospheric neutrino selection. For a point source search, such a cut could efficiently suppress low-energy atmospheric neutrinos.

- During the optimization of the search bin-size (described in section 9.2.3), the zenith angle dependence of the background (atmospheric neutrinos and muons) has been ignored. Including this dependency might give improved, angular dependent bin-sizes. Instead of taking the space angular resolution during the same optimization, the declination and right ascension resolution could be taken separately. Furthermore, it was assumed that the detector resolution for astrophysical neutrinos is equivalent to that for atmospheric neutrinos. This could be changed to optimize the search for various potential source spectra. Finally, the bin-size optimization was performed for a source detection significance of 2 sigma. This should probably be changed to 3 sigma for future analyzes.

- The description of the experimental data by the two H_0 hypotheses in section 10.4.3 might not be optimal. From the cluster search, there is evidence that the data is distributed more smoothly than expected from the H_0 hypotheses. This is not confirmed from the distributions of chance probabilities obtained from the other search techniques. But it is confirmed from the number of search bins for which *lower* flux limits were calculated. It is therefore necessary to further investigate this finding.

- The cluster search and the search for pre-selected sources could be performed with circular bins rather than with quadratic bins. This would require a second bin-size optimization, which should then be based on the case of sources in the bin centers and not the case of random source positions within the bin.

It is estimated that if all these suggestions would be implemented, the combined effect could improve the flux limits obtained by $\sim 30\,\%$. Much larger improvements are expected from topics not specific for this work:

- Improvements in the Monte Carlo simulation of the experimental data are crucial. They should allow to improve the cut selection and hence the neutrino passing rate during data processing. Furthermore they should reduce the systematic uncertainties.

- New reconstruction techniques are being developed. A better reconstruction (i.e. a better resolution) should improve signal passing rates and allow for smaller search cones. This is especially relevant for the energy range $E_\mu \gtrsim 2\,\mathrm{TeV}$, where the resolution of present reconstructions starts to degrade, but which is expected to be important for extraterrestrial neutrinos.

- Most important of all: More data needs to be analyzed. The data taken in 1998 and 1999 (AMANDA-B13) as well as that of 2000 and 2001 (AMANDA-II) are on tape and their analysis has started. These larger arrays have significantly larger effective areas and intrinsically better resolutions. The latter benefit will result in better signal passing rates and will allow the usage of smaller search cones. It is estimated that with the data from these four years, the number of neutrino candidates can increase by a factor of ~ 20 and the limits can improve correspondingly.

References

[1] Aglietta M. et al. "Muon "depth-intensity" relation measured by the LVD underground experiment and cosmic-ray muon spectrum at sea level." *Physical Review D*, **58**(9):092005.1–092005.6 (1998). arXive:hep-ex/9806001.

[2] Aharonian F.A. for the HEGRA Collaboration. "TeV gamma rays from the blazar H1426+428 and the diffuse extragalactic background radiation." *Astronomy and Astrophysics Letters* (2002). Accepted for publication.

[3] Ahmad Q.R. for the SNO Collaboration. "Measurement of the Rate of $\nu_e + d \rightarrow p + p + e^-$ Interactions Produced by ^{8}B Solar Neutrinos at the Sudbury Neutrino Observatory." *Physical Review Letters*, **87**(7):071301.1–071301.6 (2001).

[4] Ahrens J. for the AMANDA Collaboration. "Search for Supernova Neutrino-Bursts with the AMANDA Detector." *Astroparticle Physics*, **16**(4):345–359 (2002). arXive:astro-ph/0105460.

[5] Alexandreas D.E. et al. "Point source search techniques in ultra high energy gama ray astronomy." *Nuclear Instruments and Methods in Physics Research A*, **328**:570–577 (1993).

[6] Alvarez-Muñiz J., Halzen F. and Hooper D.W. "High Energy Neutrinos from Gamma Ray Bursts: Event Rates in Neutrino Telescopes." *Physical Review D*, **62**(9):093015.1–093015.7 (2000). arXive:astro-ph/0006027.

[7] Ambrosio M. et al. "Neutrino Astronomy with the MACRO Detector." *Astrophysical Journal*, **546**(2):1038–1054 (2001). arXive:astro-ph/0002492.

[8] Andrés E. for the AMANDA Collaboration. "The AMANDA neutrino telescope: principle of operation and first results." *Astroparticle Physics*, **13**(1):1–20 (2000). arXive:astro-ph/9906203.

[9] Andrés E. for the AMANDA Collaboration. "Observation of High Energy Neutrinos with Cherenkov detectors embedded in deep Antarctic Ice." *Nature*, **410**(6827):441–443 (2001).

[10] Askebjer P. for the AMANDA Collaboration. "Optical Properties of Deep Ice at the South Pole: Absorption." *Applied Optics*, **36**(18):4168–4180 (1997). ISSN 0003-6935.

[11] Askebjer P. for the AMANDA Collaboration. "UV and optical light transmission properties in deep ice at the South Pole." *Geophysical Research Letters*, **24**(11):1355–1358 (1997).

[12] Atoyan A.M. and Dermer C.D. "High-Energy Neutrinos from Photomeson Processes in Blazars." *Physical Review Letters*, **87**(22):221102.1–221102.4 (2001). arXive:astro-ph/0108053.

[13] Atoyan A.M. et al. "On the gamma-ray fluxes expected from Cassiopeia A." *Astronomy and Astrophysics*, **355**(1):211–220 (2000). arXive:astro-ph/0001186.

[14] Auger Collaboration. "The Pierre Auger Project Design Report, Second Revised Edition." *Technical Report FERMILAB-PUB-96-024*, FNAL/Technical Division, Chicago, USA (1997). URL `http://www-f9.ijs.si/auger/private/DesignReport/`.

[15] Axford W.I., Leer E. and Skadron G. "The Acceleration of Cosmic Rays by Shock Waves." In "Proceedings of the 15^{th} International Cosmic-Ray Conference," volume 11, pages 132–137. Plovdiv, Bulgaria (1977).

[16] Bahcall J.N. and Waxman E. "High Energy Astrophysical Neutrinos: the Upper Bound is Robust." *Physical Review D*, **64**(2):023002.1–023002.8 (2001). arXive:hep-ph/9902383.

[17] Bai X. for the AMANDA Collaboration. "Calibration and Survey of AMANDA with SPASE." In Heinzelmann et al. [116], pages 977–980. HE.208.

[18] Balkanov V.A. for the BAIKAL Collaboration. "Registration of atmospheric neutrinos with the BAIKAL Neutrino Telescope NT-96." *Astroparticle Physics*, **12**(1–2):75–86 (1999). arXive:astro-ph/9903341.

[19] Balkanov V.A. for the BAIKAL Collaboration. "The Lake Baikal Neutrino Experiment: Selected Results." *Physics of Atomic Nuclei*, **63**(6):951–961 (2000). arXive:astro-ph/0001151.

[20] Barbagli G. for the GASP Collaboration. "The development of the gamma-ray Cherenkov telescope at the South Pole." *Nuclear Physics B Proceedings Supplements*, **32**(1–3):156–162 (1993). Proceedings of the Third International Conference on Advanced Technology and Particle Physics, Como, Italy, 22 - 26 June 1992, ed. E. Borchi, T. Ferbel, D. Hygren, A. Penzo and P.G. Rancoita.

[21] Barlow R.J. "Statistics – A guide to the Use of Statistical Methods in the Physical Science". The Manchester Physics Series. Wiley, New York, USA (1999). ISBN 0-471-92294-3.

[22] Barwick S.W. for the AMANDA Collaboration. "Potential of AMANDA-II in HE neutrino astrophysics." In Heinzelmann et al. [116], pages 1101–1104. HE.2.05.2.

[23] Bay R.C. "Search fo High Energy Neutrino Emission from Gamma-Ray Bursts with the Antarctic Muon and Neutrino Detector Array (AMANDA)." Ph.D. thesis, University of California at Berkeley, Berkeley, California, USA (2000). URL `http://area51.berkeley.edu/manuscripts/`. arXive:astro-ph/0008255.

[24] Beaman G. for the SPASE Collaboration. "Performance of the South Pole Air Shower Experiment during 1987 to 1992." *Physical Review D*, **48**(10):4495 (1993).

[25] Becker-Szendy R. et al. "Neutrino measurements with the IMB detector ." *Nuclear Physics B Proceedings Supplements*, **38**(1–3):331–336 (1995). Proceedings of the 16th International Conference on Neutrino Physics and Astrophysics, Eilat, Israel, May 1994.

[26] Bednarek W. and Protheroe R.J. "Gamma-rays from interactions of stars with active galactic nucleus jets." *Monthly Notices of the Royal Astronomical Society*, **287**:L9–L13 (1997).

[27] Bednarek W. and Protheroe R.J. "Gamma-ray and neutrino flares produced by protons accelerated on an accretion disc surface in active galactic nuclei." *Monthly Notices of the Royal Astronomical Society*, **302**(2):373–380 (1999). arXive:astro-ph/9802288.

[28] Begelmann M.C., Blandford R.D. and Rees M.J. "Theory of extragalactic radio sources." *Reviews of Modern Physics*, **56**(2):255–351 (1984).

[29] Belolaptikov I.A. for the BAIKAL Collaboration. "The Baikal underwater neutrino telescope: Design, performance and first results." *Astroparticle Physics*, **7**:263–282 (1997).

[30] Berezinsky V.S. and Dokuchaev V.I. "Hidden Source of High-Energy Neutrinos in Collapsing Galactic Nucleus." *Astroparticle Physics*, **15**(1):87–96 (2001). arXive:astro-ph/0002274.

[31] Berezinsky V.S. and Ginzburg V.L. "On high-energy neutrino radiation of quasars and active galactic nuclei." *Monthly Notices of the Royal Astronomical Society*, **194**:3–14 (1981).

[32] Berezinsky V.S. and Prilutsky O.F. "Neutrino-antineutrino annihilation around a collapsar." *Astronomy and Astrophysics*, **175**(X1–2):309–311 (1987). ISSN 0004-6361.

[33] Bergström L., Edsjö J. and Gondolo P. "Indirect detection of dark matter in km-size neutrino telescopes." *Physical Review D*, **58**(10):103519.1–103519.10 (1998). arXive:hep-ph/9607237.

[34] Bezrukov L.B. et al. "Search for Magnetic Monopoles with Deep Underwater Cherenkov Detectors at Lake Baikal." *e-preprint*, Baikal Collaboration (1996). arXive:astro-ph/9601160.

[35] Biermann P.L. "The origin of cosmic rays." *Nuclear Physics B Proceedings Supplements*, **43**(1 – 3):221–228 (1995). Proceedings of Workshop on Trends in Astroparticle Physics, arXive:astro-ph/9501006.

[36] Bionta R.M. for the IMB Collaboration. "Observation of a neutrino burst in coincidence with supernova 1987A in the Large Magellanic Cloud." *Physical Review Letters*, **58**(14):1494–1496 (1987).

[37] Biron A. "On the Rejection of Atmospheric Muons in the AMANDA Detector." Diploma thesis, Humboldt-Universität zu Berlin, Berlin, Germany (1998). URL `http://area51.berkeley.edu/manuscripts/`. DESY-THESIS-1998-014.

[38] Biron A. "Reconstruction Uncertainties due to Time Calibration Errors." *Internal report AIR/20001101*, AMANDA Collaboration (2000).

[39] Biron A. "Alexander Biron's Skyplot Package." Website (2001). URL `http://www-zeuthen.desy.de/~biron/amanda/skyplot.html`.

[40] Biron A., Leuthold M.J. and Wiebusch C.H.V. "First and Second Level Reconstruction of 97 Muon Data." *Internal report AIR/19990701*, AMANDA Collaboration (1999).

[41] Biron A., Leuthold M.J. and Wiebusch C.H.V. "Separation of ν_μ event candidates in AMANDA-B." *Internal report AIR/19990902*, AMANDA Collaboration (1999).

[42] Biron A., Leuthold M.J. and Wiebusch C.H.V. "Update on Level 1+2 processing of 97 muon data." *Internal report AIR/19990901*, AMANDA Collaboration (1999).

[43] Biron A. and Wissing H. "Impact of Varied OM Sensitivities on the AMANDA-B10 Analysis." *Internal report AIR/20001202*, AMANDA Collaboration (2000).

[44] Biron A. et al. "Upgrade of AMANDA-B towards AMANDA-II." Proposal to the DESY PRC, DESY-Zeuthen, Germany (1997). URL `http://www-zeuthen.desy.de/nuastro/publications/others/proposal_e.shtml`. Revised version.

[45] Biron A. et al. "Analysis of Atmospheric Neutrinos in 97 Data." *Internal report AIR/20010501*, AMANDA Collaboration (2001).

[46] Biron A. et al. "Participation of DESY-Zeuthen in the IceCube Project." Proposal to the DESY PRC, DESY-Zeuthen, Germany (2001).

[47] Blaauw A. et al. "The new I. A. U. system of galactic coordinates (1958 revision)." *Monthly Notices of the Royal Astronomical Society*, **121**(2):123–131 (1960).

[48] Blandford R.D. and Znajek R.L. "Electromagnetic extraction of energy from Kerr black holes." *Monthly Notices of the Royal Astronomical Society*, **179**:433–456 (1977).

[49] Blaufuss E. for the Super-Kamiokande Collaboration. "The flux and spectrum of solar neutrinos at Super-Kamiokande." In Heinzelmann et al. [116], pages 3005–3008. SH.1.01.02.

[50] Bly M. "The Starlink home page." Website (2001). URL `http://www.starlink.rl.ac.uk/`. Especially file /source/sla/galsup.f.

[51] Boliev M.M. et al. "Search for Astrophysical Sources of Neutrinos and Neutrino Oscillations Using the Baksan Data." In "Proceedings of the 24^{th} International Cosmic Ray Conference," volume 1, pages 722–725. Rome, Italy (1995). HE.5.2.10, presented by S.P. Mikheyev.

[52] Böser S. "Calculation of the flux of coincident muons from independent air showers." (2001). Private communication.

[53] Botner O. et al. "On the Sensitivity of AMANDA-II and B10 to oscillation parameters using zenith angle distributions." *Internal report AIR/20000402*, AMANDA Collaboration (2000).

[54] Böttcher M. and Dermer C.D. "An Evolutionary Scenario for Blazar Unification." *Astrophysical Journal* (2001). Accepted for publication, arXive:astro-ph/0106395.

[55] Bouchta A. "Muon Analysis with the AMANDA-B four-string detector." Ph.D. thesis, Stockholms Universitet, Stockholm, Sweden (1998). URL `http://area51.berkeley.edu/manuscripts/`. USIP Report 1998-07.

[56] Bouchta A. for the AMANDA Collaboration. "Seasonal variations of the muon flux seen by AMANDA." In Kieda et al. [136], pages 108–111. HE.3.2.11.

[57] Boziev S.N. et al. "Monte-Carlo Modelling of Muon Groups Measured in the Baksan Experiment (translation of russian title)." *INR-Preprint P-0630*, Russian Institute for Nuclear Research, Moscow, Russia (1989). In russian.

[58] Buckley J.H. "What the Wild Things Are." *Science*, **279**(5351):676–677 (1998).

[59] Bugaev E.V. et al. "Atmospheric muon flux at sea level, underground and underwater." *Physical Review D*, **58**(5):054001.1–054001.27 (1998). Extended version: arXive:hep-ph/9803488.

[60] Camenzind M. "Hydromagnetic flows from rapidly rotating compact objects. I - Cold relativistic flows from rapid rotators." *Astronomy and Astrophysics*, **162**(1 – 2):32–44 (1986).

[61] Capone A. for the ANTARES Collaboration. "The ANTARES Neutrino Telescope: Status report." In Heinzelmann et al. [116], pages 1233–1236. HE.2.05.01.

[62] Capone A. for the NEMO Collaboration. "Site characterization for a km^3 scale deep underwater astrophysical Neutrino observatory in the Mediterranean Sea." In Kieda et al. [136], pages 444–447. HE.6.3.05.

[63] Carroll B.W. and Ostlie D.A. "An Introduction to Modern Astrophysics". Addison-Wesley, Reading, Massachusetts, USA (1996). ISBN 0-201-54730-9.

[64] Cavaliere A. and D'Elia V. "The Blazar Main Sequence." *Astrophysical Journal* (2001). Submitted, arXive:astro-ph/0106512.

[65] CDS. "SIMBAD Astronomical Database." Website (2001). URL `http://simbad.u-strasbg.fr/`.

[66] CERN Information Technology Division. "HBOOK – Statistical Analysis and Histogramming; Reference Manual". CERN Program Library Long Writeup Y250, Geneva, Switzerland (1998). URL `ftp://asisftp.cern.ch/cernlib/doc/ps.dir/hbook.ps.gz`.

[67] CERN Information Technology Division. "PAW – Physics Analysis Workstation; User's Guide". CERN Program Library Long Writeup Q121, Geneva, Switzerland (1999). URL ftp://asisftp.cern.ch/cernlib/doc/ps.dir/paw.ps.gz.

[68] Chirkin D. and Rhode W. "Muon Monte Carlo: a new high-precision tool for tracking of muons in medium." In Heinzelmann et al. [116], pages 1017–1020. HE.220.

[69] Colafrancesco S. and Blasi P. "Clusters of galaxies and the diffuse gamma-ray background." *Astroparticle Physics*, **9**(3):227–246 (1998). arXive:astro-ph/9804262.

[70] AMANDA Collaboration. "AMANDA optical module / channel database." Website (2001). URL http://area51.berkeley.edu/amanda-private/omdb/. Not publicly accessible.

[71] Cooley J. "Studies of Thresholds and Level 2 Filters." Website (2001). URL http://alizarin.physics.wisc.edu/cooley/tests.html.

[72] Costa C.G.S. "The Prompt Lepton Cookbook." *Internal report AIR/20001003*, AMANDA Collaboration (2000).

[73] le Coultre P. and the L3 collaboration. "Momentum dependence of the vertical muon flux and charge ratio measured by the L3+C experiment." In Heinzelmann et al. [116], pages 974–976. HE.2.01.05.

[74] Cowen D.F., Hanson K. for the AMANDA Collaboration. "Time Calibration of the AMANDA Neutrino Telescope with Cosmic Ray Muons." In Heinzelmann et al. [116], pages 1133–1136. HE.237.

[75] Dalberg E. "A Monte Carlo Study of Atmospheric Muon-Neutrinos in AMANDA." *USIP Report 98-02*, Stockholms Universitet, Stockholm, Sweden (1998).

[76] Dalberg E. "A Search For Neutralino Dark Matter with the AMANDA-B10 Detector." Ph.D. thesis, Stockholms Universitet, Stockholm, Sweden (1999). URL http://area51.berkeley.edu/manuscripts/.

[77] van Dantzig R. for the ANTARES Collaboration. "ANTARES, Physics Potential, Progress and Status." *Nuclear Physics B Proceedings Supplements*, **100**(1–3):341–343 (2001). Proceedings of the Europhysics Neutrino Oscillation Workshop.

[78] Desiati P., Rhode W. for the AMANDA Collaboration. "Analysis of Atmospheric Muons with AMANDA." In Heinzelmann et al. [116], pages 985–988. HE.205.

[79] Deutsche Physikalische Gesellschaft. "Verhandlungen", volume 33 of *VI*. Physik-Verlag, Weinheim, Germany, Freiburg, Germany (1998). ISSN 0420-0195.

[80] Deutsche Physikalische Gesellschaft. "Verhandlungen", volume 34 of *VI*. Physik-Verlag, Weinheim, Germany, Heidelberg, Germany (1999). ISSN 0420-0195.

[81] Deutsche Physikalische Gesellschaft. "Verhandlungen", volume 35 of *VI*. Physik-Verlag, Weinheim, Germany, Dresden, Germany (2000). ISSN 0420-0195.

[82] Deutsche Physikalische Gesellschaft. "Verhandlungen", volume 36 of *VI*. Physik-Verlag, Weinheim, Germany, Bonn Germany (2001). ISSN 0420-0195.

[83] DeYoung T.R. "Observation of Atmospheric Muon Neutrinos with AMANDA." Ph.D. thesis, University of Wisconsin at Madison, Madison, Wisconsin, USA (2001). URL http://area51.berkeley.edu/manuscripts/.

[84] Dickinson J.E. for the SPASE Collaboration. "A new air-Cherenkov array at the South Pole." *Nuclear Instruments and Methods in Physics Research A*, **440**(1):95 (2000).

[85] Duffett-Smith P.J. "Practical Astronomy With Your Calculator". Cambridge University Press, Cambridge, United Kingdom, 3rd edition (1999). ISBN 0-521-35699-7.

[86] Dziewonski A.M. and Anderson D.L. "Preliminary Reference Earth Model (PREM)." *Physics of the Earth and Planetary Interiors*, **25**:297–356 (1981).

[87] Falcke H., Gopal-Krishna and Biermann P.L. "Unified schemes for active galaxies: a clue from the missing Fanaroff-Riley type I quasar population." *Astronomy and Astrophysics*, **298**:395–399 (1995). arXive:astro-ph/9411106 and MPIFR-Bonn #594.

[88] Falcke H., Wilson A.S. and Simpson C. "HST and VLA Observations of Seyfert 2 Galaxies: The Relationship Between Radio Ejecta and the Narrow Line Region." *Astrophysical Journal*, **502**:199–221 (1998). arXive:astro-ph/9801086.

[89] Feldman G.J. and Cousins R.D. "Unified approach to the classical statistical analysis of small signals." *Physical Review D*, **57**(7):3873–3889 (1998).

[90] Fermi E. "On the Origin of Cosmic Radiation." *Physical Review*, **75**(8):1169–1174 (1949).

[91] Fermi E. "Galactic Magnetic Fields and the Origin of Cosmic Radiation." *Astrophysical Journal*, **119**:1–6 (1954).

[92] Ferrarese L. and Merritt D. "A Fundamental Relation Between Supermassive Black Holes and Their Host Galaxies." *Astrophysical Journal (Letters)*, **539**(1):L9–L12 (2000).

[93] Ferrarese L. et al. "Supermassive Black Holes in Active Galactic Nuclei. I. The Consistency of Black Hole Masses in Quiescent and Active Galaxies." *Astrophysical Journal (Letters)*, **555**(2):L79–L82 (2001). arXive:astro-ph/0104380.

[94] Fukuda Y. for the Super-Kamiokande Collaboration. "Evidence for Oscillation of Atmospheric Neutrinos." *Physical Review Letters*, **81**(8):1562–1567 (1998).

[95] Gaisser T.K. "Cosmic Rays and Particle Physics". Cambridge University Press, UK, 1st edition (1990). ISBN 0-521-32667-2.

[96] Gaisser T.K. "Uncertainty in Flux of Atmospheric Neutrinos: Implications for Upward Muons in AMANDA-B10." *Internal report AIR/20001201*, AMANDA Collaboration (2000).

[97] Gaisser T.K., Halzen F. and Stanev T.S. "Particle astrophysics with high energy neutrinos." *Physics Reports*, **258**(3):173–236 (1995). Erratum published in [98].

[98] Gaisser T.K., Halzen F. and Stanev T.S. "Erratum: Particle astrophysics with high energy neutrinos." *Physics Reports*, **271**(5–6):355–356 (1996). Erratum to [97].

[99] Gaisser T.K., Protheroe R.J. and Stanev T.S. "Gamma-Ray Production in Supernova Remnants." *Astrophysical Journal*, **492**:219–227 (1998). arXive:astro-ph/9609044.

[100] Gaisser T.K. and Stanev T.S. "Path length distributions of atmospheric neutrinos." *Physical Review D*, **57**(3):1977–1982 (1998).

[101] Gandhi R. et al. "Ultrahigh-energy neutrino interactions." *Astroparticle Physics*, **5**(2):81–110 (1996). arXive:hep-ph/9512364.

[102] Gaug M. "CutEval." Website (2000). URL `http://www-zeuthen.desy.de/~gaug/cuteval/`. Including manual.

[103] Gaug M. "Detection of Atmospheric Muon Neutrinos with the AMANDA Neutrino Telescope." Diploma thesis, Humboldt-Universität zu Berlin, Berlin, Germany (2000). URL `http://area51.berkeley.edu/manuscripts/`.

[104] Gebhardt K. et al. "A Relationship between Nuclear Black Hole Mass and Galaxy Velocity Dispersion." *Astrophysical Journal (Letters)*, **539**(1):L13–L16 (2000).

[105] Giddings S.B. "Black Hole Production in TeV Scale Gravity, and the Future of High-Energy Physics." In "APS / DPF / DPB Summer Study on the Future of Particle Physics (Snowmass 2001)," Snowmass, Colorado, USA (2001). arXive:hep-ph/0110127.

[106] Giraud-Heraud Y. and Van J.T.T., editors. "Proceedings of the XXXIInd Recontres de Moriond on Very High Energy Phenomena in the Universe", Éditions Frontière. Les Arcs, France (1997).

[107] Goodman M. for the SOUDAN 2 Collaboration. "Atmospheric Neutrinos in SOUDAN 2." In Heinzelmann et al. [116], pages 1085–1088. HE.2.03.08.

[108] Gove P.B. "Webster's Third New International Dictionary of the English Language". Merriam-Webster, Springfield, Massachusetts, USA, 3rd edition (1993). ISBN 3-8290-5292-8.

[109] Greisen K. "Cosmic Ray Showers." *Annual Reviews of Nuclear Science*, **271**:63–108 (1960).

[110] Grieder P.K.F. for the NESTOR Collaboration. "NESTOR Neutrino Telescope Status Report." *Nuclear Physics B Proceedings Supplements*, **97**(1–3):105–108 (2001). Proceedings of the 11th International Symposium on Very-High-Energy Cosmic Ray Interactions.

[111] Habig A., Scholberg K. and Vagins M. "The SNEWS Home Page." Website (1999). URL `http://hep.bu.edu/~snnet/`.

[112] Halzen F. and Hooper D.W. "Neutrino Event Rates from Gamma Ray Bursts." *Astrophysical Journal (Letters)*, **527**(2):L93–L96 (1999). arXive:astro-ph/9908138.

[113] Hartman R.C. et al. "The Third EGRET Catalog of High-Energy Gamma-Ray Sources." *Astrophysical Journal Supplement Series*, **123**(1):79–202 (1999).

[114] He Y.D. and Price P.B. "Remote Sensing of Dust in Deep Ice at the South Pole." *Journal Geophysical Research D*, **103**(14):17041–17056 (1998).

[115] Heck D. et al. "*CORSIKA*: A Monte Carlo code to simulate extensive air showers." *Wissenschaftlicher Bericht FZKA 6019*, Forschungszentrum Karlsruhe, Karlsruhe, Germany (1998). URL `http://hikwww4.fzk.de/hbk/literatur/FZKA_Berichte/FZKA6019.pdf`. See also URL `http://www-ik3.fzk.de/~heck/corsika`.

[116] Heinzelmann G., Kampert K.H. and Spiering C., editors. Proceedings of the 27th International Cosmic Ray Conference. Hamburg, Germany (2001).

[117] de los Heros C.P. for the AMANDA Collaboration. "Search for Neutrinos from WIMP annihilations with the AMANDA detector." In Heinzelmann et al. [116], pages 1557–1557. HE.324.

[118] Hill G. "Application of Importance Sampling to the atmospheric muon generator *basiev*." *Internal report AIR/20000904*, AMANDA Collaboration (2000).

[119] Hill G.C. "Experimental and Theoretical Aspects of High Energy Neutrino Astrophysics." Ph.D. thesis, University of Adelaide, Adelaide, Australia (1996).

[120] Hill G.C. "Detecting neutrinos from AGN: New fluxes and cross sections." *Astroparticle Physics*, **6**:215–227 (1997). arXive:astro-ph/9607140.

[121] Hill G.C. "Bayesian event reconstruction and background rejection in neutrino detectors." In Heinzelmann et al. [116], pages 1279–1282. HE.267.

[122] Hirata K. for the Kamiokande-II Collaboration. "Observation of a Neutrino Burst from the Supernova 1987A." *Physical Review Letters*, **58**(14):1490–1493 (1987).

[123] Hoffmann W. for the H.E.S.S. Collaboration. "Status of the High Energy Stereoscopic System (H.E.S.S.) Project." In Heinzelmann et al. [116], pages 2785–2788. OG.2.05.06.

[124] Hundertmark S. "*AMASIM* Neutrino Detector Simulation Program." In Spiering [216], pages 276–286.

[125] Hundertmark S. "Simulation und Analyse von Myonereignissen im AMANDA-B4 Neutrinoteleskop." Ph.D. thesis, Humboldt-Universität zu Berlin, Berlin, Germany (1999). URL `http://area51.berkeley.edu/manuscripts/`. In german.

[126] Hundertmark S. "Vertical Ice Properties for the AMANDA Simulation." *Internal report AIR/20001001*, AMANDA Collaboration (2000).

[127] Ingelman G. and Thunman M. "High energy neutrino production by cosmic ray interaction in the Sun." *Physical Review D*, **54**(7):4385–4392 (1996). arXive:hep-ph/9604288.

[128] Jackson J.D. "Classical Electrondynamics". Wiley, New York, USA, 3rd edition (1996). ISBN 0-471-30932-X.

[129] James F., Lyons L. and Perrins Y., editors. "Proceedings of Workshop on Confidence Limits". CERN, Geneva, Switzerland (2000). CERN yellow report 2000-005.

[130] James F. and the CERN Computing and Networks Division. "MINUIT – Function Minimization and Error Analysis; Reference Manual". CERN Program Library Long Writeup D506, Geneva, Switzerland, 94th edition (1994). URL `ftp://asisftp.cern.ch/cernlib/doc/ps.dir/minuit.ps.gz`.

[131] Jordan M. for the VERITAS Collaboration. "Multiwavelength Observations of Markarian 421." In Heinzelmann et al. [116], pages 2691–2694. OG.2.03.16.

[132] Jorstad S.G. et al. "Multi-Epoch VLBA Observations of EGRET-Detected Quasars and BL LAC Objects: Connection between Superluminal Ejections and Gamma-Ray Flares in Blazars." *Astrophysical Journal*, **556**(2):738–748 (2001). arXive:astro-ph/0102012.

[133] Jungman G., Kamionkowsi M. and Griest K. "Supersymmetric dark matter." *Physics Reports*, **267**(5 – 6):195–373 (1996). arXive:hep-ph/9506380.

[134] Kameda J. for the Super-Kamiokande Collaboration. "Resent Results from Super-Kamiokande on atmospheric neutrinos." In Heinzelmann et al. [116], pages 1057–1059. HE.2.03.01.

[135] Karle A. "Monte Carlo simulation of photon transport and detection in deep ice: muons and cascades." In Spiering [216], pages 174–185.

[136] Kieda D., Salamon M. and Dingus B., editors. Proceedings of the 26^{th} International Cosmic Ray Conference. Salt Lake City, USA (1999).

[137] Kim J.H. for the AMANDA Collaboration. "A Search for Point Sources of High Energy Neutrinos with the AMANDA Neutrino Telescope." In Kieda et al. [136], pages 196–199. HE.4.1.14.

[138] Klapdor-Kleingrothaus H.V. and Zuber K. "Teilchenastrophysik". Teubner Studienbücher, Stuttgart, Germany, 1st edition (1997). ISBN 3-519-03094-2.

[139] Klose S., Greiner J. and Hartmann D.H. "Gamma-Ray Bursts." *Physikalische Blätter*, **57**(12):47–52 (2001).

[140] Klug J. "Enhancement of the Up/Down Signal Ratio and Crosstalk Studies in AMANDA." Diploma thesis, Uppsala University, Uppsala, Sweden (1997). ISV-9/1997.

[141] Kohnle D.H.A. et al. "Multiwavelength Observations of Markarian 421 in a flaring state in 2001 with HEGRA and RXTE." In Heinzelmann et al. [116], pages 106–109. OG.2.03.07.

[142] Kopp R., Lohmann W. and Voss R. "*mudedx*, Parametrization and Monte Carlo generation of energy loss of high energy muons (1 – 10000 GeV) and, for astrophysicists, also up to 100000 GeV, Version 2.02." (1995). Private communication.

[143] Kowalski M. "On the Reconstruction of Cascade-Like Events in the AMANDA Detector." Diploma thesis, Humboldt-Universität zu Berlin, Berlin, Germany (1999). URL `http://area51.berkeley.edu/manuscripts/`.

[144] Krawczynski H. "Search for TeV Counterparts of Gamma-Ray Bursts with the HEGRA Detector." Ph.D. thesis, Universität Hamburg, Hamburg, Germany (1997). URL `http://www-hegra.desy.de/publications.html`. HH-HEGRA/97-01.

[145] Krymski G.F. "A Regular Mechanism for the Acceleration of Charged Particles on the Front of a Shock Wave." *Soviet Physics Doklady*, **22**:327–328 (1977). English translation of original in Dokl. Akad. Nauk. SSSR 234:1306-1308 (1977).

[146] Kuzmichev L.A. "On the Velocity of Light Signals in the Deep Underwater Neutrino Experiments." *e-preprint*, Moscow State University (2000). arXive:hep-ex/0005036.

[147] Lai H.L. et al. "Global QCD analysis and the CTEQ parton distribution." *Physical Review D*, **51**(9):4763–4782 (1995). arXive:hep-ph/9410404.

[148] Lang K.R. "Astrophysical Formulae", volume 2. Springer Verlag, Heidelberg, Germany, 3rd edition (1999). ISBN 3-540-64664-7.

[149] Learned J.G. and Mannheim K. "High-Energy Neutrino Astrophysics." *Annual Reviews of Nuclear and Particle Science*, **50**:679–749 (2000).

[150] Learned J.G. et al. "Proposal to construct a 148,000m2. Sr Deep Ocean Lab for the study of High Energy Neutrino Astrophysics & Particle Physics." *Proposal HDC-2-88*, University of Hawai'i at Manoa, Manoa, Hawaii, USA (1988).

[151] Leuthold M.J. "Search for Cosmic High Energy Neutrinos with the AMANDA-B10 Detector." Ph.D. thesis, Humboldt-Universität zu Berlin, Berlin, Germany (2001). URL `http://www-zeuthen.desy.de/~leuthold/`.

[152] Leuthold M.J. for the AMANDA Collaboration. "Energiemessung atmosphärischer Neutrinos: AMANDA und IceCube." In "Verhandlungen," [81], page 284. T 402.7.

[153] Levinson A. and Waxman E. "Probing Micro-quasars with TeV Neutrinos." *Physical Review Letters*, **87**(17):171101.01–171101.04 (2001). arXive:astro-ph/0106102.

[154] Li T.P. and Ma Y.Q. "Analysis Methods for Results in Gamma-Ray Astronomy." *Astrophysical Journal*, **272**(1):317–324 (1983).

[155] Lipari P. "Lepton spectra in the earth's atmosphere." *Astroparticle Physics*, **1**(2):195–227 (1993).

[156] Lipari P. and Stanev T.S. "Propagation of multi-TeV muons." *Physical Review D*, **44**(11):3543–3554 (1991).

[157] Lohmann W., Kopp R. and Voss R. "Energy Loss of Muons in the Range 1 – 10000 GeV." *CERN yellow report 85-03*, CERN, Geneva, Switzerland (1985).

[158] Lorenz E. for the MAGIC Collaboration. "Status of the 17 m diameter Magic telescope." In Heinzelmann et al. [116], pages 2789–2792. OG.2.05.07.

[159] Ma F. and Wills B.J. "Discovery of hidden Blazars." *Science*, **292**(5524):2050–2053 (2001). arXive:astro-ph/0106171.

[160] Mailov A., Grupen C. for the COSMOALEPH Collaboration. "Study of cosmic ray muons with ALEPH detector." In Heinzelmann et al. [116], pages 970–973. HE.2.01.04.

[161] Mannheim K. "γ-rays and neutrinos from a powerful cosmic accelerator." *Physical Review D*, **48**(6):2408–2414 (1993).

[162] Mannheim K. "AGN Models: High-Energy Emission." In Giraud-Heraud and Van [106], page 255. arXive:astro-ph/9703184.

[163] Mannheim K., Protheroe R.J. and Rachen J.P. "On the cosmic ray bound for models of extragalactic neutrino production." *Physical Review D*, **63**(2):023003.1–023003.16 (2001). arXive:astro-ph/9812398.

[164] Markov M.A. "On High Energy Neutrino Physics." In Sudarshan E.C.G., editor, "Proceedings of the 1960 Annual International Conference on HEP at Rochester," pages 578–581. Rochester, UK (1960). Weak Interactions - Session S4.

[165] Martin A.D., Stirling W.J. and Roberts R.G. "Pinning down the glue in the proton." *Physics Letters B*, **354**:155–162 (1995).

[166] Matsuno S. for the Super-Kamiokande Collaboration. "A search for Astronomical Neutrino Sources with the Super-Kamiokande Detector." In Heinzelmann et al. [116], pages 1065–1068. HE.2.03.03.

[167] Meszaros P. and Rees M.J. "Relativistic fireballs and their impact on external matter - Models for cosmological gamma-ray bursts." *Astrophysical Journal*, **405**(1):278–284 (1993).

[168] Miller C.J. et al. "Controlling the False Discovery Rate in Astrophysical Data Analysis." *Astronomical Journal* (2001). Submitted to Astronomical Journal, arXive:astro-ph/0107034.

[169] Miller T. for the SPASE Collaboration and for the AMANDA Collaboration. "Calibration of AMANDA with Coincident Events from SPASE-2." In Kieda et al. [136], pages 465–466. HE.6.3.11.

[170] Miočinović P. "Muon energy reconstruction in the Antarctic Muon and Neutrino Detector Array (AMANDA)." Ph.D. thesis, University of California at Berkeley, Berkeley, California, USA (2001). URL `http://area51.berkeley.edu/manuscripts/`.

[171] Mirabel I.F. "Microquasars: Open Questions and Future Perspectives, Summary of discussions." In Castro-Tirado A.J., Greiner J. and Paredes M., editors, "Proceedings of 3^{rd} Microquasar workshop," volume 276 of *Astrophysics and Space Science*, pages 319–327. Granada (2000). arXive:astro-ph/0011315.

[172] Mirabel I.F. and Rodríguez L.F. "Microquasars in our Galaxy." *Nature*, **392**(6678):673–676 (1998).

[173] Mirabel I.F. and Rodríguez L.F. "Sources of Relativistic Jets in the Galaxy." *Annual Review of Astronomy and Astrophysics*, **37**:409–443 (1999).

[174] Misaki A. et al. "Atmospheric muon fluxes underwater as a tool to probe the small-x gluon distribution." In Heinzelmann et al. [116], pages 1025–1028. HE.226.

[175] Montaruli T. for the MACRO Collaboration. "Results on high-energy atmospheric neutrino oscillations with MACRO." In Heinzelmann et al. [116], pages 1069–1072. HE.2.03.04.

[176] Motz H. and Shiff L.I. "Cherenkov Radiation in a Dispersive Medium." *American Journal of Physics*, **21**:258–259 (1953).

[177] Mücke A. and Protheroe R.J. "A proton synchrotron blazar model for flaring Markarian 501." *Astroparticle Physics*, **15**(2):121–136 (2001).

[178] Mücke A. and Protheroe R.J. "Neutrino Emission from HBLs and LBLs." In Heinzelmann et al. [116], pages 1153–1156. HE.2.04.02.

[179] Murray C.A. "The transformation of coordinates between the systems of B1950.0 and J2000.0, and the principal galactic axes referred to J2000.0." *Astronomy and Astrophysics*, **218**(1-2):325–329 (1989). ISSN 0004-6361. 1989.

[180] NASA. "NASA/IPAC Extragalactic Database (NED)." Website (2001). URL `http://nedwww.ipac.caltech.edu/`.

[181] NASA Goddard Space Flight Center. "Astronomical Data Center (ADC)." Website (2001). URL `http://adc.gsfc.nasa.gov/adc.html`.

[182] Nellen L., Mannheim K. and Biermann P.L. "Neutrino production through hadronic cascades in AGN accretion disks." *Physical Review D*, **47**(12):5270–5274 (1993). arXive:hep-ph/9211257.

[183] Niessen P. "Search for relativistic magnetic monopoles with the AMANDA detector." Ph.D. thesis, Humboldt-Universität zu Berlin, Berlin, Germany (2000).

[184] Olbrechts P. and Wiebusch C.H.V. "On the angular sensitivity of optical modules in ice." *Internal report AIR/20010102*, AMANDA Collaboration (2001).

[185] Oppelt A. "Étude de la résolution angulaire du télescope à neutrinos ANTARES." Ph.D. thesis, Université de la Méditerranée Aix-Marseille II, Marseille, France (2001). URL `http://antares.in2p3.fr/users/pohl/`. In french.

[186] Paciesas W.S. et al. "The Fourth BATSE Gamma-Ray Burst Catalog (Revised)." *Astrophysical Journal Supplement Series*, **122**(2):465–495 (1999). URL `http://gammaray.msfc.nasa.gov/batse/`. arXive:astro-ph/9903205.

[187] Padovani P. "High energy emission from AGN and unified schemes." In "Proceedings of the Vulcano Workshop *Frontier Objects in Astrophysics and Particle Physics*," Vulcano, Italy (1999). arXive:astro-ph/9901130.

[188] Pandel D. "Bestimmung von Wasser- und Detektorparametern und Rekonstruction von Myonen bis 100 TeV mit dem Baikal-Neutrinoteleskop NT-72." Diploma thesis, Humboldt-Universität zu Berlin, Berlin, Germany (1996). URL `http://www-zeuthen.desy.de/nuastro/publications/diploma/index_e.shtml`.

[189] de Paolis F. et al. "High-energy neutrino emission from Gamma-Ray Bursts." e-preprint (2001). arXive:astro-ph/0107589.

[190] Parker E.N. "Origin and Dynamics of Cosmic Rays." *Physical Review*, **109**(4):1328–1344 (1958).

[191] PDG. "Review of Particle Properties." *European Physical Journal C*, **15**(1–4) (2000).

[192] Perkins D.H. "Introduction to high energy physics". Addison-Wesley, New York, USA, 4th edition (2000). ISBN 0-521-62196-8.

[193] Pesce J.E. et al. "Detection of an X-ray jet in 3C 371 with *Chandra*." *Astrophysical Journal (Letters)*, **556**(2):L79–L82 (2001). arXive:astro-ph/0106426.

[194] Porrata R.A. "The Energy Spectrum of Pointlike Events in AMANDA-A." Ph.D. thesis, University of California at Irvine, Irvine, California, USA (1997).

[195] Potgieter M.S., Raubenheimer B.C. and van der Walt D.J., editors. Proceedings of the 25^{th} International Cosmic Ray Conference. Durban, South Africa (1997).

[196] Prahl J. "Suche nach kosmischen γ-Punktquellen oberhalb von 20 TeV mit den HEGRA Detektorfeldern." Ph.D. thesis, Universität Hamburg, Hamburg, Germany (1999). URL `http://www.sub.uni-hamburg.de/disse/82/`.

[197] Press W.H. et al. "Numerical Recipies in C – The Art of Scientific Computing". Cambridge University Press, Cambridge, UK, 2nd edition (1997). ISBN 0-521-43108-5. URL `http://www.nr.com/`.

[198] Price P.B. and Bergström L. "Optical Properties of Deep Ice at the South Pole: scattering." *Applied Optics*, **36**(18):4181–4194 (1997). ISSN 0003-6935.

[199] Price P.B. and Woschnagg K. "Role of Group and Phase Velocity in High-Energy Neutrino Observatories." *Astroparticle Physics*, **15**(1):97–100 (2001). arXive:hep-ex/0008001.

[200] Price P.B. and Woschnagg K. "Temperature Dependence of Absorption in Ice at 532 nm." *Applied Optics*, **40**(15):2496–2500 (2001). URL `http://area51.berkeley.edu/manuscripts/`.

[201] Price P.B., Woschnagg K. and Chirkin D. "Age vs depth of glacial ice at South Pole." *Geophysical Research Letters*, **27**(13) (2000). URL `http://area51.berkeley.edu/manuscripts/`.

[202] Quinn J. for the VERITAS Collaboration. "VERITAS: The Very Energetic Radiation Imaging Telescope Array." In Heinzelmann et al. [116], pages 2781–2784. OG.2.05.04.

[203] Rachen J.P. "Hadronic Correlated Flares from Mrk 501." In "gamma-2000 conference," Heidelberg, Germany (2000). arXive:astro-ph/0010289.

[204] Rachen J.P., Protheroe R.J. and Mannheim K. "The relation of extragalactic cosmic ray and neutrino fluxes: the logic of the upper bound debate." Comment presented at the 19^{th} Texas Symposium, Paris, December 1998 (1998). arXive:astro-ph/9908031.

[205] Rawlins K. "Measuring the Composition of Cosmic Rays with the SPASE and AMANDA Detectors." Ph.D. thesis, University of Wisconsin at Madison, Madison, Wisconsin, USA (2001). URL `http://area51.berkeley.edu/manuscripts/`.

[206] Rhode W. "The Dipole Approximation for Track Reconstructions." (2000). Private communication.

[207] Rochester K. "Report on improving track resolution in SPASE-2-AMANDA coincidences from mass composition studies." *Internal report AIR/20000202*, SPASE and AMANDA Collaboration (2000).

[208] Saunders W. et al. "The PSCz catalogue." *Monthly Notices of the Royal Astronomical Society*, **317**(1):55–64 (2000).

[209] Scarpa R. and Urry C.M. "On The Parent Population of Radio Galaxies and the FRI - FRII Dichotomy." *Astrophysical Journal*, **556**(2):749–755 (2001). arXive:astro-ph/0104183.

[210] Schmidt T. "Phd Thesis of Thorsten Schmidt on AMANDA." Ph.D. thesis, Humboldt-Universität zu Berlin, Berlin, Germany (2002). To be submitted.

[211] Schroeder F., Rhode W. and Meyer H. "Muon Flux Simulation and Comparison with Frejus Measurement." In Heinzelmann et al. [116], pages 1013–1016. HE.2.02.01.

[212] Sigl G. "Ultra-High Energy Cosmic Rays: A Probe of Physics and Astrophysics at Extreme Energies." *Science*, **291**(5501):73–79 (2001). arXive:astro-ph/0104291.

[213] Silvestri A. "Search for Neutrino Bursts from Supernovae with the AMANDA Detector." Diploma thesis, Humboldt-Universität zu Berlin, Berlin, Germany (2000). URL `http://area51.berkeley.edu/manuscripts/`. DESY-THESIS-2000-028.

[214] Sjöstrand T. "High-energy-physics event generation with PYTHIA 5.7 and JETSET 7.4." *Computer Physics Communications*, **82**:74–89 (1994).

[215] Sokalski I.A., Bugaev E.V. and Klimushin S.I. "MUM: flexible precise Monte Carlo code for high energy muon propagation through thick layers of matter." In Heinzelmann et al. [116], pages 1001–1004. HE.221.

[216] Spiering C., editor. "Proceedings of Workshop on the Simulation and Analysis Methods for Large Neutrino Telescopes", DESY-Proc-1999-01. DESY Zeuthen, Germany (1999). ISSN 1435-8077.

[217] Stanghellini C. et al. "A complete sample of GHz-Peaked-Spectrum radio sources and its radio properties." *Astronomy and Astrophysics Supplement Series*, **131**:303–315 (1998).

[218] Stecker F.W. and Salamon M.H. "High Energy Neutrinos from Quasars." *Space Science Reviews*, **75**:341–355 (1996). arXive:astro-ph/9501064.

[219] Stecker, Floyd W.; Done, C.; Salamon, Michael H.; Sommers P. "High-energy neutrinos from active galactic nuclei." *Physical Review Letters*, **66**(21):2697–2700 (1991). ISSN 0031-9007. Erratum published in [220].

[220] Stecker, Floyd W.; Done, C.; Salamon, Michael H.; Sommers P. "Erratum: High-energy neutrinos from active galactic nuclei." *Physical Review Letters*, **69**(18):2738–2738 (1992). ISSN 0031-9007. Erratum to [219].

[221] Stenger V.J. "Track fitting for DUMAND-II Octagon Array." *External Report HDC-1-90*, University of Hawai'i at Manoa, Manoa, Hawaii, USA (1990).

[222] Streicher O. "Entwicklung einer Methode zur Rekonstuktion der Energie von Myonen mit dem BAIKAL Neutrinoteleskop NT-96." Ph.D. thesis, Humboldt-Universität zu Berlin, Berlin, Germany (2001). URL `http://www-zeuthen.desy.de/~ole/`. In german.

[223] Streicher O. et al. "The SiEGMuND software package" (2001). URL `http://www.ifh.de/nuastro/software/siegmund/`.

[224] Sudhoff P. "Systematische Untersuchungen an Optischen Modulen im AMANDA-Experiment." Diploma thesis, Humboldt-Universität zu Berlin, Berlin, Germany (2001). URL `http://www-zeuthen.desy.de/~sudhoff/Amanda/Thesis/thesis.html`. In german.

[225] Suzuki Y. for the Super-Kamiokande Collaboration. "Solar Neutrino Results from Super-Kamiokande." *Nuclear Physics B Proceedings Supplements*, **91**(1 – 3):29–35 (2000). Proceedings of the XIXth International Conference on Neutrino Physics and Astrophysics (NEUTRINO 2000).

[226] Teshima M. for the AGASA Collaboration. "Anisotropy of cosmic-ray arrival directions at 10^{18} eV observed by AGASA." In Heinzelmann et al. [116], pages 337–340. HE.1.04.03.

[227] Thorne K.S. and Żytkow A.N. "Stars with degenerate neutron cores. I - Structure of equilibrium models." *Astrophysical Journal*, **212**(1):832–858 (1977).

[228] Tinyakov P.G. and Tkachev I.I. "BL Lacartae are sources of the observed ultra-high energy cosmic rays." *Journal of Experimental and Theoretical Physics Letteres* (2001). Accepted for publication, arXive:astro-ph/0102476.

[229] Uchihori Y. et al. "Cluster Analysis of Extremely High Energy Cosmic Rays in the Northern Sky." *Astroparticle Physics*, **13**(2–3):151–160 (2000). arXive:astro-ph/9908193.

[230] Uehara Y. "Production and Detection of Black Holes at Neutrino Array." *University of Tokyo report UT-973*, University of Tokyo, Japan (2001). arXive:hep-ph/0110382.

[231] University of Chicago. "Astroparticle Physics at Chicago - Cosmic Ray Spectrum Picture." Website (1997). URL `http://astroparticle.uchicago.edu/cosmic_ray_spectrum_picture.htm`.

[232] Urry C.M. and Padovani P. "Unified Schemes for Radio-Loud Active Galactic Nuclei." *Publications of the Astronomical Society of the Pacific*, **107**(715):803–890 (1995).

[233] de Vaucouleurs G., de Vaucouleurs A. and Corwin H.G. "2nd reference catalogue of bright galaxies containing information on 4364 galaxies with reference to papers published between 1964 and 1975." University of Texas Monographs in Astronomy, University of Texas Press, Austin, Texas, USA (1976).

[234] Veron-Cetty M.P. and Veron P. "Quasars and Active Galactic Nuclei (9th edition)." *European Southern Observatory Scientific Report 19*, ESO (2000). Superseded by 10th edition since may 2001.

[235] Voges W. et al. "The ROSAT all-sky survey bright source catalogue." *Astronomy and Astrophysics*, **349**:389–405 (1999).

[236] Waltham C. for the SNO Collaboration. "Solar Neutrinos in the Sudbury Neutrino Observatory." In Heinzelmann et al. [116], pages 3001–3004. SH.1.01.01.

[237] Wang K. et al. "A Survey of the Northern Sky for TeV Point Sources." *Astrophysical Journal*, **558**(2):477–481 (2001). arXive:astro-ph/0103353 (extended version).

[238] Warren S.G. "Optical constants of ice from the ultraviolet to the microwave." *Applied Optics*, **23**:1206–1225 (1984). ISSN 0003-6935.

[239] Waxman E. "High Energy Neutrinos from Gamma-Ray Bursts." *Nuclear Physics B Proceedings Supplements*, **91**(1 – 3):494–500 (2000). Proceedings of the XIXth International Conference on Neutrino Physics and Astrophysics (NEUTRINO 2000), arXive:hep-ph/0009152.

[240] Waxman E. and Bahcall J.N. "High Energy Astrophysical Neutrinos: An Upper Bound." *Physical Review D*, **59**(2):023002.1–023002.8 (1999). arXive:astro-ph/9807282.

[241] Waxman E. and Loeb A. "TeV Neutrinos and GeV Photons from Shock Breakout in Supernovae." *Physical Review Letters*, **87**(7):071101–071104 (2001). arXive:astro-ph/0102317.

[242] Webb G.M. "Hydrodynamical constraints on cosmic-ray acceleration in relativistic shocks." *Astrophysical Journal*, **319**:215–236 (1987).

[243] Weekes T.C. "The Atmospheric Cherenkov Technique in Very High Energy Gamma-Ray Astronomy." *Space Science Reviews*, **1**:1–15 (1996).

[244] Weekes T.C. "Status of VHE Astronomy c.2000." In "Proceedings of the International Symposium on High Energy Gamma-Ray Astronomy," Heidelberg (2000). AIP Conference Proceedings 558, arXive:astro-ph/0010431.

[245] Westerhoff S. "Search for extragalactic γ-ray point sources with the HEGRA air shower array." Ph.D. thesis, Bergische Universität und Gesamthochschule Wuppertal, Wuppertal, Germany (1996). WUB-DIS 96-18.

[246] Wiebusch C.H. "The detection of Faint Light in Deep Underwater Neutrino Telescopes." Ph.D. thesis, Rheinisch Westfälische Technische Hochschule Aachen, Aachen, Germany (1995). URL `http://www-zeuthen.desy.de/~wiebusch/publication.html`. PITHA 95/37.

[247] Wiebusch C.H. "Muon reconstruction with AMANDA." In Spiering [216], pages 302–316.

[248] Wissing H. "Detection of Cosmic Muon-Neutrinos with IceCube." Diploma thesis, Humboldt-Universität zu Berlin, Berlin, Germany (2001). URL `http://www-zeuthen.desy.de/~hwissing/`.

[249] Woschnagg K. "Matching/combining laser/drill geometries." (1999). URL `http://amanda.berkeley.edu/kurt/interstring/matchgeo.html`. AMANDA internal note.

[250] Woschnagg K. "The refractive index of AMANDA ice." (2001). Private communication.

[251] Young S. "A Search for Point Sources of High Energy Neutrinos with the AMANDA-B10 Neutrino Telescope." Ph.D. thesis, University of California at Irvine, Irvine, California, USA (2001). URL `http://area51.berkeley.edu/manuscripts/`.

[252] Zech G. "Comparing Statistical Data to Monte Carlo Simulation - Parameter Fitting and Unfolding." DESY report 95-113 (1995).

A Astrophysical Parameters

A.1 Units

Due to the large distances involved, the unit meter is not considered appropriate in astrophysics. Various other units are used instead:

AU One *astronomical unit* is the semi-major axis of the earth's orbit about the sun:

$$1\,\mathrm{AU} = 1.49 \cdot 10^{11}\,\mathrm{m}\ . \tag{A.1}$$

ly One *lightyear* is the distance light travels within one year:

$$1\,\mathrm{ly} = 0.946 \cdot 10^{16}\,\mathrm{m} = 6.33 \cdot 10^{4}\,\mathrm{AU}\ . \tag{A.2}$$

pc One *parsec* is the distance of an object whose parallax is one second of an arc:

$$1\,\mathrm{pc} \equiv 1\,\mathrm{AU} \,/\, \left(3600 \cdot \frac{360}{2\pi}\right) = 3.09 \cdot 10^{16}\,\mathrm{m} = 3.26\,\mathrm{ly} = 2.06 \cdot 10^{5}\,\mathrm{AU}\ . \tag{A.3}$$

An object's parallax is half of its apparent angular displacement when measuring it from positions 2 AU apart; e.g. from opposite sides of the earth's orbit. Extra-solar distances are typically referred to in units of Megaparsec (10^6 pc).

z The *redshift* z is defined via the ratio of detected and emitted wavelength:

$$1 + z = \lambda_d / \lambda_e\ . \tag{A.4}$$

In a strict sense it is not a distance measure. An important case is the limit when the difference between time of photon emission and detection is small compared to the inverse Hubble expansion rate, (or in other words if $z \ll 1$ or $d \ll 4\,\mathrm{Gpc}$). Then, one can approximate $z \approx H_0 \cdot d/c$, where $c \sim 3 \cdot 10^5\,\mathrm{km\,s^{-1}}$ is the velocity of light in vacuum, d is the distance to the source and $H_0 = 100 \cdot h_0\,\mathrm{km\,s^{-1}\,Mpc^{-1}}$ is the Hubble expansion rate, with $h_0 \sim 0.65$ [191]. Cosmological distances are typically referred to in units of redshift. For large distances however, z is not linearly proportional to the distance any more. An often quoted redshift is $z \approx 1030$, which corresponds to the young universe at the time when the photon and matter fields decoupled.

Likewise, the SI energy unit Joule is not often used; neither in the astrophysical, nor in the particle physics literature. Units used instead are:

eV One *electron Volt* is the energy gained by a unit charge when traversing an electric field of one Volt. To relate the electron Volt with the unit Joule, one has to remember that the energy gained by a charge of one Coulomb is equivalent to one Joule:

$$1\,\mathrm{eV} = 1\frac{\mathrm{e}}{\mathrm{C}}\,\mathrm{J} = 1.60 \cdot 10^{-19}\,\mathrm{J} \tag{A.5}$$

The electron Volt is the unit of energy for so-called "natural units" where the velocity of light in vacuum c and the reduced Planck constant $\hbar$ are both set to unity. These units are commonly used in particle physics.

erg The SI system is based on the meter, the kilogram and the second and is also referred to as the "mks" system. There also exists an equivalent system based on the centimeter, the gram and the second called "cgs" system. It is often used by theoreticians and in astrophysics:

$$1\,\mathrm{erg} = 1\,\mathrm{g\,cm^2 s^{-2}} = 1\cdot 10^{-7}\,\mathrm{kg\,m^2 s^{-2}} = 1\cdot 10^{-7}\,\mathrm{J} = 6.24\cdot 10^{11}\,\mathrm{eV}\ . \qquad (A.6)$$

Finally, the strength of signals measured by various radio, X-ray, gamma-ray or neutrino experiments are given in various units: absolute counts, rates, fluxes or *Jansky*. The Jansky is the typical unit used by radio telescopes: $1\,\mathrm{Jy} = 1\cdot 10^{-26}\,\mathrm{W\,m^{-2}\,Hz^{-1}}$.

A.2 Astronomical Coordinate Systems

The position of an astronomical object is usually defined in spherical coordinates: by the direction towards it and its distance from earth. The definition of the two angles distinguishes the various coordinate systems in use. In standard Euclidean mathematics, the azimuth angle ϕ is the angle measured within a reference plane (containing the origin) from a reference direction (containing the origin) towards the projection of the object onto the plane. The zenith angle θ is the angle along a great circle centered on the origin and containing object and its projection onto the plane. An astronomical coordinate system is thus defined by the origin, the reference plane and the reference axis and a convention on the allowed values for the two angles.

A.2.1 Celestial Coordinates

coordinates	origin	ref. plane	ref. direction	azimuth	zenith
Horizon Coordinates	observer	observer horizon	north	azimuth A $0° < A < 360°$	altitude h $-90° < h < 90°$
Equatorial Coordinates	earth	equator	vernal equinox Υ	right ascension α $0h < \alpha < 24h$	declination δ $-90° < \delta < 90°$
Ecliptic Coordinates	earth	earth orbit	vernal equinox Υ	ecl. longitude λ $0° < \lambda < 360°$	ecl. latitude β $-90° < \beta < 90°$
Galactic Coordinates	sun	galactic plane	galactic center	gal. longitude l $0° < l < 360°$	gal. latitude b $-90° < b < 90°$
Super-Galactic Coordinates	sun	super-galactic plane	super-galactic center	super-gal. longitude sl $0° < sl < 360°$	super-gal. latitude sb $-90° < sb < 90°$

Table A.1: The definitions of various astronomical coordinate systems. The vernal equinox Υ, used in the definition of the equatorial and ecliptic coordinate systems, is the direction of the sun when it crosses the earth's equatorial plane northbound (on March 20^{th}). To be very precise in nomenclature, the galactic longitude should be referred to as $l2$, since an old definition $l1$ exists as well. It was based on the reference direction defined by the intersection of galactic and equatorial plane. Since this old system is ignored here, $l2 \equiv l$.

The horizon coordinates have the advantage of being most readily determined. Their disadvantage is that the coordinates are depending on the position of the observer and on

the time of the measurement (due to the ecliptic motion and the rotation of the earth). Definitions for it, the equatorial and ecliptic coordinates are taken from [85, 148].

The equatorial coordinates are not depending on the position of the observer. The time dependency is also very much reduced – but not zero: Due to the non-spherical shape of our planet and its gravitational interaction with the sun and the other planets, the rotational axis of the earth has a precession of 25,770 years period. This causes a 50.14 arc-seconds per year westward motion of the vernal equinox. One therefore fixes the reference direction to the vernal equinox of certain years called *epochs*. At present the common standard is the epoch 2000, the previous one was epoch 1950. Equatorial coordinates are the most commonly used coordinates for cosmic data sets. Due to AMANDA's location at the South Pole, a very simple relationship exists between the detector coordinate "zenith angle θ" and the equatorial coordinate "declination δ":

$$\delta = \theta - 90^\circ \tag{A.7}$$

The ecliptic coordinates are mainly used for solar system data since all planet orbits are restricted to values of small ecliptic latitude.

Likewise, the galactic coordinates define the natural coordinate system for galactic data, since most stars of our Galaxy are close to the galactic plane. Definitions for the galactic coordinates are taken from [47] (galactic coordinates, system B1950), and [179] (transformation to system J2000.0).

Most nearby galaxies (and AGNs) on the other hand are concentrated within a few degrees around the super-galactic plane at $sbb \approx 0$. Data of our local super-cluster can thus be presented in super-galactic coordinates. They are rarely used in astronomy but might be appropriate for neutrino-astronomy if nearby AGNs dominate the detected extraterrestrial neutrino flux. The corresponding coordinate system was introduced in [233]. However the value for the galactic longitude of the super-galactic origin is wrong in that reference. The correct value is $l = 137.37$ [50].

The transformations between the various coordinate systems can be found in the references stated. The only time-dependent transformation is that to ecliptic coordinates. This is due to the inclination between equator and plane of motion of the earth. Therefore the sun (at ecliptic latitude=0) has a positive declination in the summer, but a negative declination in the winter.

Note that the origins of the systems are fixed to the earth (or the earth's mean position over the year $\equiv$ the sun), not at the centers of large mass distributions. These coordinates are hence not appropriate for studying kinematics and dynamics for example in our Galaxy. For such studies, an alternative, cylindrical coordinate systems exists which has its origin in the center of the Galaxy and has coordinates R, Θ and Z. Yet another coordinate system puts the motion of the solar neighborhood to zero. This *local standard of rest* has coordinates Π_{LSR}, Θ_{LSR} and Z_{LSR} [63].

A.2.2 Detector Coordinates

Often it makes sense to define detector coordinates - for example to make use of symmetries within the detector. In case of AMANDA, this is particular useful since horizon coordinates cannot be defined: The reference direction "north" required for the horizon coordinates

is not defined at the South pole. Instead, "grid north" is used as reference direction. It is pointing from the South Pole towards Greenwich. The origin is taken in the detector center, the reference plane is parallel to the surface horizon and the angles are restricted to $0^\circ \leq \phi < 360^\circ$ and $0^\circ \leq \theta \leq 180^\circ$ ($180^\circ \equiv$ vertical up-going).

A.2.3 Co-moving Coordinate Systems

When looking for particles from (or obscured by) a source within our solar system, one can set the source to fixed locations within an appropriately defined co-moving coordinate system. This can for example be interesting during an analysis of neutrinos from WIMP-annihilations inside the sun or for an analysis of the shadow of the moon in atmospheric muons. These co-moving coordinates are simply defined as follows (example: sun):

$$\delta_\odot(t) \equiv \begin{cases} 180^\circ - (\delta - \delta(sun,\, t)) & \text{if} \quad \delta - \delta(sun,\, t) > +90^\circ \\ \delta - \delta(sun,\, t) & \text{if} \quad -90^\circ \leq \delta - \delta(sun,\, t) \leq +90^\circ \\ -180^\circ - (\delta - \delta(sun,\, t)) & \text{if} \quad \delta - \delta(sun,\, t) < -90^\circ \end{cases} \tag{A.8}$$

$$\hat{\alpha}_\odot(t) \equiv \begin{cases} \alpha - \alpha(sun,\, t) & \text{if} \quad -90^\circ \leq \delta - \delta(sun,\, t) \leq +90^\circ \\ \alpha - \alpha(sun,\, t) + 12\,\mathrm{h} & \text{otherwise} \end{cases} \tag{A.9}$$

$$\alpha_\odot(t) \equiv \begin{cases} \hat{\alpha}_\odot(t) - 48\,\mathrm{h} & \text{if} \quad \hat{\alpha}_\odot(t) > 48\,\mathrm{h} \\ \hat{\alpha}_\odot(t) - 24\,\mathrm{h} & \text{if} \quad 24\,\mathrm{h} < \hat{\alpha}_\odot \leq 48\,\mathrm{h} \\ \hat{\alpha}_\odot(t) & \text{if} \quad 0\,\mathrm{h} \leq \hat{\alpha}_\odot \leq 24\,\mathrm{h} \\ \hat{\alpha}_\odot(t) + 24\,\mathrm{h} & \text{if} \quad \hat{\alpha}_\odot(t) < 0\,\mathrm{h} \end{cases} \tag{A.10}$$

Here, the index "$\odot$" denotes the coordinate system co-moving with the sun, while no subscript represents the coordinate in the normal equatorial coordinate system. In particular: $\alpha_\odot(sun,\, t) \equiv 0\,\mathrm{h}$ and $\delta_\odot(sun,\, t) \equiv 0^\circ$ for all t.

A.2.4 Projections

Most of the coordinate systems introduced are based on spherical coordinates. Directions are given by two angles. The projection (or *mapping*) of the two coordinates onto a 2-dimensional flat surface is an ancient problem of geometry. It is well known that choices have to be made between equal-area, equal-angle and equal-distance projections. In the case of searches for point sources, equal-area projections are a natural choice. The equal-area projection chosen to represent data in this work is the *Hammer-Aitoff* projection. The transformation and its inverse are defined via

transformation	inverse transformation
$t = \sqrt{\frac{2}{1 + \cos(\delta) \cdot \cos(\alpha/2)}}$	$z = \sqrt{(1 - (0.25 \cdot x)^2 - (0.5 \cdot y)^2)}$
$x = 2 \cdot t \cdot \cos(\delta) \cdot \sin(\alpha/2)$	$\alpha = 2 \cdot \arctan\left(\frac{z \cdot x}{4 \cdot z^2 - 2}\right)$
$y = t \cdot \sin(\delta)$	$\delta = \arcsin(y \cdot z)$

(A.11)

More information on this projection and scripts implementing it can be found in [39].

B Relativistic 2-body scattering

B.1 Δ Resonance

In equation 1.1, the condition for the production of the $\Delta(1232)$ resonance was stated to be $4 \cdot E_p \cdot E_\gamma > (m_\Delta^2 - m_p^2)$. In the following, this shall be derived, independently of the frame of reference. Let the subscripts p, γ and Δ represent the particles proton, background radiation photon and Δ resonance. And let $\mathbf{P}$ represent the energy-momentum four-vector combining the energy E and the three-momentum $\vec{\boldsymbol{p}}$. Finally, let $\sphericalangle(p, \gamma)$ be the scattering angle between proton and photon. Then, in an arbitrary frame of reference,

$$m_\Delta^2 = \mathbf{P}_\Delta^2 = (\mathbf{P}_p + \mathbf{P}_\gamma)^2 \ . \tag{B.1}$$

The first equality holds true for any particle and the second one represents the conservation of energy and momentum. Then:

$$\begin{aligned} m_\Delta^2 &= \mathbf{P}_p^2 + \mathbf{P}_\gamma^2 + 2 \cdot \mathbf{P}_p \cdot \mathbf{P}_\gamma \\ m_\Delta^2 &= m_p^2 + 0 + 2 \cdot (E_p \cdot E_\gamma - \vec{\boldsymbol{p}}_p \cdot \vec{\boldsymbol{p}}_\gamma) \\ m_\Delta^2 &= m_p^2 + 2 \cdot E_p \cdot E_\gamma \cdot (1 - \cos[\sphericalangle(p, \gamma)]) \ . \end{aligned} \tag{B.2}$$

$\cos[\sphericalangle(p, \gamma)] \geq -1$, therefore:

$$\begin{aligned} &m_\Delta^2 \leq m_p^2 + 4 \cdot E_p \cdot E_\gamma, \text{ or} \\ &4 \cdot E_p \cdot E_\gamma \geq (m_\Delta^2 - m_p^2) \end{aligned} \tag{B.3}$$

B.2 Electron Pair Production

The derivation of the condition $4 \cdot E_\gamma \cdot E_{\hat{\gamma}} \geq 2 \cdot (m_e)^2$ (equation 1.2) for the pair production of electrons in photon-photon scattering is similar to the one for the Δ resonance. This time, subscripts e and $\hat{e}$ represent the two electrons and γ and $\hat{\gamma}$ the two photons. Then:

$$\begin{aligned} (\mathbf{P}_\gamma + \mathbf{P}_\gamma)^2 &= (\mathbf{P}_e + \mathbf{P}_{\hat{e}})^2 \\ 0 + 2 \cdot (E_\gamma \cdot E_{\hat{\gamma}} - \vec{\boldsymbol{p}}_\gamma \cdot \vec{\boldsymbol{p}}_{\hat{\gamma}}) &= 2 \cdot m_e^2 + 2 \cdot (E_e \cdot E_{\hat{e}} - \vec{\boldsymbol{p}}_e \cdot \vec{\boldsymbol{p}}_{\hat{e}}) \\ 2 \cdot E_\gamma \cdot E_{\hat{\gamma}} \cdot (1 - \cos[\sphericalangle(\gamma, \hat{\gamma})]) &= 2 \cdot m_e^2 + 2 \cdot E_e \cdot E_{\hat{e}} \cdot (1 - \cos[\sphericalangle(e, \hat{e})]) \end{aligned} \tag{B.4}$$

Making use of

$$\begin{aligned} &\cos[\sphericalangle(\gamma, \hat{\gamma})] \geq -1 \text{ and} \\ &\cos[\sphericalangle(e, \hat{e})] \leq 1 \ , \end{aligned} \tag{B.5}$$

one obtains

$$4 \cdot E_\gamma \cdot E_{\hat{\gamma}} \geq 2 \cdot (m_e)^2 \tag{B.6}$$

C Glossary of AGN Nomenclature

Since the AGN literature is full of terminology invented at a time when no systematic classification scheme existed for these objects, it is useful to summarize definitions of the most frequent expressions:

AGN - Active Galactic Nucleus; a class of extragalactic objects whose properties are dominated by non-stellar processes and whose locations can sometimes clearly be associated with the cores of galaxies.

Blazar Broader term including → *BL Lacertae objects* and → *FSQRs*. They have rapid multi-wavelength variability – often associated with → *super-luminal* motion [132]. During so-called flares their luminosity is strongly increased over limited time periods, the relative increase rises with rising energy of the photons emitted. Blazars have significant and variable polarization and show strong high frequency radio emission. Furthermore, they are powerful γ-ray emitters (with energies up to and beyond 10 MeV) and emit strong high frequency radio waves from compact cores. In [64], a "blazar main sequence" is proposed connecting FSQRs and BL Lacs via the different mass accretion rate of their black holes.

BL Lacertae objects A subclass of → *Blazars*. Their characteristic is a nearly featureless electromagnetic frequency spectrum, where the width of emission lines is weaker than 5 Å [187]. Their integrated radiative powers are $L < 10^{46}\,\mathrm{erg\,s^{-1}}$. Their top spectral energies are up to 10 TeV. The class is named after its most prominent prototype member: BL Lacertae, found in the northern constellation of Lacerta (the Lizard). BL Lacertaes are sometimes subdivided into *High Frequency BL Lacs* (HBL), also called *blue BL Lacs* and *Low Frequency BL Lacs* (LBL), also called *red BL Lacs*. HBLs have their emission peaks in the UV and X-Ray region, LBLs have them in the IR and optical region (LBL). LBLs seem to have an intrinsically less dense photon field than HBLs [178]. They are sometimes considered an intermediate step in an evolution scenario from FSQRs to HBLs [54]. Other authors claim that BL Lacs are the only class of AGNs which do not show any signs of cosmological evolution [64].

BLRG - Broad Line Radio Galaxy; → *Radio Galaxy* and → *Broad Line AGN*. Assumed to be the local version of a → *Quasar*.

Broad Line AGN AGN with broad emission lines which can be associated to Dopper broadening from particles of velocities larger 1000 km/s [187].

Core-dominated AGN An AGN where the dominant fraction of the energy detected on earth comes from the core. These AGNs are seen at intermediate angles with respect to the line of sight. They are also called → *Seyfert* 1 galaxies, → *QSOs*, → *BLRGs* or → *Quasars*.

FR galaxy - Fanaroff-Riley galaxy; also called → *NLRG*. FR galaxies are distinguished according to their radio morphology: The low-luminosity FR-I galaxies don't show a clear double-lobed radio structure, whereas the high-luminosity FR-II galaxies do.

FSQR - Flat-Spectrum Radio Quasars; → *Quasar*. Flat spectra are typical for emission from compact objects, so FSQRs are believed to be core dominated. FSQR have strongly polarized hubble emission lines and belong to the class of → *Blazars*. Their integrated radiative powers are as strong as $L \sim 10^{46}\,\mathrm{erg\,s^{-1}}$. Their top spectral energies observed so far are $\sim 10\,\mathrm{GeV}$.

Jet-dominated AGN An AGN where the observer is looking into the jet and all physics observations registered are dominated by processes from within the jet. These AGNs are also called → *Blazars*.

LINER - Low-Ionization Nuclear Emission-line Region; gaseous regions common in the centers of many kinds of galaxies. Some of these have been shown to be low-luminosity active galactic nuclei. They might represent a continuous transition between AGNs and non-active galaxies.

Lobe-dominated AGN An AGN seen edge on, where the central part is blocked from direct observation by a dust torus. Most of the energy detected on earth is released in giant radio-lobes at the end of the AGN jets.

Microquasar An X-ray binary containing a stellar mass black hole which is accreting matter from a companion star. This is not an AGN. But since its properties are similar to a micro-sized AGN, it is called microquasar. Due to its name it is sometimes confused and only therefore listed here.

Narrow Line AGN AGN with narrow emission lines which can be associated to Dopper broadening from particles of velocities less 1000 km/s [187].

NLR - Narrow Line Region; the source region of photons with narrow absorption lines. The region dominates the picture of type 2 AGN. The region is located in the interstellar medium (ISM) close to the jet. The ISM is probably compressed and excited by transversal waves originating from the shock fronts within the jets [88].

NLRG - Narrow Line Radio Galaxy; → *Radio Galaxy*. The radio emission is lobe-dominated.

Quasar - QUAsi StellAr Radio source; an object at large redshift ($z > 0.1$) showing strong broad emission lines. Variability shows that the energy must arise in a small region (on astrophysical scales), though some quasars have hundreds of times the energy output of normal galaxies. Their radio structures often include jets and lobes similar to what is seen in radio galaxies, but no host galaxies are resolved. When their radio flux $F(\nu \sim 5\,\mathrm{GHz}) \propto \nu^{-\alpha}$ has a spectral index $\alpha < 0.5$ they are called steep-spectrum radio quasars (SSRQs), otherwise flat-spectrum (FSRQs) [187]. In the definition used here, Quasars are always → *radio loud*. But sometimes the term quasar additionally includes → *QSOs*.

QSO - Quasi-Stellar Object; an object with optical properties are like those described for → *quasars*, but which is radio-quiet. The term "quasar" is often used more loosely than here to include QSOs.

Radio Galaxy A galaxy showing unusually strong radio emission, too intense to be produced by the normal processes of star birth and star death. This may come only from the nucleus, or from a pair of more or less symmetric lobes stretching as far as a million light-years away from the nucleus. Many radio galaxies show emission from jets connecting the nucleus to these lobes. Optical spectra of radio galaxies may show nothing unusual. But in many instances they show strong emission lines, either only narrow (*NLRG* -, like type 2 → *Seyferts*) or also including broad lines (*BLRG*, like quasars and type 1 → *Seyferts*).

Radio Loudness When plotting the optical luminosity L_{opt} (at 4400 Å) versus the radio luminosity L_r (at 5 GHz), there seems to be a bimodal AGN population. The "radio-loud" (or "radio-strong") sources have radio powers 3-4 orders of magnitude larger than the "radio-silent" (also called "radio-quiet" or "radio-weak") sources. The dividing line is usually taken at a ratio $L_r/L_{opt} \equiv R \sim 10$ [187] with about 10-15 % of all AGNs being classified as radio-loud.

SSRQ - Steep-Spectrum Radio Quasars; → *Quasar*. Their spectrum is typical for emission from extended regions: SSRQ are lobe-dominated.

Seyfert galaxy Galaxy, usually spiral or disturbed system. Their nucleus shows strong optical emission lines which are too broad and of ionization too high to be produced by the stellar population of the galaxy. Often, one observes a bright starlike nucleus associated with this. Seyfert 1 galaxies have broad emission lines that include allowed (Doppler broadening indicating speeds between 1000 and 5000 km s^{-1}) and narrower lines (from forbidden transitions, speeds around 500 km s^{-1}). Seyfert 1 galaxies only show narrow (allowed and forbidden) lines representing speeds around 500 km s^{-1}. Seyfert 1 galaxies are believed to be local representatives of → *QSO*s. Seyfert nuclei are strong X-ray sources, and many show significant radio emission.

Super-luminal Sources Radio sources which show internal motions (for example, increasing separation between the core and a knot in the jet) which appears faster than the speed of light in an observers frame of reference. The data are consistent with this being a transformation effect from seeing jets moving almost directly toward the observer, so that the emitting material almost catches up with its own radiation. This has the effect of compressing the scale of time that one measures for it, and so increasing the observed speed. It occurs when the Lorentz boost factor $\gamma > 1/\sin\phi$, where ϕ is the angle between source motion direction and line of sight.

Unusual emission lines Emission lines of an "unusual" type describe objects of unusually weak spectral features, which have strong and rapid variability: → *blazars*.

D Processing Details

D.1 OM selection

During the analysis presented in this work, some OMs were found to be generally unusable due to various reasons. They are listed in table D.1. Dead OMs were obvious choices. OMs with missing calibration information were selected according to the AMANDA OM database [70]. "Instable OMs" are neither dead, nor lack calibration information. But they have an instable ADC and/or TDC distribution and are therefore rejected. The digital OMs were individual OMs deployed to test a different read out technology. The special calibration of these was not considered as sufficiently accurate. Hits in all these OMs were always removed from the data stream.

Category	OM numbers
dead	28, 32, 34, 39, 40, 47, 50, 57, 62, 78, 96, 143
	172, 195, 197, 199, 227, 235 and 267
missing calibration: T_0, α and ADC	83, 186, 215 and 264
missing calibration: T_0	81 to 86
missing calibration: α	188, 195 and 227
missing calibration: ADC	49 and 167
"instable"	167, 186 and 190
digital OM	231, 232

Table D.1: OMs which were always removed from experimental and simulated data. T_0 and α are the two constants obtained from the timing calibration of the TDC. Together with the amplitude (ADC) calibration they are explained in section 5.

Several OMs were running stable only for parts of the data taking period. Causes were surface electronics and/or data acquisition problems which were occurring and/or solved during the year. Table D.2 lists the run-periods during which individual OMs had to be removed from the experimental data stream.

OM numbers	Runs
18	1093-1116
35	761
79	up to 770
80	up to 773
204, 214, 217, 225, 258 and 284	768-770, 833-844, 967-1001, 1082-1083 and 1116
233, 234, 259, 260 and 261	from 686 on
255	from 639 on
263	545-824

Table D.2: OMs which were removed for some runs from the experimental data stream.

For simplicity, the MC simulation tried to simulate a year-average detector and did not attempt to simulate specific experimental runs. Hence a run dependent OM selection

could not be performed for the simulated data. Instead, those OMs which were unstable for more than half of the detector live-time were always removed from the simulation. The other OMs were always kept in the data, see table D.3.

OM numbers	treatment in MC simulation
233, 234, 255, 259, 260 and 261	always removed
18, 35, 79, 80, 204, 214, 217, 225, 258, 263 and 284	never removed

Table D.3: OM selection in simulated data for those OMs which were removed for some experimental runs.

D.2 Run Information

Tables D.4 to D.8 provide information for each run in the 1997 dataset. *NOM* gives the number of stable OMs according to [56]. This input is needed for the preprocessing, see section 7.1.1. The "runtime" is the duration of the run in seconds. The column "dead-%" gives the fraction of the runtime lost due to DAQ and electronics dead-time. It is obtained from comparing the time-differences between registered events within each run to a Poissonian distribution. "Data rate" gives the measured event rate. Correcting this for the dead-time, one obtains the physical "true rate" given in the last columns.

Run	*NOM*	runtime [s]	dead-%	data rate [Hz]	true rate [Hz]	Run	*NOM*	runtime [s]	dead-%	data rate [Hz]	true rate [Hz]
304	37	509.8224165	?	?	?	484	25	163236.2365617	0.250946	75.2087	100.4049
350	156	1465.9999721	?	?	?	485	22	12471.6423002	0.252063	74.1990	99.2050
364	196	1978.6521965	?	?	?	486	12	120.6051930	0.499039	49.4838	98.7777
370	44	754.1676221	?	?	?	487	22	3085.6441517	0.247775	74.7082	99.3163
382	27	312.3845281	?	?	?	488	25	90717.9020357	0.239841	76.2337	100.2865
411	15	387.6175657	?	?	?	489	25	9579.6057013	0.237298	77.1598	101.1663
424	10	172.0024713	?	?	?	490	25	61251.9459626	0.238747	76.8630	100.9691
447	16	398.4394651	?	?	?	491	25	163027.7208914	0.238426	77.5167	101.7849
451	25	81848.7426227	?	?	?	492	25	89711.3039264	0.274506	73.4211	101.2015
453	25	13887.8371900	?	?	?	493	26	46706.7364944	0.237923	77.4297	101.6036
454	25	81659.5261592	0.236166	74.5494	97.5990	494	26	103408.9575899	0.239477	77.3505	101.7069
455	25	56272.1206856	0.237635	76.2899	100.0700	495	26	6787.4106369	0.259189	74.2809	100.2697
456	25	11816.3392780	0.249607	78.2632	104.2962	496	25	152693.0832911	0.238436	76.3668	100.2763
457	25	11236.8842526	0.273219	76.5145	105.2786	497	25	71052.0217113	0.234659	76.6095	100.0985
458	25	38159.9722542	0.245184	77.9394	103.2561	498	25	29442.7011921	0.236928	75.8274	99.3712
459	23	14395.5203106	0.243142	77.6005	102.5298	499	25	27239.9555296	0.243749	74.7672	98.8655
460	25	79703.0422484	0.245704	77.2987	102.4779	500	235	1941.9410640	0.281031	71.2334	99.0771
461	25	5140.4972373	0.241957	77.4124	102.1213	501	246	4881.0665347	0.249666	74.5614	99.3709
462	?	3123.6689210	0.267040	74.3651	101.4586	502	248	3245.7948470	0.247011	74.4807	98.9133
463	24	15968.6635599	0.253829	75.8570	101.6617	503	255	8782.9428614	0.229078	77.0580	99.9556
464	25	4245.8021890	0.317077	69.3492	101.5476	504	256	41732.8508775	0.227109	77.8153	100.6808
465	25	553.0554910	0.712493	29.4166	102.3159	505	231	1382.2235951	0.266320	73.0642	99.5859
466	25	19898.2092991	0.251895	76.4572	102.2011	506	259	12743.4294100	0.243782	75.6109	99.9856
467	24	2407.5010406	0.344888	66.8627	102.0630	507	260	112743.2956827	0.232768	76.7468	100.0308
468	13	105.7359383	0.698965	32.5433	108.1048	508	189	2147.3448590	0.830339	16.7346	98.6356
469	22	2472.3718615	0.269118	75.1723	102.8515	509	260	69417.3603463	0.238168	75.3848	98.9520
470	25	67765.9505302	0.251267	77.1552	103.0477	510	?	0.0000000	0.000000	0.0000	0.0000
471	25	11036.7097595	0.285620	73.7955	103.30	511	?	0.0000000	0.000000	0.0000	0.0000
472	17	612.4199239	0.495095	52.1227	103.2328	512	260	62291.6152975	0.224842	76.4463	98.6202
473	9	285.7100740	0.569318	44.3597	102.9987	513	259	40539.5166850	0.238891	75.0145	98.5595
474	25	113875.3350574	0.241412	78.4453	103.4097	514	253	63919.5541992	0.232901	75.9894	99.0607
475	?	0.0000000	0.285620	73.7955	103.30	515	247	2432.5093305	0.245678	75.2219	99.7212
476	25	75112.8949998	0.240922	77.3071	101.8434	516	251	57626.7314697	0.244694	76.5567	101.3585
477	25	46590.8283946	0.307675	70.3220	101.5737	517	252	7683.7042018	0.271327	73.3040	100.5992
478	25	5809.4621230	0.247285	76.4610	101.5802	518	259	49584.5436791	0.236542	76.3237	99.9712
479	25	178623.7263178	0.238472	74.7386	98.1429	519	256	122580.7423261	0.240508	76.1474	100.2609
480	24	11466.7116500	0.260717	69.9131	94.5688	520	234	1759.7728121	0.261099	74.4454	100.7515
481	25	24641.2779813	0.240564	72.1422	94.9945	521	260	54405.3131100	0.713233	28.4611	99.2482
482	25	32057.1355917	0.248690	72.7948	96.8905	522	260	14042.2570499	0.256101	73.5231	98.8348
483	25	18406.6972672	0.705494	29.6709	100.7483	523	207	818.6510392	0.292909	70.7554	100.0655

Table D.4: Information on runs 304 – 523

Run	*NOM*	runtime [s]	dead-%	data rate [Hz]	true rate [Hz]
524	260	6016.6268833	0.253550	73.8545	98.9409
525	197	685.9013879	0.299632	69.6412	99.4351
526	222	951.8593317	0.273554	71.7575	98.7788
527	247	17730.9421309	0.344610	66.4162	101.3384
528	253	13122.0973610	0.243308	75.0728	99.2117
529	210	738.9094629	0.282484	71.5230	99.6814
530	253	23676.0075583	0.238851	75.6094	99.3359
531	247	7996.1126200	0.273216	73.4039	100.9983
532	246	2983.2067597	0.338420	65.2265	98.5919
533	229	5548.5177240	0.754854	24.2625	98.9718
534	?	0.0000000	0.000000	0.0000	0.0000
535	252	56635.3310452	0.247341	74.6254	99.1490
536	257	4646.2114522	0.290094	68.8933	97.0458
537	260	19448.5342443	0.237563	73.3508	96.2057
538	260	96868.9988600	0.265377	70.3963	95.8265
539	203	729.9917145	0.250206	71.8036	95.7643
540	260	57874.3686549	0.238742	73.7976	96.9417
541	224	1337.3193185	0.361338	61.8947	96.9131
542	260	36332.2452240	0.242769	71.3573	94.2346
543	194	675.0927754	0.360299	63.0091	98.4978
544	172	446.2504519	0.320829	67.0543	98.7296
545	260	5761.7153647	0.301803	68.0429	97.4553
546	85	237.7475563	0.798870	20.2484	100.6730
547	241	1525.9002958	0.274358	71.9333	99.1305
548	204	802.9393762	0.290442	70.6579	99.5802
549	257	3655.4817540	0.272954	72.3653	99.5332
550	261	10050.8052178	0.233136	75.3841	98.3018
551	158	302.7666304	0.320153	66.7775	98.2244
552	157	393.3435881	0.395454	60.3696	99.8594
553	?	0.0000000	0.000000	0.0000	0.0000
554	247	3095.5039617	0.356915	62.6289	97.3883
555	?	0.0000000	0.000000	0.0000	0.0000
556	262	68139.8648430	0.236377	75.2376	98.5272
557	225	1659.8072637	0.454789	54.1738	99.3630
558	?	0.0000000	0.000000	0.0000	0.0000
559	?	0.0000000	0.000000	0.0000	0.0000
560	94	485.1983762	0.884136	11.6324	100.3969
561	118	243.5938017	0.426455	56.6517	98.7747
562	212	1346.9806329	0.460529	54.0386	100.1697
563	262	29348.2671395	0.243394	84.3957	111.5451
564	260	17104.7001742	0.755580	24.6665	100.9184
565	260	6917.2416867	0.271594	81.8571	112.3784
566	255	1537.9440300	0.366280	130.7310	206.2916
567	261	7666.7851955	0.253782	70.3489	94.2739
568	259	4921.9181787	0.272489	68.1911	93.7321
569	240	1842.8435145	0.307086	68.0003	98.1367
570	250	2490.9344427	0.261462	74.3902	100.7262
571	?	0.0000000	0.000000	0.0000	0.0000
572	246	1767.8244152	0.242860	76.1490	100.5745
573	259	2930.4795582	0.256875	74.0732	99.6779
574	243	1730.3565757	0.284731	71.4997	99.9620
575	219	1348.9625894	0.442022	56.2677	100.8421
576	262	5097.7993537	0.258125	74.7354	100.7385
577	261	6621.3329773	0.240443	76.1884	100.3064
578	259	4658.9143528	0.533338	74.1149	158.8191
579	262	19828.4064870	0.254211	74.8370	100.3460
580	241	1637.4180894	0.273347	72.3511	99.5675
581	261	4689.6749517	0.263947	73.1769	99.4181
582	247	2041.8260414	0.286074	71.3499	99.9401
583	262	19815.4366859	0.253165	74.6654	99.9758
584	261	7660.9194163	0.248477	75.4212	100.3578
585	221	1025.6033020	0.307217	69.0169	99.6227
586	?	0.0000000	0.000000	0.0000	0.0000
587	200	943.3863733	0.526571	47.4472	100.2202
588	212	711.7320548	0.267281	73.2720	100.0001
589	227	898.4953244	0.253263	75.0199	100.4636
590	259	5103.3138996	0.268307	72.7316	99.4018
591	260	4676.7832049	0.262245	73.4644	99.5783
592	210	869.7767779	0.279100	72.0794	99.9853
593	262	30446.3220451	0.239079	75.3083	98.9698
594	261	4843.2545931	0.259230	73.4479	99.1508
595	?	0.0000000	0.000000	0.0000	0.0000
596	258	3665.9844002	0.268678	72.4501	99.0673
597	261	13265.8288882	0.251432	74.1029	98.9929
598	130	333.3004363	0.545135	45.3405	99.6789
599	213	984.90393610	0.424822	56.2136	97.7325
600	87	132.5849210	0.583821	41.0152	98.5518
601	262	7506.4857795	0.240433	74.8108	98.4913
602	216	1022.6593796	0.350916	64.2863	99.0415
603	259	5288.0291737	0.264138	72.4268	98.4244
604	262	9451.3773277	0.239772	75.0298	98.6938

Run	*NOM*	runtime [s]	dead-%	data rate [Hz]	true rate [Hz]
605	196	584.7372806	0.314348	67.9604	99.1180
606	262	14029.4851305	0.258019	73.1055	98.5274
607	218	1073.1183592	0.294368	69.6456	98.6997
608	243	1799.8903028	0.282640	70.8521	98.7678
609	256	2782.1449381	0.293450	69.6887	98.6323
610	230	1230.1982815	0.300553	68.5979	98.0744
611	235	1211.5194447	0.293979	69.5234	98.4722
612	211	842.6876851	0.279257	70.7273	98.1310
613	239	1899.3264809	0.276994	70.8783	98.0328
614	223	1100.7664090	0.345517	64.8803	99.1321
615	231	1166.0562072	0.336053	66.2712	99.814
616	262	20243.6673837	0.242900	73.9946	97.7343
617	260	3654.3046208	0.275983	71.3816	98.5910
618	140	250.3638013	0.364037	62.9604	99.0000
619	204	630.3520766	0.281322	70.8017	98.5166
620	228	1167.9203627	0.388271	59.8534	97.8430
621	227	1216.0551569	0.284235	69.8085	97.5299
622	246	2207.4174349	0.352331	63.8583	98.5972
623	262	10952.0052436	0.258821	72.8423	98.2789
624	261	5029.5120820	0.256288	73.0453	98.2171
625	255	26730.9520305	0.250911	74.8983	99.9860
626	254	11147.0014440	0.244180	75.1246	99.3948
627	194	655.1104261	0.302121	69.6096	99.7446
628	232	1561.6108974	0.301746	69.7075	99.8311
629	255	8418.7478084	0.254162	73.7327	98.8589
630	241	2342.3365149	0.262606	72.5476	98.3838
631	262	9147.0151788	0.275206	71.4046	98.5171
632	260	4788.9437315	0.255689	73.3767	98.5834
633	240	1671.6765678	0.301832	68.7795	98.5142
634	210	1088.0601741	0.307201	68.2113	98.4575
635	219	861.2812333	0.258207	73.5788	99.1904
636	255	32230.7078586	0.239948	74.4578	97.9641
637	254	8749.0363115	0.248402	73.7119	98.0735
638	262	9522.0613715	0.257408	72.6958	97.8946
639	262	9837.2509887	0.260389	72.2904	97.7411
640	257	5867.4970917	0.416772	57.1573	98.0015
641	206	716.5967240	0.305611	68.1248	98.1076
642	259	5076.9100453	0.269452	71.2004	97.4616
643	262	15318.8317800	0.240879	74.1993	97.7437
644	258	4101.6890227	0.237107	74.7858	98.0292
645	262	14864.6233877	0.236534	75.0059	98.2439
646	262	10759.0266404	0.238047	75.3355	98.8717
647	103	153.5203732	0.506078	50.3647	101.9689
648	123	810.9458259	0.832863	17.2860	103.4238
649	174	451.1950723	0.390350	61.2041	100.3923
650	262	7623.6442574	0.262718	73.9065	100.2419
651	207	689.5360762	0.335733	67.1785	101.1318
652	262	28703.2361351	0.239294	75.2123	98.8717
653	259	6751.9717497	0.276724	71.4799	98.8279
654	238	1795.7947217	0.264510	71.5583	97.2933
655	249	1780.0238705	0.259394	72.2221	97.5176
656	245	1583.0661167	0.249969	73.3305	97.7699
657	261	4099.9853145	0.263127	71.6849	97.2825
658	262	8668.5683456	0.240848	74.4641	98.0885
659	177	533.6881522	0.455771	53.8517	98.9504
660	175	619.7996041	0.463805	53.2333	99.2798
661	128	268.0708141	0.427754	56.6753	99.0402
662	209	783.3051901	0.295408	69.2629	98.3021
663	262	5603.4998424	0.260361	72.9726	98.6598
664	262	34467.9004571	0.240751	74.9557	98.7234
665	230	1258.4182786	0.266938	72.5641	98.9877
666	261	10262.3465630	0.247219	74.5239	98.9981
667	253	3064.4252394	0.272117	71.9319	98.8235
668	227	1123.8378509	0.281926	71.6972	99.8466
669	253	7575.9265326	0.265889	72.4135	98.6410
670	256	15106.8682900	0.240382	75.6509	99.5907
671	261	28744.4180432	0.238828	76.2263	100.1434
672	261	22801.6602717	0.249487	74.9868	99.914
673	252	6005.3650730	0.307662	67.7371	97.8382
674	132	216.8618518	0.302478	63.9900	91.7392
675	235	1471.5655043	0.315591	62.6843	91.5889
676	257	3551.0224829	0.243300	69.5653	91.9325
677	258	64504.6082442	0.242449	74.0921	97.8047
678	44	65.0219471	0.749935	26.1143	104.4297
679	260	4841.0163260	0.243371	75.2894	99.5063
680	230	1193.0056297	0.245649	74.3450	98.5549
681	252	88779.1085960	0.239990	74.5484	98.0888
682	239	1923.6223400	0.235890	75.6235	98.9694
683	253	109583.4897369	0.244574	75.2033	99.5509
684	253	79193.5403757	0.245011	74.6601	98.8891
685	253	87336.6438109	0.238953	72.3779	95.1030

Table D.5: Information on runs 524 – 685

Run	*NOM*	runtime [s]	dead-%	data rate [Hz]	true rate [Hz]	Run	*NOM*	runtime [s]	dead-%	data rate [Hz]	true rate [Hz]
686	254	160906.1925871	0.241692	72.9424	96.1911	767	195	256869.8975057	0.248087	66.7168	88.7294
687	258	111592.7300808	0.225270	74.9821	96.7848	768	96	26125.8130267	0.208097	20.9897	26.5054
688	252	146037.1837182	0.261647	77.0292	104.3257	769	19	104.0135489	0.493272	13.7963	27.2262
689	258	22957.9383173	0.251378	74.8953	100.0443	770	106	19363.5788472	0.328445	33.7293	50.2256
690	257	64104.6204094	0.257608	75.8732	102.2010	771	190	6088.8706459	0.296359	56.4249	80.1899
691	256	76943.3922399	0.254692	75.2141	100.9168	772	191	15737.3310470	0.253088	59.7160	79.9505
692	256	16314.6775067	0.254894	74.5210	100.0139	773	193	35465.8912230	0.247915	69.5201	92.4366
693	257	7778.0478568	0.256278	73.7519	99.1660	774	89	132.8051857	0.531213	49.2677	105.0961
694	254	5640.8597364	0.250071	74.1844	98.9219	775	?	0.0000000	0.000000	0.0000	0.0000
695	256	70871.2549586	0.253851	75.2067	100.7932	776	254	17063.1320891	0.252930	75.2576	100.7370
696	255	92102.4991247	0.254728	75.4076	101.1813	777	259	37490.5292607	0.260676	75.6550	102.33
697	247	62398.8316995	0.261305	76.2768	103.2589	778	257	7593.3506373	0.271326	73.3310	100.6362
698	244	9757.9854711	0.242032	78.5781	103.6694	779	257	168197.4147000	0.254395	78.3419	105.0716
699	256	101763.6739272	0.243109	77.7835	102.7671	780	258	7105.0320558	0.304731	72.5590	104.3610
700	256	66725.3956168	0.259752	79.4800	107.3695	781	233	1565.0843237	0.277839	75.4905	104.5341
701	256	68085.2459174	0.240425	80.0683	105.4120	782	257	59974.1236254	0.252256	78.3341	104.7605
702	249	10469.1169920	0.287371	72.1326	101.2205	783	258	93935.7924041	0.256985	78.1457	105.1738
703	257	126480.1104046	0.239249	76.7939	100.9449	784	253	3831.1024553	0.249941	77.6244	103.4911
704	258	136487.0500254	0.254650	78.6334	105.4987	785	258	12795.7303821	0.254388	77.2852	103.6533
705	258	96222.7448920	0.243523	80.4717	106.3769	786	23	132.4393359	0.975524	17.7968	727.1115
706	258	32577.8937630	0.255637	79.1565	106.3412	787	?	0.0000000	0.000000	0.0000	0.0000
707	256	6313.3375555	0.259717	79.3295	107.1611	788	73	302.4061597	0.996421	8.9350	2496.689
708	257	88139.5591262	0.256639	79.1116	106.4242	789	?	0.0000000	0.000000	0.0000	0.0000
709	258	25896.3983192	0.262709	77.5221	105.1445	790	256	27828.2806201	0.253678	78.5465	105.2448
710	204	972.0264135	0.300765	74.2891	106.2434	791	253	15549.5520040	0.262563	75.8327	102.8327
711	191	712.3657591	0.309464	73.1394	105.9169	792	255	67274.3544751	0.253159	77.2407	103.4233
712	253	4802.6149901	0.274144	76.5916	105.5190	793	259	32964.3532967	0.253887	76.5605	102.6125
713	257	29050.1359497	0.241688	79.5779	104.9409	794	241	2091.1225600	0.253712	76.9343	103.0892
714	256	11675.0536546	0.287553	75.1925	105.5411	795	259	33885.7270000	0.252740	77.0167	103.0655
715	258	91147.2714600	0.256389	77.2601	103.8986	796	?	0.0000000	0.000000	0.0000	0.0000
716	258	94198.4946946	0.252036	78.3584	104.7622	797	259	14451.1008569	0.251440	76.4728	102.1598
717	258	41913.6645780	0.288366	74.3560	104.4863	798	?	0.0000000	0.000000	0.0000	0.0000
718	258	30587.6063576	0.256377	77.8628	104.7074	799	259	30053.1139213	0.254014	80.1592	107.4541
719	258	15151.1345653	0.257204	75.1117	101.1203	800	259	54648.1654567	0.260047	78.6900	106.3445
720	258	41107.4103117	0.253974	75.4276	101.1058	801	259	40075.4659854	0.251119	76.5059	102.1603
721	257	69885.7003642	0.246596	75.6639	100.4294	802	259	23457.9827518	0.248716	75.8813	101.0022
722	249	2684.5792109	0.288361	71.5121	100.4894	803	259	32875.7538400	0.252277	74.0893	99.0865
723	116	264.3834508	0.643720	35.8797	100.7065	804	259	92212.1293660	0.251399	74.0496	98.9173
724	258	10528.6444946	0.258825	74.9323	101.0994	805	259	139359.4584275	0.250998	76.6791	102.3751
725	258	113926.8603325	0.255563	77.3541	103.9095	806	?	0.0000000	0.000000	0.0000	0.0000
726	258	40341.8910026	0.263263	77.1732	104.75	807	251	26989.9737198	0.250821	77.0983	102.9103
727	258	20001.4097364	0.259364	77.4563	104.5808	808	259	13762.4791544	0.298355	71.5283	101.9438
728	258	78727.1641162	0.257115	77.0134	103.6680	809	139	310.6249962	0.431808	57.7352	101.6121
729	258	13019.6078849	0.256531	76.5056	102.9035	810	259	38209.7087100	0.256959	76.3029	102.69
730	258	65140.8537264	0.256753	76.9531	103.5364	811	259	320831.6487314	0.251432	77.2585	103.2085
731	258	92121.3682550	0.258375	77.6672	104.7258	812	259	10875.1945066	0.247777	77.0762	102.4646
732	258	13061.1478206	0.259253	76.2034	102.8737	813	259	52109.3462866	0.273578	75.2412	103.5778
733	258	28533.5261907	0.254368	76.2429	102.2528	814	257	12181.7276488	0.253796	76.5419	102.5751
734	258	11135.7855541	0.259704	74.9710	101.2717	815	243	1716.8716878	0.304840	69.7035	100.2697
735	258	19184.5940688	0.274927	73.2567	101.0336	816	?	0.0000000	0.000000	0.0000	0.0000
736	258	23543.9375025	0.268392	73.8458	100.9363	817	259	30148.3565091	0.286056	72.4373	101.4608
737	?	0.0000000	0.000000	0.0000	0.0000	818	259	92412.5257424	0.260985	76.4429	103.4390
738	256	26394.2108428	0.255133	75.4945	101.3529	819	259	66763.7068546	0.268482	86.2506	117.9064
739	258	28633.4599869	0.256140	75.7541	101.8393	820	103	435.4067886	0.932460	25.5370	378.1019
740	258	69524.7505856	0.253400	75.8548	101.6003	821	34	66.0835048	0.993075	15.8739	2292.168
741	258	11700.5202023	0.253469	75.4292	101.0396	822	51	50.1360715	0.979726	38.4952	1898.756
742	258	162554.542899	0.262442	76.9187	104.2883	823	33	37.9125870	0.995451	10.5242	2313.685
743	258	69528.4724128	0.255221	78.7370	105.7186	824	?	0.0000000	0.000000	0.0000	0.0000
744	258	37595.3133122	0.257495	78.5898	105.8442	825	166	528.0016213	0.689685	49.4639	159.3989
745	258	69262.3625333	0.259113	78.3918	105.8081	826	?	0.0000000	0.000000	0.0000	0.0000
746	258	138435.6241494	0.252063	78.5051	104.9622	827	?	0.0000000	0.000000	0.0000	0.0000
747	258	34368.8441299	0.263779	76.6171	104.0681	828	?	0.0000000	0.000000	0.0000	0.0000
748	257	74457.2912380	0.253151	76.8051	102.8389	829	254	41896.1013988	0.250161	77.8724	103.8521
749	249	65748.6380508	0.254575	76.4305	102.5328	830	238	1883.3855131	0.270011	75.7397	103.7546
750	258	107394.0606788	0.251868	77.1176	103.0802	831	257	133686.3711762	0.246907	78.7719	104.5979
751	257	45087.8974803	0.257054	77.1095	103.7888	832	256	188322.4596942	0.251451	78.4723	104.8326
752	254	27345.0349127	0.255964	75.3182	101.2293	833	215	18813.1530304	0.257767	72.8259	98.1172
753	258	33775.5449184	0.256351	76.5593	102.9508	834	131	1889.3701730	0.311236	30.4509	44.2109
754	258	18510.7928884	0.252144	76.8676	102.7840	835	137	1713.2727852	0.229599	34.8281	45.2077
755	256	22739.5312027	0.258469	77.5305	104.5546	836	165	15346.6506365	0.206889	35.3127	44.5242
756	257	80085.9748719	0.253733	77.8892	104.3717	837	83	416.7417099	0.206158	35.0313	44.1288
757	257	70520.1399475	0.258742	77.3261	104.3174	838	170	13781.2605093	0.213065	34.6420	44.0214
758	256	6427.2883406	0.260295	77.0302	104.1363	839	145	2869.0916928	0.208933	34.4660	43.5689
759	258	128308.3979170	0.251661	78.4874	104.8822	840	167	6011.7319707	0.207373	35.0280	44.1923
760	258	130882.2070781	0.254299	77.4485	103.86	841	135	2132.3565987	0.225752	34.8108	44.9608
761	223	1096.5398954	0.260475	80.1640	108.3993	842	171	16650.0935314	0.203421	35.7112	44.8307
762	192	88624.7076074	0.250007	65.5948	87.4605	843	129	859.5853234	0.275249	52.2287	72.0643
763	192	169149.9255130	0.247658	62.3948	82.9340	844	150	6398.9367901	0.598517	21.4919	53.5311
764	190	153489.5711518	0.247083	61.9115	82.2288	845	?	0.0000000	0.000000	0.0000	0.0000
765	190	151886.8244350	0.248474	60.5077	80.5131	846	?	0.0000000	0.000000	0.0000	0.0000
766	190	10985.8878479	0.265948	58.5220	79.7246	847	?	0.0000000	0.000000	0.0000	0.0000

Table D.6: Information on runs 686 – 847

Run	*NOM*	runtime [s]	dead-%	data rate [Hz]	true rate [Hz]	Run	*NOM*	runtime [s]	dead-%	data rate [Hz]	true rate [Hz]
848	?	0.0000000	0.000000	0.0000	0.0000	929	24	3.4482776	0.457182	52.2000	96.1648
849	?	0.0000000	0.000000	0.0000	0.0000	930	257	40547.4626501	0.246517	76.0104	100.8787
850	?	0.0000000	0.000000	0.0000	0.0000	931	257	81748.6493376	0.249932	78.1580	104.2012
851	?	0.0000000	0.000000	0.0000	0.0000	932	217	1108.9417386	0.288571	69.5420	97.7497
852	?	0.0000000	0.000000	0.0000	0.0000	933	255	13923.7983984	0.288077	69.4954	97.6165
853	193	679.7428445	0.261274	72.9173	98.7068	934	257	7687.7774680	0.239049	74.5892	98.0210
854	246	43229.4874739	0.250156	74.3301	99.1275	935	257	19482.2007970	0.240317	73.4850	96.7311
855	249	14825.9467664	0.251357	74.0378	98.896	936	257	19949.7403881	0.256032	80.2176	107.8241
856	251	40375.2414421	0.246690	73.6533	97.7729	937	255	32157.0848418	0.244883	78.7164	104.2440
857	?	0.0000000	0.000000	0.0000	0.0000	938	88	213.0229276	0.721834	28.7997	103.5343
858	252	44817.9296995	0.248723	73.9955	98.4929	939	256	6015.0852674	0.249976	77.2830	103.0408
859	251	97110.0800431	0.248107	73.7838	98.1308	940	76	180.1833051	0.772219	23.1153	101.4806
860	189	633.0499797	0.312188	68.4022	99.4490	941	198	926.9638152	0.512046	50.1465	102.7689
861	248	23231.8269184	0.262868	72.9715	98.9938	942	257	12798.9861021	0.251026	76.4944	102.1323
862	241	15116.8625908	0.253120	74.4845	99.7276	943	257	31138.5691079	0.252052	77.4463	103.5451
863	?	0.0000000	0.000000	0.0000	0.0000	944	255	22802.4327296	0.246754	76.8339	102.0037
864	?	0.0000000	0.000000	0.0000	0.0000	945	257	63169.0814454	0.247900	76.7540	102.0529
865	?	0.0000000	0.000000	0.0000	0.0000	946	257	245037.4460000	0.259021	89.0016	120.1136
866	?	0.0000000	0.000000	0.0000	0.0000	947	257	62060.8575188	0.256735	84.2970	113.4145
867	?	0.0000000	0.000000	0.0000	0.0000	948	237	1810.5506972	0.252381	78.8760	105.5030
868	?	0.0000000	0.000000	0.0000	0.0000	949	257	52090.5904587	0.248945	78.9870	105.1681
869	?	0.0000000	0.000000	0.0000	0.0000	950	257	26987.0449148	0.251493	77.6775	103.7766
870	?	0.0000000	0.000000	0.0000	0.0000	951	232	727.1670670	0.899425	155.6066	1547.175
871	?	0.0000000	0.000000	0.0000	0.0000	952	257	38365.0202256	0.566004	142.8917	329.2469
872	?	0.0000000	0.000000	0.0000	0.0000	953	257	66137.6258983	0.248160	78.2310	104.0527
873	?	0.0000000	0.000000	0.0000	0.0000	954	257	39191.5285881	0.239327	79.6273	104.68
874	?	0.0000000	0.000000	0.0000	0.0000	955	256	145473.4355958	0.272684	93.4244	128.4509
875	249	15707.3504472	0.266778	76.0928	103.7786	956	249	77960.9633077	0.242152	72.6108	95.8118
876	254	90653.1176649	0.245809	76.7541	101.7701	957	257	14030.8320017	0.241490	72.0500	94.9890
877	257	75500.6253152	0.244470	76.0612	100.6726	958	197	772.3678765	0.325785	64.4628	95.6116
878	257	67577.2098875	0.248254	75.3655	100.2540	959	256	7092.6721784	0.247294	71.3215	94.7535
879	256	19760.1124064	0.269377	76.9492	105.32	960	257	82522.5480614	0.243004	72.1019	95.2473
880	256	19935.2844488	0.256445	76.3375	102.6656	961	223	1274.9532100	0.269879	69.4629	95.1390
881	256	56137.7475765	0.244672	75.7237	100.2527	962	243	2426.7313686	0.258429	70.3411	94.8542
882	257	133280.7387104	0.244825	84.3518	111.6984	963	255	5104.4215987	0.250283	71.5985	95.5007
883	257	43152.6153655	0.247296	75.4034	100.1767	964	256	44354.4563911	0.243083	71.6289	94.6324
884	257	74984.7406721	0.248400	75.2567	100.1286	965	253	4328.4778099	0.254391	70.6364	94.7365
885	?	0.0000000	0.000000	0.0000	0.0000	966	172	16164.3238016	0.297232	46.9464	66.8021
886	257	9771.8634620	0.250514	76.6701	102.2970	967	172	13426.9219530	0.198793	29.9336	37.3606
887	?	0.0000000	0.000000	0.0000	0.0000	968	137	1962.6127662	0.194982	30.4767	37.8584
888	257	11243.7988009	0.248985	77.4561	103.1353	969	113	919.1266193	0.258117	28.4607	38.3628
889	257	12030.3553301	0.250971	77.7284	103.7722	970	15	4.5276954	0.031012	35.1172	24.1631
890	206	725.9791488	0.298912	73.3892	104.6790	971	75	455.7282007	0.316241	25.8290	37.7750
891	257	51245.7132699	0.247291	78.1065	103.7672	972	132	1836.5709099	0.212509	29.5322	37.5017
892	256	9851.3730967	0.253055	78.0472	104.4886	973	172	13140.5819079	0.190418	30.1306	37.2174
893	254	159310.8145294	0.249658	78.8502	105.0857	974	64	222.2469339	0.219891	29.9937	38.4481
894	257	14647.0127169	0.248993	77.8415	103.6495	975	165	7276.3448392	0.201388	29.9486	37.5007
895	257	10508.6028146	0.259266	77.7040	104.95	976	170	10987.4587914	0.194719	29.9490	37.1907
896	257	61551.5985726	0.248952	78.0470	103.9174	977	151	2477.6127272	0.209526	29.8303	37.7373
897	257	39233.4214049	0.253517	77.4849	103.80	978	87	701.1648652	0.207282	29.8475	37.6521
898	257	49203.4070515	0.249907	77.1385	102.8386	979	115	1330.8409458	0.219773	29.4821	37.7866
899	253	7655.6675850	0.254240	77.0886	103.3693	980	160	4742.7037217	0.215802	29.8735	38.0943
900	255	5722.8498089	0.258815	76.4509	103.1469	981	111	913.3613793	0.331840	30.5005	45.6486
901	254	4356.3161505	0.258006	76.2468	102.7593	982	171	8002.5674978	0.213375	35.7655	45.4671
902	257	59424.9135655	0.249838	77.3369	103.0936	983	155	2916.9032398	0.214113	35.6189	45.3233
903	257	82092.3890899	0.240071	109.5277	144.1288	984	?	0.0000000	0.000000	0.0000	0.0000
904	256	25311.3143032	0.516793	141.6077	293.0583	985	32	513.9289286	0.953815	2.3077	49.9663
905	254	3191.5615079	0.458149	160.1169	295.50	986	139	1824.3578888	0.211016	36.0121	45.6437
906	256	147684.1778804	0.265240	82.8848	112.8053	987	168	9659.4036000	0.211331	36.1093	45.7851
907	256	81114.7530458	0.266326	81.1070	110.5492	988	143	2261.1100853	0.207889	36.5307	46.1182
908	256	25546.9318686	0.257847	83.4857	112.4913	989	172	16871.8194422	0.212030	36.2231	45.9701
909	256	156134.5283144	0.260692	81.6417	110.4300	990	76	381.3437867	0.216534	31.7273	40.4960
910	257	13580.8078940	0.259560	76.2211	102.9402	991	172	53229.3568189	0.216342	34.3054	43.7760
911	256	31022.6783037	0.251580	77.8991	104.0847	992	171	10875.8715078	0.215014	35.3688	45.0565
912	212	1508.7213140	0.461961	57.1888	106.2913	993	173	71948.2632271	0.210034	35.6920	45.1816
913	?	0.0000000	0.000000	0.0000	0.0000	994	172	62949.1283891	0.210345	34.8176	44.0921
914	?	0.0000000	0.000000	0.0000	0.0000	995	172	73788.6296411	0.207771	34.2203	43.1949
915	146	389.9416435	0.767093	55.7289	239.2756	996	172	170726.6192673	0.201421	34.0425	42.6288
916	257	5605.4283917	0.251056	77.7635	103.8309	997	172	28374.5970299	0.198501	34.2528	42.7359
917	256	29102.1579546	0.248169	80.4529	107.0092	998	168	62276.4488626	0.203519	35.5579	44.6437
918	213	0.0000000	0.000000	0.0000	0.0000	999	169	54592.4216076	0.213144	36.0838	45.8582
919	213	1266.8090577	0.420255	59.9522	103.4114	1000	170	6745.4744871	0.202139	34.7285	43.5270
920	257	46990.5662873	0.245381	77.8514	103.1665	1001	162	4324.0322383	0.202501	35.2840	44.2433
921	257	27393.6081685	0.244020	72.9190	96.4569	1002	82	72.9095105	0.255486	76.6704	102.9804
922	222	1159.6221076	0.242333	71.5285	94.4062	1003	251	56629.1286427	0.242173	77.3014	102.0041
923	257	40571.1468322	0.242137	73.9421	97.5666	1004	208	857.0362943	0.326915	68.3518	101.5501
924	257	12448.3856638	0.249387	76.7937	102.3079	1005	252	79539.5762424	0.243162	77.4387	102.3187
925	257	40135.4104216	0.244668	76.9352	101.8561	1006	257	41243.4669169	0.242220	78.8122	104.0040
926	255	29202.0395769	0.248859	77.1647	102.73	1007	257	23326.6072831	0.248835	78.7946	104.8966
927	255	40765.4325711	0.246043	77.0326	102.1711	1008	257	18139.6824879	0.250335	78.7049	104.9868
928	257	13534.6136109	0.242149	72.9745	96.2913	1009	257	24159.6353492	0.245011	79.2095	104.9147

Table D.7: Information on runs 948 – 1009

Run	*NOM*	runtime [s]	dead-%	data rate [Hz]	true rate [Hz]	Run	*NOM*	runtime [s]	dead-%	data rate [Hz]	true rate [Hz]
1010	76	304.3764117	0.908597	9.6591	105.6763	1066	257	22865.5460647	0.255332	77.6427	104.2648
1011	88	110.4854877	0.641844	37.4167	104.4703	1067	257	108042.7606317	0.254825	77.8335	104.45
1012	230	1506.3078413	0.453676	57.3409	104.9577	1068	256	97267.3750590	0.252608	79.7174	106.6607
1013	257	12393.7395372	0.244930	78.5987	104.0946	1069	256	18382.3794532	0.255643	78.7272	105.7654
1014	138	238.2128666	0.477681	54.5562	104.4501	1070	255	11030.5959830	0.255114	79.2363	106.3738
1015	257	16787.3215566	0.249082	78.2001	104.1393	1071	256	42286.3604608	0.247247	79.5457	105.6730
1016	257	19334.0686726	0.257767	77.2583	104.0891	1072	256	25426.4748614	0.252776	79.2990	106.1248
1017	257	29223.8559455	0.239015	78.5434	103.2127	1073	256	61512.0148706	0.256794	80.2663	108.00
1018	257	43611.2798769	0.246254	77.9233	103.3814	1074	255	35897.0950710	0.257060	80.0323	107.7238
1019	256	5252.8906527	0.255240	77.3945	103.9187	1075	254	19989.3680655	0.253595	80.3264	107.6176
1020	255	3554.4996886	0.275048	75.0820	103.5682	1076	253	25173.8819631	0.253522	80.1922	107.4273
1021	209	882.3402179	0.341131	68.1971	103.5062	1077	?	0.0000000	0.000000	0.0000	0.0000
1022	243	2477.2884461	0.261339	76.3427	103.3529	1078	255	23348.2264141	0.248884	71.5597	95.2712
1023	85	102.7511322	0.571152	45.9070	107.0473	1079	252	5871.6730202	0.253736	74.6365	100.0135
1024	?	0.0000000	0.000000	0.0000	0.0000	1080	255	49376.1185607	0.253618	79.2220	106.1414
1025	257	37144.8625570	0.239542	76.1134	100.0889	1081	200	7090.2691546	0.265719	72.4146	98.6198
1026	234	1951.5546809	0.530541	48.9891	104.3523	1082	167	5445.3344519	0.222774	36.6718	47.1829
1027	8	0.5938569	0.013892	90.9310	92.2120	1083	172	241036.3279361	0.218681	36.4827	46.6938
1028	257	32088.2332494	0.249461	77.6189	103.4175	1084	?	0.0000000	0.000000	0.0000	0.0000
1029	248	1937.7415361	0.262538	76.2305	103.3687	1085	?	0.0000000	0.000000	0.0000	0.0000
1030	?	0.0000000	0.000000	0.0000	0.0000	1086	252	57031.0328791	0.256323	77.2115	103.8240
1031	257	36705.2333442	0.245320	78.3344	103.7982	1087	155	3183.9085363	0.904277	10.0490	104.9800
1032	257	16552.0074485	0.249182	78.3371	104.3357	1088	252	14572.1118510	0.254414	78.5931	105.4112
1033	257	20891.5722345	0.250929	78.3812	104.6378	1089	255	19871.5863167	0.256252	79.6197	107.0520
1034	257	66185.3970165	0.248365	78.4553	104.3796	1090	253	6492.1797491	0.259609	79.6013	107.5125
1035	254	6769.3053075	0.255652	77.3551	103.9232	1091	255	55787.2251181	0.252014	79.3538	106.0899
1036	?	0.0000000	0.000000	0.0000	0.0000	1092	255	53203.3170508	0.264247	78.7967	107.0967
1037	255	33363.1523180	0.250966	76.1989	101.7296	1093	255	29787.8669807	0.251517	77.3971	103.4054
1038	257	19660.5882582	0.352714	66.3565	102.5150	1094	255	119955.4244582	0.251123	78.8792	105.3300
1039	257	30174.4858796	0.251218	76.6926	102.4231	1095	255	108263.8571169	0.253208	80.7849	108.1759
1040	255	28747.1665200	0.299523	71.5546	102.1513	1096	255	74031.3964005	0.253610	80.4023	107.7215
1041	253	68568.3505313	0.250227	77.5092	103.3768	1097	255	23059.8528607	0.256610	80.3781	108.1237
1042	255	44208.9258435	0.251201	77.3683	103.3232	1098	241	2693.3205720	0.556227	49.3231	111.1450
1043	253	19462.4788770	0.247053	78.1070	103.7350	1099	253	28331.1412140	0.258328	81.9110	110.4411
1044	252	61325.2424409	0.248627	77.8702	103.6372	1100	254	111575.1552343	0.253046	81.5857	109.2245
1045	173	567.5032997	0.441851	58.3080	104.4667	1101	256	9684.6035916	0.257765	79.6165	107.2658
1046	255	31120.1310494	0.252825	77.7910	104.1135	1102	255	12370.8071113	0.253503	80.5257	107.8715
1047	256	57918.8035728	0.251955	77.7104	103.8847	1103	256	49354.6145140	0.255045	80.4881	108.0442
1048	256	10306.7092442	0.256632	76.8132	103.3313	1104	255	98676.4796485	0.254714	80.4557	107.9528
1049	246	2998.8952395	0.267810	75.8903	103.6484	1105	256	82667.6780456	0.273431	77.7696	107.0367
1050	255	7766.9766963	0.263677	76.2651	103.5756	1106	256	8618.9659140	0.399828	63.8369	106.3644
1051	256	39105.5605746	0.252177	77.5990	103.7665	1107	164	1237.2716395	0.749949	26.3653	105.4397
1052	255	11484.0321885	0.255119	76.7860	103.0850	1108	254	29627.7221576	0.270482	78.1707	107.1539
1053	21	2.6582769	0.231540	93.2935	121.4032	1109	97	149.3368903	0.536717	50.2421	108.4479
1054	137	211.0039437	0.391547	63.8566	104.9492	1110	176	788.6151958	0.539313	49.7708	108.0359
1055	257	16636.4668905	0.248765	77.8374	103.6127	1111	254	162890.8613264	0.254971	80.3910	107.9032
1056	257	26302.8229729	0.243249	78.5072	103.7424	1112	251	4736.2369283	0.263273	79.7433	108.24
1057	207	821.9685602	0.274925	75.1233	103.6076	1113	252	16425.4726607	0.254460	80.5246	108.0084
1058	257	59499.3060986	0.251666	78.1973	104.4952	1114	?	0.0000000	0.000000	0.0000	0.0000
1059	244	1956.7865400	0.287034	73.6227	103.2627	1115	254	54865.9612342	0.741510	80.5873	108.68
1060	23	5323.2029228	0.999392	0.0684	112.4970	1116	171	251255.0908245	0.275198	62.7311	86.5493
1061	257	66537.3228135	0.251712	77.7658	103.9250	1117	253	98278.2616859	0.262922	79.2348	107.4986
1062	256	32785.9646244	0.251849	78.0953	104.3844	1118	253	6230.2217612	0.254761	79.6306	106.8524
1063	256	29124.5682492	0.251218	78.3009	104.5711	1119	224	5031.7886087	0.817327	19.7665	108.2073
1064	257	79526.5609685	0.249933	79.0772	105.4269	1120	255	5319.3390666	0.257459	79.8103	107.4827
1065	254	2638.1554128	0.276796	77.2608	106.8313						

Table D.8: Information on runs 1012 – 1120

Summary Information: Table D.9 lists summary information for the experimental data runs. The runs are classified as good or bad according to the run selection defined in section 7.1.1. The true data rate and hence the dead time was reduced for the bad runs due to the low average number of OMs which were read out during them.

In table D.9, "av. runtime" is the average time per run, whereas "*NOM*", "dead-%", "data rate" and "true rate" are runtime weighted averages. The dead-time, data rate and true rate information were not determined for the first 10 runs (up to run 543) which were considered test runs. These runs (combined runtime: 104839.335 s) are therefore excluded from this summary information. Likewise, 57 runs of zero runtime (due to DAQ problems) scattered throughout the year are excluded. The good runs combined to a dead-time corrected lifetime of $1.124 \cdot 10^7$ seconds (130.1 years).

Class	N_{Runs}	total runtime [s]	av. runtime [s]	NOM	dead-%	data rate [Hz]	true rate [Hz]
good runs	420	15159653.7	36094.4	256.26	0.258419	76.7275	104.9718
bad runs	190	4260183.8	22422.0	107.43	0.246297	61.6044	82.6122
all runs	610	19419837.4	31835.8	223.61	0.255756	74.1726	100.0667

Table D.9: Summary information for 610 out of the 677 runs listed in tables D.4 to D.8. The information is also given separately for those runs that pass the run selection ("good") and those that fail to pass them ("bad").

D.3 Reconstruction and Filter Summary

Tables D.10 and D.11 summarize the data processing up to level 3. Up-down inverted cuts mentioned here were used in an effort to get an experimental "calibration source": When selecting the well understood down-going atmospheric muons as signal, one can systematically cross check the signal Monte Carlo simulation.

Id	Name	Remarks
Level 1		
Cut 0	$N_{ch}^{clean} \geq 5$	Pre-processing
Reco 1	Line-fit "LF"	
Cut 1	$\theta(1) > 70^\circ$ $[\theta(1) < 90^\circ]$	Zenith Line-fit
Cut 2	$v_{LF} > 0.1\,\mathrm{m/ns}$	Speed Line-fit
Reco 2	Likelihood reconstruction "$LIKE$"	Single photon arrival time likelihood
Level 2a		
Cut 3	$\theta(2) > 70^\circ$ $[\theta(2) < 90^\circ]$	Zenith, reco 2
Reco 3	Iterative reconstruction "$ITER$"	6 iterations
Cut 4	$\theta(3) > 80^\circ$ $[\theta(3) < 80^\circ]$	Zenith, reco 3
Cut 5	$L(3) < 9.5$	Likelihood parameter, reco 3
Cut 6	$N_{dir}(-20..25)(3) > 3$	Number of direct hits, reco 3
Reco 4	Energy reconstruction "$ENERGY$"	$P_{hit}P_{nohit}$, based on reco 3
Reco 5	Tensor of Inertia "$INERT$"	
Reco 6	Cascade reconstruction "$SHOWER$"	Single Photon arrival time likelihood
Level 2b		
Cut 7	$N_{ch}^{clean} > 11$	
Reco 7	Iterative reconstruction "$ITER$"	16 iterations
Cut 8	$\theta(7) > 80^\circ$ $[\theta(7) < 80^\circ]$	Equivalent to cut 4
Cut 9	$L(7) < 9.5$	Equivalent to cut 5
Cut 10	$N_{dir}(-20..25)(7) > 3$	Equivalent to cut 6
Reco 8	Energy reconstruction "$ENERGY$"	$P_{hit}P_{nohit}$, based on reco 7
Level 3		
Cut 11	$\theta(7) > 90^\circ$ $[\theta(7) < 75^\circ]$	Tightening of cut 8
Cut 12	$-100\,\mathrm{m} < z_{cog} < +170\,\mathrm{m}$	Remove corner-clippers
Cut 13	$3 \cdot I_1/(I_1 + I_2 + I_3)(5) < f_{inert}(\theta(7))$	θ-dependent cut on the sphericity of the event (Anti z_{COG} cut)

Table D.10: Overview on reconstructions and cuts up to level 3. The values of the up-down inverted cuts are given in square brackets. The reconstruction abbreviations used in section 7 are stated in apostrophes. This table is continued on the next page

Id	Name	Remarks
Cut 14	$L_{dir}(-15..+75)(7) > f_{L_{dir}}(\theta(7))$	Length of direct hits, (Anti z_{COG} cut)
Cut 15	$L(7) < 8.7$	Tightening of cut 9
Cut 16	$L(8) < 6.0$	L-parameter of the energy reco
Cut 17	$L(6)/L(7) > 0.95$	Ratio of L-parameters: track more likely than cascade
Cut 18	$N_{dir}(-15..75)(7) - N_{dir}(-15..75)(6) > 0$	Better N_{dir} for track than for cascade hypothesis
Reco 9	Weighted reconstruction "$WEIGHT$"	8 iterations
Reco 10	Dipole approximation "DA"	Original implementation
Reco 11	$P_{hit}P_{nothit} \oplus MPE$ reconstruction "MPE"	8 iterations
Reco 12	Energy reconstruction "$ENERGY$"	$P_{hit}P_{nohit}$, based on reco 11
Reco 13	Iterative reconstruction "$ITER$"	16 iterations, same 7, but new *recoos* version
Reco 14	Energy reconstruction "$ENERGY$"	$P_{hit}P_{nohit}$, based on reco 13
Level 4a		
Cut 19	$\theta(13) > 95°$ $[\theta(13) < 72.5°]$	Tightening of cut 11
Cut 20	$\theta(11) > 95°$ $[\theta(11) < 72.5°]$	Zenith, reco 11

Table D.11: Overview on reconstructions and cuts up to level 3 continued. The values of the up-down inverted cuts are given in square brackets. The reconstruction abbreviations used in section 7 are stated in apostrophes. This table continues the table from the previous page.

D.4 Level 4 Cuts

The level 4 cuts are defined by the CutEval results, see section 7.2. These results are parameterized by two linear function of the logarithm of the CutEval parameter N. Because some cuts saturate, a distinction has to be made between the regimes of larger and smaller background, see table D.12.

	fit result: $cutvalue = a + b \cdot \log_{10}(N)$			
	$N < 35$		$N > 35$	
cut parameter	a	b	a	b
$\lvert S^{P_{hit}}_{ITER}\rvert/(\theta_{MPE} - 90°)$	0.009509	0.0003148	-0.02065	0.01946
$(N_{dir,\,MPE}(-15..75) - 2) \cdot L_{dir,\,MPE}(-15..75)$	750.0	0.00000	1206	-269.6
$\log(\mathcal{L}_{down,\,ITER}) - \log(\mathcal{L}_{up,\,ITER})$	-8.702	1.058	-11.02	2.160
S^{van}_{MPE}	0.2040	0.07470	0.2398	0.05137
$\Psi(ITER, LF)$	50.00	0.00000	41.21	6.082

Table D.12: CutEval parameterization results for the level 4 cut values as function of the background CutEval parameter N.

For three values of CutEval parameter $N = 100,\ 10,\ 1$, specific data sets have been defined. The corresponding cuts are listed in table D.13. The column $N = 10$ corresponds to the default level 4 cuts for the atmospheric neutrino selection. The column $N = 100$ corresponds to the default level 4 cuts for the point source analysis.

	$N = 1$	$N = 10$	$N = 100$
$\lvert S^{P_{hit}}_{ITER}\rvert/(\theta_{MPE} - 90°)$	< 0.0095	< 0.01	< 0.018
$(N_{dir,\,MPE}(-15..75) - 2) \cdot L_{dir,\,MPE}(-15..75)$	> 750m	> 750m	> 650m
$\log(\mathcal{L}_{down,\,ITER}) - \log(\mathcal{L}_{up,\,ITER})$	< -8.7	< -7.7	< -6.7
S^{van}_{MPE}	< 0.2	< 0.28	< 0.34
$\Psi(ITER, LF)$	$< 50°$	$< 50°$	$< 50°$
$\Psi(MPE, LF)$	$< 35°$	$< 35°$	$< 35°$
$R_{S,\,dir,\,ITER}(-15..75)$	< 0.55	< 0.55	< 0.55

Table D.13: Level 4 cuts for particular values of CutEval parameter N. The cuts are rounded values from the parameterizations in table D.12. The last two cuts are not derived from CutEval, but from special investigations, see section 7.2.

D.5 Passing Rates

	Cut Level	Experiment Even days	Experiment Odd days	Experiment Bad Runs	MC Simulation Background	MC Simulation Signal
# Events	Trigger	588,636,443	589,131,415	114,694,345	276,791,645.7	5363.0
ϵ	Level 1	$0.48 \cdot 10^{-1}$	$0.48 \cdot 10^{-1}$	$0.46 \cdot 10^{-1}$	$0.35 \cdot 10^{-1}$	0.36
ϵ	Level 2	$0.44 \cdot 10^{-3}$	$0.45 \cdot 10^{-3}$	$0.57 \cdot 10^{-3}$	$0.38 \cdot 10^{-3}$	0.15
ϵ	Level 3	$0.12 \cdot 10^{-4}$	$0.13 \cdot 10^{-4}$	$0.16 \cdot 10^{-4}$	$0.69 \cdot 10^{-5}$	$0.71 \cdot 10^{-1}$
ϵ	Level 4a	$0.42 \cdot 10^{-5}$	$0.43 \cdot 10^{-5}$	$0.64 \cdot 10^{-5}$	$0.14 \cdot 10^{-5}$	$0.67 \cdot 10^{-1}$
ϵ	Level 4 ($N = 100$)	$0.34 \cdot 10^{-6}$	$0.29 \cdot 10^{-6}$	$0.33 \cdot 10^{-6}$	$0.33 \cdot 10^{-7}$	$0.51 \cdot 10^{-1}$
# Events		201	168	38	9.09	271.9
ϵ	Level 4 ($N = 10$)	$0.22 \cdot 10^{-6}$	$0.16 \cdot 10^{-6}$	$0.16 \cdot 10^{-6}$	$0.62 \cdot 10^{-8}$	$0.42 \cdot 10^{-1}$
# Events		128	95	18	1.73	224.0
ϵ	Level 4 ($N = 1$)	$0.13 \cdot 10^{-6}$	$0.10 \cdot 10^{-6}$	$0.87 \cdot 10^{-7}$	$0.16 \cdot 10^{-8}$	$0.29 \cdot 10^{-1}$
# Events		79	59	10	0.43	154.0

Table D.14: The cut passing rates of the various data sets. Shown separately is the data for odd days, even days and bad runs of the experiment, the simulated signal and the simulated background. The background simulation here combines all events simulated with the *basiev* and *CORSIKA* generator. See the text for a detailed description of the background numbers. In the case of the atmospheric neutrino signal simulation, 2-flavor $\nu_\mu \leftrightarrow \nu_\tau$ oscillations (see section 2.9) have been included. The oscillation parameters chosen were maximal mixing and $\Delta m^2 = 2.5 \cdot 10^{-3}$ eV.

Table D.14 lists the passing rates of all cut levels as well as the trigger and final event numbers. The numbers for the "bad" experimental runs are listed for comparison purposes only. They are not included in the data samples analyzed in the main part of this work. The absolute number of events is meaningless for the simulation due to its use of weights (see section 4.2). In case of the signal simulation, a lifetime much larger than the detector lifetime was simulated. All signal numbers are therefore normalized to the lifetime of the detector. For the background simulation, the choice was different. The simulated number of events was significantly smaller than that detected in the experiment. No normalization to the detector lifetime has been included to show this difference. Instead, absolute numbers of simulated background in the table refer to the number of equivalent

events. (The term *equivalent event* is defined e.g. in [252].) As will be discussed in section D.6, the normalization of the background Monte Carlo is subtle. For this table, all absolute background numbers are normalized on trigger level.

D.6 Background Normalization

The normalization of the simulation is supposedly straight forward: The simulated primary particles for background are the cosmic rays, for signal it are atmospheric neutrinos (see section 4.2). The flux Φ of the primaries is known from other experiments (cosmic rays) or taken from theory (atmospheric neutrinos). A simulated number of primaries N traversing a "generation area" A thus corresponds to a simulated lifetime $t_{sim} = \frac{N}{\Phi \cdot A}$. The simulation is therefore normalized to the experimental lifetime t_{exp} by weighing the simulated events with the ratio t_{exp}/t_{sim}.

Simulated signal is normalized with exactly this procedure. But applying it to background leads to a problem: The simulation does not reproduce the experimental trigger rate [40, 126]. The simulated trigger rate is smaller than the experimental trigger rate by $\sim 40\,\%$ [40, 126]. Various explanations for this effect can be thought of:

- The flux of atmospheric muons might be larger than simulated by the generators *CORSIKA* and *basiev*. Reason could be that the generators are mostly based on data from air shower arrays. These arrays might have insufficient sensitivity towards the high energy muon component, since they dominantly analyze photons and electrons. Laboratory measurements of the corresponding interactions are not possible: Present accelerators are energy-limited and cannot analyze very forward production of muons with energies in the $\mathcal{O}$(TeV)-scale. Direct high-resolution measurements of atmospheric muons at LEP also have not produced conclusive final results yet [73, 160].

- The energy loss of the muons in the ice might be smaller than simulated. This speculation is motivated by indications that the muon propagation at high energies is not correctly described by present muon propagation codes [78, 211].

- The sensitivity of, or the noise in the AMANDA detector might be underestimated. This assumption is in contrast to indications that the sensitivity is overestimated as discussed section 7.3.6.

The first two of these arguments are independent from the AMANDA detector. If they are the cause and cannot be corrected easily, it seems appropriate to normalize the background not to a primary flux, but to the detector trigger rate. This normalization interprets the simulated lifetime as 30.6 days. That is a factor 4 smaller than the experimental lifetime of 130.1 days.

After triggering, another challenge of the background simulation emerges: The description of the experimental cut passing rates. As can be seen from table D.14, the simulated background is suppressed more strongly than the experiment at each cut level individually. This effect can be attributed to residual noise hits or electronic artifacts, which are probably more frequent in experiment than in the simulation. Stronger than expected

scattering in the ice could also give such an effect. Another cause could be a wrong expectation about the angular sensitivity of the optical modules. (The background simulation does not use the latest model about the angular sensitivity, see section 4.2.4.).

Due to the different passing rates of simulated background and experiment, an alternative approach towards the background normalization is useful. Instead of one global normalization, one can normalize the simulated background to the experimental events after a given cut level. In this case, the signal contribution has to be taken into account for the late cut levels. Possible normalizations are summarized in table D.15

Normalization Level	Corresponding Lifetime [days]	Equivalent Events BG-100	BG-10	BG-1
Trigger	30.6	39.1 ± 11.1	7.5 ± 4.8	2.6 ± 0.10
Level 3	20.0	59.8 ± 14.3	12.1 ± 5.7	2.8 ± 2.3
Level 4a	12.0	99.6 ± 23.9	20.3 ± 9.5	4.6 ± 3.9
Selected	15.0 (definition)	79.7 ± 19.2	16.2 ± 7.6	3.7 ± 3.1

Table D.15: Summary of possible background normalizations. The "normalization level" gives the cut level which defines the normalization (see text). The "selected" normalization is defined by a lifetime of 15 days. The last three columns show the number of residual equivalent events for each normalization and for the three final data sets. Only statistical errors are given.

The background estimation in section 7.2.2 was given as 16^{+4}_{-8} (syst.) ± 8 (stat.) events for the BG-10 selection. The absolute value of 16 events corresponds to a normalization to 15 days of detector lifetime. This is a normalization in between cut levels 3 and 4a. This is a factor of 2 different from the normalization on trigger level. This "selected" normalization is used as the standard background normalization for final event samples (BG-1, BG-10 and BG-100) in this work. The only exceptions are figure 7.11 (right) and table D.14. Both the figure and the table show cut passing rates of all data samples and all cut levels. In these two cases the background is only normalized once: on trigger level. The systematic error of $^{+4}_{-8}$ (syst.) on the number of residual background events in final experimental data samples (given in section 7.2.2) incorporates the spread obtained from the various possible normalizations listed here (in table D.15).

D.7 Event List

The following tables list information about all events of the final data samples introduced in section 7.2. Measured are the day (in the year 1997) and the time of the event (GMT). The directional information (right ascension α_μ and declination δ_μ) are both obtained from the $P_{hit}P_{nothit} \oplus MPE$ reconstruction (# 11 in table D.11). The declination mismatch of that reconstruction has a RMS of 3.3°, the right ascension mismatch has a RMS of 5.9° and the space angular resolution has a median of 3.2°, see section 9.1.1. The systematic uncertainties on these values could be as large as 15 %, see section 9.1.4. The energy E_μ is taken from the energy reconstruction (# 12 in table D.11). The energy reconstruction has a resolution of ~ 0.4 in $\log(E)$ [151, 152, 170]. The column "samples" lists which of the three final data samples contain the event.

Day #	t [s]	α_μ [°]	δ_μ [°]	E_μ [GeV]	samples
96	9285	57.7	9.8	68.9	BG-100
96	59847	243.1	37.2	746.2	BG-100, BG-10
97	36267	208.9	53.5	62.3	BG-100
97	76050	58.3	30.8	72.2	BG-100, BG-10, BG-1
98	79452	340.0	27.0	63.8	BG-100
100	30458	59.4	64.0	98.0	BG-100, BG-10
100	77413	22.5	56.9	3016.2	BG-100
101	41417	169.0	32.8	310.2	BG-100
102	42836	26.3	14.2	79.2	BG-100
102	43758	22.4	46.4	53.4	BG-100, BG-10
104	20038	134.6	34.6	71.6	BG-100, BG-10, BG-1
104	54159	48.8	42.6	69.7	BG-100
105	45516	303.1	69.6	31.6	BG-100, BG-10, BG-1
108	51898	207.7	16.9	77.6	BG-100, BG-10
108	59690	228.9	17.1	68.9	BG-100, BG-10
111	16799	138.7	35.2	353.7	BG-100, BG-10
111	60185	352.6	40.4	47.4	BG-100, BG-10, BG-1
112	4687	112.4	76.6	60.3	BG-100, BG-10, BG-1
112	34973	108.2	29.3	72.3	BG-100, BG-10
112	36370	133.6	13.2	1470.1	BG-100
112	64354	39.4	19.8	1039.3	BG-100
112	78585	31.7	33.0	332.2	BG-100, BG-10
114	42142	221.8	20.3	78.7	BG-100, BG-10
114	45064	275.8	68.6	72.1	BG-100, BG-10, BG-1
114	59143	166.5	8.3	1627.7	BG-100
115	1189	201.4	48.6	62.6	BG-100, BG-10, BG-1
115	65303	356.3	74.9	44.9	BG-100, BG-10, BG-1
115	76318	145.9	32.2	67.5	BG-100, BG-10, BG-1
116	15134	123.9	74.7	73.3	BG-100, BG-10, BG-1
116	54515	71.6	36.0	662.0	BG-100
118	10664	327.2	15.3	77.3	BG-100
119	45944	181.2	13.1	63.5	BG-100
119	67866	143.7	63.4	70.9	BG-100, BG-10
122	76340	279.1	75.6	52.3	BG-100, BG-10
124	14136	135.1	66.7	83.6	BG-100
124	69313	289.2	64.5	45.1	BG-100, BG-10, BG-1
125	12316	247.7	61.5	37.9	BG-100
125	36977	336.2	24.5	97.9	BG-100, BG-10, BG-1
125	84174	330.2	12.3	234.8	BG-100
126	20374	346.5	71.5	91.9	BG-100
126	23614	114.4	11.1	1526.0	BG-100
126	34728	72.6	18.3	79.8	BG-100, BG-10
126	55260	249.2	17.1	2742.1	BG-100
127	14931	225.6	26.7	1157.5	BG-100, BG-10, BG-1
127	39144	270.7	30.6	68.9	BG-100, BG-10, BG-1
127	39498	182.8	19.2	766.1	BG-100, BG-10
128	69848	198.4	50.4	63.9	BG-100, BG-10, BG-1
128	80955	340.7	15.4	68.1	BG-100
130	20631	157.3	41.8	72.8	BG-100, BG-10
130	40222	298.3	37.4	65.4	BG-100, BG-10, BG-1
131	26308	105.3	20.3	62.9	BG-100, BG-10, BG-1
131	73508	22.6	57.0	75.0	BG-100, BG-10, BG-1
133	8328	300.7	70.4	53.2	BG-100
133	40478	155.9	16.8	907.8	BG-100
133	48064	251.1	19.6	5709.1	BG-100
133	52246	164.3	78.4	42.5	BG-100, BG-10, BG-1
134	53626	345.8	33.1	65.4	BG-100
135	17544	64.1	46.6	60.2	BG-100, BG-10, BG-1
136	7172	127.0	59.7	37.6	BG-100, BG-10
137	79532	1.7	18.9	4492.5	BG-100
138	33498	125.9	39.5	60.2	BG-100, BG-10
138	37977	248.4	38.6	778.3	BG-100, BG-10
138	67355	238.3	51.7	84.0	BG-100, BG-10
139	14646	236.4	18.8	3536.8	BG-100
139	21345	109.5	57.9	57.2	BG-100, BG-10, BG-1
140	44760	32.5	10.4	77.4	BG-100
140	46749	252.3	10.4	3211.4	BG-100
141	20069	3.3	68.0	71.0	BG-100
142	16981	315.3	31.9	53.8	BG-100
142	32086	156.0	31.1	228.7	BG-100, BG-10, BG-1
142	73198	272.4	21.3	218.6	BG-100, BG-10, BG-1
142	76962	49.2	57.2	684.0	BG-100, BG-10, BG-1
143	17846	252.4	49.5	69.8	BG-100, BG-10
144	3234	25.9	63.4	7307.8	BG-100, BG-10, BG-1
144	68567	258.6	35.4	66.6	BG-100, BG-10
144	76981	122.2	39.9	61.1	BG-100, BG-10, BG-1
145	49823	323.4	53.3	818.9	BG-100, BG-10, BG-1
145	80373	254.9	65.1	71.1	BG-100, BG-10
146	66118	281.9	9.6	837.4	BG-100
148	13565	136.2	44.5	63.9	BG-100, BG-10
148	22690	358.2	32.6	570.8	BG-100
148	42365	244.5	26.2	8017.5	BG-100, BG-10
148	70765	330.9	46.5	919.9	BG-100
149	2195	130.4	25.6	592.2	BG-100
149	59115	267.2	25.6	2510.9	BG-100
149	83697	294.3	61.6	40.5	BG-100
150	54435	80.1	57.7	71.8	BG-100, BG-10, BG-1
151	45523	247.7	15.2	3414.3	BG-100
153	6666	60.4	33.1	48.7	BG-100
153	63950	261.6	70.9	77.1	BG-100, BG-10, BG-1
154	14486	82.3	11.1	3114.8	BG-100
154	46712	41.1	12.4	72.9	BG-100
155	48909	151.7	30.5	93.1	BG-100
155	65086	254.7	80.5	48.8	BG-100, BG-10, BG-1
156	81150	112.3	73.2	64.2	BG-100
158	17664	188.7	10.9	1267.1	BG-100
159	83874	296.1	22.9	422.3	BG-100
160	30877	106.0	58.7	43.3	BG-100, BG-10, BG-1
161	31336	315.7	62.9	55.1	BG-100, BG-10, BG-1
162	4500	203.3	33.7	4107.2	BG-100, BG-10
162	6391	42.2	37.6	4347.8	BG-100, BG-10, BG-1
162	17469	108.3	81.5	68.1	BG-100, BG-10, BG-1
162	79194	329.8	52.1	66.2	BG-100, BG-10
163	26744	175.3	9.1	10328.9	BG-100
163	43554	160.0	43.7	74.9	BG-100, BG-10, BG-1
164	3937	39.0	52.8	43.4	BG-100, BG-10
164	14450	21.1	13.0	2521.9	BG-100
164	45345	48.5	13.8	80.4	BG-100
165	34441	338.2	6.1	433.5	BG-100
166	74684	237.1	69.9	329.0	BG-100, BG-10, BG-1
167	14670	117.5	31.7	653.0	BG-100, BG-10
168	52347	209.4	74.8	33.6	BG-100
168	81141	343.2	68.5	95.1	BG-100, BG-10
169	18241	292.0	9.5	786.2	BG-100
169	46474	190.0	72.0	48.4	BG-100, BG-10, BG-1
169	56925	123.1	40.8	61.4	BG-100, BG-10, BG-1
169	78421	37.2	30.6	59.1	BG-100, BG-10
170	21153	200.1	69.9	52.2	BG-100, BG-10, BG-1
171	74144	119.6	50.6	63.2	BG-100, BG-10
172	15276	166.7	68.4	35.1	BG-100, BG-10, BG-1
174	42767	142.3	14.5	498.0	BG-100, BG-10
174	85537	84.0	21.6	82.8	BG-100
175	50797	292.6	33.8	97.6	BG-100
175	52302	75.0	17.2	1001.4	BG-100, BG-10, BG-1
176	38636	99.6	40.7	925.4	BG-100
176	55019	203.5	22.2	92.4	BG-100, BG-10, BG-1
176	59351	139.6	82.2	60.4	BG-100, BG-10, BG-1
177	31087	53.7	51.6	92.4	BG-100, BG-10, BG-1
177	31966	39.8	54.8	61.8	BG-100, BG-10, BG-1
177	77591	287.0	15.0	5077.1	BG-100
177	79448	79.7	55.3	50.7	BG-100, BG-10, BG-1
178	22308	186.1	6.9	88.9	BG-100
178	41472	260.3	24.6	470.6	BG-100
178	74904	132.2	20.7	73.6	BG-100
190	67657	183.4	28.1	79.7	BG-100, BG-10, BG-1
191	50200	233.0	17.5	4077.6	BG-100
191	61911	219.3	14.4	1681.7	BG-100
192	1280	1.4	73.1	45.8	BG-100, BG-10, BG-1
193	8883	155.2	19.5	658.9	BG-100, BG-10, BG-1
193	84003	21.6	11.0	538.2	BG-100
194	32438	250.3	24.3	78.7	BG-100
194	35109	314.8	81.1	69.2	BG-100, BG-10, BG-1
195	25785	171.1	15.5	1247.2	BG-100
195	81547	174.0	48.0	668.2	BG-100, BG-10
196	70828	286.9	10.8	82.4	BG-100, BG-10
196	77991	255.7	40.4	55.5	BG-100, BG-10, BG-1
197	61135	29.4	8.5	1389.4	BG-100
197	63962	34.0	78.8	86.8	BG-100, BG-10
198	19830	201.3	33.7	75.9	BG-100
198	27065	162.3	54.0	62.9	BG-100, BG-10, BG-1
198	59713	286.4	28.7	1839.7	BG-100
199	144	147.3	40.7	50.0	BG-100
200	26094	16.7	44.2	86.4	BG-100, BG-10, BG-1
200	43443	272.1	40.4	149.5	BG-100, BG-10, BG-1
200	45056	290.1	17.5	453.4	BG-100
200	73755	42.2	67.4	64.2	BG-100, BG-10
200	82418	7.3	10.2	6404.5	BG-100
201	3582	5.6	26.8	84.0	BG-100
201	61734	326.3	42.3	58.3	BG-100
202	5311	77.9	41.7	68.2	BG-100, BG-10, BG-1
202	58586	50.8	60.8	51.9	BG-100, BG-10, BG-1
202	65518	339.3	45.5	64.0	BG-100, BG-10

Table D.16: List of events selected between day 96 and day 202

Day #	t [s]	α_μ [°]	δ_μ [°]	E_μ [GeV]	samples
202	85533	107.7	36.9	61.9	BG-100, BG-10, BG-1
203	12565	16.0	14.0	76.3	BG-100
203	25616	317.8	6.0	2616.2	BG-100
205	31436	194.1	8.0	572.3	BG-100
205	48508	3.2	49.4	67.5	BG-100, BG-10, BG-1
206	27256	54.8	45.6	61.7	BG-100, BG-10
206	32038	259.6	37.0	47.9	BG-100, BG-10, BG-1
206	50679	215.7	55.8	70.7	BG-100
206	66093	102.2	19.1	948.0	BG-100
206	81969	224.0	17.9	6995.9	BG-100
207	45316	250.4	50.3	78.3	BG-100, BG-10, BG-1
207	69877	180.9	65.5	57.8	BG-100, BG-10, BG-1
208	1217	37.8	33.1	60.3	BG-100, BG-10
209	59500	246.7	64.8	36.3	BG-100, BG-10
209	85244	267.3	54.3	67.0	BG-100, BG-10, BG-1
210	9887	104.8	59.6	691.2	BG-100, BG-10, BG-1
211	40869	117.7	55.9	1051.0	BG-100, BG-10, BG-1
211	47174	283.0	49.9	35.3	BG-100, BG-10, BG-1
211	64009	87.7	48.7	84.2	BG-100, BG-10, BG-1
212	62003	316.4	27.0	586.4	BG-100
212	74363	338.8	30.7	69.9	BG-100, BG-10
213	17000	338.6	8.5	862.2	BG-100
214	10988	142.3	27.8	63.6	BG-100, BG-10, BG-1
214	59544	173.1	25.2	74.7	BG-100, BG-10, BG-1
214	59572	223.4	45.7	64.3	BG-100, BG-10
214	71682	318.4	14.7	75.1	BG-100, BG-10
215	42545	15.8	17.5	100.0	BG-100
215	55780	354.9	6.8	2822.1	BG-100
217	67260	202.2	32.7	743.6	BG-100, BG-10, BG-1
218	9770	277.6	27.3	82.2	BG-100
218	39809	262.7	50.9	53.5	BG-100, BG-10
218	70528	94.4	55.7	53.0	BG-100, BG-10
219	25021	109.0	21.3	84.1	BG-100
219	33608	183.0	18.6	949.2	BG-100
220	45940	297.0	17.6	419.3	BG-100
221	69915	259.7	54.7	50.8	BG-100, BG-10, BG-1
221	76896	44.3	24.5	44.1	BG-100
222	38826	350.7	65.3	34.9	BG-100, BG-10, BG-1
222	39651	172.5	63.6	31.6	BG-100, BG-10, BG-1
223	32245	176.2	61.2	432.6	BG-100, BG-10
223	45326	87.8	46.8	46.1	BG-100, BG-10
224	18795	233.8	41.5	82.8	BG-100, BG-10, BG-1
224	38581	332.2	36.0	70.7	BG-100, BG-10
225	14587	53.2	56.0	490.4	BG-100, BG-10, BG-1
226	41295	165.4	73.9	62.9	BG-100
226	52678	280.9	24.8	91.1	BG-100, BG-10
226	84754	103.7	20.9	7811.1	BG-100, BG-10, BG-1
227	51004	262.9	50.7	70.7	BG-100
227	55886	13.8	85.4	55.9	BG-100, BG-10, BG-1
227	58065	39.1	24.6	51.4	BG-100
227	81668	301.6	49.6	55.1	BG-100, BG-10, BG-1
228	13818	6.1	67.0	56.2	BG-100, BG-10, BG-1
228	28455	282.5	53.1	46.9	BG-100
228	41888	68.5	77.4	48.6	BG-100
228	65392	89.3	31.6	52.7	BG-100
230	4125	172.1	49.0	39.0	BG-100, BG-10, BG-1
230	23657	18.5	41.1	38.2	BG-100, BG-10, BG-1
231	3205	155.1	6.3	1156.0	BG-100
231	18378	214.6	21.4	819.5	BG-100, BG-10
231	50261	290.1	52.2	43.1	BG-100, BG-10, BG-1
231	84460	169.5	72.7	45.9	BG-100, BG-10, BG-1
232	38572	16.5	12.7	520.0	BG-100
232	82425	278.4	75.4	37.2	BG-100, BG-10, BG-1
233	25394	116.2	84.8	32.7	BG-100, BG-10
233	44132	291.5	41.0	60.1	BG-100, BG-10, BG-1
233	59393	17.6	63.0	57.2	BG-100
234	44450	313.5	55.7	353.3	BG-100, BG-10, BG-1
234	84162	324.1	20.2	48.4	BG-100, BG-10
235	49914	284.4	9.6	2117.8	BG-100
237	65497	286.0	30.5	1207.5	BG-100
238	33968	38.7	43.4	65.7	BG-100, BG-10, BG-1
238	54194	19.1	20.5	1083.0	BG-100
239	34777	18.8	30.6	68.6	BG-100, BG-10
240	3760	146.2	41.7	72.6	BG-100, BG-10, BG-1
241	892	22.7	17.4	73.3	BG-100
241	79745	259.9	88.3	60.2	BG-100, BG-10, BG-1
242	78203	315.6	45.1	43.4	BG-100, BG-10, BG-1
244	51953	56.1	70.5	46.5	BG-100, BG-10
244	70706	262.9	39.0	90.8	BG-100, BG-10, BG-1
244	77673	206.0	41.8	700.4	BG-100, BG-10
245	23518	244.1	61.3	2216.2	BG-100, BG-10, BG-1
245	58964	39.8	29.7	76.7	BG-100, BG-10
246	25298	108.5	62.2	49.0	BG-100, BG-10, BG-1
246	62099	324.7	64.3	76.3	BG-100, BG-10, BG-1
247	18261	329.6	79.1	31.6	BG-100, BG-10
248	83356	174.5	39.0	74.8	BG-100, BG-10, BG-1
250	19398	244.3	54.9	57.9	BG-100, BG-10, BG-1
250	52373	312.9	10.6	90.7	BG-100
252	21966	333.4	29.4	1874.8	BG-100, BG-10, BG-1
252	61336	166.0	78.2	39.4	BG-100, BG-10, BG-1
252	85354	266.7	16.4	1276.4	BG-100
253	28381	261.0	50.1	39.6	BG-100, BG-10
253	45136	66.9	8.4	82.5	BG-100
253	51111	208.0	54.8	33.6	BG-100, BG-10, BG-1
253	55555	125.2	10.5	556.5	BG-100
253	69341	114.3	17.3	100.0	BG-100, BG-10
254	5431	171.5	6.0	637.4	BG-100
255	14535	34.7	20.5	5308.6	BG-100
256	44394	80.4	73.7	32.5	BG-100, BG-10, BG-1
256	67267	5.3	57.3	57.4	BG-100, BG-10
257	34816	157.5	22.4	60.8	BG-100
258	4217	133.5	67.9	45.2	BG-100, BG-10, BG-1
258	6191	94.9	18.0	79.9	BG-100
258	26514	233.8	6.3	761.3	BG-100
258	52076	320.1	14.9	735.9	BG-100
258	64303	47.6	43.1	1751.6	BG-100, BG-10
259	7802	180.2	71.2	44.3	BG-100, BG-10, BG-1
259	27866	131.0	62.3	52.3	BG-100
259	37235	46.9	37.4	61.8	BG-100, BG-10, BG-1
259	51167	221.8	27.7	401.6	BG-100
260	65708	64.6	49.5	56.7	BG-100, BG-10
260	75191	101.3	15.6	2441.3	BG-100
260	81813	220.4	54.0	67.0	BG-100, BG-10
261	20006	56.0	80.8	35.1	BG-100, BG-10, BG-1
261	33065	346.1	21.3	76.5	BG-100
261	50229	129.1	30.2	1326.6	BG-100, BG-10
261	58675	311.5	43.5	73.7	BG-100, BG-10
271	20061	350.4	11.6	5940.8	BG-100
271	33046	282.2	56.0	1016.3	BG-100
272	14691	114.6	45.6	53.5	BG-100, BG-10, BG-1
272	20175	340.2	14.2	2291.2	BG-100, BG-10, BG-1
272	66776	277.1	9.1	220.4	BG-100
272	83169	266.7	19.5	56.5	BG-100
273	11769	144.6	65.8	42.7	BG-100
273	50736	16.9	41.0	70.9	BG-100
275	1037	24.7	33.4	63.1	BG-100, BG-10, BG-1
275	2031	175.4	23.5	915.7	BG-100, BG-10
275	28222	146.0	14.8	5314.4	BG-100
276	31994	80.7	52.3	1056.4	BG-100
277	39654	197.9	6.8	4545.4	BG-100
277	71350	348.1	28.4	89.7	BG-100, BG-10, BG-1
278	14019	200.4	26.5	54.2	BG-100, BG-10, BG-1
278	21244	263.0	28.5	68.9	BG-100
278	26972	191.6	46.6	55.6	BG-100
279	25547	357.1	81.9	33.1	BG-100, BG-10, BG-1
279	59247	153.5	6.9	89.0	BG-100
279	60044	198.6	56.0	206.9	BG-100, BG-10
279	60890	246.9	72.2	49.3	BG-100, BG-10
280	9418	89.6	39.5	87.4	BG-100, BG-10, BG-1
280	9983	345.6	75.9	63.5	BG-100, BG-10
280	46749	158.1	56.2	68.9	BG-100
280	54269	204.0	69.0	699.1	BG-100, BG-10, BG-1
280	63564	22.3	34.0	129.4	BG-100, BG-10, BG-1
281	10575	227.6	15.5	47.6	BG-100
282	20313	206.4	29.2	85.4	BG-100, BG-10, BG-1
282	22485	135.9	15.1	100.0	BG-100, BG-10, BG-1
282	28723	86.2	33.7	203.0	BG-100, BG-10
283	67076	292.6	34.5	49.2	BG-100, BG-10
285	3295	324.8	15.7	87.6	BG-100
285	18132	284.2	66.5	73.2	BG-100, BG-10, BG-1
285	81592	320.3	24.6	87.7	BG-100
286	43283	302.1	51.4	42.5	BG-100, BG-10, BG-1
287	22080	115.9	15.7	64.9	BG-100
287	30385	148.9	22.6	75.8	BG-100, BG-10
287	85276	88.0	78.5	65.0	BG-100, BG-10
288	4683	84.6	48.6	73.4	BG-100, BG-10, BG-1
290	8175	236.1	23.7	3652.6	BG-100
290	26256	28.9	52.3	63.8	BG-100, BG-10, BG-1
291	4907	221.8	28.7	1506.0	BG-100, BG-10
291	34092	187.3	40.7	56.5	BG-100, BG-10
292	28720	256.2	49.8	79.2	BG-100, BG-10, BG-1
293	5163	34.2	58.7	46.8	BG-100, BG-10, BG-1

Table D.17: List of events selected between day 202 and day 293

Day #	t [s]	α_μ [°]	δ_μ [°]	E_μ [GeV]	samples
294	25839	209.4	44.9	76.1	BG-100, BG-10, BG-1
295	44611	50.5	51.8	46.6	BG-100, BG-10, BG-1
295	69591	119.3	47.3	3403.0	BG-100, BG-10
300	9164	115.7	34.5	436.7	BG-100
300	12125	283.5	20.3	49.5	BG-100, BG-10, BG-1
300	54091	304.3	36.9	489.2	BG-100, BG-10, BG-1
300	54106	96.7	13.5	1923.5	BG-100
301	28626	264.0	41.5	82.5	BG-100, BG-10, BG-1
302	23965	150.3	48.6	35.5	BG-100, BG-10, BG-1
302	25347	209.3	15.9	471.9	BG-100, BG-10, BG-1
302	33507	357.7	24.6	1487.9	BG-100, BG-10
302	69708	231.0	47.3	73.6	BG-100
303	14923	96.1	40.7	82.8	BG-100
303	35604	240.8	72.7	45.8	BG-100, BG-10, BG-1
303	42019	346.6	54.0	75.4	BG-100, BG-10
303	69333	188.8	25.2	100.0	BG-100, BG-10, BG-1
304	27502	141.9	74.6	69.2	BG-100, BG-10, BG-1
304	41810	110.1	40.3	55.3	BG-100, BG-10, BG-1
304	71447	14.4	27.3	100.0	BG-100, BG-10
305	5094	167.3	35.4	47.6	BG-100
306	7290	72.9	24.3	149.5	BG-100
307	8376	154.5	58.6	67.7	BG-100, BG-10, BG-1
307	40275	269.2	26.8	1488.4	BG-100, BG-10, BG-1
307	67929	60.4	48.5	472.4	BG-100
307	82811	311.8	63.6	86.5	BG-100, BG-10, BG-1
308	27123	28.4	40.5	56.3	BG-100, BG-10
308	40316	247.0	66.5	69.4	BG-100, BG-10, BG-1
308	47071	176.3	21.5	92.6	BG-100, BG-10
309	13264	165.7	47.8	59.9	BG-100, BG-10
310	39963	174.7	65.1	42.3	BG-100, BG-10, BG-1
310	71059	71.8	67.3	1042.5	BG-100
311	42643	289.4	11.3	3325.1	BG-100, BG-10
311	79400	302.5	46.0	51.9	BG-100
311	79464	202.2	16.3	81.4	BG-100
311	85155	61.7	34.7	75.2	BG-100, BG-10
312	15283	13.6	68.1	70.1	BG-100
312	55601	229.0	31.3	71.9	BG-100, BG-10, BG-1
312	67260	134.6	10.4	1475.9	BG-100
312	67894	89.1	15.9	44.8	BG-100, BG-10
313	19566	315.4	59.0	31.6	BG-100, BG-10
313	25373	290.5	7.0	67.1	BG-100
313	81715	127.9	11.0	74.6	BG-100
314	1564	184.1	27.7	2375.2	BG-100
317	84304	172.7	9.1	489.6	BG-100
318	26407	316.1	22.6	4011.4	BG-100, BG-10, BG-1

Table D.18: List of events selected between day 294 and day 318

E The Muon Energy

This work refers to the muon energy at several instances, see for example section 7.2.1. It is interesting to note that for large detectors like AMANDA, there exists some freedom as how to define the term *muon energy*. The muon can have very different energies at its production site, where it enters the effective detector volume, where it is closest to the detector center or where it leaves the effective detector volume. It is for example well possible for a neutrino-induced muon to start with $E_\mu = 100\,\mathrm{GeV}$ inside the detector and loose all its energy inside the detector. It is thus not evident as how to define the muon energy of that event. Is it 100 GeV, 50 GeV, 0 GeV or something else? In general, competing definitions can be considered:

The muon energy is defined at the muon production vertex. This choice is not optimal, because muons which are equivalent for the detector are not treated identically: The detector has the same efficiency for two muons which start far away and enter its vicinity with the same energy. The two muons might be produced at different distances and have thus different energies at their production vertex.

The energy is defined at the point of closest approach to the detector center. This choice is not optimal, because muons which are equivalent for the detector are not treated identically: The detector can have the same efficiency for two muons of equivalent production energy, which are both contained in the fiducial volume of the detector. One of them might be produced close to the detector center and decays close to the detector "border" and the other has the opposite direction. Their energies at the point closest to the detector center are then very different.

It is defined as the average energy inside the detector volume. This choice is not optimal because AMANDA is an open detector without well-defined boundaries. Furthermore, it is not evident over which length to take the average if the muon is starting or stopping inside the detector.

The first definition leads to a muon energy spectrum which corresponds to initial muon energies. The second definition leads to lower energies. It gives a spectrum which corresponds to the energies of muons passing through a 2-dimensional plane. This is the convention normally used by experiments whose detectors are sufficiently small that the muon energy loss within the detector is negligible. The relation between the third and second definition depends on the muon energy spectrum. The third definition is similar to what the detector registers.

The choice between the three options is an arbitrary convention. The important aspect is that it has to be used consistently. In particular it has to be followed with respect to the energy dependencies of fluxes, effective areas, efficiencies, etc. in case these numbers are used to calculate flux limits. That is not the case for this work. Here, all these parameters are investigated differentially in the neutrino energy – not the muon energy.

The convention used throughout this work is, that the muon energy is taken as the energy at the production vertex. Reason is that this definition is independent of detector properties. As compared to the other definition, this leads to higher values for the individual muon energies, but lower values for the effective areas, see equation 8.1 (the detector

trigger rate is obviously independent from any conventions.) This has to be considered when comparing numbers to that of other (more compact) experiments. They might follow other conventions.

For the neutrino energies, the choice is not debated in the literature. Experiments measuring neutrino-induced muon events define the neutrino energy as the energy at the muon-production vertex. In this work, the energy dependencies of effective areas, efficiencies, fluxes or flux limits are all taken with respect to the neutrino energies. They can thus be easily compared to other experiments. Dependencies on the muon energies given in this work are thus of illustrative character only.

F Calculating Further Limits

In this section the data is provided to calculate limits not explicitly listed in section 11. The limits have to be calculated according to equation 11.1:

$$\Phi(E,\gamma,\delta)^{limit} = \frac{\mu_{90}(N_O, \hat{N}_{BG}(\delta))}{T_{live} \cdot \bar{A}_{eff}(E,\gamma,\delta) \cdot \epsilon_{bin}(E,\gamma,\delta)} \tag{F.1}$$

For this analysis, $T_{life} = 1.1242 \cdot 10^7$ s. The $\mu_{90}(\delta)$ values for all-sky upper limits were already given in table 11.1. They are:

$\sin(\delta_\nu)$ range	δ_1 0.85 to 1	δ_2 0.7 to 0.85	δ_3 0.55 to 0.7	δ_4 0.4 to 0.55	δ_5 0.25 to 0.4	δ_6 0.1 to 0.25
$\mu_{90}(\delta)$	8.67	7.52	7.69	7.69	7.66	7.72

Table F.1: The $\mu_{90}(\delta)$ values needed for the calculation of all-sky flux limits

The necessary information about the efficiencies and energy-averaged effective areas (and their statistical uncertainties) are provided in tables F.2 to F.13 on the following pages. Depending on which kind of limits shall be calculated, the following entries have to be selected:

- If all-sky flux limits shall be calculated, the reconstruction efficiencies $\epsilon_{bin,\,grid}$ have to be taken from tables F.2 or F.3. If flux limits for pre-selected sources shall be calculated, the reconstruction efficiencies $\epsilon_{bin,\,selected}$ have to be taken. They are given in tables F.4 or F.5. The statistical uncertainties are given within these tables. The systematic uncertainties are $< 15\,\%$ for all table entries, see section 9.3.

- If muon flux limits shall be calculated, the energy-averaged muon effective areas have to be taken from tables F.6 or F.7. The energy-averaged neutrino effective areas (needed to calculate neutrino flux limits) are found in tables F.8 or F.9. The corresponding statistical uncertainties did not fit into these tables and are given in tables F.10 to F.13. The systematic uncertainties are 42 % for all table entries, see section 8.3.1.

- If the limit shall be calculated as a declination-average, then the values for $\bar{A}_{eff}$ and ϵ_{bin} both have to be taken from table-rows, in which the first column contains the key "$\overline{\sin(\delta)}$". If the limit shall be for a limited energy range, then the values have to be taken from rows where the first column contains the key "δ_n^{diff}", where n runs from 1 to 6 from optimal (large) to most challenging (shallow) declinations. Limits for declinations $0.85 \leq \sin(\delta_\nu) < 1$ thus require the key "δ_1^{diff}", declinations $0.7 < \sin(\delta_\nu) \leq 0.85$ require the key "δ_2^{diff}", etc. (This is the same ordering as in table F.1.)

- If pseudo-differential limits shall be calculated, the values for $\bar{A}_{eff}$ and ϵ_{bin} have to be taken from rows, where the second column contains the key "E_i^{diff}". Here, i runs from 1 to 8 and represents the energy intervals $10^{1.5}\,\text{GeV} \leq E_\nu \leq 10^{2.0}\,\text{GeV}$ to

$10^{5.0}\,\mathrm{GeV} \leq E_\nu \leq 10^{5.5}\,\mathrm{GeV}$ in increasing order. If in contrast integral limits shall be calculated, then the values for $\bar{A}_{eff}$ and ϵ_{bin} have to be taken from rows, where the second column contains the key "E_j^{int}". Here, j runs from 1 to 4 and represents lower energy thresholds of $E_\nu = 10^j\,\mathrm{GeV}$. In all cases the integral limits correspond to upper energy limits of $E_\nu \leq 10^{5.5}\,\mathrm{GeV}$.

- Finally, the entries for $\bar{A}_{eff}$ and ϵ_{bin} have to be taken from the column whose top two rows indicates the appropriate source spectral index.

The units of the energy-averaged effective areas listed are km^2, the efficiency is given in dimensionless numbers. The numbers listed follow the common convention that aE±b represents $a \cdot 10^{\pm b}$.

As an example, the pseudo-differential neutrino flux limit shall be calculated for Markarian 421 in the energy interval $10^{3.5}\,\mathrm{GeV} \leq E_\nu \leq 10^{4.0}\,\mathrm{GeV}$ assuming an E^{-1} spectrum. The declination of Markarian 421 is $\delta = 38.209°$ and $\mu_{90} = 3.33$ for the corresponding search bin (see table 11.3). The declination key required for the first column of the following tables is "δ_3^{diff}" since $\sin(38.209°) = 0.62$, see table F.1. The energy key required is "E_5^{diff}", due to the energy range of interest. As stated above, the energy-averaged neutrino effective area is either listed in tables F.8 or F.9. One sees that the combination of declination and energy key yields row #29 of table F.9. The entry for a spectral index of $\gamma = -1$ is $\bar{A}_{eff} = 8.50 \cdot 10^{-8}\,\mathrm{km}^2$. The entry for the efficiency $\epsilon_{bin,\,selected}$ is found via the same line of arguments in row #29 of table F.5: $\epsilon_{bin,\,selected} = 0.637$. The resulting flux limit is then $\Phi_\nu^{lim} = 1.26 \cdot 10^{-9}\,\mathrm{cm}^{-2}\mathrm{s}^{-1}$.

The pseudo-differential flux limits given in table 11.2 apply to an average declination. With the procedure outlined just before, it is straight forward to recalculate these limits for any fixed declination. Likewise, it is straight forward to recalculate the integral flux limits of table 11.1 for any other than an E_ν^{-2} spectrum.

With slightly more effort, it is even possible to calculate flux limits for specific sources not listed in section 11: The full list of events found in this analysis is given in appendix D.7. From that information, it is possible to calculate μ_{90} for any potential source when following the procedure outlined in section 10.6. Together with the appropriate values for ϵ_{bin} and $\bar{A}_{eff}$ from this section, it is then possible to calculate integral or pseudo-differential limits for any source.

$\sin(\delta_\nu)$	E_ν	Neutrino Energy Spectrum									
		$\gamma = -1.0$	$\gamma = -1.25$	$\gamma = -1.5$	$\gamma = -1.75$	$\gamma = -2.0$	$\gamma = -2.25$	$\gamma = -2.5$	$\gamma = -2.75$	$\gamma = -3.0$	atmospheric
$\overline{\sin(\delta)}$	E_1^{diff}	0.469 ± 0.017	0.465 ± 0.016	0.461 ± 0.016	0.457 ± 0.016	0.453 ± 0.016	0.449 ± 0.016	0.444 ± 0.016	0.440 ± 0.016	0.435 ± 0.015	0.434 ± 0.015
	E_2^{diff}	0.583 ± 0.009	0.582 ± 0.009	0.581 ± 0.009	0.580 ± 0.009	0.579 ± 0.009	0.577 ± 0.009	0.576 ± 0.009	0.574 ± 0.009	0.572 ± 0.009	0.564 ± 0.009
	E_3^{diff}	0.615 ± 0.008	0.614 ± 0.008	0.614 ± 0.008	0.614 ± 0.008	0.613 ± 0.008	0.613 ± 0.008	0.612 ± 0.007	0.612 ± 0.007	0.611 ± 0.007	0.603 ± 0.007
	E_4^{diff}	0.610 ± 0.007	0.610 ± 0.007	0.610 ± 0.007	0.610 ± 0.007	0.610 ± 0.007	0.610 ± 0.007	0.610 ± 0.007	0.609 ± 0.007	0.609 ± 0.007	0.593 ± 0.006
	E_5^{diff}	0.623 ± 0.006	0.624 ± 0.006	0.624 ± 0.006	0.624 ± 0.006	0.624 ± 0.006	0.624 ± 0.006	0.624 ± 0.006	0.624 ± 0.006	0.624 ± 0.006	0.604 ± 0.006
	E_6^{diff}	0.621 ± 0.006	0.621 ± 0.006	0.621 ± 0.006	0.620 ± 0.006	0.620 ± 0.006	0.619 ± 0.006	0.619 ± 0.006	0.619 ± 0.006	0.618 ± 0.006	0.584 ± 0.005
	E_7^{diff}	0.631 ± 0.006	0.631 ± 0.006	0.631 ± 0.006	0.631 ± 0.006	0.631 ± 0.006	0.631 ± 0.006	0.631 ± 0.006	0.632 ± 0.006	0.632 ± 0.006	0.599 ± 0.005
	E_8^{diff}	0.608 ± 0.005	0.609 ± 0.005	0.610 ± 0.005	0.610 ± 0.005	0.611 ± 0.005	0.612 ± 0.005	0.612 ± 0.005	0.613 ± 0.005	0.614 ± 0.005	0.586 ± 0.005
$\overline{\sin(\delta)}$	E_1^{int}	0.618 ± 0.002	0.619 ± 0.002	0.620 ± 0.002	0.620 ± 0.002	0.619 ± 0.002	0.615 ± 0.002	0.607 ± 0.002	0.596 ± 0.002	0.581 ± 0.002	0.560 ± 0.002
	E_2^{int}	0.618 ± 0.002	0.619 ± 0.002	0.620 ± 0.002	0.621 ± 0.002	0.619 ± 0.002	0.617 ± 0.002	0.612 ± 0.002	0.607 ± 0.002	0.601 ± 0.002	0.585 ± 0.002
	E_3^{int}	0.618 ± 0.003	0.619 ± 0.003	0.621 ± 0.003	0.621 ± 0.003	0.621 ± 0.003	0.620 ± 0.003	0.618 ± 0.003	0.617 ± 0.003	0.615 ± 0.003	0.595 ± 0.002
	E_4^{int}	0.617 ± 0.003	0.619 ± 0.003	0.621 ± 0.003	0.622 ± 0.003	0.622 ± 0.003	0.622 ± 0.003	0.622 ± 0.003	0.621 ± 0.003	0.621 ± 0.003	0.585 ± 0.003
δ_1^{diff}	E_1^{int}	0.685 ± 0.004	0.686 ± 0.004	0.686 ± 0.004	0.684 ± 0.004	0.678 ± 0.004	0.669 ± 0.004	0.654 ± 0.004	0.634 ± 0.004	0.608 ± 0.003	0.586 ± 0.003
	E_2^{int}	0.685 ± 0.004	0.686 ± 0.004	0.686 ± 0.004	0.684 ± 0.004	0.679 ± 0.004	0.672 ± 0.004	0.662 ± 0.004	0.650 ± 0.004	0.638 ± 0.004	0.627 ± 0.004
	E_3^{int}	0.685 ± 0.004	0.686 ± 0.004	0.687 ± 0.004	0.686 ± 0.004	0.683 ± 0.004	0.680 ± 0.004	0.676 ± 0.004	0.673 ± 0.004	0.669 ± 0.004	0.660 ± 0.004
	E_4^{int}	0.685 ± 0.005	0.687 ± 0.005	0.689 ± 0.005	0.691 ± 0.005	0.691 ± 0.005	0.692 ± 0.005	0.692 ± 0.005	0.691 ± 0.005	0.691 ± 0.005	0.690 ± 0.005
δ_2^{diff}	E_1^{int}	0.652 ± 0.005	0.655 ± 0.005	0.656 ± 0.005	0.657 ± 0.005	0.655 ± 0.005	0.650 ± 0.005	0.642 ± 0.005	0.631 ± 0.005	0.617 ± 0.005	0.605 ± 0.005
	E_2^{int}	0.652 ± 0.005	0.655 ± 0.005	0.656 ± 0.005	0.657 ± 0.005	0.655 ± 0.005	0.651 ± 0.005	0.646 ± 0.005	0.639 ± 0.005	0.634 ± 0.005	0.628 ± 0.005
	E_3^{int}	0.652 ± 0.006	0.655 ± 0.006	0.657 ± 0.006	0.658 ± 0.006	0.658 ± 0.006	0.657 ± 0.006	0.655 ± 0.006	0.653 ± 0.006	0.651 ± 0.005	0.647 ± 0.005
	E_4^{int}	0.652 ± 0.007	0.654 ± 0.007	0.657 ± 0.007	0.658 ± 0.007	0.660 ± 0.007	0.660 ± 0.007	0.660 ± 0.007	0.660 ± 0.007	0.660 ± 0.007	0.659 ± 0.007
δ_3^{diff}	E_1^{int}	0.594 ± 0.006	0.594 ± 0.006	0.593 ± 0.006	0.591 ± 0.006	0.590 ± 0.006	0.589 ± 0.006	0.587 ± 0.006	0.583 ± 0.006	0.575 ± 0.006	0.564 ± 0.006
	E_2^{int}	0.594 ± 0.006	0.594 ± 0.006	0.593 ± 0.006	0.591 ± 0.006	0.591 ± 0.006	0.591 ± 0.006	0.591 ± 0.006	0.590 ± 0.006	0.588 ± 0.006	0.584 ± 0.006
	E_3^{int}	0.594 ± 0.007	0.594 ± 0.007	0.592 ± 0.007	0.591 ± 0.007	0.589 ± 0.007	0.588 ± 0.007	0.588 ± 0.007	0.587 ± 0.007	0.587 ± 0.007	0.590 ± 0.007
	E_4^{int}	0.594 ± 0.008	0.593 ± 0.008	0.592 ± 0.008	0.590 ± 0.008	0.588 ± 0.008	0.587 ± 0.008	0.585 ± 0.008	0.584 ± 0.008	0.583 ± 0.008	0.581 ± 0.008
δ_4^{diff}	E_1^{int}	0.535 ± 0.007	0.536 ± 0.007	0.536 ± 0.007	0.534 ± 0.007	0.532 ± 0.007	0.530 ± 0.007	0.526 ± 0.007	0.520 ± 0.007	0.511 ± 0.007	0.507 ± 0.007
	E_2^{int}	0.535 ± 0.007	0.536 ± 0.007	0.536 ± 0.007	0.534 ± 0.007	0.532 ± 0.007	0.530 ± 0.007	0.529 ± 0.007	0.526 ± 0.007	0.523 ± 0.007	0.524 ± 0.007
	E_3^{int}	0.535 ± 0.008	0.536 ± 0.008	0.535 ± 0.008	0.534 ± 0.008	0.531 ± 0.008	0.529 ± 0.008	0.527 ± 0.008	0.525 ± 0.008	0.525 ± 0.008	0.532 ± 0.008
	E_4^{int}	0.536 ± 0.011	0.537 ± 0.011	0.537 ± 0.011	0.536 ± 0.011	0.534 ± 0.011	0.532 ± 0.011	0.530 ± 0.011	0.527 ± 0.011	0.525 ± 0.010	0.505 ± 0.010
δ_5^{diff}	E_1^{int}	0.502 ± 0.009	0.502 ± 0.009	0.503 ± 0.009	0.507 ± 0.009	0.512 ± 0.009	0.516 ± 0.009	0.517 ± 0.009	0.513 ± 0.009	0.505 ± 0.009	0.504 ± 0.009
	E_2^{int}	0.502 ± 0.009	0.502 ± 0.009	0.503 ± 0.009	0.507 ± 0.009	0.513 ± 0.009	0.517 ± 0.009	0.519 ± 0.009	0.518 ± 0.009	0.514 ± 0.009	0.512 ± 0.009
	E_3^{int}	0.502 ± 0.010	0.502 ± 0.010	0.503 ± 0.010	0.508 ± 0.010	0.514 ± 0.010	0.521 ± 0.010	0.528 ± 0.011	0.534 ± 0.011	0.538 ± 0.011	0.550 ± 0.011
	E_4^{int}	0.501 ± 0.013	0.498 ± 0.013	0.496 ± 0.013	0.495 ± 0.013	0.496 ± 0.013	0.497 ± 0.013	0.498 ± 0.013	0.499 ± 0.013	0.500 ± 0.013	0.511 ± 0.013
δ_6^{diff}	E_1^{int}	0.504 ± 0.013	0.501 ± 0.013	0.498 ± 0.013	0.493 ± 0.013	0.489 ± 0.012	0.486 ± 0.012	0.485 ± 0.012	0.488 ± 0.012	0.492 ± 0.013	0.492 ± 0.013
	E_2^{int}	0.504 ± 0.013	0.501 ± 0.013	0.498 ± 0.013	0.493 ± 0.013	0.489 ± 0.013	0.486 ± 0.013	0.485 ± 0.013	0.489 ± 0.013	0.496 ± 0.013	0.493 ± 0.013
	E_3^{int}	0.504 ± 0.014	0.501 ± 0.014	0.497 ± 0.014	0.493 ± 0.014	0.487 ± 0.014	0.480 ± 0.014	0.473 ± 0.014	0.467 ± 0.013	0.461 ± 0.013	0.438 ± 0.013
	E_4^{int}	0.505 ± 0.018	0.504 ± 0.018	0.502 ± 0.018	0.500 ± 0.018	0.498 ± 0.018	0.496 ± 0.018	0.493 ± 0.018	0.491 ± 0.018	0.489 ± 0.018	0.470 ± 0.017

Table F.2: The spectrum, energy and angle dependency of the efficiency (and its statistical uncertainty) for all sky (grid) searches.

$\sin(\delta_\nu)$	E_ν	Neutrino Energy Spectrum									
		$\gamma = -1.0$	$\gamma = -1.25$	$\gamma = -1.5$	$\gamma = -1.75$	$\gamma = -2.0$	$\gamma = -2.25$	$\gamma = -2.5$	$\gamma = -2.75$	$\gamma = -3.0$	atmospheric
δ_1^{diff}	E_1^{diff}	0.423 ± 0.025	0.418 ± 0.025	0.413 ± 0.024	0.408 ± 0.024	0.403 ± 0.024	0.397 ± 0.023	0.391 ± 0.023	0.384 ± 0.023	0.377 ± 0.022	0.378 ± 0.022
	E_2^{diff}	0.611 ± 0.015	0.609 ± 0.015	0.607 ± 0.015	0.604 ± 0.015	0.601 ± 0.015	0.598 ± 0.015	0.595 ± 0.015	0.591 ± 0.015	0.587 ± 0.015	0.588 ± 0.015
	E_3^{diff}	0.658 ± 0.012	0.657 ± 0.012	0.656 ± 0.012	0.655 ± 0.012	0.654 ± 0.012	0.653 ± 0.012	0.652 ± 0.012	0.652 ± 0.012	0.651 ± 0.012	0.653 ± 0.012
	E_4^{diff}	0.665 ± 0.011	0.664 ± 0.011	0.663 ± 0.011	0.662 ± 0.011	0.662 ± 0.011	0.661 ± 0.011	0.660 ± 0.011	0.659 ± 0.011	0.658 ± 0.011	0.653 ± 0.010
	E_5^{diff}	0.678 ± 0.010	0.678 ± 0.010	0.679 ± 0.010	0.679 ± 0.010	0.680 ± 0.010	0.680 ± 0.010	0.680 ± 0.010	0.681 ± 0.010	0.681 ± 0.010	0.675 ± 0.010
	E_6^{diff}	0.691 ± 0.010	0.691 ± 0.010	0.690 ± 0.010	0.690 ± 0.010	0.690 ± 0.010	0.690 ± 0.010	0.689 ± 0.010	0.689 ± 0.010	0.688 ± 0.010	0.689 ± 0.010
	E_7^{diff}	0.697 ± 0.009	0.697 ± 0.009	0.698 ± 0.009	0.699 ± 0.009	0.700 ± 0.009	0.700 ± 0.009	0.701 ± 0.009	0.702 ± 0.009	0.702 ± 0.009	0.703 ± 0.009
	E_8^{diff}	0.675 ± 0.008	0.676 ± 0.008	0.677 ± 0.008	0.677 ± 0.008	0.678 ± 0.008	0.679 ± 0.008	0.679 ± 0.008	0.680 ± 0.008	0.681 ± 0.008	0.679 ± 0.008
δ_2^{diff}	E_1^{diff}	0.502 ± 0.040	0.499 ± 0.039	0.496 ± 0.039	0.493 ± 0.039	0.489 ± 0.039	0.485 ± 0.038	0.481 ± 0.038	0.476 ± 0.038	0.472 ± 0.037	0.463 ± 0.037
	E_2^{diff}	0.632 ± 0.021	0.632 ± 0.021	0.632 ± 0.021	0.632 ± 0.021	0.631 ± 0.021	0.630 ± 0.021	0.630 ± 0.021	0.629 ± 0.021	0.628 ± 0.021	0.627 ± 0.021
	E_3^{diff}	0.623 ± 0.016	0.623 ± 0.016	0.623 ± 0.016	0.622 ± 0.016	0.622 ± 0.016	0.621 ± 0.016	0.620 ± 0.016	0.619 ± 0.016	0.618 ± 0.016	0.617 ± 0.016
	E_4^{diff}	0.645 ± 0.014	0.645 ± 0.014	0.644 ± 0.014	0.644 ± 0.014	0.643 ± 0.014	0.643 ± 0.014	0.642 ± 0.014	0.642 ± 0.014	0.642 ± 0.014	0.639 ± 0.014
	E_5^{diff}	0.661 ± 0.014	0.662 ± 0.014	0.662 ± 0.014	0.662 ± 0.014	0.662 ± 0.014	0.663 ± 0.014	0.663 ± 0.014	0.663 ± 0.014	0.663 ± 0.014	0.669 ± 0.014
	E_6^{diff}	0.659 ± 0.013	0.659 ± 0.013	0.659 ± 0.013	0.658 ± 0.013	0.658 ± 0.013	0.658 ± 0.013	0.658 ± 0.013	0.658 ± 0.013	0.658 ± 0.013	0.658 ± 0.013
	E_7^{diff}	0.669 ± 0.012	0.669 ± 0.012	0.669 ± 0.012	0.670 ± 0.012	0.670 ± 0.012	0.670 ± 0.012	0.670 ± 0.012	0.670 ± 0.012	0.671 ± 0.012	0.671 ± 0.012
	E_8^{diff}	0.641 ± 0.010	0.642 ± 0.011	0.643 ± 0.011	0.645 ± 0.011	0.646 ± 0.011	0.647 ± 0.011	0.648 ± 0.011	0.648 ± 0.011	0.649 ± 0.011	0.652 ± 0.011
δ_3^{diff}	E_1^{diff}	0.503 ± 0.042	0.500 ± 0.042	0.497 ± 0.041	0.494 ± 0.041	0.490 ± 0.041	0.487 ± 0.041	0.483 ± 0.040	0.479 ± 0.040	0.475 ± 0.040	0.463 ± 0.039
	E_2^{diff}	0.559 ± 0.022	0.558 ± 0.022	0.558 ± 0.022	0.557 ± 0.022	0.557 ± 0.022	0.557 ± 0.022	0.556 ± 0.022	0.556 ± 0.022	0.556 ± 0.022	0.545 ± 0.021
	E_3^{diff}	0.623 ± 0.019	0.622 ± 0.019	0.622 ± 0.019	0.622 ± 0.019	0.622 ± 0.019	0.622 ± 0.019	0.622 ± 0.019	0.623 ± 0.019	0.623 ± 0.019	0.628 ± 0.019
	E_4^{diff}	0.582 ± 0.016	0.583 ± 0.016	0.584 ± 0.016	0.585 ± 0.016	0.586 ± 0.016	0.587 ± 0.016	0.587 ± 0.016	0.588 ± 0.016	0.588 ± 0.016	0.590 ± 0.016
	E_5^{diff}	0.601 ± 0.016	0.599 ± 0.015	0.597 ± 0.015	0.595 ± 0.015	0.594 ± 0.015	0.592 ± 0.015	0.591 ± 0.015	0.589 ± 0.015	0.588 ± 0.015	0.589 ± 0.015
	E_6^{diff}	0.578 ± 0.015	0.578 ± 0.015	0.578 ± 0.015	0.578 ± 0.015	0.579 ± 0.015	0.579 ± 0.015	0.579 ± 0.015	0.579 ± 0.015	0.580 ± 0.015	0.579 ± 0.015
	E_7^{diff}	0.601 ± 0.015	0.600 ± 0.015	0.599 ± 0.014	0.598 ± 0.014	0.596 ± 0.014	0.595 ± 0.014	0.594 ± 0.014	0.593 ± 0.014	0.592 ± 0.014	0.598 ± 0.014
	E_8^{diff}	0.594 ± 0.014	0.594 ± 0.014	0.595 ± 0.014	0.595 ± 0.014	0.596 ± 0.014	0.596 ± 0.014	0.596 ± 0.014	0.597 ± 0.014	0.597 ± 0.014	0.598 ± 0.015
δ_4^{diff}	E_1^{diff}	0.500 ± 0.047	0.495 ± 0.046	0.489 ± 0.046	0.484 ± 0.045	0.479 ± 0.045	0.473 ± 0.044	0.468 ± 0.044	0.463 ± 0.043	0.459 ± 0.043	0.451 ± 0.042
	E_2^{diff}	0.471 ± 0.025	0.472 ± 0.025	0.473 ± 0.025	0.474 ± 0.025	0.475 ± 0.025	0.476 ± 0.025	0.477 ± 0.025	0.479 ± 0.025	0.480 ± 0.025	0.487 ± 0.026
	E_3^{diff}	0.567 ± 0.022	0.566 ± 0.022	0.565 ± 0.022	0.564 ± 0.022	0.563 ± 0.022	0.563 ± 0.022	0.562 ± 0.022	0.562 ± 0.022	0.561 ± 0.022	0.560 ± 0.022
	E_4^{diff}	0.505 ± 0.018	0.506 ± 0.018	0.508 ± 0.018	0.509 ± 0.018	0.511 ± 0.018	0.512 ± 0.018	0.514 ± 0.018	0.515 ± 0.018	0.516 ± 0.019	0.529 ± 0.019
	E_5^{diff}	0.534 ± 0.018	0.535 ± 0.018	0.536 ± 0.018	0.536 ± 0.018	0.537 ± 0.018	0.538 ± 0.018	0.539 ± 0.018	0.540 ± 0.018	0.541 ± 0.018	0.548 ± 0.019
	E_6^{diff}	0.521 ± 0.017	0.520 ± 0.017	0.519 ± 0.017	0.519 ± 0.017	0.518 ± 0.017	0.518 ± 0.017	0.518 ± 0.017	0.517 ± 0.017	0.517 ± 0.017	0.500 ± 0.017
	E_7^{diff}	0.568 ± 0.019	0.567 ± 0.019	0.566 ± 0.019	0.565 ± 0.019	0.563 ± 0.019	0.562 ± 0.019	0.561 ± 0.019	0.560 ± 0.019	0.559 ± 0.019	0.555 ± 0.019
	E_8^{diff}	0.521 ± 0.019	0.522 ± 0.019	0.522 ± 0.019	0.522 ± 0.019	0.523 ± 0.019	0.523 ± 0.019	0.524 ± 0.019	0.524 ± 0.019	0.525 ± 0.019	0.531 ± 0.019
δ_5^{diff}	E_1^{diff}	0.428 ± 0.057	0.430 ± 0.057	0.432 ± 0.058	0.435 ± 0.058	0.438 ± 0.059	0.442 ± 0.059	0.446 ± 0.060	0.450 ± 0.060	0.455 ± 0.061	0.470 ± 0.063
	E_2^{diff}	0.515 ± 0.032	0.513 ± 0.032	0.512 ± 0.032	0.510 ± 0.032	0.508 ± 0.032	0.506 ± 0.032	0.503 ± 0.032	0.501 ± 0.031	0.499 ± 0.031	0.493 ± 0.031
	E_3^{diff}	0.484 ± 0.025	0.486 ± 0.025	0.487 ± 0.026	0.489 ± 0.026	0.491 ± 0.026	0.492 ± 0.026	0.493 ± 0.026	0.494 ± 0.026	0.496 ± 0.026	0.501 ± 0.026
	E_4^{diff}	0.547 ± 0.024	0.547 ± 0.025	0.548 ± 0.025	0.548 ± 0.025	0.549 ± 0.025	0.549 ± 0.025	0.549 ± 0.025	0.550 ± 0.025	0.550 ± 0.025	0.556 ± 0.025
	E_5^{diff}	0.533 ± 0.023	0.533 ± 0.023	0.534 ± 0.023	0.534 ± 0.023	0.534 ± 0.023	0.534 ± 0.023	0.534 ± 0.023	0.534 ± 0.023	0.533 ± 0.023	0.543 ± 0.023
	E_6^{diff}	0.522 ± 0.022	0.520 ± 0.022	0.519 ± 0.022	0.517 ± 0.022	0.515 ± 0.022	0.514 ± 0.022	0.512 ± 0.022	0.511 ± 0.022	0.509 ± 0.022	0.516 ± 0.022
	E_7^{diff}	0.453 ± 0.021	0.453 ± 0.021	0.453 ± 0.021	0.453 ± 0.021	0.454 ± 0.021	0.454 ± 0.021	0.455 ± 0.021	0.456 ± 0.021	0.458 ± 0.021	0.462 ± 0.021
	E_8^{diff}	0.521 ± 0.025	0.520 ± 0.025	0.520 ± 0.025	0.519 ± 0.025	0.519 ± 0.025	0.518 ± 0.025	0.518 ± 0.025	0.517 ± 0.025	0.517 ± 0.025	0.511 ± 0.024
δ_6^{diff}	E_1^{diff}	0.523 ± 0.095	0.519 ± 0.095	0.515 ± 0.094	0.511 ± 0.093	0.507 ± 0.092	0.502 ± 0.091	0.497 ± 0.091	0.492 ± 0.090	0.486 ± 0.089	0.499 ± 0.091
	E_2^{diff}	0.568 ± 0.054	0.565 ± 0.054	0.562 ± 0.054	0.559 ± 0.053	0.556 ± 0.053	0.554 ± 0.053	0.552 ± 0.053	0.550 ± 0.053	0.549 ± 0.052	0.544 ± 0.052
	E_3^{diff}	0.516 ± 0.039	0.513 ± 0.039	0.510 ± 0.039	0.508 ± 0.039	0.505 ± 0.038	0.503 ± 0.038	0.500 ± 0.038	0.498 ± 0.038	0.496 ± 0.038	0.495 ± 0.038
	E_4^{diff}	0.468 ± 0.032	0.465 ± 0.032	0.462 ± 0.031	0.459 ± 0.031	0.456 ± 0.031	0.453 ± 0.031	0.450 ± 0.031	0.447 ± 0.030	0.444 ± 0.030	0.421 ± 0.029
	E_5^{diff}	0.473 ± 0.030	0.474 ± 0.030	0.474 ± 0.030	0.474 ± 0.030	0.475 ± 0.030	0.475 ± 0.030	0.475 ± 0.030	0.475 ± 0.030	0.476 ± 0.030	0.470 ± 0.030
	E_6^{diff}	0.484 ± 0.028	0.483 ± 0.028	0.483 ± 0.028	0.483 ± 0.028	0.483 ± 0.028	0.483 ± 0.028	0.482 ± 0.028	0.482 ± 0.028	0.482 ± 0.028	0.465 ± 0.027
	E_7^{diff}	0.539 ± 0.034	0.535 ± 0.034	0.532 ± 0.034	0.529 ± 0.033	0.527 ± 0.033	0.525 ± 0.033	0.523 ± 0.033	0.521 ± 0.033	0.520 ± 0.033	0.507 ± 0.032
	E_8^{diff}	0.492 ± 0.033	0.490 ± 0.033	0.487 ± 0.033	0.485 ± 0.033	0.484 ± 0.033	0.484 ± 0.033	0.483 ± 0.033	0.484 ± 0.033	0.485 ± 0.033	0.499 ± 0.034

Table F.3: The spectrum, energy and angle dependency of the efficiency (and its statistical uncertainty) for all sky (grid) searches.

$\sin(\delta_\nu)$	E_ν	Neutrino Energy Spectrum									
		$\gamma = -1.0$	$\gamma = -1.25$	$\gamma = -1.5$	$\gamma = -1.75$	$\gamma = -2.0$	$\gamma = -2.25$	$\gamma = -2.5$	$\gamma = -2.75$	$\gamma = -3.0$	atmospheric
$\overline{\sin(\delta)}$	E_1^{diff}	0.475 ± 0.024	0.470 ± 0.024	0.466 ± 0.024	0.461 ± 0.023	0.456 ± 0.023	0.450 ± 0.023	0.445 ± 0.023	0.439 ± 0.022	0.433 ± 0.022	0.429 ± 0.022
	E_2^{diff}	0.612 ± 0.013	0.611 ± 0.013	0.609 ± 0.013	0.608 ± 0.013	0.606 ± 0.013	0.605 ± 0.013	0.603 ± 0.013	0.601 ± 0.013	0.599 ± 0.013	0.591 ± 0.013
	E_3^{diff}	0.642 ± 0.011	0.641 ± 0.011	0.641 ± 0.011	0.640 ± 0.011	0.639 ± 0.011	0.638 ± 0.011	0.637 ± 0.011	0.636 ± 0.011	0.636 ± 0.011	0.626 ± 0.010
	E_4^{diff}	0.640 ± 0.009	0.640 ± 0.009	0.641 ± 0.009	0.641 ± 0.009	0.641 ± 0.009	0.642 ± 0.009	0.642 ± 0.009	0.642 ± 0.009	0.642 ± 0.009	0.628 ± 0.009
	E_5^{diff}	0.653 ± 0.009	0.653 ± 0.009	0.653 ± 0.009	0.653 ± 0.009	0.653 ± 0.009	0.653 ± 0.009	0.653 ± 0.009	0.653 ± 0.009	0.653 ± 0.009	0.635 ± 0.009
	E_6^{diff}	0.649 ± 0.008	0.648 ± 0.008	0.648 ± 0.008	0.648 ± 0.008	0.647 ± 0.008	0.647 ± 0.008	0.646 ± 0.008	0.646 ± 0.008	0.646 ± 0.008	0.611 ± 0.008
	E_7^{diff}	0.663 ± 0.008	0.663 ± 0.008	0.662 ± 0.008	0.662 ± 0.008	0.662 ± 0.008	0.662 ± 0.008	0.661 ± 0.008	0.661 ± 0.008	0.661 ± 0.008	0.632 ± 0.007
	E_8^{diff}	0.643 ± 0.007	0.644 ± 0.007	0.645 ± 0.007	0.646 ± 0.007	0.646 ± 0.007	0.647 ± 0.007	0.648 ± 0.007	0.649 ± 0.007	0.650 ± 0.007	0.628 ± 0.007
$\overline{\sin(\delta)}$	E_1^{int}	0.650 ± 0.003	0.651 ± 0.003	0.652 ± 0.003	0.651 ± 0.003	0.648 ± 0.003	0.644 ± 0.003	0.635 ± 0.003	0.623 ± 0.003	0.605 ± 0.003	0.582 ± 0.003
	E_2^{int}	0.650 ± 0.003	0.651 ± 0.003	0.652 ± 0.003	0.651 ± 0.003	0.649 ± 0.003	0.646 ± 0.003	0.641 ± 0.003	0.635 ± 0.003	0.628 ± 0.003	0.612 ± 0.003
	E_3^{int}	0.650 ± 0.004	0.651 ± 0.004	0.652 ± 0.004	0.652 ± 0.004	0.651 ± 0.004	0.650 ± 0.004	0.648 ± 0.004	0.647 ± 0.004	0.646 ± 0.004	0.629 ± 0.004
	E_4^{int}	0.650 ± 0.004	0.652 ± 0.004	0.652 ± 0.004	0.652 ± 0.004	0.652 ± 0.004	0.652 ± 0.004	0.651 ± 0.004	0.650 ± 0.004	0.649 ± 0.004	0.613 ± 0.004
δ_1^{diff}	E_1^{int}	0.705 ± 0.005	0.706 ± 0.005	0.706 ± 0.005	0.703 ± 0.005	0.698 ± 0.005	0.689 ± 0.005	0.674 ± 0.005	0.654 ± 0.005	0.628 ± 0.005	0.604 ± 0.005
	E_2^{int}	0.705 ± 0.005	0.706 ± 0.005	0.706 ± 0.005	0.703 ± 0.005	0.699 ± 0.005	0.692 ± 0.005	0.682 ± 0.005	0.671 ± 0.005	0.658 ± 0.005	0.645 ± 0.005
	E_3^{int}	0.705 ± 0.006	0.706 ± 0.006	0.706 ± 0.006	0.705 ± 0.006	0.703 ± 0.006	0.700 ± 0.006	0.697 ± 0.006	0.695 ± 0.006	0.692 ± 0.006	0.687 ± 0.006
	E_4^{int}	0.706 ± 0.007	0.707 ± 0.007	0.709 ± 0.007	0.709 ± 0.007	0.709 ± 0.007	0.709 ± 0.007	0.709 ± 0.007	0.709 ± 0.007	0.708 ± 0.007	0.708 ± 0.007
δ_2^{diff}	E_1^{int}	0.688 ± 0.007	0.689 ± 0.007	0.690 ± 0.007	0.689 ± 0.007	0.685 ± 0.007	0.680 ± 0.007	0.670 ± 0.007	0.656 ± 0.007	0.639 ± 0.007	0.621 ± 0.006
	E_2^{int}	0.688 ± 0.007	0.689 ± 0.007	0.690 ± 0.007	0.689 ± 0.007	0.686 ± 0.007	0.682 ± 0.007	0.675 ± 0.007	0.668 ± 0.007	0.661 ± 0.007	0.654 ± 0.007
	E_3^{int}	0.688 ± 0.008	0.690 ± 0.008	0.690 ± 0.008	0.690 ± 0.008	0.689 ± 0.008	0.687 ± 0.008	0.685 ± 0.008	0.684 ± 0.008	0.682 ± 0.008	0.682 ± 0.008
	E_4^{int}	0.688 ± 0.009	0.690 ± 0.009	0.691 ± 0.009	0.692 ± 0.009	0.692 ± 0.009	0.692 ± 0.009	0.691 ± 0.009	0.691 ± 0.009	0.690 ± 0.009	0.688 ± 0.009
δ_3^{diff}	E_1^{int}	0.626 ± 0.009	0.627 ± 0.009	0.627 ± 0.009	0.627 ± 0.009	0.626 ± 0.009	0.625 ± 0.009	0.623 ± 0.009	0.617 ± 0.009	0.608 ± 0.008	0.598 ± 0.008
	E_2^{int}	0.626 ± 0.009	0.627 ± 0.009	0.627 ± 0.009	0.627 ± 0.009	0.627 ± 0.009	0.627 ± 0.009	0.627 ± 0.009	0.627 ± 0.009	0.626 ± 0.009	0.625 ± 0.009
	E_3^{int}	0.626 ± 0.010	0.627 ± 0.010	0.627 ± 0.010	0.626 ± 0.010	0.626 ± 0.010	0.625 ± 0.010	0.624 ± 0.010	0.623 ± 0.010	0.623 ± 0.010	0.624 ± 0.010
	E_4^{int}	0.626 ± 0.012	0.626 ± 0.012	0.626 ± 0.012	0.626 ± 0.012	0.625 ± 0.012	0.625 ± 0.012	0.625 ± 0.012	0.625 ± 0.012	0.625 ± 0.012	0.622 ± 0.012
δ_4^{diff}	E_1^{int}	0.573 ± 0.011	0.573 ± 0.011	0.573 ± 0.011	0.572 ± 0.011	0.569 ± 0.011	0.564 ± 0.011	0.557 ± 0.011	0.547 ± 0.010	0.533 ± 0.010	0.521 ± 0.010
	E_2^{int}	0.573 ± 0.011	0.573 ± 0.011	0.573 ± 0.011	0.572 ± 0.011	0.569 ± 0.011	0.566 ± 0.011	0.562 ± 0.011	0.559 ± 0.011	0.555 ± 0.011	0.554 ± 0.011
	E_3^{int}	0.573 ± 0.012	0.573 ± 0.012	0.573 ± 0.012	0.572 ± 0.012	0.570 ± 0.012	0.567 ± 0.012	0.565 ± 0.012	0.563 ± 0.012	0.562 ± 0.012	0.560 ± 0.012
	E_4^{int}	0.573 ± 0.016	0.574 ± 0.016	0.574 ± 0.016	0.573 ± 0.016	0.571 ± 0.016	0.568 ± 0.016	0.565 ± 0.015	0.562 ± 0.015	0.559 ± 0.015	0.540 ± 0.015
δ_5^{diff}	E_1^{int}	0.552 ± 0.014	0.548 ± 0.013	0.545 ± 0.013	0.544 ± 0.013	0.545 ± 0.013	0.546 ± 0.013	0.544 ± 0.013	0.538 ± 0.013	0.529 ± 0.013	0.525 ± 0.013
	E_2^{int}	0.552 ± 0.014	0.548 ± 0.014	0.545 ± 0.013	0.544 ± 0.013	0.545 ± 0.013	0.547 ± 0.014	0.546 ± 0.013	0.541 ± 0.013	0.534 ± 0.013	0.528 ± 0.013
	E_3^{int}	0.552 ± 0.015	0.548 ± 0.015	0.546 ± 0.015	0.545 ± 0.015	0.548 ± 0.015	0.554 ± 0.015	0.561 ± 0.015	0.568 ± 0.016	0.575 ± 0.016	0.585 ± 0.016
	E_4^{int}	0.552 ± 0.020	0.546 ± 0.020	0.541 ± 0.019	0.536 ± 0.019	0.530 ± 0.019	0.525 ± 0.019	0.520 ± 0.019	0.515 ± 0.018	0.510 ± 0.018	0.506 ± 0.018
δ_6^{diff}	E_1^{int}	0.553 ± 0.019	0.548 ± 0.019	0.544 ± 0.019	0.540 ± 0.019	0.537 ± 0.019	0.535 ± 0.019	0.537 ± 0.019	0.539 ± 0.019	0.540 ± 0.019	0.537 ± 0.019
	E_2^{int}	0.553 ± 0.020	0.548 ± 0.019	0.544 ± 0.019	0.540 ± 0.019	0.537 ± 0.019	0.535 ± 0.019	0.537 ± 0.019	0.541 ± 0.019	0.545 ± 0.019	0.541 ± 0.019
	E_3^{int}	0.553 ± 0.022	0.548 ± 0.022	0.544 ± 0.021	0.539 ± 0.021	0.534 ± 0.021	0.530 ± 0.021	0.525 ± 0.021	0.521 ± 0.020	0.517 ± 0.020	0.499 ± 0.020
	E_4^{int}	0.554 ± 0.028	0.550 ± 0.027	0.546 ± 0.027	0.542 ± 0.027	0.539 ± 0.027	0.536 ± 0.027	0.535 ± 0.027	0.534 ± 0.027	0.533 ± 0.027	0.508 ± 0.025

Table F.4: The spectrum, energy and angle dependency of the efficiency (and its statistical uncertainty) for searches for pre-selected sources.

$\sin(\delta_\nu)$	E_ν	Neutrino Energy Spectrum									
		$\gamma = -1.0$	$\gamma = -1.25$	$\gamma = -1.5$	$\gamma = -1.75$	$\gamma = -2.0$	$\gamma = -2.25$	$\gamma = -2.5$	$\gamma = -2.75$	$\gamma = -3.0$	atmospheric
δ_1^{diff}	E_1^{diff}	0.445 ± 0.038	0.439 ± 0.038	0.433 ± 0.037	0.427 ± 0.037	0.420 ± 0.036	0.414 ± 0.035	0.407 ± 0.035	0.399 ± 0.034	0.392 ± 0.034	0.392 ± 0.034
	E_2^{diff}	0.633 ± 0.022	0.631 ± 0.022	0.629 ± 0.022	0.626 ± 0.022	0.623 ± 0.021	0.619 ± 0.021	0.616 ± 0.021	0.612 ± 0.021	0.608 ± 0.021	0.605 ± 0.021
	E_3^{diff}	0.678 ± 0.017	0.676 ± 0.017	0.675 ± 0.017	0.674 ± 0.017	0.672 ± 0.017	0.671 ± 0.017	0.670 ± 0.017	0.668 ± 0.017	0.667 ± 0.017	0.667 ± 0.017
	E_4^{diff}	0.688 ± 0.015	0.687 ± 0.015	0.687 ± 0.015	0.687 ± 0.015	0.686 ± 0.015	0.686 ± 0.015	0.686 ± 0.015	0.685 ± 0.015	0.685 ± 0.015	0.683 ± 0.015
	E_5^{diff}	0.699 ± 0.014	0.699 ± 0.014	0.700 ± 0.014	0.700 ± 0.014	0.700 ± 0.014	0.700 ± 0.014	0.700 ± 0.014	0.699 ± 0.014	0.699 ± 0.014	0.696 ± 0.014
	E_6^{diff}	0.705 ± 0.013	0.705 ± 0.013	0.705 ± 0.013	0.705 ± 0.013	0.705 ± 0.013	0.705 ± 0.013	0.705 ± 0.013	0.705 ± 0.013	0.705 ± 0.013	0.707 ± 0.013
	E_7^{diff}	0.717 ± 0.012	0.718 ± 0.012	0.719 ± 0.012	0.719 ± 0.012	0.720 ± 0.012	0.720 ± 0.012	0.721 ± 0.012	0.721 ± 0.012	0.722 ± 0.012	0.722 ± 0.012
	E_8^{diff}	0.698 ± 0.011	0.699 ± 0.011	0.700 ± 0.011	0.701 ± 0.011	0.702 ± 0.011	0.703 ± 0.011	0.703 ± 0.011	0.704 ± 0.011	0.705 ± 0.011	0.702 ± 0.011
δ_2^{diff}	E_1^{diff}	0.482 ± 0.055	0.478 ± 0.054	0.474 ± 0.054	0.469 ± 0.053	0.464 ± 0.053	0.459 ± 0.052	0.453 ± 0.052	0.447 ± 0.051	0.440 ± 0.050	0.422 ± 0.048
	E_2^{diff}	0.654 ± 0.029	0.653 ± 0.029	0.651 ± 0.029	0.650 ± 0.029	0.648 ± 0.029	0.646 ± 0.029	0.644 ± 0.029	0.641 ± 0.029	0.639 ± 0.028	0.637 ± 0.028
	E_3^{diff}	0.659 ± 0.023	0.660 ± 0.023	0.660 ± 0.023	0.660 ± 0.023	0.659 ± 0.023	0.659 ± 0.023	0.659 ± 0.023	0.658 ± 0.023	0.657 ± 0.023	0.655 ± 0.023
	E_4^{diff}	0.673 ± 0.020	0.674 ± 0.020	0.674 ± 0.020	0.674 ± 0.020	0.675 ± 0.020	0.675 ± 0.020	0.676 ± 0.020	0.676 ± 0.020	0.677 ± 0.020	0.679 ± 0.020
	E_5^{diff}	0.687 ± 0.019	0.687 ± 0.019	0.687 ± 0.019	0.688 ± 0.019	0.688 ± 0.019	0.688 ± 0.019	0.688 ± 0.019	0.688 ± 0.019	0.688 ± 0.019	0.693 ± 0.019
	E_6^{diff}	0.691 ± 0.018	0.691 ± 0.018	0.690 ± 0.018	0.690 ± 0.018	0.690 ± 0.018	0.690 ± 0.018	0.689 ± 0.018	0.689 ± 0.018	0.689 ± 0.018	0.687 ± 0.018
	E_7^{diff}	0.701 ± 0.016	0.701 ± 0.016	0.700 ± 0.016	0.699 ± 0.016	0.699 ± 0.016	0.698 ± 0.016	0.697 ± 0.016	0.697 ± 0.016	0.696 ± 0.016	0.695 ± 0.016
	E_8^{diff}	0.681 ± 0.015	0.682 ± 0.015	0.683 ± 0.015	0.685 ± 0.015	0.686 ± 0.015	0.687 ± 0.015	0.688 ± 0.015	0.689 ± 0.015	0.690 ± 0.015	0.696 ± 0.015
δ_3^{diff}	E_1^{diff}	0.503 ± 0.059	0.499 ± 0.058	0.496 ± 0.058	0.492 ± 0.058	0.488 ± 0.057	0.484 ± 0.057	0.480 ± 0.056	0.476 ± 0.056	0.472 ± 0.055	0.459 ± 0.054
	E_2^{diff}	0.609 ± 0.032	0.609 ± 0.032	0.609 ± 0.032	0.610 ± 0.032	0.610 ± 0.032	0.610 ± 0.032	0.610 ± 0.032	0.610 ± 0.032	0.610 ± 0.032	0.605 ± 0.032
	E_3^{diff}	0.653 ± 0.027	0.652 ± 0.027	0.651 ± 0.027	0.650 ± 0.027	0.650 ± 0.027	0.649 ± 0.027	0.648 ± 0.027	0.648 ± 0.027	0.648 ± 0.027	0.653 ± 0.027
	E_4^{diff}	0.613 ± 0.023	0.614 ± 0.023	0.615 ± 0.023	0.616 ± 0.023	0.617 ± 0.023	0.618 ± 0.023	0.619 ± 0.023	0.619 ± 0.023	0.620 ± 0.023	0.624 ± 0.024
	E_5^{diff}	0.637 ± 0.022	0.635 ± 0.022	0.634 ± 0.022	0.633 ± 0.022	0.631 ± 0.022	0.630 ± 0.022	0.629 ± 0.022	0.628 ± 0.022	0.627 ± 0.022	0.623 ± 0.022
	E_6^{diff}	0.619 ± 0.021	0.620 ± 0.021	0.620 ± 0.021	0.621 ± 0.021	0.621 ± 0.021	0.622 ± 0.021	0.623 ± 0.021	0.624 ± 0.021	0.625 ± 0.021	0.621 ± 0.021
	E_7^{diff}	0.639 ± 0.021	0.637 ± 0.021	0.636 ± 0.021	0.634 ± 0.021	0.632 ± 0.021	0.630 ± 0.021	0.629 ± 0.021	0.627 ± 0.020	0.625 ± 0.020	0.625 ± 0.020
	E_8^{diff}	0.620 ± 0.020	0.621 ± 0.020	0.621 ± 0.020	0.622 ± 0.020	0.623 ± 0.021	0.623 ± 0.021	0.624 ± 0.021	0.624 ± 0.021	0.625 ± 0.021	0.630 ± 0.021
δ_4^{diff}	E_1^{diff}	0.486 ± 0.065	0.479 ± 0.064	0.472 ± 0.063	0.465 ± 0.062	0.457 ± 0.061	0.450 ± 0.060	0.443 ± 0.059	0.437 ± 0.058	0.430 ± 0.057	0.415 ± 0.055
	E_2^{diff}	0.512 ± 0.037	0.513 ± 0.037	0.515 ± 0.037	0.517 ± 0.037	0.518 ± 0.038	0.520 ± 0.038	0.522 ± 0.038	0.524 ± 0.038	0.527 ± 0.038	0.532 ± 0.039
	E_3^{diff}	0.582 ± 0.032	0.581 ± 0.031	0.580 ± 0.031	0.579 ± 0.031	0.578 ± 0.031	0.577 ± 0.031	0.576 ± 0.031	0.575 ± 0.031	0.574 ± 0.031	0.574 ± 0.031
	E_4^{diff}	0.540 ± 0.027	0.542 ± 0.027	0.543 ± 0.027	0.544 ± 0.027	0.546 ± 0.027	0.547 ± 0.027	0.548 ± 0.027	0.550 ± 0.027	0.551 ± 0.027	0.552 ± 0.027
	E_5^{diff}	0.581 ± 0.027	0.582 ± 0.027	0.582 ± 0.027	0.582 ± 0.027	0.583 ± 0.027	0.583 ± 0.027	0.583 ± 0.027	0.583 ± 0.027	0.584 ± 0.027	0.588 ± 0.027
	E_6^{diff}	0.561 ± 0.026	0.559 ± 0.026	0.558 ± 0.026	0.556 ± 0.026	0.555 ± 0.025	0.553 ± 0.025	0.552 ± 0.025	0.551 ± 0.025	0.550 ± 0.025	0.534 ± 0.024
	E_7^{diff}	0.600 ± 0.028	0.599 ± 0.028	0.599 ± 0.028	0.599 ± 0.028	0.599 ± 0.028	0.598 ± 0.028	0.598 ± 0.028	0.598 ± 0.028	0.598 ± 0.028	0.596 ± 0.028
	E_8^{diff}	0.561 ± 0.028	0.561 ± 0.028	0.561 ± 0.028	0.561 ± 0.028	0.561 ± 0.028	0.561 ± 0.028	0.561 ± 0.028	0.561 ± 0.028	0.561 ± 0.028	0.566 ± 0.028
δ_5^{diff}	E_1^{diff}	0.484 ± 0.089	0.487 ± 0.089	0.490 ± 0.090	0.493 ± 0.090	0.496 ± 0.091	0.499 ± 0.092	0.503 ± 0.092	0.506 ± 0.093	0.509 ± 0.093	0.528 ± 0.097
	E_2^{diff}	0.503 ± 0.045	0.502 ± 0.044	0.502 ± 0.044	0.501 ± 0.044	0.501 ± 0.044	0.500 ± 0.044	0.499 ± 0.044	0.499 ± 0.044	0.498 ± 0.044	0.496 ± 0.044
	E_3^{diff}	0.517 ± 0.038	0.518 ± 0.038	0.518 ± 0.038	0.518 ± 0.038	0.518 ± 0.038	0.518 ± 0.038	0.517 ± 0.038	0.517 ± 0.038	0.516 ± 0.038	0.513 ± 0.038
	E_4^{diff}	0.590 ± 0.036	0.591 ± 0.036	0.592 ± 0.036	0.593 ± 0.036	0.594 ± 0.036	0.594 ± 0.036	0.595 ± 0.036	0.596 ± 0.036	0.596 ± 0.036	0.596 ± 0.036
	E_5^{diff}	0.557 ± 0.033	0.558 ± 0.033	0.559 ± 0.033	0.560 ± 0.033	0.561 ± 0.033	0.561 ± 0.033	0.561 ± 0.033	0.561 ± 0.033	0.561 ± 0.033	0.573 ± 0.034
	E_6^{diff}	0.537 ± 0.031	0.533 ± 0.031	0.529 ± 0.031	0.525 ± 0.031	0.521 ± 0.030	0.516 ± 0.030	0.512 ± 0.030	0.508 ± 0.030	0.504 ± 0.029	0.503 ± 0.029
	E_7^{diff}	0.509 ± 0.032	0.510 ± 0.032	0.511 ± 0.033	0.513 ± 0.033	0.514 ± 0.033	0.516 ± 0.033	0.518 ± 0.033	0.520 ± 0.033	0.522 ± 0.033	0.525 ± 0.033
	E_8^{diff}	0.577 ± 0.037	0.577 ± 0.037	0.576 ± 0.037	0.576 ± 0.037	0.576 ± 0.037	0.576 ± 0.037	0.575 ± 0.037	0.575 ± 0.037	0.575 ± 0.037	0.572 ± 0.037
δ_6^{diff}	E_1^{diff}	0.569 ± 0.144	0.564 ± 0.143	0.558 ± 0.141	0.553 ± 0.140	0.547 ± 0.139	0.541 ± 0.137	0.535 ± 0.135	0.528 ± 0.134	0.521 ± 0.132	0.534 ± 0.135
	E_2^{diff}	0.633 ± 0.082	0.629 ± 0.081	0.624 ± 0.080	0.618 ± 0.080	0.612 ± 0.079	0.606 ± 0.078	0.600 ± 0.077	0.593 ± 0.076	0.586 ± 0.076	0.580 ± 0.075
	E_3^{diff}	0.567 ± 0.059	0.564 ± 0.058	0.561 ± 0.058	0.558 ± 0.058	0.556 ± 0.057	0.553 ± 0.057	0.551 ± 0.057	0.549 ± 0.057	0.548 ± 0.057	0.543 ± 0.056
	E_4^{diff}	0.526 ± 0.049	0.523 ± 0.049	0.520 ± 0.049	0.518 ± 0.048	0.515 ± 0.048	0.513 ± 0.048	0.510 ± 0.048	0.508 ± 0.047	0.505 ± 0.047	0.487 ± 0.045
	E_5^{diff}	0.533 ± 0.046	0.533 ± 0.047	0.533 ± 0.046	0.533 ± 0.046	0.532 ± 0.046	0.531 ± 0.046	0.531 ± 0.046	0.530 ± 0.046	0.529 ± 0.046	0.522 ± 0.046
	E_6^{diff}	0.516 ± 0.042	0.517 ± 0.042	0.519 ± 0.042	0.520 ± 0.042	0.522 ± 0.042	0.523 ± 0.042	0.525 ± 0.043	0.527 ± 0.043	0.528 ± 0.043	0.503 ± 0.041
	E_7^{diff}	0.575 ± 0.050	0.571 ± 0.050	0.567 ± 0.049	0.564 ± 0.049	0.560 ± 0.049	0.558 ± 0.048	0.555 ± 0.048	0.553 ± 0.048	0.551 ± 0.048	0.550 ± 0.048
	E_8^{diff}	0.551 ± 0.051	0.548 ± 0.050	0.546 ± 0.050	0.544 ± 0.050	0.543 ± 0.050	0.542 ± 0.050	0.542 ± 0.050	0.543 ± 0.050	0.544 ± 0.050	0.566 ± 0.052

Table F.5: The spectrum, energy and angle dependency of the efficiency (and its statistical uncertainty) for searches for pre-selected sources.

Table F.6: The spectrum, energy and angle dependency of the energy averaged effective muon area.

$\sin(\delta_\nu)$	E_ν	Neutrino Energy Spectrum									
		$\gamma = -1.0$	$\gamma = -1.25$	$\gamma = -1.5$	$\gamma = -1.75$	$\gamma = -2.0$	$\gamma = -2.25$	$\gamma = -2.5$	$\gamma = -2.75$	$\gamma = -3.0$	atmospheric
$\overline{\sin(\delta)}$	E_1^{diff}	8.58E-04	8.21E-04	7.83E-04	7.45E-04	7.06E-04	6.66E-04	6.28E-04	5.89E-04	5.52E-04	4.22E-04
	E_2^{diff}	2.94E-03	2.90E-03	2.86E-03	2.82E-03	2.77E-03	2.73E-03	2.68E-03	2.63E-03	2.59E-03	1.91E-03
	E_3^{diff}	3.95E-03	3.94E-03	3.93E-03	3.91E-03	3.90E-03	3.89E-03	3.88E-03	3.86E-03	3.85E-03	2.71E-03
	E_4^{diff}	4.85E-03	4.83E-03	4.81E-03	4.79E-03	4.77E-03	4.75E-03	4.73E-03	4.70E-03	4.68E-03	3.04E-03
	E_5^{diff}	5.40E-03	5.39E-03	5.38E-03	5.37E-03	5.36E-03	5.35E-03	5.34E-03	5.33E-03	5.33E-03	2.87E-03
	E_6^{diff}	5.64E-03	5.65E-03	5.65E-03	5.65E-03	5.65E-03	5.65E-03	5.65E-03	5.66E-03	5.66E-03	2.56E-03
	E_7^{diff}	5.32E-03	5.34E-03	5.35E-03	5.37E-03	5.38E-03	5.40E-03	5.42E-03	5.43E-03	5.45E-03	2.14E-03
	E_8^{diff}	4.35E-03	4.38E-03	4.41E-03	4.44E-03	4.47E-03	4.50E-03	4.53E-03	4.55E-03	4.58E-03	1.67E-03
$\overline{\sin(\delta)}$	E_1^{int}	4.81E-03	4.94E-03	5.04E-03	5.05E-03	4.83E-03	4.16E-03	3.01E-03	1.82E-03	9.94E-04	5.87E-04
	E_2^{int}	4.81E-03	4.94E-03	5.05E-03	5.09E-03	5.02E-03	4.78E-03	4.41E-03	4.00E-03	3.62E-03	2.36E-03
	E_3^{int}	4.80E-03	4.94E-03	5.07E-03	5.17E-03	5.22E-03	5.21E-03	5.14E-03	5.06E-03	4.97E-03	2.97E-03
	E_4^{int}	4.78E-03	4.91E-03	5.04E-03	5.17E-03	5.29E-03	5.39E-03	5.47E-03	5.53E-03	5.57E-03	2.50E-03
δ_1^{diff}	E_1^{int}	2.87E-02	2.71E-02	2.50E-02	2.21E-02	1.82E-02	1.33E-02	8.25E-03	4.49E-03	2.31E-03	1.61E-03
	E_2^{int}	2.87E-02	2.72E-02	2.51E-02	2.26E-02	1.96E-02	1.66E-02	1.39E-02	1.17E-02	1.01E-02	8.64E-03
	E_3^{int}	2.88E-02	2.74E-02	2.57E-02	2.38E-02	2.20E-02	2.03E-02	1.88E-02	1.77E-02	1.69E-02	1.54E-02
	E_4^{int}	2.97E-02	2.90E-02	2.83E-02	2.76E-02	2.70E-02	2.65E-02	2.60E-02	2.57E-02	2.54E-02	2.47E-02
δ_2^{diff}	E_1^{int}	1.98E-02	1.88E-02	1.75E-02	1.57E-02	1.32E-02	9.99E-03	6.48E-03	3.65E-03	1.91E-03	1.38E-03
	E_2^{int}	1.98E-02	1.88E-02	1.75E-02	1.59E-02	1.39E-02	1.19E-02	1.01E-02	8.57E-03	7.48E-03	6.58E-03
	E_3^{int}	1.98E-02	1.89E-02	1.78E-02	1.65E-02	1.52E-02	1.40E-02	1.30E-02	1.22E-02	1.16E-02	1.07E-02
	E_4^{int}	2.03E-02	1.97E-02	1.91E-02	1.86E-02	1.80E-02	1.75E-02	1.71E-02	1.68E-02	1.65E-02	1.57E-02
δ_3^{diff}	E_1^{int}	1.04E-02	1.02E-02	9.86E-03	9.25E-03	8.20E-03	6.56E-03	4.49E-03	2.64E-03	1.43E-03	1.05E-03
	E_2^{int}	1.04E-02	1.02E-02	9.88E-03	9.35E-03	8.58E-03	7.64E-03	6.67E-03	5.84E-03	5.18E-03	4.56E-03
	E_3^{int}	1.04E-02	1.02E-02	9.99E-03	9.63E-03	9.19E-03	8.71E-03	8.24E-03	7.84E-03	7.50E-03	6.88E-03
	E_4^{int}	1.05E-02	1.04E-02	1.04E-02	1.03E-02	1.02E-02	1.01E-02	9.95E-03	9.86E-03	9.77E-03	9.41E-03
δ_4^{diff}	E_1^{int}	4.92E-03	4.95E-03	4.95E-03	4.84E-03	4.52E-03	3.82E-03	2.76E-03	1.69E-03	9.47E-04	7.48E-04
	E_2^{int}	4.92E-03	4.95E-03	4.95E-03	4.88E-03	4.69E-03	4.37E-03	3.97E-03	3.56E-03	3.20E-03	2.90E-03
	E_3^{int}	4.92E-03	4.96E-03	4.99E-03	4.98E-03	4.93E-03	4.83E-03	4.70E-03	4.58E-03	4.46E-03	4.21E-03
	E_4^{int}	4.93E-03	4.98E-03	5.03E-03	5.10E-03	5.16E-03	5.21E-03	5.26E-03	5.31E-03	5.34E-03	5.24E-03
δ_5^{diff}	E_1^{int}	2.62E-03	2.67E-03	2.72E-03	2.73E-03	2.63E-03	2.31E-03	1.72E-03	1.07E-03	5.89E-04	4.79E-04
	E_2^{int}	2.62E-03	2.67E-03	2.72E-03	2.75E-03	2.72E-03	2.62E-03	2.44E-03	2.23E-03	2.03E-03	1.91E-03
	E_3^{int}	2.62E-03	2.68E-03	2.73E-03	2.79E-03	2.82E-03	2.83E-03	2.81E-03	2.78E-03	2.74E-03	2.72E-03
	E_4^{int}	2.61E-03	2.65E-03	2.70E-03	2.75E-03	2.81E-03	2.86E-03	2.91E-03	2.96E-03	3.00E-03	3.00E-03
δ_6^{diff}	E_1^{int}	1.10E-03	1.13E-03	1.16E-03	1.17E-03	1.15E-03	1.02E-03	7.69E-04	4.74E-04	2.59E-04	2.13E-04
	E_2^{int}	1.10E-03	1.13E-03	1.16E-03	1.18E-03	1.18E-03	1.15E-03	1.07E-03	9.70E-04	8.70E-04	7.84E-04
	E_3^{int}	1.10E-03	1.13E-03	1.16E-03	1.19E-03	1.22E-03	1.23E-03	1.23E-03	1.22E-03	1.21E-03	1.19E-03
	E_4^{int}	1.10E-03	1.12E-03	1.15E-03	1.19E-03	1.22E-03	1.26E-03	1.29E-03	1.31E-03	1.33E-03	1.28E-03

$\sin(\delta_\nu)$	E_ν	Neutrino Energy Spectrum									
		$\gamma=-1.0$	$\gamma=-1.25$	$\gamma=-1.5$	$\gamma=-1.75$	$\gamma=-2.0$	$\gamma=-2.25$	$\gamma=-2.5$	$\gamma=-2.75$	$\gamma=-3.0$	atmospheric
δ_1^{diff}	E_1^{diff}	2.00E-03	1.91E-03	1.81E-03	1.72E-03	1.62E-03	1.53E-03	1.43E-03	1.34E-03	1.25E-03	1.19E-03
	E_2^{diff}	7.51E-03	7.39E-03	7.26E-03	7.12E-03	6.99E-03	6.85E-03	6.70E-03	6.56E-03	6.42E-03	6.23E-03
	E_3^{diff}	1.13E-02	1.13E-02	1.12E-02	1.12E-02	1.11E-02	1.10E-02	1.10E-02	1.09E-02	1.08E-02	1.06E-02
	E_4^{diff}	1.57E-02	1.56E-02	1.55E-02	1.54E-02	1.53E-02	1.52E-02	1.50E-02	1.49E-02	1.48E-02	1.44E-02
	E_5^{diff}	2.00E-02	1.99E-02	1.98E-02	1.97E-02	1.96E-02	1.95E-02	1.94E-02	1.93E-02	1.92E-02	1.86E-02
	E_6^{diff}	2.53E-02	2.52E-02	2.51E-02	2.51E-02	2.50E-02	2.50E-02	2.49E-02	2.48E-02	2.48E-02	2.45E-02
	E_7^{diff}	2.84E-02	2.83E-02	2.82E-02	2.81E-02	2.80E-02	2.79E-02	2.78E-02	2.77E-02	2.77E-02	2.69E-02
	E_8^{diff}	3.29E-02	3.28E-02	3.27E-02	3.26E-02	3.25E-02	3.25E-02	3.24E-02	3.23E-02	3.23E-02	3.19E-02
δ_2^{diff}	E_1^{diff}	1.47E-03	1.41E-03	1.34E-03	1.26E-03	1.19E-03	1.12E-03	1.05E-03	9.82E-04	9.15E-04	8.84E-04
	E_2^{diff}	5.79E-03	5.72E-03	5.64E-03	5.56E-03	5.48E-03	5.39E-03	5.30E-03	5.21E-03	5.13E-03	4.95E-03
	E_3^{diff}	7.87E-03	7.84E-03	7.82E-03	7.79E-03	7.75E-03	7.72E-03	7.68E-03	7.64E-03	7.60E-03	7.54E-03
	E_4^{diff}	1.08E-02	1.07E-02	1.06E-02	1.05E-02	1.05E-02	1.04E-02	1.03E-02	1.02E-02	1.01E-02	9.92E-03
	E_5^{diff}	1.36E-02	1.36E-02	1.35E-02	1.35E-02	1.34E-02	1.33E-02	1.33E-02	1.32E-02	1.32E-02	1.30E-02
	E_6^{diff}	1.62E-02	1.62E-02	1.61E-02	1.60E-02	1.60E-02	1.59E-02	1.59E-02	1.58E-02	1.58E-02	1.54E-02
	E_7^{diff}	1.91E-02	1.90E-02	1.90E-02	1.89E-02	1.89E-02	1.88E-02	1.87E-02	1.87E-02	1.86E-02	1.82E-02
	E_8^{diff}	2.21E-02	2.21E-02	2.20E-02	2.19E-02	2.19E-02	2.18E-02	2.17E-02	2.16E-02	2.16E-02	2.10E-02
δ_3^{diff}	E_1^{diff}	1.30E-03	1.24E-03	1.18E-03	1.12E-03	1.05E-03	9.89E-04	9.24E-04	8.61E-04	7.99E-04	7.60E-04
	E_2^{diff}	4.19E-03	4.14E-03	4.09E-03	4.03E-03	3.97E-03	3.92E-03	3.86E-03	3.80E-03	3.73E-03	3.59E-03
	E_3^{diff}	5.50E-03	5.46E-03	5.43E-03	5.40E-03	5.36E-03	5.33E-03	5.30E-03	5.27E-03	5.24E-03	4.99E-03
	E_4^{diff}	6.80E-03	6.75E-03	6.71E-03	6.67E-03	6.63E-03	6.59E-03	6.55E-03	6.51E-03	6.48E-03	6.29E-03
	E_5^{diff}	9.14E-03	9.12E-03	9.11E-03	9.09E-03	9.08E-03	9.07E-03	9.06E-03	9.05E-03	9.04E-03	8.78E-03
	E_6^{diff}	9.84E-03	9.80E-03	9.75E-03	9.72E-03	9.68E-03	9.65E-03	9.61E-03	9.59E-03	9.56E-03	9.30E-03
	E_7^{diff}	1.07E-02	1.07E-02	1.07E-02	1.06E-02	1.06E-02	1.06E-02	1.06E-02	1.05E-02	1.05E-02	1.04E-02
	E_8^{diff}	1.05E-02	1.05E-02	1.05E-02	1.05E-02	1.05E-02	1.06E-02	1.06E-02	1.06E-02	1.06E-02	1.01E-02
δ_4^{diff}	E_1^{diff}	9.93E-04	9.60E-04	9.25E-04	8.88E-04	8.51E-04	8.13E-04	7.74E-04	7.36E-04	6.98E-04	6.78E-04
	E_2^{diff}	2.39E-03	2.37E-03	2.35E-03	2.33E-03	2.30E-03	2.28E-03	2.26E-03	2.23E-03	2.21E-03	2.16E-03
	E_3^{diff}	3.53E-03	3.51E-03	3.50E-03	3.48E-03	3.47E-03	3.45E-03	3.44E-03	3.42E-03	3.40E-03	3.36E-03
	E_4^{diff}	4.33E-03	4.31E-03	4.30E-03	4.28E-03	4.26E-03	4.24E-03	4.22E-03	4.19E-03	4.16E-03	4.06E-03
	E_5^{diff}	5.03E-03	5.00E-03	4.96E-03	4.93E-03	4.89E-03	4.86E-03	4.82E-03	4.79E-03	4.75E-03	4.51E-03
	E_6^{diff}	5.36E-03	5.37E-03	5.37E-03	5.38E-03	5.38E-03	5.39E-03	5.40E-03	5.41E-03	5.41E-03	5.28E-03
	E_7^{diff}	5.10E-03	5.10E-03	5.11E-03	5.11E-03	5.12E-03	5.13E-03	5.14E-03	5.15E-03	5.17E-03	4.94E-03
	E_8^{diff}	4.74E-03	4.75E-03	4.75E-03	4.75E-03	4.75E-03	4.75E-03	4.75E-03	4.75E-03	4.75E-03	4.59E-03
δ_5^{diff}	E_1^{diff}	4.38E-04	4.21E-04	4.03E-04	3.86E-04	3.69E-04	3.52E-04	3.35E-04	3.19E-04	3.03E-04	2.85E-04
	E_2^{diff}	1.74E-03	1.72E-03	1.69E-03	1.66E-03	1.63E-03	1.60E-03	1.57E-03	1.53E-03	1.50E-03	1.48E-03
	E_3^{diff}	2.14E-03	2.13E-03	2.13E-03	2.12E-03	2.12E-03	2.11E-03	2.11E-03	2.10E-03	2.09E-03	2.06E-03
	E_4^{diff}	2.74E-03	2.73E-03	2.72E-03	2.71E-03	2.69E-03	2.68E-03	2.67E-03	2.66E-03	2.65E-03	2.71E-03
	E_5^{diff}	3.06E-03	3.03E-03	3.00E-03	2.97E-03	2.94E-03	2.91E-03	2.88E-03	2.85E-03	2.82E-03	2.68E-03
	E_6^{diff}	2.98E-03	3.00E-03	3.01E-03	3.02E-03	3.04E-03	3.05E-03	3.07E-03	3.08E-03	3.09E-03	3.05E-03
	E_7^{diff}	2.70E-03	2.70E-03	2.70E-03	2.70E-03	2.70E-03	2.70E-03	2.70E-03	2.70E-03	2.70E-03	2.61E-03
	E_8^{diff}	2.49E-03	2.51E-03	2.52E-03	2.53E-03	2.55E-03	2.57E-03	2.58E-03	2.60E-03	2.62E-03	2.59E-03
δ_6^{diff}	E_1^{diff}	2.36E-04	2.27E-04	2.18E-04	2.09E-04	2.00E-04	1.90E-04	1.81E-04	1.71E-04	1.62E-04	1.53E-04
	E_2^{diff}	7.38E-04	7.20E-04	7.02E-04	6.83E-04	6.63E-04	6.44E-04	6.24E-04	6.05E-04	5.86E-04	5.62E-04
	E_3^{diff}	9.43E-04	9.40E-04	9.37E-04	9.33E-04	9.30E-04	9.26E-04	9.21E-04	9.17E-04	9.13E-04	8.36E-04
	E_4^{diff}	1.19E-03	1.19E-03	1.18E-03	1.17E-03	1.17E-03	1.16E-03	1.15E-03	1.14E-03	1.14E-03	1.14E-03
	E_5^{diff}	1.22E-03	1.22E-03	1.23E-03	1.24E-03	1.24E-03	1.25E-03	1.26E-03	1.28E-03	1.29E-03	1.29E-03
	E_6^{diff}	1.38E-03	1.38E-03	1.39E-03	1.39E-03	1.39E-03	1.39E-03	1.39E-03	1.39E-03	1.39E-03	1.31E-03
	E_7^{diff}	1.18E-03	1.18E-03	1.18E-03	1.17E-03	1.17E-03	1.17E-03	1.17E-03	1.17E-03	1.18E-03	1.10E-03
	E_8^{diff}	1.01E-03	1.01E-03	1.01E-03	1.02E-03	1.02E-03	1.02E-03	1.02E-03	1.03E-03	1.03E-03	1.02E-03

Table F.7: The spectrum, energy and angle dependency of the energy averaged effective muon area.

$\sin(\delta_\nu)$	E_ν	Neutrino Energy Spectrum									
		$\gamma = -1.0$	$\gamma = -1.25$	$\gamma = -1.5$	$\gamma = -1.75$	$\gamma = -2.0$	$\gamma = -2.25$	$\gamma = -2.5$	$\gamma = -2.75$	$\gamma = -3.0$	atmospheric
$\overline{\sin(\delta)}$	E_1^{diff}	1.03E-11	9.55E-12	8.80E-12	8.07E-12	7.39E-12	6.74E-12	6.14E-12	5.58E-12	5.06E-12	5.17E-17
	E_2^{diff}	1.87E-10	1.77E-10	1.67E-10	1.58E-10	1.49E-10	1.41E-10	1.33E-10	1.25E-10	1.18E-10	1.10E-16
	E_3^{diff}	1.73E-09	1.65E-09	1.57E-09	1.49E-09	1.42E-09	1.35E-09	1.28E-09	1.22E-09	1.16E-09	9.03E-17
	E_4^{diff}	1.17E-08	1.12E-08	1.08E-08	1.03E-08	9.88E-09	9.48E-09	9.10E-09	8.74E-09	8.40E-09	4.95E-17
	E_5^{diff}	5.79E-08	5.59E-08	5.40E-08	5.21E-08	5.03E-08	4.86E-08	4.70E-08	4.55E-08	4.40E-08	1.59E-17
	E_6^{diff}	1.92E-07	1.88E-07	1.84E-07	1.79E-07	1.75E-07	1.71E-07	1.68E-07	1.64E-07	1.61E-07	3.13E-18
	E_7^{diff}	4.54E-07	4.46E-07	4.38E-07	4.31E-07	4.23E-07	4.16E-07	4.09E-07	4.03E-07	3.97E-07	3.61E-19
	E_8^{diff}	7.64E-07	7.58E-07	7.52E-07	7.46E-07	7.40E-07	7.35E-07	7.30E-07	7.25E-07	7.20E-07	3.11E-20
$\overline{\sin(\delta)}$	E_1^{int}	1.65E-07	5.04E-08	1.13E-08	2.28E-09	4.81E-10	1.14E-10	3.15E-11	1.03E-11	3.91E-12	3.57E-17
	E_2^{int}	2.12E-07	9.56E-08	3.60E-08	1.28E-08	4.79E-09	2.00E-09	9.67E-10	5.41E-10	3.45E-10	3.84E-17
	E_3^{int}	2.96E-07	1.92E-07	1.17E-07	7.04E-08	4.40E-08	2.94E-08	2.12E-08	1.64E-08	1.34E-08	1.38E-17
	E_4^{int}	4.70E-07	4.10E-07	3.55E-07	3.09E-07	2.71E-07	2.41E-07	2.18E-07	2.01E-07	1.87E-07	1.18E-18
δ_1^{diff}	E_1^{int}	3.61E-07	1.15E-07	2.68E-08	5.68E-09	1.25E-09	3.06E-10	8.67E-11	2.87E-11	1.10E-11	8.54E-17
	E_2^{int}	4.64E-07	2.18E-07	8.59E-08	3.20E-08	1.24E-08	5.38E-09	2.66E-09	1.52E-09	9.78E-10	9.20E-17
	E_3^{int}	6.49E-07	4.39E-07	2.78E-07	1.74E-07	1.13E-07	7.76E-08	5.71E-08	4.47E-08	3.69E-08	2.95E-17
	E_4^{int}	1.02E-06	9.18E-07	8.22E-07	7.35E-07	6.62E-07	6.03E-07	5.55E-07	5.17E-07	4.87E-07	2.13E-18
δ_2^{diff}	E_1^{int}	3.97E-07	1.19E-07	2.58E-08	5.06E-09	1.03E-09	2.38E-10	6.45E-11	2.07E-11	7.79E-12	6.59E-17
	E_2^{int}	5.10E-07	2.25E-07	8.25E-08	2.85E-08	1.03E-08	4.20E-09	1.99E-09	1.10E-09	7.01E-10	7.26E-17
	E_3^{int}	7.13E-07	4.53E-07	2.69E-07	1.57E-07	9.53E-08	6.22E-08	4.41E-08	3.37E-08	2.73E-08	2.50E-17
	E_4^{int}	1.14E-06	9.80E-07	8.34E-07	7.11E-07	6.12E-07	5.36E-07	4.78E-07	4.34E-07	4.02E-07	2.05E-18
δ_3^{diff}	E_1^{int}	2.54E-07	7.68E-08	1.69E-08	3.37E-09	7.01E-10	1.64E-10	4.48E-11	1.45E-11	5.52E-12	5.06E-17
	E_2^{int}	3.26E-07	1.46E-07	5.42E-08	1.90E-08	6.98E-09	2.88E-09	1.37E-09	7.64E-10	4.87E-10	5.45E-17
	E_3^{int}	4.56E-07	2.93E-07	1.76E-07	1.04E-07	6.43E-08	4.25E-08	3.03E-08	2.32E-08	1.89E-08	1.94E-17
	E_4^{int}	7.27E-07	6.29E-07	5.39E-07	4.63E-07	4.02E-07	3.54E-07	3.17E-07	2.90E-07	2.69E-07	1.63E-18
δ_4^{diff}	E_1^{int}	1.48E-07	4.50E-08	1.00E-08	2.03E-09	4.29E-10	1.02E-10	2.83E-11	9.34E-12	3.63E-12	3.90E-17
	E_2^{int}	1.91E-07	8.55E-08	3.21E-08	1.14E-08	4.27E-09	1.79E-09	8.61E-10	4.80E-10	3.05E-10	3.96E-17
	E_3^{int}	2.66E-07	1.72E-07	1.04E-07	6.26E-08	3.92E-08	2.63E-08	1.90E-08	1.48E-08	1.21E-08	1.51E-17
	E_4^{int}	4.23E-07	3.67E-07	3.16E-07	2.74E-07	2.40E-07	2.14E-07	1.94E-07	1.79E-07	1.68E-07	1.32E-18
δ_5^{diff}	E_1^{int}	9.76E-08	2.96E-08	6.57E-09	1.33E-09	2.80E-10	6.63E-11	1.83E-11	5.91E-12	2.24E-12	2.79E-17
	E_2^{int}	1.25E-07	5.62E-08	2.10E-08	7.47E-09	2.79E-09	1.17E-09	5.62E-10	3.13E-10	1.99E-10	3.09E-17
	E_3^{int}	1.75E-07	1.13E-07	6.84E-08	4.11E-08	2.57E-08	1.73E-08	1.25E-08	9.71E-09	7.96E-09	1.27E-17
	E_4^{int}	2.78E-07	2.40E-07	2.06E-07	1.77E-07	1.55E-07	1.37E-07	1.24E-07	1.15E-07	1.08E-07	1.17E-18
δ_6^{diff}	E_1^{int}	5.42E-08	1.62E-08	3.54E-09	6.99E-10	1.43E-10	3.25E-11	8.64E-12	2.71E-12	1.01E-12	1.52E-17
	E_2^{int}	6.97E-08	3.08E-08	1.13E-08	3.93E-09	1.42E-09	5.73E-10	2.65E-10	1.42E-10	8.71E-11	1.63E-17
	E_3^{int}	9.75E-08	6.21E-08	3.70E-08	2.17E-08	1.33E-08	8.67E-09	6.12E-09	4.64E-09	3.74E-09	7.83E-18
	E_4^{int}	1.56E-07	1.34E-07	1.15E-07	9.87E-08	8.59E-08	7.60E-08	6.86E-08	6.29E-08	5.86E-08	9.58E-19

Table F.8: The spectrum, energy and angle dependency of the energy averaged effective neutrino area.

$\sin(\delta_\nu)$	E_ν	Neutrino Energy Spectrum									
		$\gamma=-1.0$	$\gamma=-1.25$	$\gamma=-1.5$	$\gamma=-1.75$	$\gamma=-2.0$	$\gamma=-2.25$	$\gamma=-2.5$	$\gamma=-2.75$	$\gamma=-3.0$	atmospheric
δ_1^{diff}	E_1^{diff}	2.89E-11	2.67E-11	2.45E-11	2.24E-11	2.05E-11	1.86E-11	1.69E-11	1.53E-11	1.39E-11	1.24E-16
	E_2^{diff}	5.33E-10	5.04E-10	4.77E-10	4.50E-10	4.24E-10	4.00E-10	3.77E-10	3.55E-10	3.35E-10	2.72E-16
	E_3^{diff}	5.01E-09	4.78E-09	4.56E-09	4.34E-09	4.13E-09	3.94E-09	3.75E-09	3.57E-09	3.41E-09	2.24E-16
	E_4^{diff}	3.27E-08	3.14E-08	3.02E-08	2.90E-08	2.78E-08	2.67E-08	2.56E-08	2.46E-08	2.37E-08	1.09E-16
	E_5^{diff}	1.56E-07	1.50E-07	1.45E-07	1.40E-07	1.36E-07	1.31E-07	1.27E-07	1.23E-07	1.19E-07	3.19E-17
	E_6^{diff}	5.11E-07	4.99E-07	4.88E-07	4.77E-07	4.66E-07	4.56E-07	4.46E-07	4.37E-07	4.28E-07	5.73E-18
	E_7^{diff}	1.08E-06	1.06E-06	1.05E-06	1.04E-06	1.03E-06	1.02E-06	1.01E-06	9.95E-07	9.84E-07	6.12E-19
	E_8^{diff}	1.47E-06	1.47E-06	1.47E-06	1.47E-06	1.46E-06	1.46E-06	1.46E-06	1.46E-06	1.46E-06	4.17E-20
δ_2^{diff}	E_1^{diff}	1.83E-11	1.68E-11	1.55E-11	1.42E-11	1.29E-11	1.18E-11	1.07E-11	9.67E-12	8.74E-12	8.50E-17
	E_2^{diff}	3.79E-10	3.59E-10	3.40E-10	3.22E-10	3.04E-10	2.87E-10	2.72E-10	2.57E-10	2.43E-10	2.12E-16
	E_3^{diff}	3.42E-09	3.26E-09	3.11E-09	2.96E-09	2.82E-09	2.68E-09	2.55E-09	2.43E-09	2.32E-09	1.71E-16
	E_4^{diff}	2.35E-08	2.26E-08	2.16E-08	2.07E-08	1.99E-08	1.90E-08	1.83E-08	1.76E-08	1.69E-08	9.04E-17
	E_5^{diff}	1.18E-07	1.14E-07	1.10E-07	1.06E-07	1.03E-07	9.91E-08	9.59E-08	9.28E-08	9.00E-08	2.85E-17
	E_6^{diff}	4.06E-07	3.96E-07	3.87E-07	3.77E-07	3.68E-07	3.60E-07	3.51E-07	3.44E-07	3.37E-07	5.41E-18
	E_7^{diff}	1.06E-06	1.04E-06	1.02E-06	1.00E-06	9.83E-07	9.65E-07	9.47E-07	9.29E-07	9.13E-07	6.87E-19
	E_8^{diff}	1.96E-06	1.94E-06	1.92E-06	1.90E-06	1.88E-06	1.86E-06	1.84E-06	1.82E-06	1.80E-06	6.09E-20
δ_3^{diff}	E_1^{diff}	1.57E-11	1.44E-11	1.32E-11	1.21E-11	1.10E-11	9.94E-12	8.98E-12	8.09E-12	7.26E-12	7.39E-17
	E_2^{diff}	2.72E-10	2.57E-10	2.43E-10	2.29E-10	2.16E-10	2.04E-10	1.92E-10	1.81E-10	1.71E-10	1.60E-16
	E_3^{diff}	2.41E-09	2.29E-09	2.17E-09	2.06E-09	1.96E-09	1.86E-09	1.77E-09	1.68E-09	1.60E-09	1.24E-16
	E_4^{diff}	1.59E-08	1.52E-08	1.46E-08	1.40E-08	1.34E-08	1.29E-08	1.24E-08	1.19E-08	1.14E-08	6.84E-17
	E_5^{diff}	8.50E-08	8.21E-08	7.94E-08	7.67E-08	7.42E-08	7.17E-08	6.94E-08	6.72E-08	6.52E-08	2.35E-17
	E_6^{diff}	2.76E-07	2.69E-07	2.62E-07	2.56E-07	2.49E-07	2.44E-07	2.38E-07	2.33E-07	2.28E-07	4.32E-18
	E_7^{diff}	6.98E-07	6.83E-07	6.68E-07	6.54E-07	6.41E-07	6.28E-07	6.16E-07	6.04E-07	5.94E-07	5.29E-19
	E_8^{diff}	1.21E-06	1.20E-06	1.19E-06	1.18E-06	1.17E-06	1.16E-06	1.15E-06	1.14E-06	1.13E-06	4.47E-20
δ_4^{diff}	E_1^{diff}	1.17E-11	1.09E-11	1.01E-11	9.40E-12	8.69E-12	8.02E-12	7.39E-12	6.80E-12	6.25E-12	7.15E-17
	E_2^{diff}	1.49E-10	1.42E-10	1.35E-10	1.28E-10	1.22E-10	1.16E-10	1.10E-10	1.05E-10	9.96E-11	1.06E-16
	E_3^{diff}	1.58E-09	1.50E-09	1.42E-09	1.35E-09	1.28E-09	1.22E-09	1.15E-09	1.10E-09	1.04E-09	9.54E-17
	E_4^{diff}	1.07E-08	1.03E-08	9.87E-09	9.48E-09	9.10E-09	8.73E-09	8.38E-09	8.04E-09	7.73E-09	5.45E-17
	E_5^{diff}	5.18E-08	4.99E-08	4.80E-08	4.63E-08	4.45E-08	4.29E-08	4.14E-08	3.99E-08	3.85E-08	1.70E-17
	E_6^{diff}	1.72E-07	1.68E-07	1.65E-07	1.61E-07	1.58E-07	1.55E-07	1.52E-07	1.49E-07	1.46E-07	3.53E-18
	E_7^{diff}	3.89E-07	3.81E-07	3.74E-07	3.67E-07	3.61E-07	3.55E-07	3.49E-07	3.43E-07	3.38E-07	3.78E-19
	E_8^{diff}	7.09E-07	7.01E-07	6.92E-07	6.84E-07	6.75E-07	6.67E-07	6.59E-07	6.51E-07	6.44E-07	3.36E-20
δ_5^{diff}	E_1^{diff}	5.06E-12	4.69E-12	4.34E-12	4.01E-12	3.70E-12	3.41E-12	3.15E-12	2.90E-12	2.67E-12	3.33E-17
	E_2^{diff}	1.11E-10	1.05E-10	9.89E-11	9.31E-11	8.75E-11	8.23E-11	7.73E-11	7.27E-11	6.84E-11	8.44E-17
	E_3^{diff}	9.50E-10	9.05E-10	8.62E-10	8.20E-10	7.80E-10	7.41E-10	7.05E-10	6.71E-10	6.38E-10	6.83E-17
	E_4^{diff}	7.19E-09	6.89E-09	6.59E-09	6.31E-09	6.04E-09	5.78E-09	5.54E-09	5.32E-09	5.11E-09	4.56E-17
	E_5^{diff}	3.59E-08	3.44E-08	3.30E-08	3.16E-08	3.02E-08	2.89E-08	2.77E-08	2.65E-08	2.54E-08	1.44E-17
	E_6^{diff}	1.08E-07	1.06E-07	1.04E-07	1.02E-07	1.00E-07	9.85E-08	9.68E-08	9.53E-08	9.38E-08	3.14E-18
	E_7^{diff}	2.48E-07	2.43E-07	2.39E-07	2.34E-07	2.29E-07	2.25E-07	2.21E-07	2.17E-07	2.13E-07	3.39E-19
	E_8^{diff}	4.78E-07	4.74E-07	4.70E-07	4.66E-07	4.63E-07	4.60E-07	4.57E-07	4.54E-07	4.52E-07	3.41E-20
δ_6^{diff}	E_1^{diff}	2.78E-12	2.59E-12	2.40E-12	2.22E-12	2.05E-12	1.88E-12	1.73E-12	1.58E-12	1.45E-12	2.18E-17
	E_2^{diff}	4.66E-11	4.36E-11	4.08E-11	3.81E-11	3.55E-11	3.31E-11	3.09E-11	2.88E-11	2.68E-11	3.95E-17
	E_3^{diff}	4.32E-10	4.11E-10	3.90E-10	3.70E-10	3.51E-10	3.32E-10	3.15E-10	2.99E-10	2.84E-10	3.56E-17
	E_4^{diff}	3.16E-09	3.03E-09	2.89E-09	2.76E-09	2.64E-09	2.52E-09	2.41E-09	2.31E-09	2.21E-09	2.53E-17
	E_5^{diff}	1.61E-08	1.56E-08	1.52E-08	1.47E-08	1.43E-08	1.39E-08	1.36E-08	1.32E-08	1.29E-08	1.10E-17
	E_6^{diff}	6.11E-08	5.98E-08	5.84E-08	5.71E-08	5.58E-08	5.45E-08	5.32E-08	5.19E-08	5.07E-08	2.54E-18
	E_7^{diff}	1.41E-07	1.37E-07	1.34E-07	1.31E-07	1.28E-07	1.26E-07	1.23E-07	1.21E-07	1.19E-07	3.01E-19
	E_8^{diff}	2.66E-07	2.63E-07	2.59E-07	2.56E-07	2.53E-07	2.50E-07	2.47E-07	2.45E-07	2.43E-07	3.08E-20

Table F.9: The spectrum, energy and angle dependency of the energy averaged effective neutrino area.

$\sin(\delta_\nu)$	E_ν	Neutrino Energy Spectrum									
		$\gamma=-1.0$	$\gamma=-1.25$	$\gamma=-1.5$	$\gamma=-1.75$	$\gamma=-2.0$	$\gamma=-2.25$	$\gamma=-2.5$	$\gamma=-2.75$	$\gamma=-3.0$	atmospheric
$\overline{\sin(\delta)}$	E_1^{diff}	2.44E-05	2.33E-05	2.23E-05	2.12E-05	2.00E-05	1.89E-05	1.78E-05	1.67E-05	1.57E-05	1.20E-05
	E_2^{diff}	4.01E-05	3.95E-05	3.90E-05	3.84E-05	3.78E-05	3.72E-05	3.65E-05	3.59E-05	3.53E-05	2.60E-05
	E_3^{diff}	4.21E-05	4.20E-05	4.19E-05	4.18E-05	4.17E-05	4.15E-05	4.14E-05	4.12E-05	4.11E-05	2.90E-05
	E_4^{diff}	4.58E-05	4.57E-05	4.55E-05	4.53E-05	4.51E-05	4.49E-05	4.47E-05	4.45E-05	4.42E-05	2.87E-05
	E_5^{diff}	4.82E-05	4.81E-05	4.80E-05	4.79E-05	4.79E-05	4.78E-05	4.77E-05	4.77E-05	4.76E-05	2.56E-05
	E_6^{diff}	4.82E-05	4.82E-05	4.82E-05	4.82E-05	4.82E-05	4.83E-05	4.83E-05	4.83E-05	4.83E-05	2.18E-05
	E_7^{diff}	4.33E-05	4.35E-05	4.36E-05	4.37E-05	4.38E-05	4.40E-05	4.41E-05	4.42E-05	4.44E-05	1.75E-05
	E_8^{diff}	3.39E-05	3.41E-05	3.43E-05	3.46E-05	3.48E-05	3.50E-05	3.52E-05	3.55E-05	3.57E-05	1.30E-05
$\overline{\sin(\delta)}$	E_1^{int}	1.62E-05	1.67E-05	1.70E-05	1.71E-05	1.63E-05	1.40E-05	1.02E-05	6.15E-06	3.35E-06	1.98E-06
	E_2^{int}	1.65E-05	1.70E-05	1.74E-05	1.75E-05	1.72E-05	1.64E-05	1.52E-05	1.38E-05	1.25E-05	8.12E-06
	E_3^{int}	1.82E-05	1.87E-05	1.92E-05	1.96E-05	1.98E-05	1.98E-05	1.95E-05	1.92E-05	1.89E-05	1.13E-05
	E_4^{int}	2.25E-05	2.31E-05	2.37E-05	2.43E-05	2.48E-05	2.53E-05	2.57E-05	2.60E-05	2.62E-05	1.17E-05
δ_1^{diff}	E_1^{int}	1.59E-04	1.51E-04	1.39E-04	1.23E-04	1.01E-04	7.37E-05	4.58E-05	2.49E-05	1.28E-05	8.94E-06
	E_2^{int}	1.67E-04	1.58E-04	1.46E-04	1.31E-04	1.14E-04	9.66E-05	8.08E-05	6.81E-05	5.85E-05	5.03E-05
	E_3^{int}	1.91E-04	1.82E-04	1.70E-04	1.58E-04	1.46E-04	1.34E-04	1.25E-04	1.18E-04	1.12E-04	1.02E-04
	E_4^{int}	2.50E-04	2.44E-04	2.38E-04	2.32E-04	2.27E-04	2.23E-04	2.19E-04	2.16E-04	2.14E-04	2.08E-04
δ_2^{diff}	E_1^{int}	1.42E-04	1.35E-04	1.25E-04	1.12E-04	9.45E-05	7.15E-05	4.64E-05	2.61E-05	1.37E-05	9.85E-06
	E_2^{int}	1.46E-04	1.39E-04	1.29E-04	1.17E-04	1.03E-04	8.77E-05	7.41E-05	6.32E-05	5.52E-05	4.86E-05
	E_3^{int}	1.63E-04	1.56E-04	1.47E-04	1.36E-04	1.25E-04	1.15E-04	1.07E-04	1.01E-04	9.56E-05	8.81E-05
	E_4^{int}	2.08E-04	2.03E-04	1.97E-04	1.91E-04	1.85E-04	1.80E-04	1.76E-04	1.72E-04	1.69E-04	1.61E-04
δ_3^{diff}	E_1^{int}	9.32E-05	9.16E-05	8.86E-05	8.31E-05	7.37E-05	5.89E-05	4.04E-05	2.37E-05	1.28E-05	9.46E-06
	E_2^{int}	9.54E-05	9.38E-05	9.08E-05	8.60E-05	7.89E-05	7.02E-05	6.14E-05	5.37E-05	4.77E-05	4.20E-05
	E_3^{int}	1.07E-04	1.05E-04	1.03E-04	9.93E-05	9.47E-05	8.97E-05	8.50E-05	8.08E-05	7.73E-05	7.09E-05
	E_4^{int}	1.37E-04	1.36E-04	1.35E-04	1.34E-04	1.33E-04	1.31E-04	1.30E-04	1.29E-04	1.28E-04	1.23E-04
δ_4^{diff}	E_1^{int}	5.74E-05	5.78E-05	5.77E-05	5.65E-05	5.27E-05	4.46E-05	3.22E-05	1.98E-05	1.11E-05	8.73E-06
	E_2^{int}	5.86E-05	5.90E-05	5.90E-05	5.81E-05	5.59E-05	5.20E-05	4.72E-05	4.23E-05	3.81E-05	3.46E-05
	E_3^{int}	6.58E-05	6.63E-05	6.67E-05	6.66E-05	6.58E-05	6.45E-05	6.28E-05	6.11E-05	5.96E-05	5.62E-05
	E_4^{int}	8.52E-05	8.61E-05	8.71E-05	8.82E-05	8.92E-05	9.02E-05	9.11E-05	9.18E-05	9.24E-05	9.06E-05
δ_5^{diff}	E_1^{int}	3.87E-05	3.95E-05	4.02E-05	4.03E-05	3.88E-05	3.41E-05	2.54E-05	1.57E-05	8.70E-06	7.08E-06
	E_2^{int}	3.93E-05	4.00E-05	4.08E-05	4.12E-05	4.08E-05	3.92E-05	3.65E-05	3.34E-05	3.05E-05	2.85E-05
	E_3^{int}	4.41E-05	4.50E-05	4.60E-05	4.68E-05	4.74E-05	4.75E-05	4.72E-05	4.67E-05	4.60E-05	4.57E-05
	E_4^{int}	5.71E-05	5.80E-05	5.91E-05	6.03E-05	6.15E-05	6.26E-05	6.37E-05	6.47E-05	6.56E-05	6.56E-05
δ_6^{diff}	E_1^{int}	2.31E-05	2.36E-05	2.43E-05	2.46E-05	2.41E-05	2.15E-05	1.61E-05	9.94E-06	5.44E-06	4.46E-06
	E_2^{int}	2.34E-05	2.39E-05	2.46E-05	2.51E-05	2.51E-05	2.43E-05	2.27E-05	2.06E-05	1.85E-05	1.67E-05
	E_3^{int}	2.59E-05	2.66E-05	2.74E-05	2.82E-05	2.88E-05	2.91E-05	2.91E-05	2.89E-05	2.85E-05	2.81E-05
	E_4^{int}	3.29E-05	3.37E-05	3.46E-05	3.56E-05	3.67E-05	3.77E-05	3.86E-05	3.93E-05	3.99E-05	3.84E-05

Table F.10: The spectrum, energy and angle dependency of the absolute statistical uncertainty on the energy averaged effective muon area.

$\sin(\delta_\nu)$	E_ν	Neutrino Energy Spectrum									
		$\gamma = -1.0$	$\gamma = -1.25$	$\gamma = -1.5$	$\gamma = -1.75$	$\gamma = -2.0$	$\gamma = -2.25$	$\gamma = -2.5$	$\gamma = -2.75$	$\gamma = -3.0$	atmospheric
δ_1^{diff}	E_1^{diff}	9.26E-05	8.83E-05	8.40E-05	7.95E-05	7.51E-05	7.07E-05	6.63E-05	6.21E-05	5.80E-05	5.52E-05
	E_2^{diff}	1.68E-04	1.65E-04	1.62E-04	1.59E-04	1.56E-04	1.53E-04	1.50E-04	1.47E-04	1.43E-04	1.39E-04
	E_3^{diff}	1.99E-04	1.98E-04	1.97E-04	1.96E-04	1.95E-04	1.94E-04	1.92E-04	1.91E-04	1.90E-04	1.85E-04
	E_4^{diff}	2.49E-04	2.48E-04	2.46E-04	2.45E-04	2.43E-04	2.41E-04	2.40E-04	2.38E-04	2.36E-04	2.29E-04
	E_5^{diff}	3.11E-04	3.10E-04	3.08E-04	3.07E-04	3.05E-04	3.04E-04	3.02E-04	3.01E-04	2.99E-04	2.90E-04
	E_6^{diff}	3.85E-04	3.85E-04	3.84E-04	3.83E-04	3.82E-04	3.81E-04	3.80E-04	3.79E-04	3.78E-04	3.73E-04
	E_7^{diff}	4.14E-04	4.13E-04	4.11E-04	4.10E-04	4.09E-04	4.07E-04	4.06E-04	4.05E-04	4.04E-04	3.92E-04
	E_8^{diff}	4.62E-04	4.60E-04	4.59E-04	4.58E-04	4.57E-04	4.55E-04	4.54E-04	4.53E-04	4.53E-04	4.47E-04
δ_2^{diff}	E_1^{diff}	9.54E-05	9.10E-05	8.64E-05	8.18E-05	7.72E-05	7.26E-05	6.81E-05	6.36E-05	5.92E-05	5.72E-05
	E_2^{diff}	1.67E-04	1.65E-04	1.63E-04	1.60E-04	1.58E-04	1.56E-04	1.53E-04	1.50E-04	1.48E-04	1.43E-04
	E_3^{diff}	1.81E-04	1.81E-04	1.80E-04	1.79E-04	1.79E-04	1.78E-04	1.77E-04	1.76E-04	1.75E-04	1.74E-04
	E_4^{diff}	2.21E-04	2.19E-04	2.18E-04	2.16E-04	2.14E-04	2.12E-04	2.11E-04	2.09E-04	2.08E-04	2.03E-04
	E_5^{diff}	2.67E-04	2.66E-04	2.65E-04	2.64E-04	2.63E-04	2.61E-04	2.60E-04	2.59E-04	2.58E-04	2.54E-04
	E_6^{diff}	3.07E-04	3.06E-04	3.05E-04	3.04E-04	3.03E-04	3.02E-04	3.01E-04	3.00E-04	2.99E-04	2.92E-04
	E_7^{diff}	3.40E-04	3.39E-04	3.39E-04	3.38E-04	3.37E-04	3.35E-04	3.34E-04	3.33E-04	3.32E-04	3.24E-04
	E_8^{diff}	3.74E-04	3.73E-04	3.72E-04	3.71E-04	3.70E-04	3.68E-04	3.67E-04	3.66E-04	3.65E-04	3.55E-04
δ_3^{diff}	E_1^{diff}	8.89E-05	8.48E-05	8.06E-05	7.63E-05	7.20E-05	6.75E-05	6.32E-05	5.88E-05	5.46E-05	5.19E-05
	E_2^{diff}	1.40E-04	1.38E-04	1.36E-04	1.35E-04	1.33E-04	1.31E-04	1.29E-04	1.27E-04	1.25E-04	1.20E-04
	E_3^{diff}	1.50E-04	1.49E-04	1.48E-04	1.47E-04	1.46E-04	1.45E-04	1.44E-04	1.44E-04	1.43E-04	1.36E-04
	E_4^{diff}	1.67E-04	1.66E-04	1.65E-04	1.64E-04	1.63E-04	1.62E-04	1.61E-04	1.60E-04	1.60E-04	1.55E-04
	E_5^{diff}	2.12E-04	2.12E-04	2.12E-04	2.11E-04	2.11E-04	2.11E-04	2.11E-04	2.10E-04	2.10E-04	2.04E-04
	E_6^{diff}	2.27E-04	2.26E-04	2.25E-04	2.24E-04	2.23E-04	2.23E-04	2.22E-04	2.21E-04	2.21E-04	2.15E-04
	E_7^{diff}	2.40E-04	2.39E-04	2.38E-04	2.38E-04	2.37E-04	2.36E-04	2.36E-04	2.36E-04	2.35E-04	2.32E-04
	E_8^{diff}	2.36E-04	2.36E-04	2.37E-04	2.37E-04	2.37E-04	2.37E-04	2.38E-04	2.38E-04	2.38E-04	2.28E-04
δ_4^{diff}	E_1^{diff}	7.50E-05	7.25E-05	9.25E-04	8.88E-04	8.51E-04	8.13E-04	7.74E-04	7.36E-04	6.98E-04	6.78E-04
	E_2^{diff}	2.39E-03	2.37E-03	2.35E-03	2.33E-03	2.30E-03	2.28E-03	2.26E-03	2.23E-03	2.21E-03	2.16E-03
	E_3^{diff}	3.53E-03	3.51E-03	3.50E-03	3.48E-03	3.47E-03	3.45E-03	3.44E-03	3.42E-03	3.40E-03	3.36E-03
	E_4^{diff}	4.33E-03	4.31E-03	4.30E-03	4.28E-03	4.26E-03	4.24E-03	4.22E-03	4.19E-03	4.16E-03	4.06E-03
	E_5^{diff}	5.03E-03	5.00E-03	4.96E-03	4.93E-03	4.89E-03	4.86E-03	4.82E-03	4.79E-03	4.75E-03	4.51E-03
	E_6^{diff}	5.36E-03	5.37E-03	5.37E-03	5.38E-03	5.38E-03	5.39E-03	5.40E-03	5.41E-03	5.41E-03	5.28E-03
	E_7^{diff}	5.10E-03	5.10E-03	5.11E-03	5.11E-03	5.12E-03	5.13E-03	5.14E-03	5.15E-03	5.17E-03	4.94E-03
	E_8^{diff}	4.74E-03	4.75E-03	4.75E-03	4.75E-03	4.75E-03	4.75E-03	4.75E-03	4.75E-03	4.75E-03	4.59E-03
δ_5^{diff}	E_1^{diff}	4.38E-04	4.21E-04	4.03E-04	3.86E-04	3.69E-04	3.52E-04	3.35E-04	3.19E-04	3.03E-04	2.85E-04
	E_2^{diff}	1.74E-03	1.72E-03	1.69E-03	1.66E-03	1.63E-03	1.60E-03	1.57E-03	1.53E-03	1.50E-03	1.48E-03
	E_3^{diff}	2.14E-03	2.13E-03	2.13E-03	2.12E-03	2.12E-03	2.11E-03	2.11E-03	2.10E-03	2.09E-03	2.06E-03
	E_4^{diff}	2.74E-03	2.73E-03	2.72E-03	2.71E-03	2.69E-03	2.68E-03	2.67E-03	2.66E-03	2.65E-03	2.71E-03
	E_5^{diff}	3.06E-03	3.03E-03	3.00E-03	2.97E-03	2.94E-03	2.91E-03	2.88E-03	2.85E-03	2.82E-03	2.68E-03
	E_6^{diff}	2.98E-03	3.00E-03	3.01E-03	3.02E-03	3.04E-03	3.05E-03	3.07E-03	3.08E-03	3.09E-03	3.05E-03
	E_7^{diff}	2.70E-03	2.70E-03	2.70E-03	2.70E-03	2.70E-03	2.70E-03	2.70E-03	2.70E-03	2.70E-03	2.61E-03
	E_8^{diff}	2.49E-03	2.51E-03	2.52E-03	2.53E-03	2.55E-03	2.57E-03	2.58E-03	2.60E-03	2.62E-03	2.59E-03
δ_6^{diff}	E_1^{diff}	2.36E-04	2.27E-04	2.18E-04	2.09E-04	2.00E-04	1.90E-04	1.81E-04	1.71E-04	1.62E-04	1.53E-04
	E_2^{diff}	7.38E-04	7.20E-04	7.02E-04	6.83E-04	6.63E-04	6.44E-04	6.24E-04	6.05E-04	5.86E-04	5.62E-04
	E_3^{diff}	9.43E-04	9.40E-04	9.37E-04	9.33E-04	9.30E-04	9.26E-04	9.21E-04	9.17E-04	9.13E-04	8.36E-04
	E_4^{diff}	1.19E-03	1.19E-03	1.18E-03	1.17E-03	1.17E-03	1.16E-03	1.15E-03	1.14E-03	1.14E-03	1.14E-03
	E_5^{diff}	1.22E-03	1.22E-03	1.23E-03	1.24E-03	1.24E-03	1.25E-03	1.26E-03	1.28E-03	1.29E-03	1.29E-03
	E_6^{diff}	1.38E-03	1.38E-03	1.39E-03	1.39E-03	1.39E-03	1.39E-03	1.39E-03	1.39E-03	1.39E-03	1.31E-03
	E_7^{diff}	1.18E-03	1.18E-03	1.18E-03	1.17E-03	1.17E-03	1.17E-03	1.17E-03	1.17E-03	1.18E-03	1.10E-03
	E_8^{diff}	1.01E-03	1.01E-03	1.01E-03	1.02E-03	1.02E-03	1.02E-03	1.02E-03	1.03E-03	1.03E-03	1.02E-03

Table F.11: The spectrum, energy and angle dependency of the absolute statistical uncertainty on the energy averaged effective muon area.

$\sin(\delta_\nu)$	E_ν	Neutrino Energy Spectrum									
		$\gamma = -1.0$	$\gamma = -1.25$	$\gamma = -1.5$	$\gamma = -1.75$	$\gamma = -2.0$	$\gamma = -2.25$	$\gamma = -2.5$	$\gamma = -2.75$	$\gamma = -3.0$	atmospheric
$\overline{\sin(\delta)}$	E_1^{diff}	2.92E-13	2.70E-13	2.49E-13	2.28E-13	2.09E-13	1.91E-13	1.73E-13	1.58E-13	1.43E-13	1.46E-18
	E_2^{diff}	2.49E-12	2.36E-12	2.23E-12	2.11E-12	1.99E-12	1.88E-12	1.77E-12	1.67E-12	1.58E-12	1.46E-18
	E_3^{diff}	1.78E-11	1.70E-11	1.62E-11	1.54E-11	1.46E-11	1.39E-11	1.32E-11	1.26E-11	1.20E-11	9.31E-19
	E_4^{diff}	1.05E-10	1.01E-10	9.70E-11	9.30E-11	8.92E-11	8.55E-11	8.21E-11	7.88E-11	7.58E-11	4.46E-19
	E_5^{diff}	4.89E-10	4.72E-10	4.56E-10	4.40E-10	4.25E-10	4.10E-10	3.97E-10	3.84E-10	3.72E-10	1.34E-19
	E_6^{diff}	1.53E-09	1.50E-09	1.46E-09	1.43E-09	1.40E-09	1.37E-09	1.34E-09	1.31E-09	1.28E-09	2.50E-20
	E_7^{diff}	3.42E-09	3.36E-09	3.30E-09	3.24E-09	3.19E-09	3.13E-09	3.08E-09	3.04E-09	2.99E-09	2.72E-21
	E_8^{diff}	5.45E-09	5.40E-09	5.36E-09	5.32E-09	5.28E-09	5.24E-09	5.21E-09	5.17E-09	5.14E-09	2.21E-22
$\overline{\sin(\delta)}$	E_1^{int}	5.32E-10	1.63E-10	3.64E-11	7.37E-12	1.56E-12	3.68E-13	1.02E-13	3.32E-14	1.27E-14	1.15E-19
	E_2^{int}	6.89E-10	3.11E-10	1.17E-10	4.18E-11	1.56E-11	6.52E-12	3.15E-12	1.76E-12	1.12E-12	1.25E-19
	E_3^{int}	1.05E-09	6.83E-10	4.15E-10	2.50E-10	1.56E-10	1.04E-10	7.53E-11	5.82E-11	4.76E-11	4.89E-20
	E_4^{int}	2.04E-09	1.78E-09	1.54E-09	1.34E-09	1.18E-09	1.05E-09	9.47E-10	8.71E-10	8.13E-10	5.11E-21
δ_1^{diff}	E_1^{int}	1.73E-09	5.49E-10	1.28E-10	2.71E-11	5.96E-12	1.46E-12	4.14E-13	1.37E-13	5.27E-14	4.08E-19
	E_2^{int}	2.23E-09	1.05E-09	4.13E-10	1.54E-10	5.97E-11	2.58E-11	1.28E-11	7.28E-12	4.70E-12	4.42E-19
	E_3^{int}	3.37E-09	2.28E-09	1.45E-09	9.06E-10	5.87E-10	4.03E-10	2.97E-10	2.32E-10	1.92E-10	1.54E-19
	E_4^{int}	6.38E-09	5.75E-09	5.15E-09	4.61E-09	4.15E-09	3.77E-09	3.48E-09	3.24E-09	3.05E-09	1.33E-20
δ_2^{diff}	E_1^{int}	2.61E-09	7.81E-10	1.70E-10	3.33E-11	6.81E-12	1.57E-12	4.25E-13	1.36E-13	5.13E-14	4.34E-19
	E_2^{int}	3.38E-09	1.49E-09	5.46E-10	1.89E-10	6.83E-11	2.78E-11	1.32E-11	7.29E-12	4.64E-12	4.80E-19
	E_3^{int}	5.12E-09	3.25E-09	1.93E-09	1.13E-09	6.84E-10	4.47E-10	3.16E-10	2.42E-10	1.96E-10	1.79E-19
	E_4^{int}	9.90E-09	8.50E-09	7.23E-09	6.16E-09	5.30E-09	4.64E-09	4.14E-09	3.77E-09	3.48E-09	1.78E-20
δ_3^{diff}	E_1^{int}	2.17E-09	6.57E-10	1.45E-10	2.89E-11	5.99E-12	1.40E-12	3.83E-13	1.24E-13	4.72E-14	4.33E-19
	E_2^{int}	2.81E-09	1.26E-09	4.67E-10	1.64E-10	6.02E-11	2.48E-11	1.18E-11	6.59E-12	4.19E-12	4.70E-19
	E_3^{int}	4.34E-09	2.79E-09	1.68E-09	9.93E-10	6.12E-10	4.04E-10	2.88E-10	2.21E-10	1.79E-10	1.84E-19
	E_4^{int}	8.65E-09	7.48E-09	6.42E-09	5.51E-09	4.78E-09	4.21E-09	3.78E-09	3.45E-09	3.20E-09	1.94E-20
δ_4^{diff}	E_1^{int}	1.68E-09	5.11E-10	1.14E-10	2.30E-11	4.86E-12	1.16E-12	3.22E-13	1.06E-13	4.12E-14	4.43E-19
	E_2^{int}	2.19E-09	9.81E-10	3.68E-10	1.31E-10	4.90E-11	2.05E-11	9.88E-12	5.51E-12	3.50E-12	4.54E-19
	E_3^{int}	3.41E-09	2.20E-09	1.33E-09	8.01E-10	5.01E-10	3.36E-10	2.44E-10	1.89E-10	1.55E-10	1.93E-19
	E_4^{int}	6.98E-09	6.05E-09	5.21E-09	4.51E-09	3.95E-09	3.52E-09	3.20E-09	2.96E-09	2.77E-09	2.17E-20
δ_5^{diff}	E_1^{int}	1.42E-09	4.30E-10	9.54E-11	1.93E-11	4.07E-12	9.62E-13	2.65E-13	8.59E-14	3.25E-14	4.05E-19
	E_2^{int}	1.84E-09	8.23E-10	3.08E-10	1.10E-10	4.09E-11	1.71E-11	8.24E-12	4.59E-12	2.91E-12	4.53E-19
	E_3^{int}	2.88E-09	1.85E-09	1.12E-09	6.73E-10	4.22E-10	2.83E-10	2.05E-10	1.59E-10	1.31E-10	2.08E-19
	E_4^{int}	5.93E-09	5.11E-09	4.39E-09	3.78E-09	3.30E-09	2.93E-09	2.65E-09	2.45E-09	2.30E-09	2.50E-20
δ_6^{diff}	E_1^{int}	1.13E-09	3.38E-10	7.38E-11	1.45E-11	2.97E-12	6.77E-13	1.80E-13	5.65E-14	2.09E-14	3.16E-19
	E_2^{int}	1.47E-09	6.49E-10	2.39E-10	8.27E-11	2.99E-11	1.20E-11	5.57E-12	2.99E-12	1.83E-12	3.43E-19
	E_3^{int}	2.28E-09	1.45E-09	8.63E-10	5.07E-10	3.10E-10	2.02E-10	1.43E-10	1.08E-10	8.72E-11	1.83E-19
	E_4^{int}	4.63E-09	3.98E-09	3.41E-09	2.93E-09	2.55E-09	2.26E-09	2.03E-09	1.87E-09	1.74E-09	2.84E-20

Table F.12: The spectrum, energy and angle dependency of the absolute statistical uncertainty on the energy averaged effective neutrino area.

$\sin(\delta_\nu)$	E_ν	Neutrino Energy Spectrum									
		$\gamma=-1.0$	$\gamma=-1.25$	$\gamma=-1.5$	$\gamma=-1.75$	$\gamma=-2.0$	$\gamma=-2.25$	$\gamma=-2.5$	$\gamma=-2.75$	$\gamma=-3.0$	atmospheric
δ_1^{diff}	E_1^{diff}	1.32E-12	1.22E-12	1.12E-12	1.02E-12	9.35E-13	8.51E-13	7.73E-13	7.00E-13	6.34E-13	5.66E-18
	E_2^{diff}	1.12E-11	1.06E-11	9.99E-12	9.43E-12	8.90E-12	8.39E-12	7.90E-12	7.45E-12	7.03E-12	5.71E-18
	E_3^{diff}	7.87E-11	7.51E-11	7.16E-11	6.82E-11	6.50E-11	6.18E-11	5.89E-11	5.61E-11	5.36E-11	3.52E-18
	E_4^{diff}	4.46E-10	4.29E-10	4.12E-10	3.96E-10	3.80E-10	3.64E-10	3.50E-10	3.36E-10	3.23E-10	1.49E-18
	E_5^{diff}	1.98E-09	1.92E-09	1.85E-09	1.79E-09	1.73E-09	1.67E-09	1.62E-09	1.57E-09	1.52E-09	4.07E-19
	E_6^{diff}	6.03E-09	5.90E-09	5.77E-09	5.64E-09	5.51E-09	5.39E-09	5.27E-09	5.16E-09	5.06E-09	6.77E-20
	E_7^{diff}	1.17E-08	1.16E-08	1.15E-08	1.13E-08	1.12E-08	1.11E-08	1.10E-08	1.08E-08	1.07E-08	6.67E-21
	E_8^{diff}	1.48E-08	1.47E-08	1.47E-08	1.47E-08	1.47E-08	1.47E-08	1.47E-08	1.47E-08	1.47E-08	4.19E-22
δ_2^{diff}	E_1^{diff}	1.17E-12	1.08E-12	9.95E-13	9.11E-13	8.32E-13	7.57E-13	6.87E-13	6.22E-13	5.62E-13	5.46E-18
	E_2^{diff}	1.05E-11	9.99E-12	9.46E-12	8.95E-12	8.46E-12	7.99E-12	7.55E-12	7.14E-12	6.76E-12	5.90E-18
	E_3^{diff}	7.42E-11	7.08E-11	6.74E-11	6.42E-11	6.11E-11	5.82E-11	5.54E-11	5.28E-11	5.03E-11	3.71E-18
	E_4^{diff}	4.42E-10	4.23E-10	4.06E-10	3.89E-10	3.73E-10	3.57E-10	3.43E-10	3.30E-10	3.17E-10	1.70E-18
	E_5^{diff}	2.06E-09	1.99E-09	1.92E-09	1.86E-09	1.79E-09	1.73E-09	1.68E-09	1.62E-09	1.57E-09	4.98E-19
	E_6^{diff}	6.68E-09	6.51E-09	6.35E-09	6.20E-09	6.05E-09	5.91E-09	5.77E-09	5.65E-09	5.53E-09	8.89E-20
	E_7^{diff}	1.60E-08	1.57E-08	1.54E-08	1.51E-08	1.48E-08	1.45E-08	1.43E-08	1.40E-08	1.38E-08	1.03E-20
	E_8^{diff}	2.71E-08	2.68E-08	2.66E-08	2.63E-08	2.60E-08	2.57E-08	2.55E-08	2.52E-08	2.50E-08	8.45E-22
δ_3^{diff}	E_1^{diff}	1.06E-12	9.78E-13	8.97E-13	8.19E-13	7.45E-13	6.75E-13	6.10E-13	5.49E-13	4.93E-13	5.02E-18
	E_2^{diff}	8.83E-12	8.36E-12	7.90E-12	7.45E-12	7.03E-12	6.62E-12	6.25E-12	5.89E-12	5.56E-12	5.21E-18
	E_3^{diff}	6.29E-11	5.98E-11	5.68E-11	5.40E-11	5.12E-11	4.86E-11	4.62E-11	4.40E-11	4.19E-11	3.25E-18
	E_4^{diff}	3.70E-10	3.55E-10	3.40E-10	3.26E-10	3.13E-10	3.00E-10	2.88E-10	2.77E-10	2.67E-10	1.59E-18
	E_5^{diff}	1.83E-09	1.77E-09	1.71E-09	1.66E-09	1.60E-09	1.55E-09	1.50E-09	1.45E-09	1.41E-09	5.08E-19
	E_6^{diff}	5.85E-09	5.70E-09	5.56E-09	5.42E-09	5.29E-09	5.16E-09	5.04E-09	4.93E-09	4.83E-09	9.15E-20
	E_7^{diff}	1.42E-08	1.39E-08	1.36E-08	1.33E-08	1.30E-08	1.27E-08	1.25E-08	1.23E-08	1.21E-08	1.07E-20
	E_8^{diff}	2.46E-08	2.44E-08	2.42E-08	2.40E-08	2.38E-08	2.36E-08	2.34E-08	2.33E-08	2.31E-08	9.09E-22
δ_4^{diff}	E_1^{diff}	8.77E-13	8.18E-13	7.61E-13	7.06E-13	6.53E-13	6.03E-13	5.56E-13	5.11E-13	4.70E-13	5.38E-18
	E_2^{diff}	6.35E-12	6.04E-12	5.74E-12	5.46E-12	5.18E-12	4.92E-12	4.68E-12	4.45E-12	4.24E-12	4.53E-18
	E_3^{diff}	5.18E-11	4.92E-11	4.67E-11	4.43E-11	4.21E-11	3.99E-11	3.79E-11	3.60E-11	3.43E-11	3.13E-18
	E_4^{diff}	3.15E-10	3.02E-10	2.91E-10	2.79E-10	2.68E-10	2.57E-10	2.47E-10	2.37E-10	2.28E-10	1.60E-18
	E_5^{diff}	1.45E-09	1.39E-09	1.34E-09	1.29E-09	1.25E-09	1.20E-09	1.16E-09	1.11E-09	1.08E-09	4.74E-19
	E_6^{diff}	4.72E-09	4.62E-09	4.53E-09	4.44E-09	4.35E-09	4.26E-09	4.18E-09	4.10E-09	4.02E-09	9.72E-20
	E_7^{diff}	1.11E-08	1.09E-08	1.06E-08	1.05E-08	1.03E-08	1.01E-08	9.93E-09	9.77E-09	9.63E-09	1.08E-20
	E_8^{diff}	2.12E-08	2.09E-08	2.06E-08	2.04E-08	2.01E-08	1.99E-08	1.97E-08	1.94E-08	1.92E-08	1.00E-21
δ_5^{diff}	E_1^{diff}	5.42E-13	5.03E-13	4.66E-13	4.30E-13	3.97E-13	3.66E-13	3.37E-13	3.11E-13	2.87E-13	3.57E-18
	E_2^{diff}	5.67E-12	5.36E-12	5.05E-12	4.75E-12	4.47E-12	4.20E-12	3.95E-12	3.71E-12	3.49E-12	4.30E-18
	E_3^{diff}	4.04E-11	3.85E-11	3.67E-11	3.49E-11	3.32E-11	3.15E-11	3.00E-11	2.85E-11	2.72E-11	2.91E-18
	E_4^{diff}	2.66E-10	2.54E-10	2.44E-10	2.33E-10	2.23E-10	2.14E-10	2.05E-10	1.96E-10	1.89E-10	1.68E-18
	E_5^{diff}	1.28E-09	1.23E-09	1.17E-09	1.12E-09	1.07E-09	1.03E-09	9.84E-10	9.43E-10	9.05E-10	5.14E-19
	E_6^{diff}	3.73E-09	3.66E-09	3.59E-09	3.53E-09	3.47E-09	3.41E-09	3.35E-09	3.29E-09	3.24E-09	1.09E-19
	E_7^{diff}	9.24E-09	9.06E-09	8.88E-09	8.71E-09	8.54E-09	8.38E-09	8.22E-09	8.07E-09	7.93E-09	1.26E-20
	E_8^{diff}	1.88E-08	1.86E-08	1.85E-08	1.83E-08	1.82E-08	1.81E-08	1.80E-08	1.79E-08	1.78E-08	1.34E-21
δ_6^{diff}	E_1^{diff}	4.01E-13	3.74E-13	3.47E-13	3.21E-13	2.96E-13	2.72E-13	2.50E-13	2.29E-13	2.09E-13	3.15E-18
	E_2^{diff}	3.67E-12	3.44E-12	3.22E-12	3.00E-12	2.80E-12	2.61E-12	2.43E-12	2.27E-12	2.11E-12	3.11E-18
	E_3^{diff}	2.65E-11	2.52E-11	2.39E-11	2.27E-11	2.15E-11	2.04E-11	1.94E-11	1.84E-11	1.75E-11	2.18E-18
	E_4^{diff}	1.74E-10	1.66E-10	1.59E-10	1.52E-10	1.45E-10	1.38E-10	1.32E-10	1.27E-10	1.21E-10	1.39E-18
	E_5^{diff}	8.38E-10	8.13E-10	7.89E-10	7.66E-10	7.45E-10	7.24E-10	7.05E-10	6.88E-10	6.72E-10	5.71E-19
	E_6^{diff}	2.92E-09	2.86E-09	2.79E-09	2.73E-09	2.67E-09	2.61E-09	2.54E-09	2.48E-09	2.43E-09	1.22E-19
	E_7^{diff}	7.33E-09	7.16E-09	7.00E-09	6.84E-09	6.69E-09	6.55E-09	6.42E-09	6.30E-09	6.18E-09	1.57E-20
	E_8^{diff}	1.46E-08	1.44E-08	1.42E-08	1.40E-08	1.38E-08	1.37E-08	1.35E-08	1.34E-08	1.33E-08	1.69E-21

Table F.13: The spectrum, energy and angle dependency of the absolute statistical uncertainty on the energy averaged effective neutrino area.

Acknowledgment

First of all, I am indebted to Michaela, my family and my friends for all their kind help, leniency and distractions during the past years. Without them I wouldn't have survived this.

The DESY-Zeuthen AMANDA group provided most of the support directly related to this work – be it supervising my work, physics discussions, sharing analysis efforts, providing software, proof-reading or any other support. It would be too much to give a detailed account of each single one's specific aid. Therefore I simply want to say thank you very much to Dr. Christopher Wiebusch, Dr. Christian Spiering, Dr. Peter Steffen, Markus Gaug, Dr. Peter Niessen, Dr. Ralf Wischnewski, Dr. Matthias Leuthold, Henrike Wissing, Dr. Adam Bouchta, Dr. Paolo Desiati, Marek Kowalski, Thorsten Schmidt, Sebastian Boeser, Tonio Hauschild, Dr. Ole Streicher, Dr. Matthieu Ribordy and Peter Sudhoff.

But also the rest of the AMANDA collaboration provided great assistance. In particular, I want to acknowledge the permanent feedback from our atmospheric neutrino partners in Madison (Dr. Robert Tyce de Young and Dr. Gary Hill), the discussions on the point source analysis techniques with Prof. Steven Barwick and Dr. Scott Young and the non-Zeuthen Monte Carlo simulation provided by Dr. Stephan Hundertmark, Patrik Ekström and others.

During my stay at the Gesamthochschule Wuppertal, Dr. Wolfgang Rhode, Andrea Silvestri, Heidi Bojahr and others assisted me in finding appropriate AGN catalogs. For this, many discussions on AGN physics and for the great early "warnings" of new HEGRA results, I am very thankful.

I also want to thank Prof. Wolfgang Biermann from the Max-Planck-Institut für Radioastronomie in Bonn for fruitful discussions on AGN theories and on his help in defining the AGN selection schemes used in section 11.2.

As mentioned in section 9.1.3, I undertook an effort to detect the shadow of the moon in down-going atmospheric muons. During this effort, Prof. Erwin Flückiger and his team from the university of Bern kindly provided a simulation of the propagation of charged cosmic rays in the earth magnetic field. Despite the unsuccessful outcome of that analysis, I want to say thanks a lot to them.

This research has made use of the NASA/IPAC Extragalactic Database (NED) which is operated by the Jet Propulsion Laboratory, California Institute of Technology, under contract with the National Aeronautics and Space Administration [180], of the SIMBAD database, operated at CDS, Strasbourg, France [65] and of the Astronomical Data Center (ADC) at NASA Goddard Space Flight Center [181].

Erklärung

Berlin, den . . . . . .

Hiermit erkläre ich, die Dissertation selbstständig und ohne unerlaubte fremde Hilfe angefertigt zu haben. Ich habe mich anderwärts nicht um einen Doktorgrad beworben und besitze einen entsprechenden Doktorgrad nicht. Ich erkläre die Kenntnisnahme der dem Verfahren zugrunde liegenden Promotionsordnung der Mathematisch-Naturwissenschaftlichen Fakultät I der Humboldt-Universität zu Berlin.

Alexander Prinz Biron von Curland

Curriculum Vitae

Personal Data

Name	:	Alexander Prinz Biron von Curland
Date of birth	:	18.09.1972, München, Germany
Residence	:	Berlin, Germany

Primary School

Sep. 1978	-	Jul. 1982	Rothbuchenschule, München, Germany

Secondary School

Sep. 1982	-	Jul. 1984	Theodolindengymnasium, München, Germany
Sep. 1984	-	Jul. 1988	Maria-Theresia-Gymnasium, München, Germany
Sep. 1988	-	Jul. 1989	Oundle Public School, Northhamptonshire, UK
Sep. 1989	-	Jul. 1991	Maria-Theresia-Gymnasium, München, Germany
		Jul. 1991	"Abitur" Examinations; Average Grade: 1.5

Military Service

Jul. 1991	-	Jun. 1992	Mountain Ranger, German Bundeswehr

University

Oct. 1992	-	Sep. 1994	"Grundstudium" at the Ruprecht-Karls-Universität, Heidelberg, Germany
		Jun. 1994	"Vordiplom" Examinations; Grade: 1.3
Sep. 1994	-	Jun. 1995	Edinburgh University, Edinburgh, UK
Oct. 1995	-	Mar. 1997	"Hauptstudium" at the Humboldt-Universität, Berlin Major Subjects: Particle- and Solid State Physics
Apr. 1997	-	Mar. 1998	"Diplomarbeit" at DESY Zeuthen, Germany; Titel: "On the Rejection of Atmospheric Muons in the AMANDA Detector"
		Mar. 1998	"Diplomabschluß"; Grade: 1.1
May 1998	-	Jan. 2002	Phd thesis at DESY Zeuthen, Germany; Titel: "Search for Atmospheric Muon-Neutrinos and Extraterrestric Neutrino Point Sources in the 1997 AMANDA-B10 Data"

Alexander Prinz Biron von Curland, Berlin, den . . . . . .

Publications

Refereed Journals

- Ahrens J. for the AMANDA Collaboration. "Search for Supernova Neutrino-Bursts with the AMANDA Detector". *Astroparticle Physics*, **16**(4):345–359 (2002). arXive:astro-ph/0105460.
- Andrés E. for the AMANDA Collaboration. "Observation of High Energy Neutrinos with Cherenkov detectors embedded in deep Antarctic Ice". *Nature*, **410**(6827):441–443 (2001).
- Andrés E. for the AMANDA Collaboration. "The AMANDA neutrino telescope: principle of operation and first results". *Astroparticle Physics*, **13**(1):1–20 (2000). arXive:astro-ph/9906203.

Diploma Thesis

- Biron A. "On the Rejection of Atmospheric Muons in the AMANDA Detector". Diploma thesis, Humboldt-Universität zu Berlin, Berlin, Germany (1998). URL `http://area51.berkeley.edu/manuscripts/`. DESY-THESIS-1998-014.

Conferences – Personally presented

- Biron A., Wischnewski R.P. for the AMANDA Collaboration. "Punktquellensuche mit dem AMANDA-Neutrinoteleskop". In "Verhandlungen", [82], page 67. T 601.6.
- Biron A. for the AMANDA Collaboration. "Neutrino-Kandidaten im AMANDA Detektor". In "Verhandlungen", [81], page 269. T 202.3.
- Biron A. for the AMANDA Collaboration. "Physics results from the AMANDA-B10 experiment". *Physics of Particles and Nuclei Letters*, **3**(106):7–20 (2001). Proceedings of the International Workshop on Non-Accelerator New Physics In Neutrino Observations (NANPino 2000), Dubna, Russia, July 2000.
- Biron A. "Application of Artificial Neural Networks for Background Rejection in AMANDA". In Spiering [216], pages 317–327.
- Biron A. for the AMANDA Collaboration. "Qualitätsfilterung von AMANDA-Ereignissen mit Hilfe neuronaler Netzwerke". In "Verhandlungen", [79], page 16. T 106.4.

AMANDA Internal reports

- Biron A., Leuthold M.J. and Wiebusch C.H.V. "First and Second Level Reconstruction of 97 Muon Data". *Internal report AIR/19990701*, AMANDA Collaboration (1999).
- Biron A., Leuthold M.J. and Wiebusch C.H.V. "Update on Level 1+2 processing of 97 muon data". *Internal report AIR/19990901*, AMANDA Collaboration (1999).
- Biron A., Leuthold M.J. and Wiebusch C.H.V. "Separation of ν_μ event candidates in AMANDA-B". *Internal report AIR/19990902*, AMANDA Collaboration (1999).
- Biron A. "Reconstruction Uncertainties due to Time Calibration Errors". *Internal report AIR/20001101*, AMANDA Collaboration (2000).
- Biron A. and Wissing H. "Impact of Varied OM Sensitivities on the AMANDA-B10 Analysis". *Internal report AIR/20001202*, AMANDA Collaboration (2000).

- Biron A. et al. "Analysis of Atmospheric Neutrinos in 97 Data". *Internal report AIR/20010501*, AMANDA Collaboration (2001).

Proposals to the DESY PRC

- Biron A. et al. "Upgrade of AMANDA-B towards AMANDA-II". Proposal to the DESY PRC, (1997).
  URL `http://www-zeuthen.desy.de/nuastro/publications/others/proposal_e.shtml`.
  Revised version.
- Biron A. et al. "Participation of DESY-Zeuthen in the IceCube Project". Proposal to the DESY PRC, DESY-Zeuthen, Germany (2001).

Conferences – Presented by Others – 2001

- Hill G.C. for the AMANDA Collaboration. "Results from AMANDA". In "Proceedings of the XXXVIth Recontres de Moriond on Electroweak Interactions and Unified Theories", (2001). arXive:astro-ph/0106064.
- Karle A. for the AMANDA Collaboration. "Results from AMANDA". In Baldo-Ceolin M., editor, "Proceedings of the 9th Internationsl Workshop on Neutrino Telescopes", volume 2, pages 569–580. Venice, Italy (2001). arXive:astro-ph/9906205.
- Kowalski M. for the AMANDA Collaboration. "Physics Results from the AMANDA Neutrino Detector". In "Proceedings of the International Europhysics Conference on High Energy Physics", Budapest, Hungary (2001). To be published in Journal of High Energy and Nuclear Physics, arXive:hep-ph/0112083.

AMANDA Contributions to the 36th DPG Frühjahrstagung

- Desiati P. for the AMANDA Collaboration. "Atmospheric Muon Angular Distribution at the South Pole". In "Verhandlungen", [82], page 36. T 201.5.
- Feser T. for the AMANDA Collaboration. "Ein neuer Trigger für das AMANDA-Neutrinoteleskop zur Erniedriegung der Energieschwelle". In "Verhandlungen", [82], page 65. T 508.1.
- the AMANDA Collaboration M.G. "Nachweis hochenergetischer atmosphärischer Neutrinos mit dem AMANDA-Teleskop". In "Verhandlungen", [82], page 66. T 601.2.
- Kowalski M. for the AMANDA Collaboration. "Suche nach kaskadenartigen Ereignissen im AMANDA-Detektor". In "Verhandlungen", [82], page 66. T 601.4.
- Leuthold M.J. for the AMANDA Collaboration. "Suche nach hochenergetischen Neutrinos mit dem AMANDA-B10 Detektor". In "Verhandlungen", [82], page 67. T 601.5.
- Neunhöffer T. for the AMANDA Collaboration. "Verbesserter Supernova-Nachweis mit dem AMANDA-Experiment". In "Verhandlungen", [82], page 67. T 601.7.
- Niessen P. for the AMANDA Collaboration. "Suche nach relativistischen magnetischen Monopolen mit dem AMANDA-Detektor". In "Verhandlungen", [82], page 56. T 406.3.
- Schmidt T. et al. "Analog-optische Signalübertragung mit großem dynamischem Bereich für AMANDA/IceCube". In "Verhandlungen", [82], page 58. T 408.1.
- Wiebusch C.H. for the AMANDA Collaboration. "Status des AMANDA-Experiments". In "Verhandlungen", [82], page 66. T 601.1.

- Wissing H., Leuthold M.J. for the AMANDA Collaboration. "Monte-Carlo-Studien zum IceCube-Detektor". In "Verhandlungen", [82], page 67. T 601.9.

AMANDA Contributions to the 27^{th} ICRC

- Bai X. for the AMANDA Collaboration. "Calibration and Survey of AMANDA with SPASE". In Heinzelmann et al. [116], pages 977–980. HE.208.
- Barwick S.W. for the AMANDA Collaboration. "Potential of AMANDA-II in HE neutrino astrophysics". In Heinzelmann et al. [116], pages 1101–1104. HE.2.05.2.
- Cowen D.F., Hanson K. for the AMANDA Collaboration. "Time Calibration of the AMANDA Neutrino Telescope with Cosmic Ray Muons". In Heinzelmann et al. [116], pages 1133–1136. HE.237.
- Desiati P., Rhode W. for the AMANDA Collaboration. "Analysis of Atmospheric Muons with AMANDA". In Heinzelmann et al. [116], pages 985–988. HE.205.
- Hardtke R., Barouch G. for the AMANDA Collaboration. "The AMANDA Search for High Energy Neutrinos from Gamma-Ray Bursts". In Heinzelmann et al. [116], pages 1121–1124. HE.232.
- de los Heros C.P. for the AMANDA Collaboration. "Search for Neutrinos from WIMP annihilations with the AMANDA detector". In Heinzelmann et al. [116], pages 1557–1557. HE.324.
- Hill G.C., Leuthold M.J. for the AMANDA Collaboration. "Search for a Diffuse Flux from Sources of High Energy Neutrinos with AMANDA-B10". In Heinzelmann et al. [116], pages 1113–1116. HE.2.03.08.
- Hundertmark S. for the AMANDA Collaboration. "A Method to Detect UHE Neutrinos with AMANDA". In Heinzelmann et al. [116], pages 1129–1132. HE.236.
- Neunöffer T. for the AMANDA Collaboration. "Supernova Neutrino-Burst Search with the AMANDA Detector". In Heinzelmann et al. [116], pages 1125–1128. HE.231.
- Niessen P., Spiering C. for the AMANDA Collaboration. "Search for Relativistic Monopoles with the AMANDA Detector". In Heinzelmann et al. [116], pages 1496–1498. HE.315.
- Taboada I., Kowalski M. for the AMANDA Collaboration. "Search for Cascade-like events in the AMANDA-B10 Detector". In Heinzelmann et al. [116], pages 1117–1120. HE.232.
- Wiebusch C.H.V. for the AMANDA Collaboration. "Observation of High Energy Atmospheric Neutrinos with AMANDA". In Heinzelmann et al. [116], pages 1109–1112. HE.2.03.07.
- Wischnewski R. for the AMANDA Collaboration. "Performance of the AMANDA-II detector". In Heinzelmann et al. [116], pages 1105–1108. HE.233.

IceCube Contributions to the 27^{th} ICRC

- Goldschmidt A. for the IceCube Collaboration. "The IceCube detector". In Heinzelmann et al. [116], pages 1237–1240. HE.2.05.01.
- Leuthold M.J. for the IceCube Collaboration. "Performance studies for IceCube". In Heinzelmann et al. [116], pages 1241–1241. HE.255.

- Spiering C. for the IceCube Collaboration. "Science potential of the IceCube detector". In Heinzelmann et al. [116], pages 1242–1245. HE.256.

Conferences – Presented by Others – 2000

- Barwick S.W. for the AMANDA Collaboration. "Results from the AMANDA High Energy Neutrino Detector". *Nuclear Physics B Proceedings Supplements*, **91**(1–3):423–430 (2001). Proceedings of the 19^{th} International Conference on Neutrino Physics and Astrophysics (Neutrino 2000), Sudburry, Canada, June 2000, ed. J. Law, R.W. Ollerhead and J.J. Simpson, arXive:astro-ph/0009242.

- Cowen D.F. for the AMANDA Collaboration. "Recent Results from AMANDA". In "Proceedings of the meeting of the Division of Particle Physics and Fields of the American Physical Society (DPF 2000)", Columbus, Ohio, USA (2000). To be published in International Journal of Modern Physics A.

- Edsjö J. for the AMANDA Collaboration. "WIMP Searches with AMANDA-B10". In "Proceedings of the 3^{rd} International Workshop on the Identification of Dark Matter (IDM 2000), York, United Kingdom, Sep. 2000", pages 499–505. World Scientific, Singapore, Singapore (2002). To be published, arXive:astro-ph/0012285.

- Karle A. for the AMANDA Collaboration. "Observation of High Energy Atmospheric Neutrinos with AMANDA". In "Proceedings of the 7^{th} Conference On Intersections Between Particle And Nuclear Physics (CIPANP 2000)", Quebec City, Canada (2000).

- Rhode W. for the AMANDA Collaboration. "Status of the Neutrino Telescope AMANDA: Monopoles and WIMP"s. In "Proceedings of the Third International Conference on Dark Matter in Astro and Particle Physics (dark 2000)", pages 699–706. Heidelberg, Germany (2000).

AMANDA Contributions to the 35^{th} DPG Frühjahrstagung

- Bouchta A., Wischnewski R.P. for the AMANDA Collaboration. "Seasonal variation of muon trigger rates". In "Verhandlungen", [81], page 283. T 402.1.

- Bouchta A. for the AMANDA Collaboration. "Overview over physics results from AMANDA". In "Verhandlungen", [81], page 269. T 202.2.

- Feser T. for the AMANDA Collaboration. "Verbesserung der Akzeptanz von AMANDA für niederenergetische Ereignisse". In "Verhandlungen", [81], page 283. T 402.5.

- Gaug M. for the AMANDA Collaboration. "Cutentwicklung und -prüfung bei AMANDA-B10". In "Verhandlungen", [81], page 283. T 402.6.

- Hellwig M. for the AMANDA Collaboration. "Ein neues Supernova-Datennahmesystem für AMANDA". In "Verhandlungen", [81], page 283. T 402.2.

- Kowalski M., Wiebusch C.H. for the AMANDA Collaboration. "Rekonstruktion von kaskadenartigen Ereignissen in AMANDA". In "Verhandlungen", [81], page 269. T 202.4.

- Silvestri A. for the AMANDA Collaboration. "Supernova-Analyse mit dem AMANDA-B10 Detektor". In "Verhandlungen", [81], page 283. T 402.3.

Conferences – Presented by Others – 1999

- Barwick S.W. for the AMANDA Collaboration. "Initial Results from the AMANDA High-Energy Neutrino Detector". *Nuclear Physics B Proceedings Supplements*, **87**(1–3):402–404 (2000). Proceedings of the Sixth International Workshop on Topics in Astroparticle and Underground Physics (TAUP 99), September 1999.
- Karle A. for the AMANDA Collaboration. "Observation of Atmospheric Neutrino Events with the AMANDA Experiment". In "Proceedings of the 17^{th} International Workshop on Weak Interactions and Neutrinos (WIN 99), Cape Town, South Africa, Jan. 1999, ed. C.A. Dominguez and R.D. Viollier", pages 258–262. World Scientific, Singapore, Singapore (2000). arXive:astro-ph/9904379.
- Miller T. for the AMANDA Collaboration. "From AMANDA to IceCube: Current and Future High Energy Neutrino Telescopes at the South Pole". In Domoskos G. and Kovesi-Domoskos S., editors, "Proceedings of the 23^{rd} Johns Hopkins Workshop on Current Problems in Particle Theory: Neutrinos In The New Millennium, Baltimore, USA, June 1999", pages 47–61. World Scientific, Singapore, Singapore (2000).
- Niessen P. for the AMANDA Collaboration. "Searching for relativistic magnetic monopoles with AMANDA-B10". In "6^{th} Topical Seminar on Neutrino and Astro-Particle Physics", San Miniato, Italy (1999).
- Spiering C. for the AMANDA Collaboration. "AMANDA: Status, Results and Future". In "Proceedings of the 8^{th} International Workshop on Neutrino Telescopes", volume 2, pages 63–79. Venice, Italy (1999). arXive:astro-ph/9906205.
- Wischnewski R.P. for the AMANDA Collaboration. "The AMANDA Neutrino Detector - Status Report". *Nuclear Physics B Proceedings Supplements*, **85**(1–3):141–145 (2000). Proceedings of the 6^{th} Topical Seminar on Neutrino and Astro-Particle Physics, San Miniato, Italy, May 1999, ed. G. Bruni and F.-L. Navarria and P. G. Pelfer.

AMANDA Contributions to the 34^{th} DPG Frühjahrstagung

- Leuthold M.J. for the AMANDA Collaboration. "Untersuchung verschiedener Konfigurationen für den IceCube-Detektor am Südpol". In "Verhandlungen", [80].
- Niessen P. for the AMANDA Collaboration. "Suche nach relativistischen magnetischen Monopolen mit AMANDA-B10". In "Verhandlungen", [80].
- Schmidt T. for the AMANDA Collaboration. "Entwurf eines digitalen optischen moduls für das AMANDA Experiment". In "Verhandlungen", [80].
- Spiering C. for the AMANDA Collaboration. "Status, Ergebnisse und Perspektiven von AMANDA und BAIKAL". In "Verhandlungen", [80].
- Wiebusch C.H. for the AMANDA Collaboration. "Suche nach neutrino-induzierten Myon-Ereignissen im AMANDA Experiment". In "Verhandlungen", [80].

AMANDA Contributions to the 26^{th} ICRC

- Bay R. for the AMANDA Collaboration. "AMANDA Search for High-Energy Neutrinos Accompanying Gamma Ray Bursts". In Kieda et al. [136], pages 225–228. HE.4.2.06.
- Bouchta A. for the AMANDA Collaboration. "Seasonal variations of the muon flux seen by AMANDA". In Kieda et al. [136], pages 108–111. HE.3.2.11.

- Dalberg E. for the AMANDA Collaboration. "Nearly Vertical Upgoing Muons in the AMANDA-B10 Detector". In Kieda et al. [136], pages 348–351. HE.5.3.06.
- Frichter G.M. for the RICE Collaboration and for the AMANDA Collaboration. "Status of the RICE Experiment". In Kieda et al. [136], pages 467–470. HE.6.3.12.
- Halzen F. for the AMANDA Collaboration. "From the First Neutrino Telescop, the Antarctic Muon and Neuitrino Detector Array AMANDA, to the IceCube Observatory". In Kieda et al. [136], pages 428–431. HE.6.3.01.
- Hill G. for the AMANDA Collaboration. "The AMANDA-B10 String Array". In Kieda et al. [136], pages 432–435. HE.6.3.02.
- Hundertmark S. for the AMANDA Collaboration. "Up- and Down-Going Muons in the AMANDA-B4 Prototype Detector". In Kieda et al. [136], pages 12–15. HE.3.1.06.
- Karle A. for the AMANDA Collaboration. "Observation of Atmospheric Neutrino Events with AMANDA". In Kieda et al. [136], pages 221–224. HE.4.2.05.
- Kim J.H. for the AMANDA Collaboration. "A Search for Point Sources of High Energy Neutrinos with the AMANDA Neutrino Telescope". In Kieda et al. [136], pages 196–199. HE.4.1.14.
- Miller T. for the SPASE Collaboration and for the AMANDA Collaboration. "Calibration of AMANDA with Coincident Events from SPASE-2". In Kieda et al. [136], pages 465–466. HE.6.3.11.
- Niessen P. for the AMANDA Collaboration. "Search for Relativistic Monopoles with the AMANDA Detector". In Kieda et al. [136], pages 344–347. HE.5.3.05.
- Wischnewski R.P. for the AMANDA Collaboration. "Supernova Burst Analysis with the AMANDA Neutrino Telescope". In Kieda et al. [136], pages 229–232. HE.4.2.07.
- Woschnagg K. for the AMANDA Collaboration. "Optical Properties of South Pole Ice at Depths from 140 to 2300 Meters". In Kieda et al. [136], pages 200–203. HE.4.1.15.

Conferences – Presented by Others – 1998

- Barwick S.W. for the AMANDA Collaboration. "Initial Results from the AMANDA High-Energy Neutrino Detector". In "Proceedings from the 29^{th} International Conference on High Energy Physics (ICHEP 98), Vancouver, Canada, July 1998", volume II, pages 1447–1452. World Scientific, Singapore, Singapore (1999).
- Bergström L. for the AMANDA Collaboration. "The Identification of Dark Matter". In Spooner N.J.C. and Kudryavtsev V., editors, "Proceedings of the Second International Conference on Dark Matter in Astro and Particle Physics (dark 1998), Sheffield, United Kingdom, 1998", page 501. World Scientific, Singapore, Singapore (1999).
- Halzen F. for the AMANDA Collaboration. "The AMANDA Neutrino Telescope and the Indirect Search for Dark Matter". *Physics Reports*, **307**:243–252 (1998). Proceedings of the 3^{rd} International Symposium on Sources and Detection of Dark Matter in the Universe (DM 98), Marina del Rey, California, USA, Feb. 1998 arXive:hep-ph/9804007.
- Halzen F. for the AMANDA Collaboration. "The AMANDA Neutrino Telescope". *Nuclear Physics B Proceedings Supplements*, **77**(1–3):474–485 (1999). Proceedings of the 18^{th} International Conference on Neutrino Physics and Astrophysics (Neutrino 98), Takayama, Japan, June 1998, arXive:astro-ph/9809025, MADPH-98-1078.

- de los Heros C.P. for the AMANDA Collaboration. "Preliminary Results from the AMANDA Neutrino Telescope". In Medina J., editor, "Proceedings of the 16^{th} European Cosmic Ray Symposium", Alcalá de Henares, Spain (1998).
- Wischnewski R.P. for the AMANDA Collaboration. "The AMANDA Neutrino Detector". *Nuclear Physics B Proceedings Supplements*, **75 A**(1–2):412–414 (1999). Proceedings of the 10^{th} International Symposium on Very High Energy Cosmic Ray Interactions, Gran Sasso, Italy, July 1998, ed. O. Saavedra and A. Castallina.

AMANDA Contributions to the 33^{th} DPG Frühjahrstagung

- Hundertmark S. for the AMANDA Collaboration. "Analyse der AMANDA-B Daten des Jahres 1996". In "Verhandlungen", [79], page 26. T 206.5.
- Niessen P. for the AMANDA Collaboration. "Das Datennahmesystem des AMANDA-II-Detektors". In "Verhandlungen", [79], page 26. T 206.3.
- Spiering C. for the AMANDA Collaboration. "Status des AMANDA-Experiments". In "Verhandlungen", [79], page 16. T 106.1.

Conferences – Presented by Others – 1997

- Hulth P.O. for the AMANDA Collaboration. "Status of the AMANDA experiment". *Nuclear Physics B Proceedings Supplements*, **70**(1–3):448–452 (1999). Proceedings of the Fifth International Workshop on Topics in Astroparticle and Underground Pysics (TAUP 97), September 1997.
- Price P.B. for the AMANDA Collaboration. "Latest Results from AMANDA". In Giraud-Heraud and Van [106], page 255.
- Wiebusch C.H. for the AMANDA Collaboration. "Neutrino Astronomy with AMANDA". In "Proceedings of the 4th SFB-375 Ringberg Workshop on Neutrino Astrophysics", pages 121–126. Ringberg Castle, Germany (1997).

AMANDA Contributions to the 25^{th} ICRC

- Barwick S.W. for the AMANDA Collaboration. "The Status of the AMANDA High-Energy Neutrino Detector". In Potgieter et al. [195], pages 1–4.
- Miller T. for the SPASE Collaboration and for the AMANDA Collaboration. "Analysis of SPASE-AMANDA Coincidence Events". In Potgieter et al. [195], pages 237–240.
- Porrata R.A. for the AMANDA Collaboration. "Analysis of Cascades in AMANDA-A". In Potgieter et al. [195], pages 9–12.
- Tilav S. for the AMANDA Collaboration. "First Look at AMANDA-B Data". In Potgieter et al. [195], pages 5–8.
- Wiebusch C.H.V. for the AMANDA Collaboration. "Muon Reconstruction with AMANDA-B". In Potgieter et al. [195], pages 13–16.